

Canadian Technical Report of Hydrography and Ocean Sciences 268

2010

## Current Surge through a Shelf Internal Tide

by

H. Sandstrom and J.A. Elliott

Ocean Sciences Division  
Maritimes Region  
Fisheries and Oceans Canada  
Bedford Institute of Oceanography  
1 Challenger Dr.  
Dartmouth, Nova Scotia  
Canada B2Y 4A2

© Her Majesty the Queen in Right of Canada. 2010  
Cat. No. Fs 97-18/268E ISSN 1488-5417

Correct citation for this publication:

Sandstrom, H. and Elliott J.A. 2010. Current Surge through a Shelf Internal Tide. Can. Tech. Rep. Hydrogr. Ocean Sci. 268: vii + 140pp.

## Table of Contents

Table of Contents.....	iii
Abstract.....	v
Résumé.....	v
Acknowledgements.....	vii
1. Introduction.....	1
2. Cruise Planning and Instrumentation.....	8
3. Scotian Gulf Potential Energy.....	10
3.1 Field Program.....	10
3.2 Gravitational Potential Energy Perturbation.....	13
3.3 Processing of Batfish Data.....	14
3.4 Extended Mean Density Field: Scotian Gulf.....	17
3.5 Potential Energy Contour Plots.....	20
3.6 Potential Energy Scatter Diagram.....	22
4. Grand Bank Potential Energy.....	23
4.1 Field Program.....	23
4.2 Processing of Batfish Data.....	25
4.3 Potential Energy Contour Plots.....	26
4.4 Potential Energy Scatter Diagram.....	28
5. The Gully Potential Energy.....	29
5.1 Field Program.....	29
5.2 Processing of Batfish Data.....	31
5.3 Potential Energy Contour Plots.....	32
5.4 Potential Energy Scatter Diagram.....	34
6. Modelling of Internal Tide and Comparison with Observations.....	36
6.1 Analytical Model.....	36
6.2 Comparison with Field Measurements.....	39
7. Batfish Sampling Scheme.....	47
7.1 Problems of Resolution?.....	47
7.2 Density Inversions, Apparent or Real?.....	51
7.3 Comparison with Mooring Data.....	58
8. Evidence for Non-linearity.....	60
8.1 The Non-linear PDE for Isopycnal Displacement.....	60
8.2 Evidence for Non-linearity in Long Waves.....	61
8.3 Groups of High Amplitude Internal(solitary) Waves, Internal Bores.....	64
9. Dissipation of Internal Wave Energy.....	69
10. Summary and Discussion.....	77
11. References.....	81
12. Appendices.....	84
Appendix 1 Aircraft SLAR Data.....	84
Appendix 2 Bow Drill Thermister Chain.....	88
Appendix 3 Data pitfalls, problems and solutions.....	104
Appendix 4 Stability of the Extended Mean Density Field.....	106
Appendix 5 Potential Energy Contour Plots.....	108

Appendix 6 Forcing Functions.....	121
Appendix 7 Current Meters and Analysis of Current.....	125
Appendix 8 CTD section in The Gully.....	137



## **Abstract**

Sandstrom, H. and Elliott J.A. 2010. Current Surge through a Shelf Internal Tide. Can. Tech. Rep. Hydrogr. Ocean Sci. 268: vii + 140pp.

An analysis of repeated transects of Batfish (CTD in an undulating body towed behind a ship) data reveals the spatial and temporal characteristics of the internal wave field, including the semi-diurnal internal tide. Field programs were carried out at three separate continental shelf edge sites off the Canadian east coast. The main aim of the investigation was to clarify the dynamics of the generation, transformation and dissipation of internal wave energy through an analysis of the potential energy budget in the water column. To accomplish this goal, mean density fields were constructed for the three sites, to which displacement could be referred. We describe the principal characteristics of estimated energy within a conceptual framework, where an internal tide is generated, propagates shoreward from the shelf edge, is transformed by non-linear effects (energy concentration in isopycnal depressions) into shorter undulations such as solitary waves and internal bores, and dissipates energy by shear instability. Turbulence and mixing is expected to occur as energy is lost. From our observations, the rate of energy dissipation is smallest on the Grand Bank, where the energy loss was  $0.007 \text{ Watts/m}^2$  over a 30 km decay distance. In the Scotian Gulf the loss rate was  $0.05 \text{ Watts/m}^2$  over a 13 km distance. At The Gully site, where the energy concentrations were the largest, dissipation was estimated to be as large as  $0.2 \text{ Watts/m}^2$  over a 10 km distance.

## **Résumé**

Sandstrom, H. and Elliott J.A. 2010. Current Surge through a Shelf Internal Tide. Can. Tech. Rep. Hydrogr. Ocean Sci. 268: vii + 140pp.

Une analyse de transects répétés de données Batfish (un instrument de mesure de la conductivité, de la température et de la profondeur [CTP] dans un poisson ondulant remorqué derrière un navire) révèle les caractéristiques spatiales et temporelles du champ d'onde interne, y compris la marée semi-diurne interne. Des programmes sur le terrain ont été réalisés à trois sites distincts en bordure de la plate-forme continentale au large de la côte Est du Canada. Le principal objectif de l'étude consistait à clarifier la dynamique de la génération, de la transformation et de la dissipation de l'énergie des ondes internes au moyen d'une analyse du bilan énergétique possible dans la colonne d'eau. Afin d'atteindre cet objectif, des champs de densité moyenne ont été élaborés pour les trois sites, afin de servir de référence pour le déplacement. Nous décrivons les principales caractéristiques de l'énergie estimée dans un cadre conceptuel, où l'onde interne est générée, se propage vers le rivage depuis la bordure de la plate-forme continentale, est transformée par des effets non linéaires (concentration de l'énergie dans des dépressions isopycniques) en ondulations plus courtes, notamment des ondes solitaires et des mascarets internes, et dissipe de l'énergie par instabilité de cisaillement. On peut s'attendre à de la turbulence et à un brassage à mesure que l'énergie est perdue. D'après nos observations, le taux de dissipation était le plus faible sur le Grand Banc, où la perte d'énergie était de  $0,007 \text{ watts/m}^2$  sur une distance d'amortissement de 30 km. Dans le golfe Scotian, le taux de dissipation était de  $0,05 \text{ watts/m}^2$  sur une distance de 13 km. Au

site du Goulet, où les concentrations d'énergie étaient les plus élevées, la dissipation a été estimée à 0,2 watts/m<sup>2</sup> sur une distance de 10 km.

## **Acknowledgements**

This study was part of the core program of the Dept. of Fisheries and Oceans at the Bedford Institute of Oceanography while we were career employees and were able to continue as emeritus scientists. We received additional funding support through the NRCan 'Panel on Energy Research and Development' program that allowed us to expand the Scotian Gulf initial field work and to include other sites and SLAR surveys. All field work was completed with the collaboration and fortitude of the officers and crew of the *C.S.S. Dawson*. Many staff and colleagues of the (now historical) Atlantic Oceanographic Laboratory, BIO, assisted our efforts and contributed in many ways to make the field work pleasant and rewarding. Much of the initial data processing was completed under contract through PERD funding; additional support from the DFO 'Marine Sciences Project' permitted us to develop a successful data analysis package with the assistance of Tineke van den Baren. Advice and support from many staff and colleagues was provided at various stages of analysis and report preparation; the colourful graphics are due to the assistance from fellow scientist Igor Yashayaev. Encouragement and support by John Loder is much appreciated.

## 1. Introduction

In the early 1980s the authors undertook a series of five cruises aboard the CSS Dawson to explore the connection between tidal currents and turbulent mixing at sites near the edge of the continental shelf. The zone of interest is the so-called ‘shelf break strip’, the narrow transition zone between continental shelf and oceanic waters. In addition to forming a flexible dynamic boundary between the coastal waters and the deeper waters off the shelf, it is also a prime site of production of internal tidal energy. The rapid change in tidal currents, especially on the steep upper slope, requires an appropriate vertical adjustment of the density field, i.e. the generation of an internal tide. The current shears of the internal (baroclinic) tidal fields, if large enough, are a source of instability and can cause turbulence and thus mixing, especially in those parts of the water column where the current shears are largest. This possibility of vertical mixing of the water column by the internal tides and the associated vertical transport of nutrients was the motivation for us to collect detailed data to study the connection between internal tides and turbulent mixing.

The initial cruise in 1980 (80-039) was centered at longitude  $63^{\circ} 30'$  W and the 200 m bathymetric contour, approximately 200 km south of Halifax. It was exploratory in nature, with an observational strategy based on the predictions of theoretical models in which the topographic interaction and the transfer of energy from the barotropic to the baroclinic tide could be described by two-dimensional and linear dynamics. The application of the models to realistic topography and stratification was facilitated by the use of the so-called ray (or characteristic) theory, which emphasized the importance of ‘critical’ and near-critical bottom slopes as sites of optimum topographic interaction (Baines 1974, Sandstrom 1976). The rays emanating from these sites were predicted to be the location of greatest current shears. Earlier work on internal tides near this site using data from moorings (Petrie 1975) indicated strong generation of an internal tide on the upper slope. From his analysis Petrie concluded that “The internal tide may be a significant source of mixing energy on the outer shelf.” He also concluded that this internal tide dissipated within about 10 km of the shelf break. Guided by the critical ray analysis we set out to measure turbulence levels with Octuprobe (Oakey 1977) along with CTD, thermistor-chain, and current measurements. Analysis of results of the first experiment showed that, rather than along the critical ray paths, the dominant current shear occurred at the base of the mixed layer, which was also where microstructure activity appeared most intense. Vertical displacements in the pycnocline were large enough to show that non-linearity of the internal tide must be taken into account in its generation and evolution.

We returned to the site in 1981 (81-042) to monitor events along a north-south line at  $63^{\circ} 30'$  W employing moorings, CTD surveys, Batfish tows, and acoustic sounder records. The observational strategy and tools were chosen with the previous experience in mind. The Batfish, a depth controlled towed body fitted with a CTD, had been under development at BIO over a number of years (Dessureault 1976) and by the early 1980s re-engineered by A.S. Bennett and colleagues in Metrology to facilitate spatial measurements of open ocean internal waves and oceanographic fronts (Bennett 1972).

Through this effort the Batfish was a robust and seaworthy instrument with capability of vertical and horizontal resolution suitable to monitor the shelf-edge internal tides over a tidal cycle. The objective was to delineate the spatial and temporal characteristics of the internal tide near the shelf break. While compiling data to this purpose, we became aware of numerous high-amplitude events, especially evident in the acoustic record (Sandstrom and Elliott 1984). Some of these could be identified as internal solitary waves. The indication was that a large fraction of the energy in internal tides appeared in the form of these high energy bursts. Because of their short duration and spatial extent, they are more readily dissipated and are probably the primary source of mixing in the shelf break zone. The tidal phase, propagation speed and duration of these events were consistent with expectations from theory and with observations by others of similar phenomena at other sites (Halpern 1971, Haury et al. 1979). (Note: the Batfish data from 81-042 has been lost from the BIO archive.)

A few years earlier Osborne and Burch (1980) had brought to the attention of the offshore oil industry a new environmental loading factor, namely internal waves. Wave-induced current could be strong enough to affect the positioning of, for example, a drill ship (Hodgins and Westergard 1981). Sometimes a 'surface-rip' – band of rough sea surface due to convergence of wave-induced current – was observed and the term 'tide rip' came to be associated with the current surges. There was expanding activity by the offshore oil industry along the Canadian East Coast continental shelves during this same time period, and we recognized a need for additional research into the nature of this newly found potential environmental hazard. The Office of Energy Research and Development (OERD) had an interest because of their concern for safety at oil drilling operations that could be impacted by current surges from high amplitude internal waves of the type we observed in the initial cruises. With financial support from OERD for operating expenses we were able to continue this series of studies.

Beginning in 1983 we undertook a more extensive survey of shelf-edge internal tides over a 3 year period. From various studies, including ours, it had become evident that a very close connection existed between the barotropic tidal field and the large-amplitude internal waves on continental shelves and other confined sea areas. Although it was not clear how the large amplitude waves were linked to the tidal field, their widespread occurrence could be predicted with certainty. The increased support enabled us to widen the scope of our studies to include additional experimental sites for ship-based observations, to add a remote sensing component to the ship-based studies, and to use a drilling rig as a platform to monitor short period temperature fluctuations in the water column. Embarking upon this expanded program, we posed the following questions:

1. How is some of the barotropic tidal energy converted into the short-lasting and short-wavelength intense packets of baroclinic energy?
2. How is this process influenced by bottom topography and density stratification?
3. Is the flow of energy first from barotropic to baroclinic tide and thence by way of non-linear and dispersive processes to short internal waves, or is the tidal interaction with topography itself an inherently unstable process?

4. Are there certain areas on the continental shelves where the process is more pronounced than elsewhere?

If we knew the answers to these questions, we would be able to better predict their occurrence under different environmental conditions and thus assess their importance as an environmental factor in a given region. Thus we set the scientific goals of the program as follows:

1. Observational mapping of the tidal fields (barotropic and baroclinic) in time and space; determination of the relationship between the baroclinic and barotropic tide.
2. Observational mapping of the packets of (or solitary) internal waves in time and space and their relation to the tidal field.
3. Construction of theoretical/numerical models of the tidal fields, including the processes that produce the short internal waves.
4. Acquisition of understanding of the process to be able to model and predict the 'hot spots' of internal wave activity.

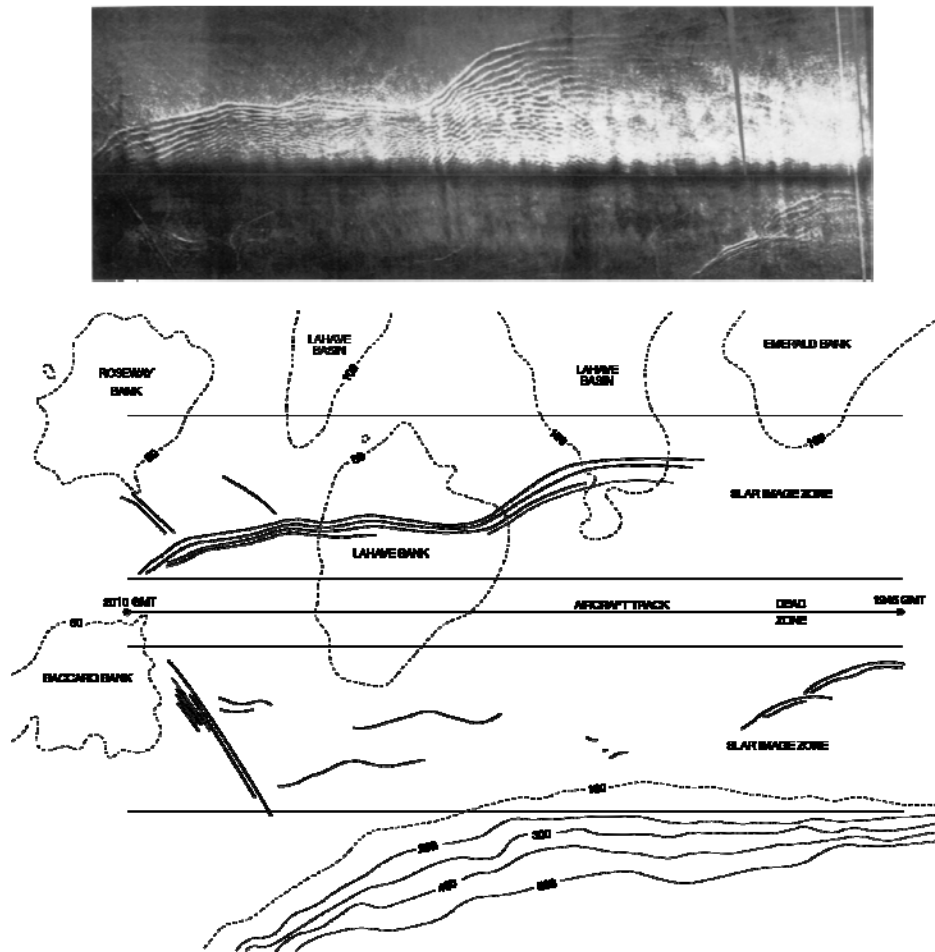


Figure 1.1: Top is SLAR imagery from the Scotian Shelf near 64°W. Below shows an interpretation of wave-fronts over topography; bottom contours are in metres.

During an experiment in late summer of 1983 at the same location at the edge of the Scotian Shelf as the first two experiments, we observed for a number of tidal cycles the complete sequence of generation of the internal tide by tidal flow–topography interaction, and the growth of large amplitude internal wave groups or occasionally internal solitary waves as the propagating internal tide was transformed. The eventual dissipation of the wave packets formed the final stage of the sequence. While carrying out the observation program, it was noted first visually and then on the ship’s X-band radar that a surface pattern of rough and smooth bands occurred at each crossing of the wave packet. Immediately following the ship-based experiment a research aircraft with a Side Looking Aperture Radar (SLAR) completed three flights over the Scotian Shelf. The SLAR system is roughly equivalent to the X-band shipboard radar, but capable of providing a wide swath image. Figure 1.1 is an example of SLAR imagery from one section of our first flight along the edge of the Scotia Shelf.

The SLAR image swath is approximately 60 kilometres wide with a dead zone directly below the aircraft about 10 kilometres wide. Overlain on the bathymetry is an interpretation of the leading edge of the wave groups. The type of banding/wave-group-structure observed and phase of tide for this image agree with the earlier findings from our ship-based observations. On the western half of the Scotian Shelf, where the bathymetry is fairly regular, the SLAR imagery clearly showed long-crested groups of waves aligned with isobaths. The pattern on the eastern Scotia Shelf was more confused with most of the ‘tide rip’ seen near the submarine canyons, particularly on the eastern flank of The Gully. From this initial flight, SLAR imagery was seen to be an excellent method for searching a broad area of a shelf for evidence of internal wave groups for a given tidal cycle. The following year (1984) two series of aircraft radar flights over the Scotian Shelf and the Grand Banks of Newfoundland confirmed the previous year’s findings on the Scotian Shelf and showed that on the Grand Banks the surface manifestations of internal waves generally extended along all edges of the banks with local ‘hot spots’ at the heads of the larger canyons along the southeast and southwest edge, whereas relatively long-crested waves were observed along the northeast slope and extending shoreward from the shelf edge as far as the Hibernia drill site. From our experience with ship-based observations we had timed the flights relative to high tide to maximize the opportunity of imaging the wave groups. With aircraft flight duration of 4 to 5 hours, a distance covered of greater than 1000 kilometres per flight was possible.

Composites of sample flights are shown in Figures 1.2 and 1.3. From the SLAR imagery, which detects the propagating wave groups, only the lead wave is shown. The multiple traces at any one location are from multiple passes, different colors different days. These data confirmed our growing impression that internal solitary-like waves can be a regular occurrence along the continental margin, are relatively long-crested, and appear to dissipate within a short distance of the shelf edge. Since the propagation speed of the wave group is somewhat less than one metre per second, wave groups would travel about 30 to 40 kilometres in one tidal cycle. The pattern seen in the SLAR data indicates dissipation within one tidal cycle in general, with some notable exceptions: in the Scotian Gulf (south of Halifax) wave groups associated with more than one tidal cycle were

observed. The shelf there is deeper than in adjacent areas. Refer to Appendix 1 for more detail on the area sampled by the SLAR imagery and the analysis of imagery.

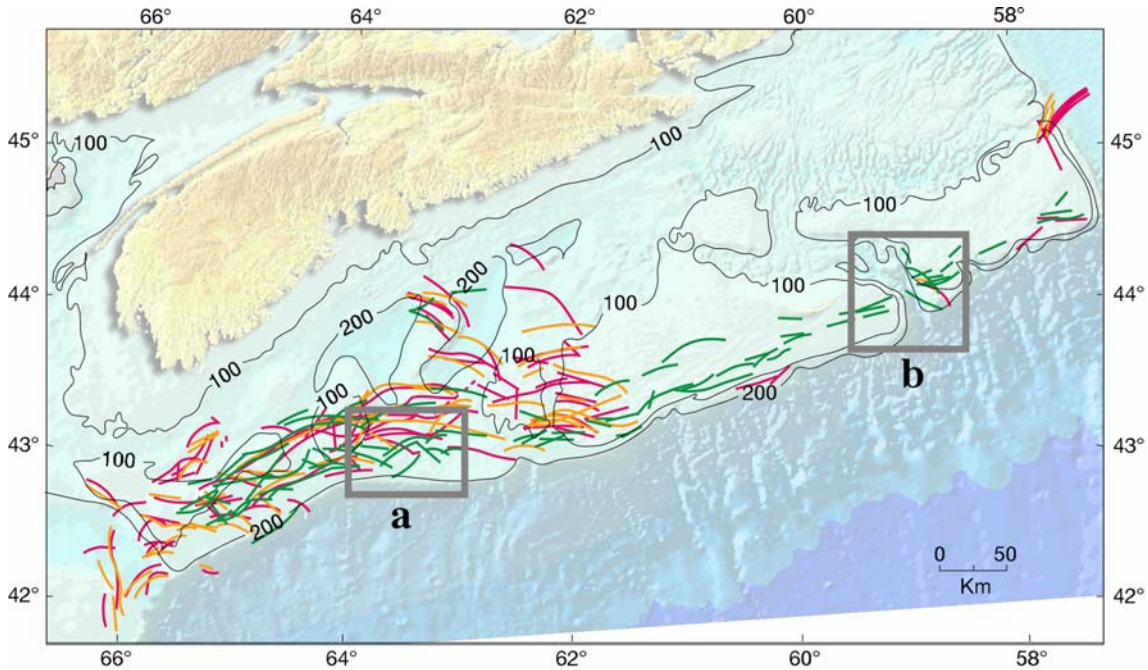


Figure 1.2: Composite of observations from SLAR imagery for the Scotian Shelf. The boxes labeled a and b are the shipboard study sites Scotian Gulf and The Gully respectively.

SLAR imagery has been collected by Ice Branch, AES, Ottawa, over many years and is stored in the AES SLAR archive as SLAR film with corresponding flight logs. This archive was searched for evidence of internal wave activity on Canada's northern shelves. The most interesting features appear in two clusters, one at the mouth of Ungava Bay and the other at the mouth of Hudson Bay (see Appendix 1).

The SLAR flights give excellent area coverage, but provide only a snapshot in time. To obtain a better time-history at a site, a thermistor chain was deployed for a month on one of the offshore rigs, Bow Drill, located near The Gully (see Appendix 2 for detail). The data from this four- week record has given us the first concrete indication of the spring-neap modulation of the internal tide and the associated groups of short waves.

Guided by the remotely sensed wave patterns, two additional ship-based experiments were undertaken in 1984 and 1985, the first in the area of The Gully, near Sable Island on the Scotian Shelf (Figure 1.2) and the second in the area between the Hibernia site and the shelf edge on the Grand Banks of Newfoundland (Figure 1.3). The choice of these two study areas was influenced by the needs of the offshore industry, but also allowed us to gather data from sites with differing topography and density structure from what we had hitherto studied. Comparison of internal tidal energy at the three sites (Scotian Gulf, The Gully, Grand Bank) showed that the eastern flank of The Gully and the adjacent



western edge of Banquereau Bank were the most energetic. The least internal tidal energy was found in the Hibernia area and on the western side of The Gully closer to Sable Island.

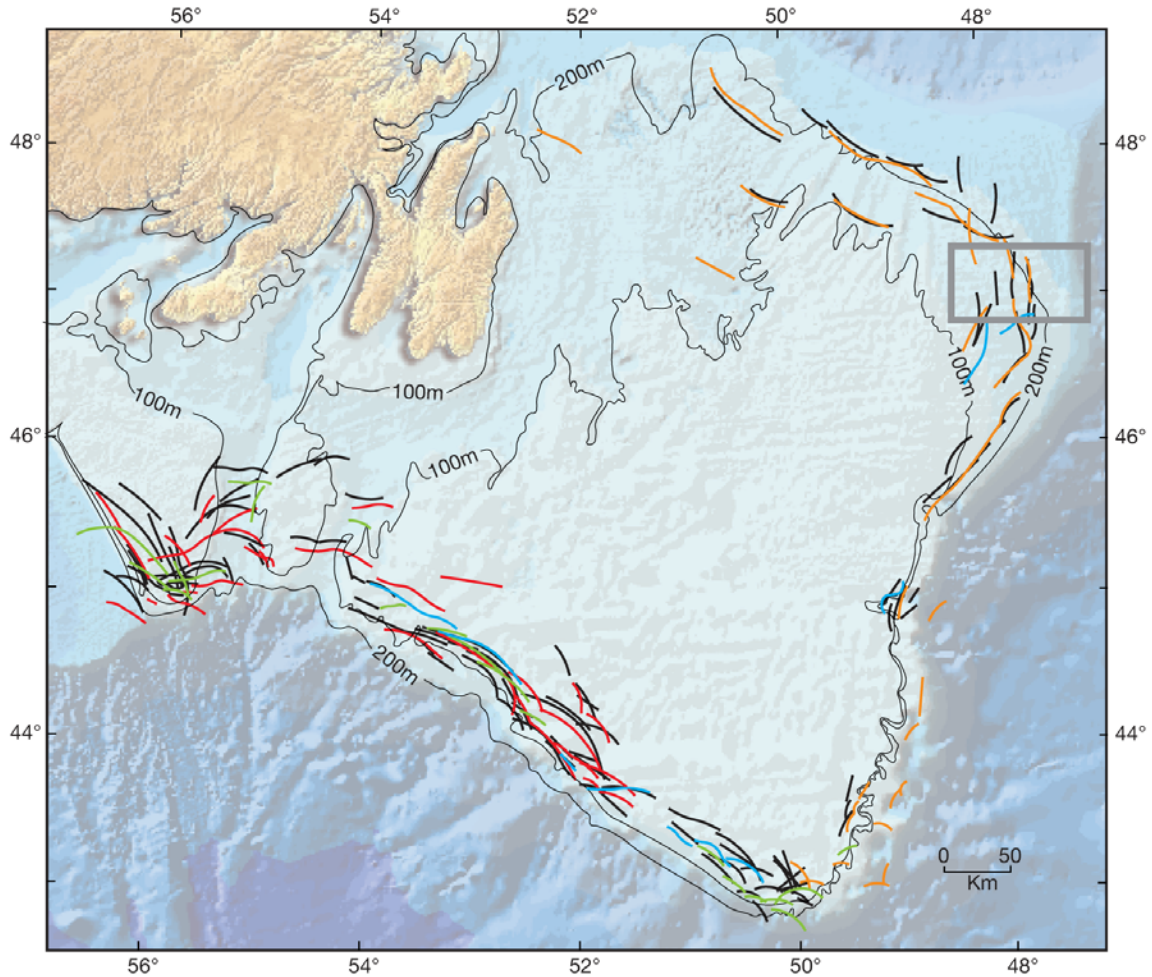


Figure 1.3: Composite of observations from SLAR imagery for the Grand Bank. The box in the upper right hand corner is the site of the field study on the Grand Bank.

The field data from all three sites were processed and compiled in the form of four data atlases (Canadian Technical Report of Hydrography and Ocean Sciences, Nos. 77, 114, 117, 121). On each of these cruises data were collected by an extensive CTD survey around the site, deployment of moorings, and numerous continuous line-surveys over a tidal cycle with the Batfish, and operation of an acoustic velocity profiler and a backscattering sounder. A portion of the data from the area of The Gully has been published (Sandstrom, Elliott, and Cochrane 1989; Sandstrom and Elliott 2002).

This report presents a composite analysis of the data, focussing on the last three cruises (83-024, 84-034, 85-024). We felt that our 1980's data set remains unique for studies of internal wave generation and dissipation at the edge of continental shelves on the east coast and for continental shelves in general. In recent years there has been an increased

interest in mixing activities at the shelf edge. The Gully, for example, has recently been designated as a marine protected area. The Gully, which separates Banquereau and Sable Banks, is a deep canyon feature with depths over 2000 metres. It is unique among canyons of the eastern Canadian margin because of its great depth, steep slopes, and extension far into the continental shelf. It is significant biologically, especially noteworthy for its biodiversity. In 1999, DFO funded a two-year research program to help fill some of the information gaps about The Gully region. Among the projects funded was support of this analysis of tidal circulation and internal waves (e.g., Gordon and Fenton 2002).

The data are sufficiently detailed to permit investigating the dynamics of the generation and dissipation of the wave groups through an analysis of the potential energy budget of the water column so as to include the internal tide and its evolution into an internal bore and solitary-type waves that dissipate. Mixing of the water column is inferred from the dissipation process. The data from the Scotian Gulf, being the most extensive and from a site that could be treated as two-dimensional, were used to guide the processing. In contrast, data from The Gully are the most complex, given its three-dimensional character, and are the most challenging to interpret.

## 2. Cruise Planning and Instrumentation

The description of the instrumentation in this section is applicable to those used at all three study areas. At each site the cruise activities followed a similar sequence of events: an initial CTD survey to provide an overview of the local density field; 2 moorings, deployed for the duration of the cruise, equipped with current meters; the use of Batfish to measure the spatial and temporal variability of the density field; and a 12 kHz acoustic sounder to monitor backscattering in the water column along the Batfish track. (Other observations not used for detailed analysis in this report included an Ametek Straza Doppler Current Profiler, 120 kHz sounders, thermistor chains, and the deployment of bottom pressure sensors for tidal analysis).

The CTD survey was completed at the beginning of the cruise to serve two main purposes. A section or sections were occupied perpendicular to the shelf edge in the main study area and extending offshore to a water depth of at least 1000 metres to provide an initial overview of the density field including any features that we needed to monitor, such as density fronts on the shelf. CTD data were also used to supplement the Batfish data beyond their range; as required, to construct a mean density field for analysis. The instrument was a Guildline Digital 8700 series mounted on a rosette. With application of the calibrations from the bottle samples nominal accuracy was within  $\pm 0.005\text{ }^{\circ}\text{C}$ ,  $\pm 0.01\text{ }_{\text{‰}}$ ,  $\pm 1\text{ db}$  and  $\pm 0.01\text{ sigma t}$ .

Moorings deployed near the shelf edge were of standard BIO design. Fairey floats were located at 15 m or 20 m, sufficiently deep so that wave contamination was minimal given the sea states encountered. A shallow float was desired in order to place a current meter well within the surface layer. All moorings were fitted with Aanderaa meters at the surface, bottom, and up to four distributed vertically. In one case VACM's were added just below the surface Fairey float to check on possible wave contamination. Sampling rate was 15 minutes for the VACM. The standard sampling interval of Aanderaa meters was 2 minutes, although at The Gully site the interval was set to 5 minutes to extend battery life. Hence in addition to monitoring mean flow and tides, higher frequency baroclinic components, including the high amplitude wave groups, could be resolved. In spite of some instrument failures, all sites had adequate coverage. Accuracy with calibrations was  $\pm 2\%$  in speed and  $\pm 5^{\circ}$  in azimuth.

The Batfish was our main tool to capture events associated with the internal tide by monitoring the local density field. The mode of operation with the Batfish was normally one of two patterns: 1) a time-series (t.s.) where a geographically fixed path 10 to 30km long was repeatedly sampled for at least a semi-diurnal tidal cycle in order to determine the mean density field and its variability for that tidal cycle; and 2) a tracking mode (t.m.) where the ship track was adjusted to be perpendicular to the developing main wave front in order to sample the wave group repeatedly for about one tidal cycle as the wave group propagated shoreward. It was with this latter mode that the ship's radar and the 12 kHz sounder were used to good effect in keeping track of the wave group. Typical parameters

for the Batfish were to cycle between 10 and 100 or 10 and 50 m, with a climb/dive rate of about 1 m/s, which, when combined with a ship speed of about 13 km/hour (3.5 m/s), gave a maximum horizontal sampling rate of slightly more than 3 deep or 7 shallow profiles/km. Depending on wave conditions, the actual climb/dive rate varied somewhat due to the ship's heave; however, during most of the three cruises the sea state was moderate to light. The choice of path length for each station/tidal cycle was a compromise to achieve the best combination of spatial and temporal resolution.

Important to the accurate measurement of the depth of a given isopycnal is the time response of the Batfish instrumentation. The CTD used was a Guildline 8700 series digital instrument which has a specification for the time constant of 50 ms. However, the ability to resolve thermal ocean gradients with this CTD has been controversial. Bennett and Huaide (1986) explored this issue in detail with application to typical offshore data. They concluded that, for Batfish applications, a spectral resolution out to about 1 Hz was achievable. R.M. Hendry (personal communication) also undertook a thorough study; his comparisons from numerous selected vertical profiles showed a loss of coherence between temperature and conductivity at frequencies beyond 1 Hz for a 1 m/s descent rate. Based on these efforts we feel that in all our applications we were able to monitor depth changes of a selected isopycnal to better than 1 m. All of the Batfish data are archived as ODF files as one second averages with an expected accuracy of  $\pm 0.05$  in sigma.

### 3. Scotian Gulf Potential Energy

#### 3.1 Field Program

A detailed bathymetric map of the Scotian Gulf study area 'a' in Figure 1.2 is shown in Figure 3.1.1. The shelf edge at this site has little along shelf variability and we could expect internal tide generation processes to be nearly 2-D in nature, and as shown by the SLAR imagery in Figures 1.1 and 1.2, surface manifestations of the internal wave groups show long crested wave fronts aligned with the shelf edge bathymetry. The SLAR image in Figure 1.1 is centered over the upper left side in Figure 3.1.1. Overlain on the bathymetry in Figure 3.1.1 are notations for the location of the sampling sites.

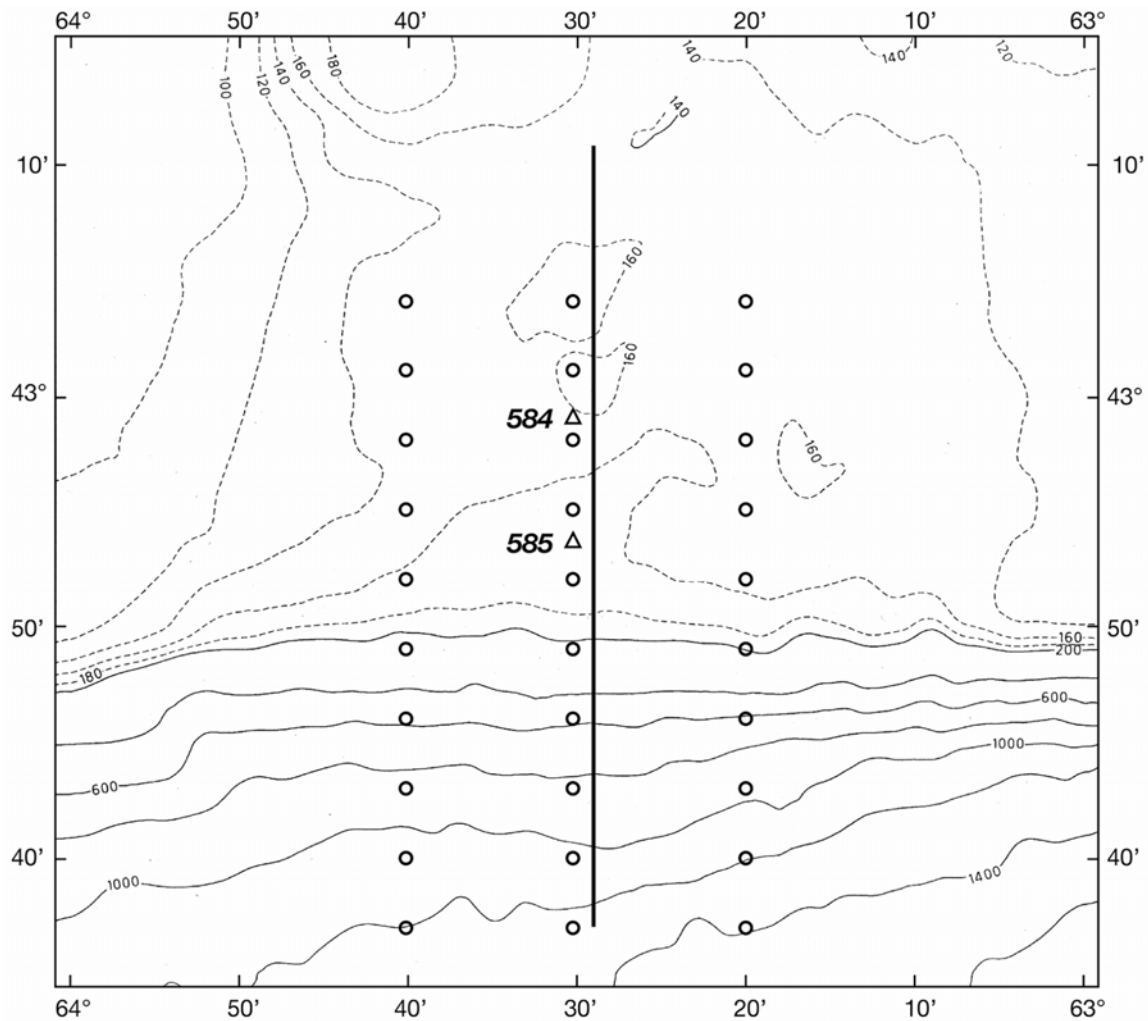


Figure 3.1.1: Bathymetry for the Scotian Gulf study site. Depth contours are in m; CTD casts are shown as open circles; mooring locations are shown by open triangles labeled 584 and 585; and the track for all Batfish data is from the N-S section near 63° 30' W along the solid line.

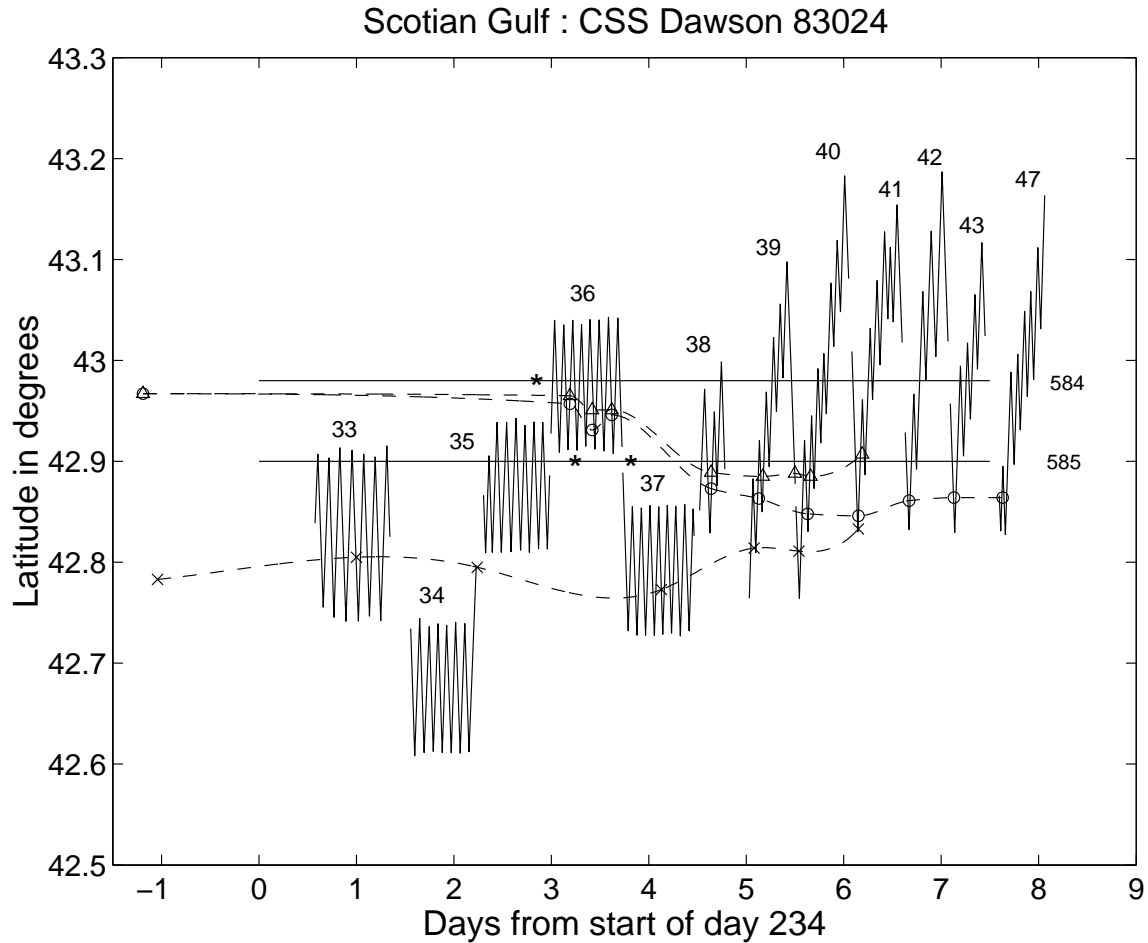


Figure 3.1.2: Time history of data collected at the Scotian Gulf. Batfish data are the time series stations 33 to 37 and tracking mode stations 38 to 47; moorings are 584 and 585 at the latitudes and times shown by the solid line; and the dashed lines and symbols are associated with frontal features at the site (see 3.4).

A time history of the data collection is shown in Figure 3.1.2. The CTD survey (not shown) composed of three sections (see Figure 3.1.1) was completed in the days preceding Day 234. Two moorings, 584 and 585, were then deployed for the 'duration' of the field program as designated by the solid line at the latitudes shown. The Batfish stations are the sequence 33 through to 47. Stations 33 to 37 are 'time series' data consisting of repeated occupations of a fixed portion of the overall section for a complete M2 tidal cycle. Taken together, the time series data were intended to cover the shelf region where generation and shoreward propagation of the internal tide could be monitored. By contrast, the stations 38 to 47 are 'tracking mode' data where the repeated cycling was concentrated on the energetic part of the internal tide as the wave propagated shoreward over a tidal cycle. A typical good example of Batfish data for a tracking mode station (Scotian Gulf station 47) is given in Figure 3.1.3. Plotted are contours of constant sigma (22.5 to 26.0 in steps of 0.5). In the top panel the internal tide has begun to steepen behind its crest with the initial signs of high amplitude waves

appearing. By the third panel, an internal hydraulic jump has fully developed with numerous waves forming the “wave group”. The bottom three panels show most of the energy now in a group of high-amplitude short-wave-length waves that are progressively dissipating. The separation in time between the first and last panels is approximately 9 hours.

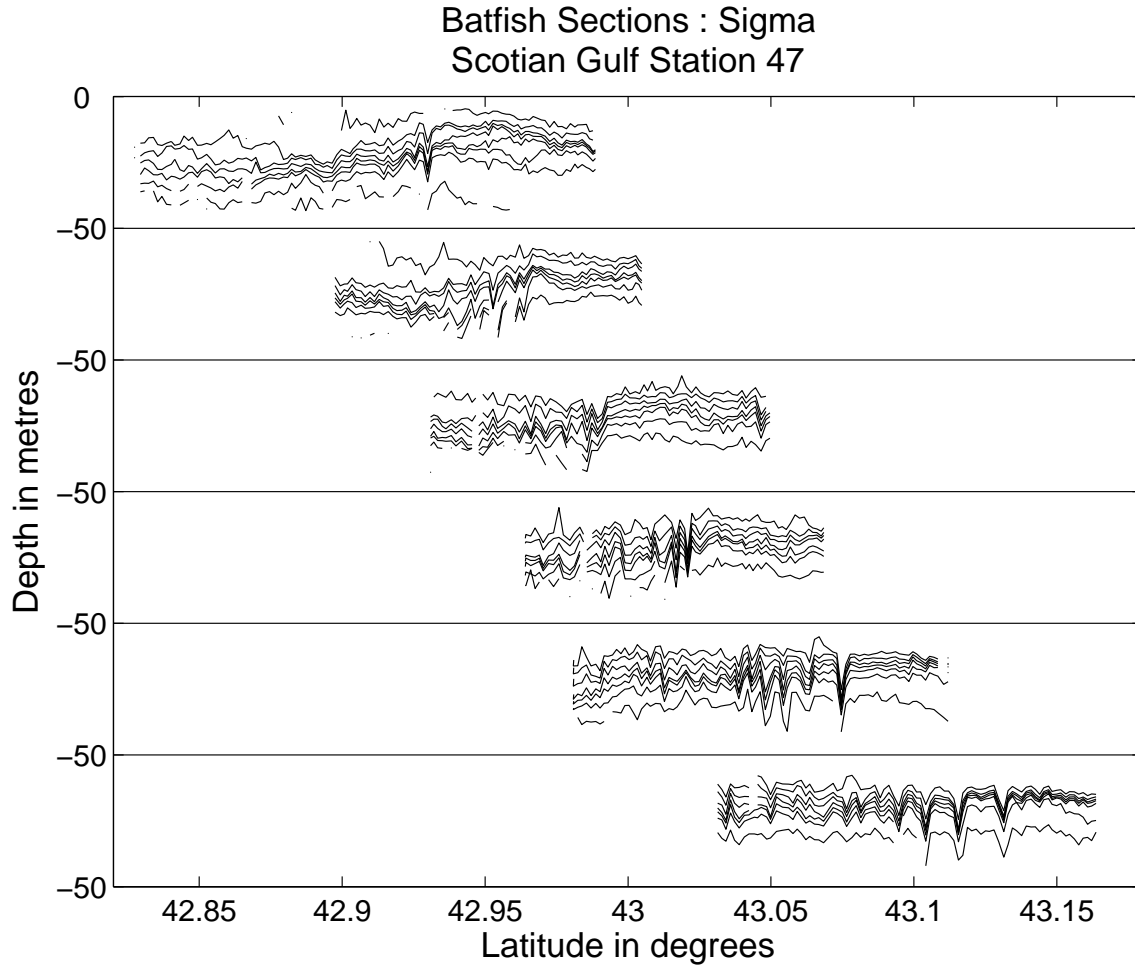


Figure 3.1.3: Example of 6 Batfish transects along  $63^{\circ} 30' W$  showing the evolution of density surfaces. In all panels ship and the waves travel in the same direction. Shown are contours of constant sigma from 22.5 to 26.0 at intervals of 0.5.

The object of the discussion to follow is to clarify how the data shown in Figure 3.1.3 were derived and how the data are used to calculate the potential energy in the baroclinic field. As stated above, of the three study areas the data set from the Scotian Gulf is the most detailed and complete and is the guide for the processing routine followed throughout.

### 3.2 Gravitational Potential Energy Perturbation

The perturbation potential energy in a stratified fluid per unit area is given by

$$PE = \frac{1}{2} \int_{-h}^0 \rho_0(z) N^2(z) \zeta^2(x, z, t) dz \quad (3.2,1)$$

Where  $\zeta(x, z, t)$  is the displacement of a fluid element from its equilibrium position,  $\rho_0(z)$  is the equilibrium density and  $N^2(z)$  is defined by

$$N^2(z) = -g \frac{1}{\rho_0(z)} \frac{d\rho_0}{dz} \quad (3.2,2)$$

and is a measure of vertical stability in the water column.  $N$ , if real, has the dimension of frequency. It is called *buoyancy frequency* or *stability frequency*, in the oceanographic context often *Väisälä frequency* and in atmospheric context the *Brunt frequency*.

In view of (3.2,2) the potential energy in sigma space may be simply written as

$$PE = \frac{1}{2} g \int_{\sigma_0}^{\sigma_h} \zeta^2(x, \sigma, t) d\sigma \quad (3.2,3)$$

where  $\sigma_0$  and  $\sigma_h$  are the sigma values at top and bottom of the water column respectively. (3.2,3) is more suitable for our purposes, since we have referred displacements to isopycnal surfaces, rather than to particular depths. We note also that when displacement is expressed as a sum of normal modes

$$\zeta(x, \sigma, t) = \sum_{n=1}^{\infty} a_n(x, t) \Phi_n(\sigma) \quad (3.2,4)$$

potential energy will be a sum of products of modal amplitude squared and the integral of the normal mode squared in sigma space.

$$PE(x, t) = \frac{1}{2} g \sum_{n=1}^{\infty} a_n^2 \int_{\sigma_0}^{\sigma_h} \Phi_n^2(\sigma) d\sigma \quad (3.2,5)$$



### 3.3 Processing of Batfish Data

The main objective in using the Batfish data was to delineate the spatial and temporal features of the gravitational potential energy perturbation, including its growth and dissipation.

In order to reach the main objective, the ancillary objectives were to derive the elevations of isopycnal surfaces, calculate the mean elevations of those surfaces and then calculate the displacements from their means. As part of this process, internal tidal parameters could be extracted.

The large amount of data (cruises 83-024, 84-034 and 85-024) to be processed dictated the adoption of fairly general processing procedures, mostly done on a contractual basis. The Matlab processing routines were written using Matlab Release 11 (A. van der Baaren) to reflect the processing objectives. It was later found during the analysis stage that some procedures were inadequate for parts of the data and had to be modified to accentuate some of the exceptional features in the data. The modifications will be discussed in conjunction with analysis in appropriate sections of this report.

The archived Batfish data consist of separate data files (.ODF format) for each transect or section (ship transit from point A to B) of each particular station. Data was recorded continuously while the Batfish ascended/descended numerous times during the transect. Parameters recorded were: day, time, pressure, temperature, conductivity ratio, latitude and longitude. All of the parameters were averaged over consecutive one second intervals (see discussion in Appendix 3) and density ( $\sigma$ ) was calculated using equation of state. The archived data contain the averaged to one second parameters only.

#### **Order of processing:**

1. Splitting – the long data fields in ODF data (100+ ascents/descents) were split into separate up/downcasts using pressure as criterion. The up/downcasts were then considered essentially as vertical CTD casts.
2. Sorting – in each ‘cast’ pressure decreases/increases monotonically, but density ( $\sigma$ ) sometimes does not. In order to invert the functional relationship between  $\sigma$  as function of pressure to pressure as function of  $\sigma$  we must sort the data according to increasing value of  $\sigma$ . In the case of density reversals, this was accomplished by removal of multiple values of  $\sigma$ . The other parameters were then interpolated to predefined  $\sigma$  surfaces, generally  $22.5 \leq \sigma \leq 27.0$  in steps of 0.1 in  $\sigma$ . Interpolated negative pressure now defines the elevation of a given  $\sigma$  at that location and time.
3. Day and time – these fields were translated into hours of the Julian day at the start of a given station.
4. Averaging – The hours, latitude and longitude were then averaged for each cast: expressed as meanhour, meanlat and meanlong.

The previous procedures applied to all the data. The next procedures applied only to those stations, where a single geographical section was sampled repeatedly over at least the

semi-diurnal tidal period. Typically such a section was  $\sim 15$  kms in length and was traversed 14 – 16 times at an average ship's speed of  $\sim 7$  knots ( $\approx 13$  km/hour). The data from each such station was used to derive the mean state of the density field along that geographical section for the duration of the station.

5. The data was sorted into overlapping geographic blocks along the length of each traverse. In each case block length was 3 km and the centre of blocks was shifted by 1 km. The data in each block was then averaged for each density surface, for which sufficient data existed. Normally 11 – 12 blocks for each station would contain the averaged over 3 km data.
6. The time-series of the averaged over 3 km elevation for each sigma-surface is then analyzed for least-squares fit with a test function that includes mean, trend,  $M_2$  and  $M_4$  period cosines (on one occasion adding diurnal component, when two stations at the same location in combination yielded a much longer time-series). The mean of the fit is taken as the mean elevation of the given sigma-surface for that particular block. The means from all blocks and all sigma surfaces form the spatial structure of the mean density field for a particular station. Combination of several such stations in adjacent geographical locations enables us to construct an extended mean density field to be used as basis for processing the tracking mode data.

**N.B.** Although the mean density field for each station is appropriate for deriving the displacement of each density surface as the measured elevation minus the mean for the duration of the station, the extended mean density field combines results from different tidal periods and extends over a much longer time span, during which the mean field may undergo longer period or episodic changes. The problem of stability of the mean field will be discussed in the context of constructing the mean fields for each survey area separately. The discussion has a bearing on how to further extend the mean field into geographical areas, where data was collected but no repeated sampling was done. This happened during stations when groups of waves were tracked beyond the extent of the previously derived mean density field.

As products of the least-squares fit, the  $M_2$  and  $M_4$  tidal amplitude and phase of each density surface in each geographical block is obtained, describing the temporal behavior of the tidal components in each block, and spatial variation as well when all blocks are combined.

Anticipating the results of constructing appropriate mean density fields in each survey area, the additional common processing steps for all the data were:

7. Computing the displacements of each sigma-surface in all casts by subtracting the mean sigma-level at the cast location from the instantaneous sigma-level.
8. Computing the un-corrected and corrected gravitational potential energy for each cast. The un-corrected potential energy was calculated by summing  $\zeta^2(x, \sigma_i, t)$

over all  $\sigma_i$ , for which data existed. Since the Batfish range covered only part of the water column, some chosen sigma levels, both near surface and bottom, had no or only intermittent data for potential energy calculation. Missing data on deeper sigma levels was especially noticeable when isopycnals were deeply depressed and thus outside the Batfish range during passing of large amplitude solitary-like waves. Such waves have also short wavelengths and sampling them with the slantwise moving Batfish can be a problem. That aspect will be discussed later in this report. The problem of missing data in the vertical was to a great extent overcome by having noted that the displacements were, at least on the shelf, predominantly of the first mode. The following method of correcting for missing data was adopted:

Step 1. The 1st mode eigenfunction  $\Phi_1(\sigma_i)$  for displacement for all sigma values was constructed using the previously derived mean density field, supplemented where needed by CTD density data outside the Batfish range.

Step 2. The sum of  $\Phi_1^2(\sigma_i)$  over the same isopycnals, that were used for the un-corrected calculation, was obtained.

Step 3. The sum of  $\Phi_1^2(\sigma_i)$  for all  $\sigma_i$  in the water column was calculated.

Step 4. The corrected potential energy was obtained as the result of un-corrected PE being multiplied by the ratio of Steps 3 and 2.

In general the correction was relatively small (5 – 15%). It was larger (sometimes > 50%), when large-amplitude solitary waves were encountered, and then particularly when the Batfish depth range was smaller in order to get better horizontal resolution. However, the large-amplitude waves were predominantly of first mode and thus most amenable to the correction procedure adopted. In addition, the data with increased horizontal resolution has allowed us to reconstruct the shape of the solitary wave in a few instances and calculate the potential energy from the wave parameters. The agreement between such a calculation and the corrected potential energy at ~ 10 – 20% level gives us confidence that corrected results are reasonable.

9. Sorting and averaging the corrected potential energy in 3 km long blocks (as was done in step 5 for elevation). For some stations, where the casts only reached 50 metres depth and better spatial resolution resulted, potential energy was also averaged in 1 km long blocks.

### 3.4 Extended Mean Density Field: Scotian Gulf

As indicated under step 6 in section 3.3 above, a key component in the processing of Batfish data is computing a representative and suitably accurate mean density field composed of reference levels for each of the selected sigma surfaces. For each of the time series stations (stations 33 to 37) the mean is derived from the data collected during that tidal cycle. However, for the tracking mode (stations 38 to 47) we are limited to a construct based on the time series stations and other ancillary data. As can be seen in Figure 3.1.2, tracking mode data were collected shoreward beyond the region covered by the time series data. After initial analysis it became apparent that throughout the period of data collection a well defined alongshore current was present at the site, and that the position of this frontal feature had shifted in an offshore direction by about 5 km mid-way through the cruise. It was important therefore to have a history of the fronts behaviour and understanding of impact on the mean field.

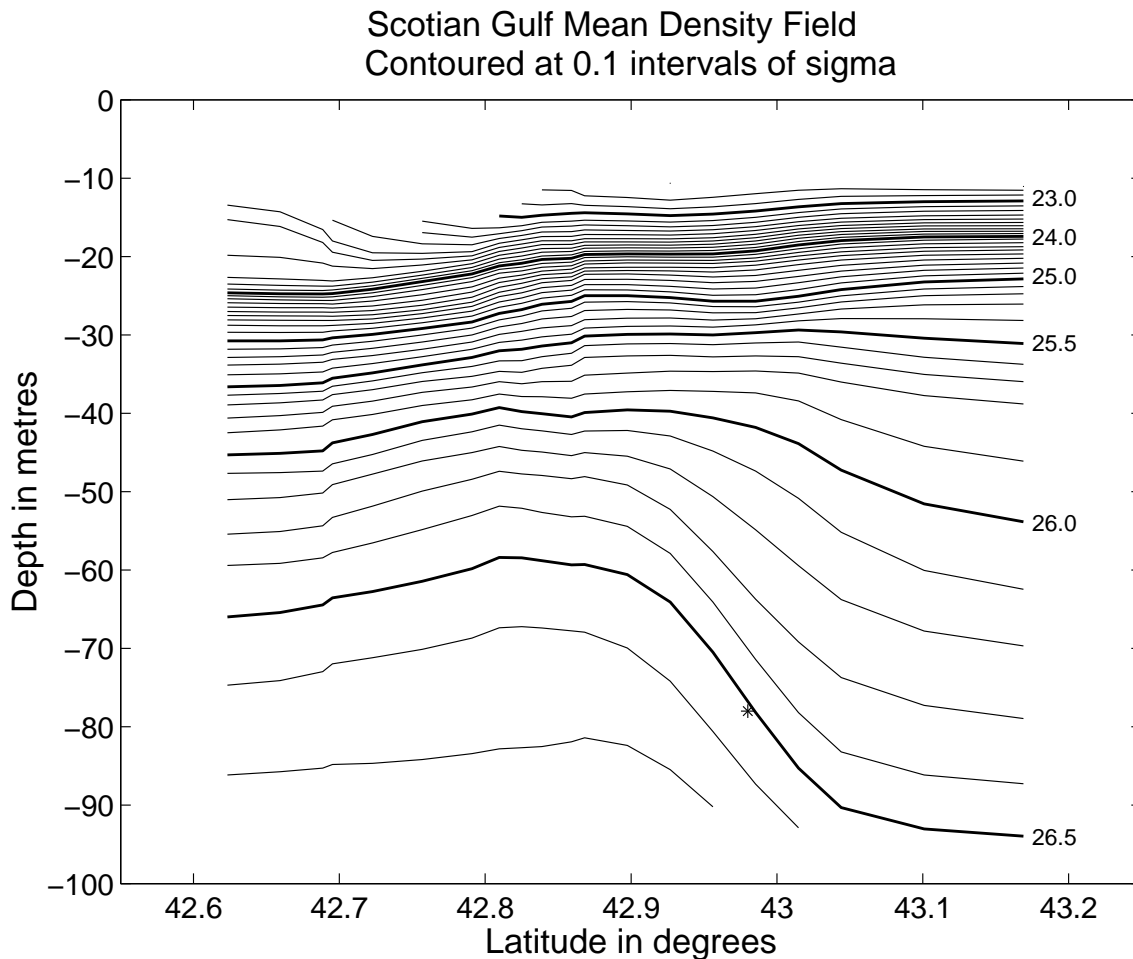


Figure 3.4.1: The 'Mean Density Field' for the Scotian Gulf at 63° 50' W.

Based on data available from the CTD, Batfish and current meters, an extended mean density field was constructed. The final result is shown in Figure 3.4.1. In the plot, the

contours of constant sigma between latitude 42.6 and 43.0 are based primarily on the 3km averages for stations 34 to 37. Where overlap occurs, the average was used. A vertical mismatch of about 1m is apparent at the junction between stations. The contours are extended shoreward of station 36 based on a weighted average of CTD data collected at the beginning of the cruise and a number of tracking mode Batfish profiles selected to be well removed from the dominant wave groups and at a time when we felt that the background ‘noise’ was minimal and could be averaged for a representative mean. In our favour is that at the inshore end of the study area the isopycnals are essentially horizontal and remained suitably stable throughout the cruise; the main adjustment to the features in Figure 3.4.1 was some offshore movement of the position of the front. The tracking mode stations begin near the front then follow events into the region of relatively horizontal isopycnals.

Evidence for the behaviour of the frontal feature is shown in Figure 3.1.2. Three dashed lines represent three identifiable ‘temperature features’ near the front: 1) the inshore position of the 8°C contour at the ‘nose’ of an inversion found in the offshore at about 50m, 2) similarly, the offshore position of the 6°C contour of an inversion found at 50m on the inshore side, and 3) the position of the 8°C isotherm at 75m. Termination of the 8°C line is because the Batfish profiles are then limited to 50m. Also plotted as an asterisk are the times when a rapid temperature shift was seen to pass the moorings. Refer to the plots in the data atlas for details on temperature profiles, Sandstrom and Elliott (1989a).

As depicted in Figure 3.1.2, our tracking of the frontal feature indicates that throughout the period when we were collecting the time series and tracking mode data the position of the front remained relatively stable except for the adjustment occurring during the latter stages of station 35 and during station 36. A more detailed analysis of the history of the 26.5 sigma contour within the front near Latitude 43° at a depth of 78m, shown by the \* symbol in Figure 3.4.1, is given in Appendix 4. The analysis supports the conclusion of a relatively stable position of the density front for the tracking mode analysis.

The question arises as to how significant these shifts in the mean field are in the determination of the displacement fields and the resultant potential energy. In addition to the one-time shift of the density front in offshore direction, it is also influenced by the barotropic current fluctuation at tidal frequency.

As stated in section 3.3 at step 6 the average depth of each sigma surface at a given location is taken as the mean in the test function for least squares fit. For the majority of the time series the trend in the test function, i.e. the temporal change of the mean, is insignificant. However, at locations where the isopycnals slope considerably, the trend may be significant. We have re-analyzed the data of stations 35 and 36 with this in mind and compared the results for potential energy for the two cases of stationary and time-dependent isopycnal ‘mean depths’. Computation of displacements and potential energy in both cases follows the procedure as outlined in section 3.3. The principal result of the comparison is that the potential energy levels with the time-dependent mean depths are approximately 10 % lower than with the stationary depths between latitudes of ~ 42.88

and 42.98. We note from Figure 3.4.1 that the density front is steepest between the same latitudes. The major shift of the density front is over by the latter half of station 36 and that is confirmed by the comparison of potential energies derived by using time-dependent and stationary mean fields in the later transects. This gives us confidence in using the mean field for the subsequent analysis of the tracking-mode stations.

The one-time shift of the density front affects primarily the potential energy calculations for stations 35 and 36. Additional sources of error in estimating potential energy, which affect all stations, are imbedded in how the Batfish samples the density field. In section 7.1 we discuss the problem of resolution of data, especially where high-amplitude and short wavelength features are present. Table 7.1 indicates that calculated energy, when averaged over longer scales (3 km) underestimates the actual energy by only a few percent. The sampling frequency in any of the 3 km geographic blocks averaging to one sample/hour is low and leads to uncertainties in mean elevation determinations. The accuracy of the mean field we estimate to be of the order of  $\pm 1$  m over a wide range of isopycnals. The corresponding error in potential energy is 5 – 10 %, where energy levels are low to moderate, but  $< 5$  % in higher energy regions. Our considered estimate for the total error in potential energy is 10 – 15 % for stations 35 and 36 and  $< 10$  % for the other stations.

### 3.5 Potential Energy Contour Plots

The calculated baroclinic potential energy content can be presented in various ways, one of which is to show it as space-time plots, where the energy density ( $\text{Joules/m}^2$ ) isolines are shown as contours. In the Scotian Gulf, where the Batfish data were collected along NS lines, distance from the 1000 m isobath is used for the space axis. Time refers to hours of a Julian day of 1983 (cf. Figure 3.1.2). In this section two example plots are shown: the first is a time-series station; the second is a tracking-mode station. The complete set of plots for all stations is shown in Appendix 5, together with similar plots for the Grand Bank and The Gully sites.

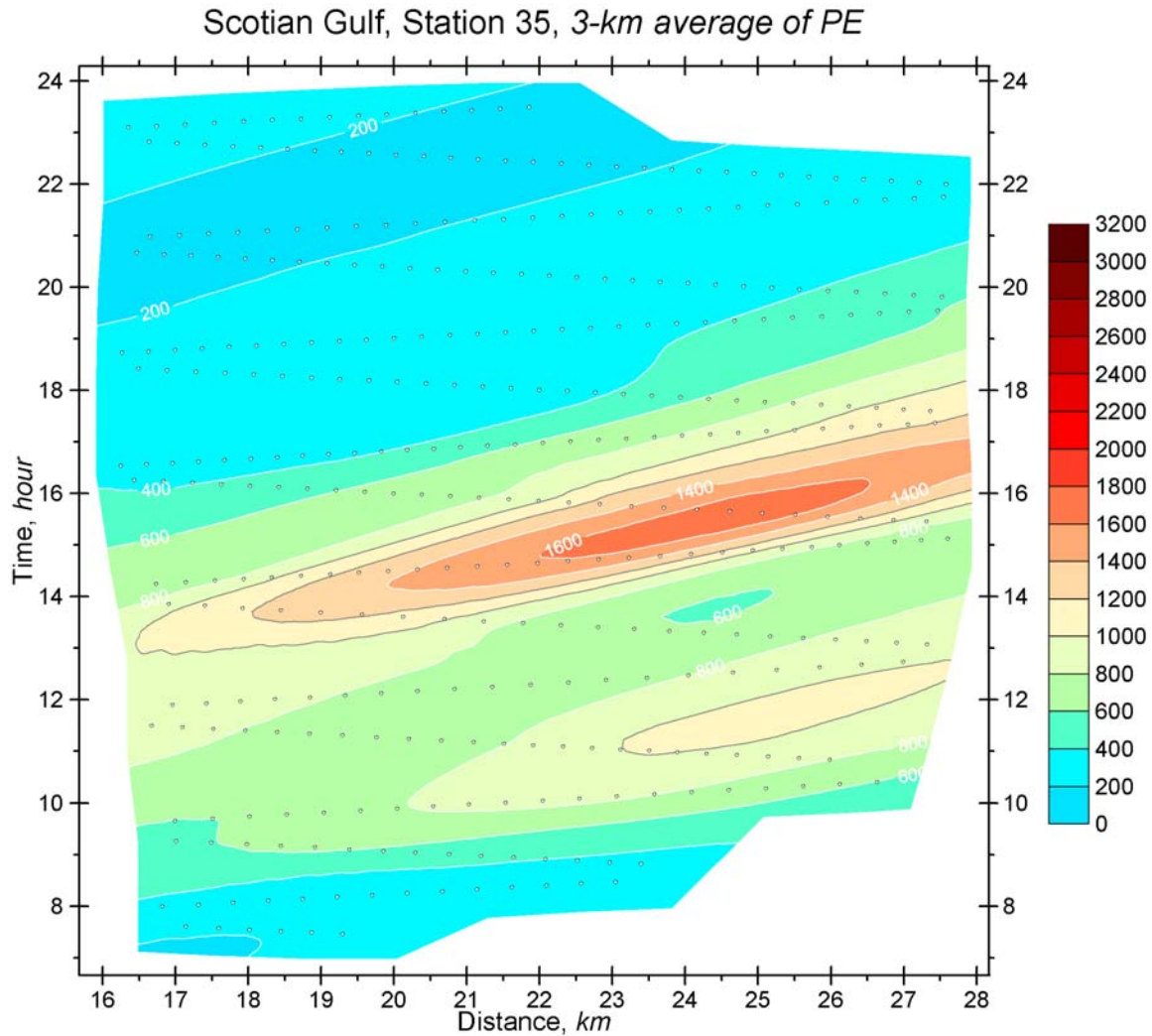


Figure 3.5.1: Time-series station 35 in the Scotian Gulf.

Note that in the figure the energy density isolines slope predominantly at the rate of 3 km/hour, which corresponds to the effective propagation speed of the internal bore observed during transects 8 and 9 of the station (see section 8.3).

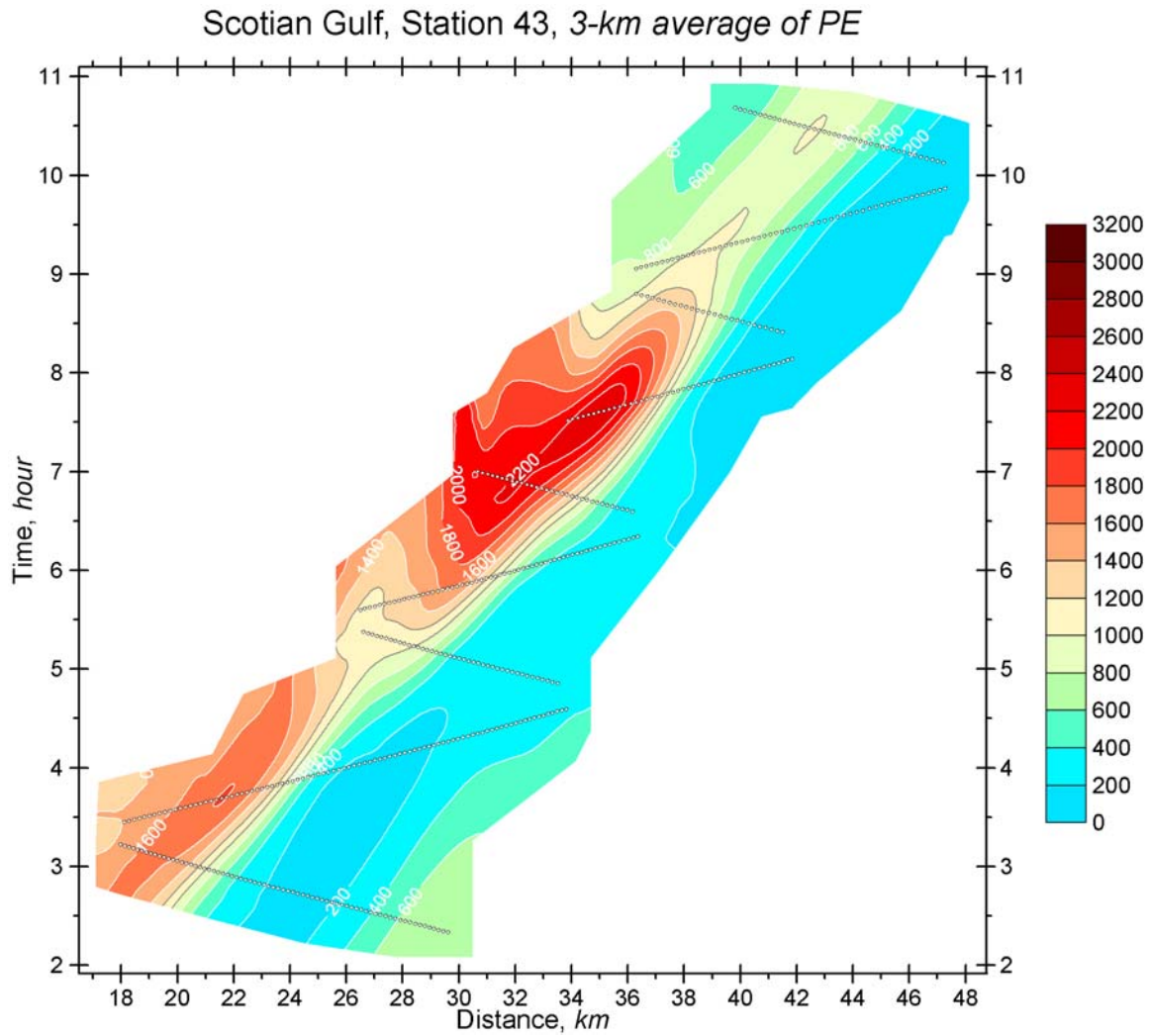


Figure 3.5.2: Tracking-mode station 43.

The data of station 43 were accumulated while tracking an advancing internal bore shoreward. Ahead of the wavefront the energy levels are low. In hindsight it appears that in tracking the bore the track could have been shifted somewhat offshore in order to sample more of the rear of the bore, but the dominant part of the bore was sampled quite adequately. An energy maximum in the bore is seen between approximately 30 and 35 km, but energy dissipates rapidly thereafter. The apparent propagation speed of energy from the figure is 3 km/hour, or the same as from Figure 3.5.1.



### 3.6 Potential Energy Scatter Diagram

The potential energy content of internal waves for two stations was illustrated by contouring it in the preceding section in time-distance domain. Similar plots for all stations are in Appendix 5. The same data are presently summarized by plotting it as a function of distance only for all Scotian Gulf stations. At a given distance (measured from 1000 m isobath) variability within a tidal period as well as variability from tide to tide is included.

Figure 3.6.1 depicts clearly the growth of energy over the top of the slope and shelf edge, peaking in the vicinity of latitude 43 degrees and dissipation thereafter. In the following sections 6-9 we discuss the result in terms of energy generation, transformation and dissipation in greater detail.

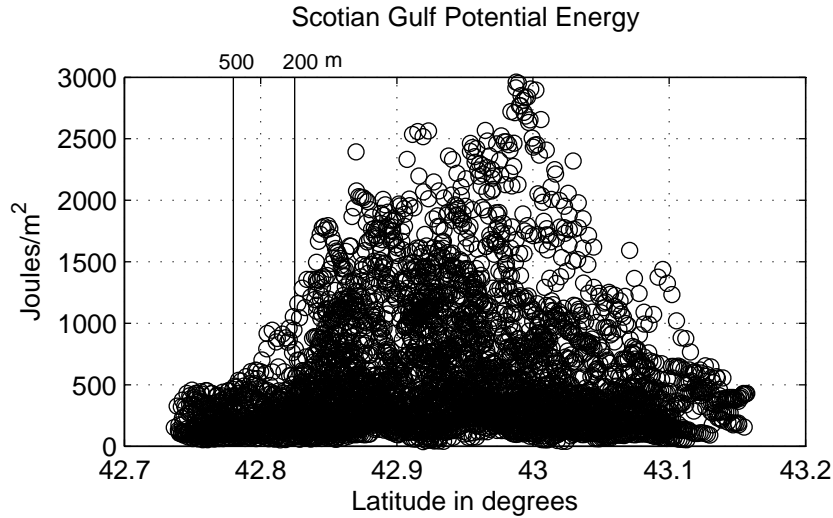


Figure 3.6.1: Scotian Gulf scatter plot of 3 km averages of potential energy as a function of distance from 1000 m isobath. The two vertical lines denote the location of water depths of 500 and 200 m.

## 4. Grand Bank Potential Energy

### 4.1 Field Program

The Grand Bank site was chosen to be within the region of the shelf where internal wave groups propagating past the Hibernia oil field production activities would be generated (see Figure 1.3). Our work at the site on the Grand Bank followed a pattern very similar to that used for the Scotian Gulf study. Figure 4.1.1 shows the bathymetry and data collection locations. The Hibernia production platform is situated about 30 km to the west of Figure 4.1.1 at  $46^{\circ} 45' \text{ N}$ ,  $48^{\circ} 47' \text{ W}$ . The location of our initial CTD survey is denoted by the open circles; the following deployment of two moorings, 698 and 699, by the open triangles; and the path for the subsequent detailed Batfish surveys by the solid line. The bathymetry at this site is nearly 2-D, with a N-S orientation at the steep slope where generation occurs, and a relatively flat and gently sloping shelf.

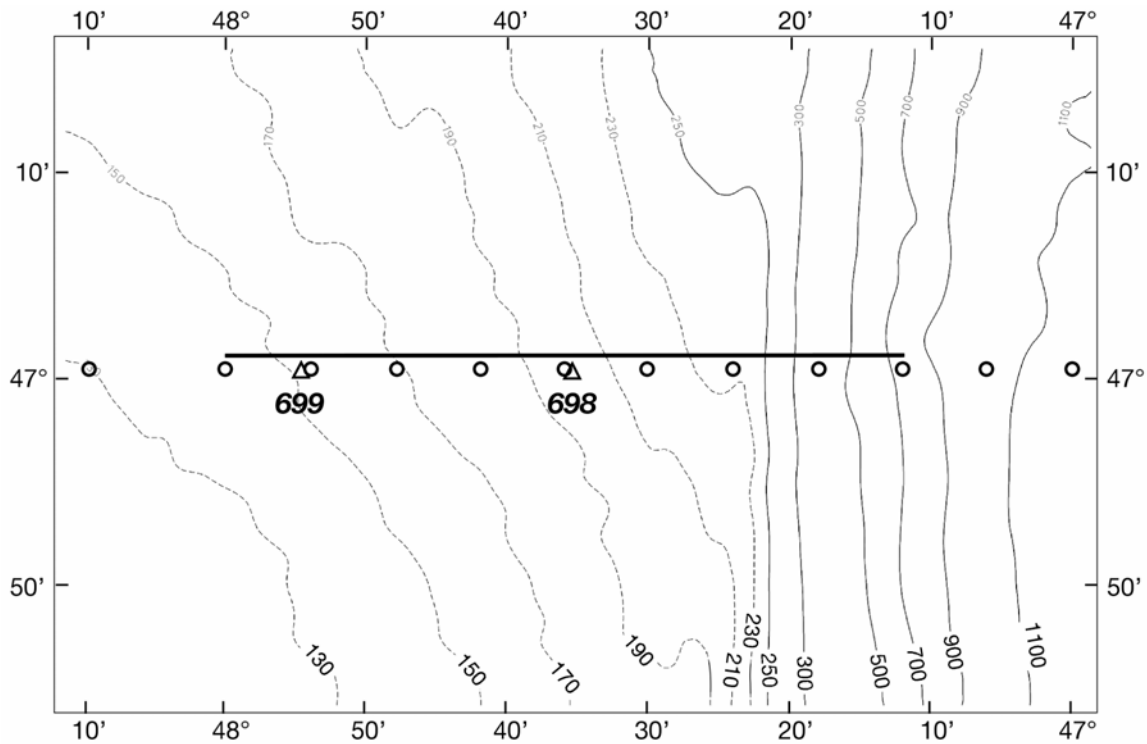


Figure 4.1.1: Bathymetry at the study site on The Grand Bank. Depth contours are in m; CTD casts circles; mooring sites are triangles; and the track for all Batfish data are along the solid line.

Figure 4.1.2 shows the sequence of the observations. The initial CTD survey (not shown) immediately preceded Day 229, followed by the deployment of the two moorings 698 and 699 for the duration of the study at the longitudes and times shown by the solid lines. The Batfish data consist of four non-overlapping time series surveys lasting one complete

M2 tidal cycle, followed by eight surveys in the tracking mode where the data sampling concentrated on the energetic part of the internal tide.

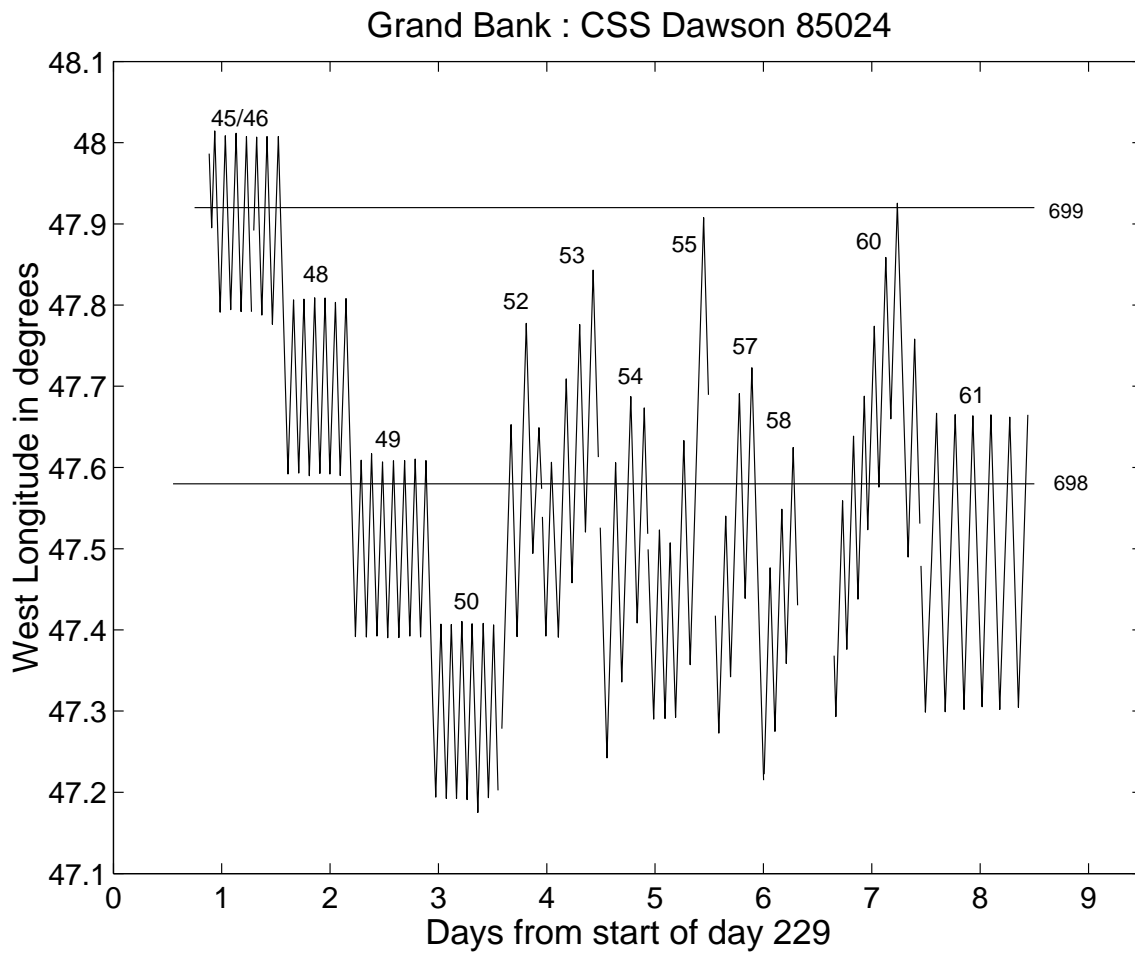


Figure 4.1.2: Time history of data collected at the Grand Bank site. Batfish data are the repeated cycling labeled as stations 45/46 to 61; and moorings are 698 and 699 at the longitudes and times shown by the solid lines.

## 4.2 Processing of Batfish Data

Processing of the data followed the general procedure as outlined in section 3.3. Repeated cycling of the same geographic area over at least the semi-diurnal tidal cycle was carried out during stations 45-46, 48, 49 and 50. These stations are the basis for the construction of the mean density field shown in Figure 4.2.1. It is used in further analysis of both time-series and tracking-mode stations. There are horizontal density gradients in the section, especially noticeable near the shelf break, but there is no indication that the mean field is changing during our stay at the site. The latter conclusion is based on both Batfish and ancillary data.

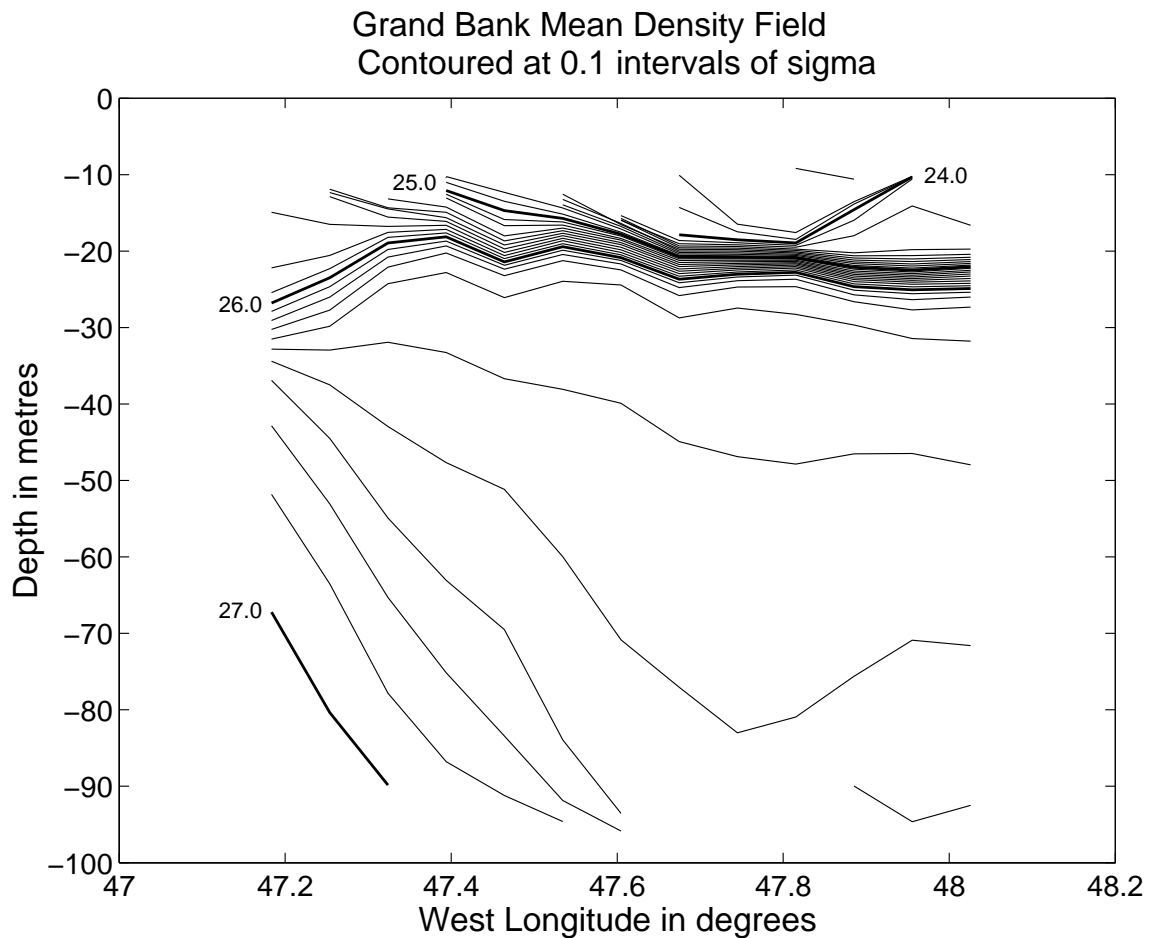


Figure 4.2.1: Mean Density Field for the Grand Bank analysis at 47° 01' N.

### 4.3 Potential Energy Contour Plots

To follow the pattern used for the Scotian Gulf we show in this section two contour plots of potential energy density in units of  $Joules/m^2$ . The first is of a time-series station and the second represents one of the tracking-mode stations. The contour plots of all stations are shown in Appendix 5. Distance on the Grand Bank is given from east to west from the 1000 m isobath along latitude 47 degrees.

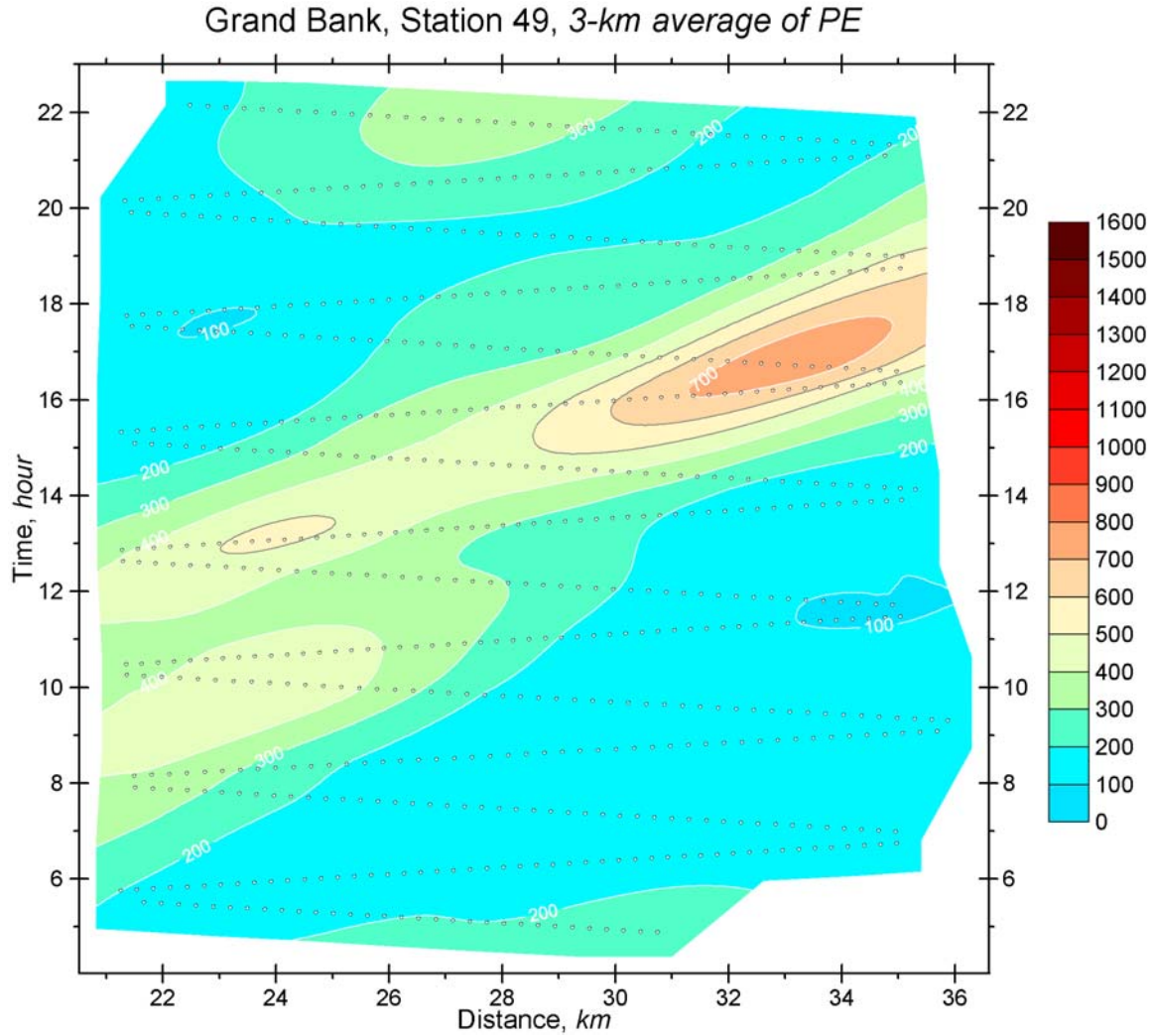


Figure 4.3.1: Time-series station 49 on the Grand Bank.

The energy density on the Grand Bank is considerably lower than in the Scotian Gulf. The energy propagation speed is also smaller. The energy density isolines in Figure 4.3.1 have slopes of approximately 2.5 km/hour.

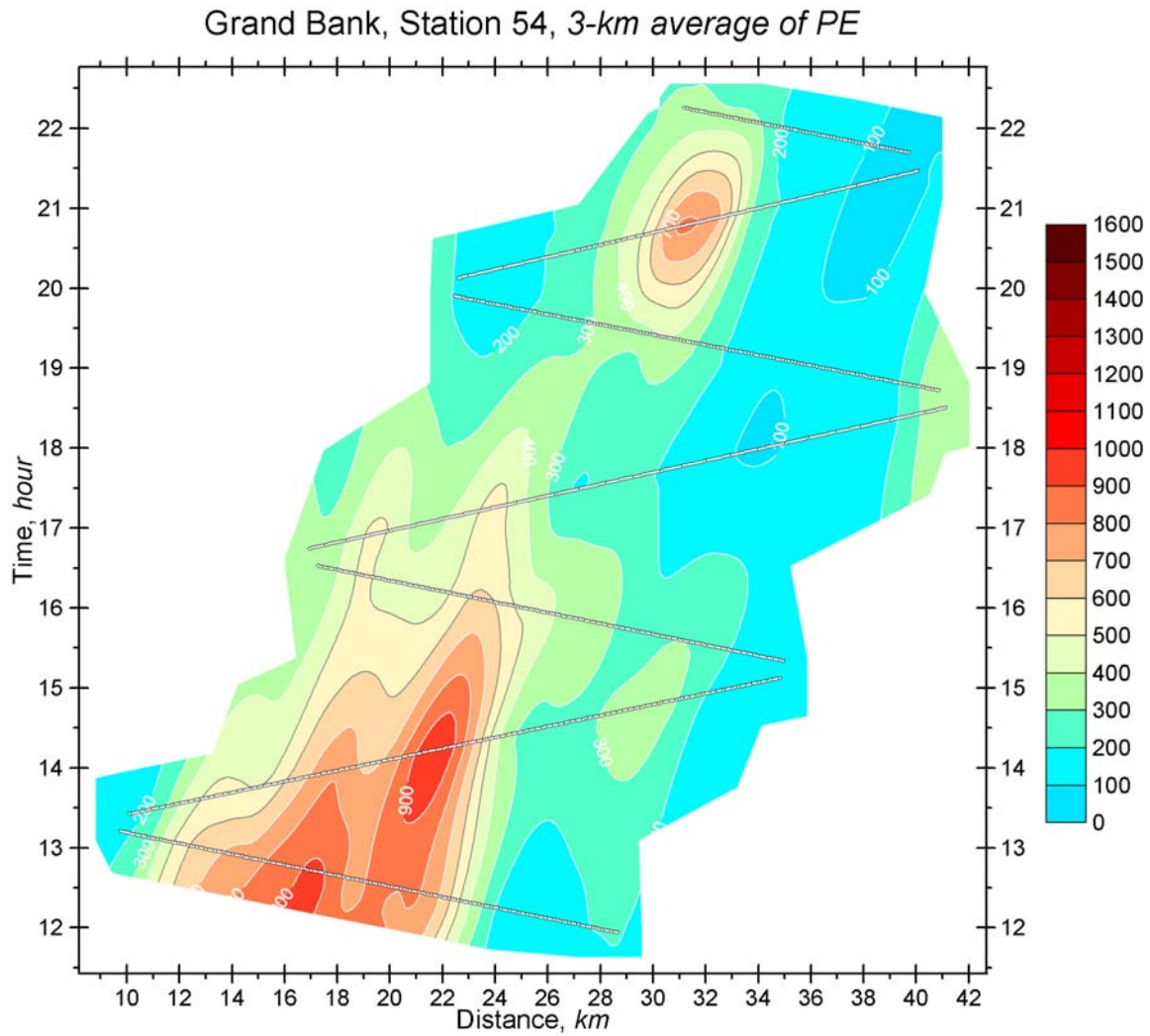


Figure 4.3.2: Tracking-mode station 54.

The wave groups on the Grand Bank are weaker and less coherent than in the Scotian Gulf. In Figure 4.3.2 the maximum energy density is seen in the vicinity of 20 km distance. The apparent energy propagation speed is estimated to be between 2.0 and 2.5 km/hour.

#### 4.4 Potential Energy Scatter Diagram

In the preceding section the potential energy content of internal waves for two example stations was illustrated by contouring it in time-distance domain. The same data for all stations, see Appendix 5, are presently summarized by plotting it as a function of distance only. At a given distance (measured from 1000 m isobath) variability within a tidal period as well as variability from tide to tide is included.

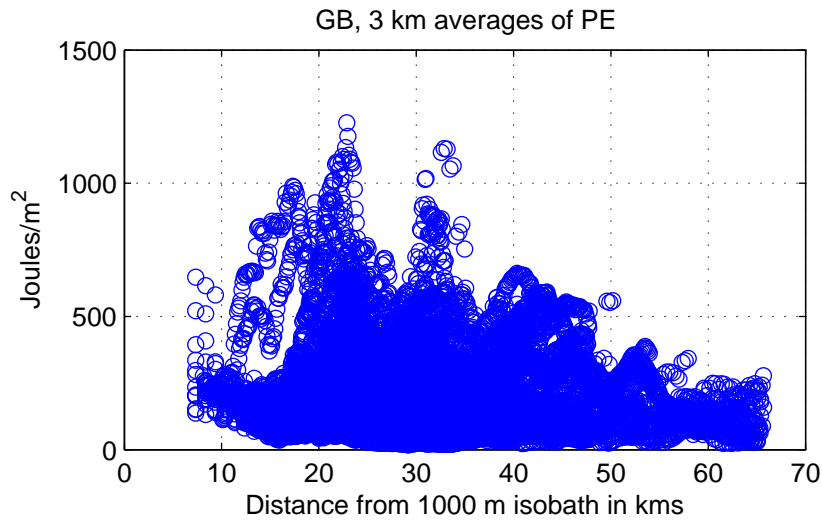


Figure 4.4.1: Grand Bank scatter plot of 3 km averages of potential energy as a function of distance from 1000 m isobath.

## 5. The Gully Potential Energy

### 5.1 Field Program

Compared to the nearly uniform 2-D shelf with long crested internal waves that we encountered at the other two sites, we expected a more complex internal wave regime in the vicinity of The Gully. Preliminary observations of the internal tide activity, from SLAR images near region 'b' in Figure 1.2 (see also Appendix 1), and the analysis of thermistor chain data from the Bow Drill platform, a site located on the eastern flank of The Gully (Appendix 2), identified features similar to those seen on the other parts of the Scotian shelf. However, wave fronts propagating at various orientations (Figure 1.2)

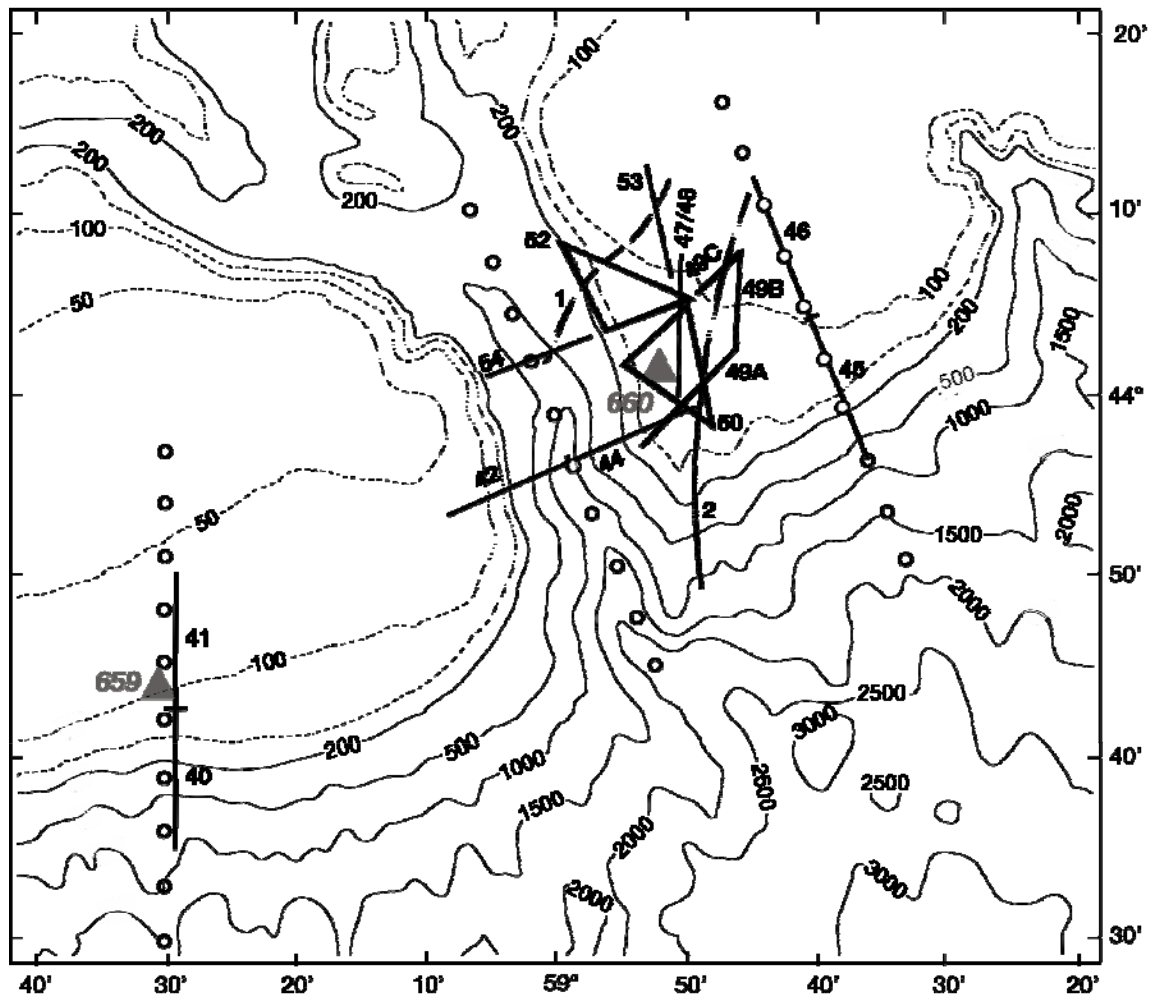


Figure 5.1.1: Bathymetry for The Gully site. Depth contours are in m; CTD casts circles; mooring sites are triangles; and the tracks for Batfish data are the solid lines. The dashed lines denote the paths used in analysis of depth gradients (see Appendix 6).



indicated that multiple generation zones were likely. For this reason, the field program was designed to survey several potential generation zones around the mouth of the canyon.

The locations of the observations in relation to the detailed bathymetry are shown in Figure 5.1.1. The open circles are the locations of a preliminary CTD survey, the solid triangles the sites of two moorings, and the solid lines the ship track during the Batfish surveys. The surveys are numbered between 40 and 54. The stations 50 and 52 are each a triangular track occupied in a clockwise direction.

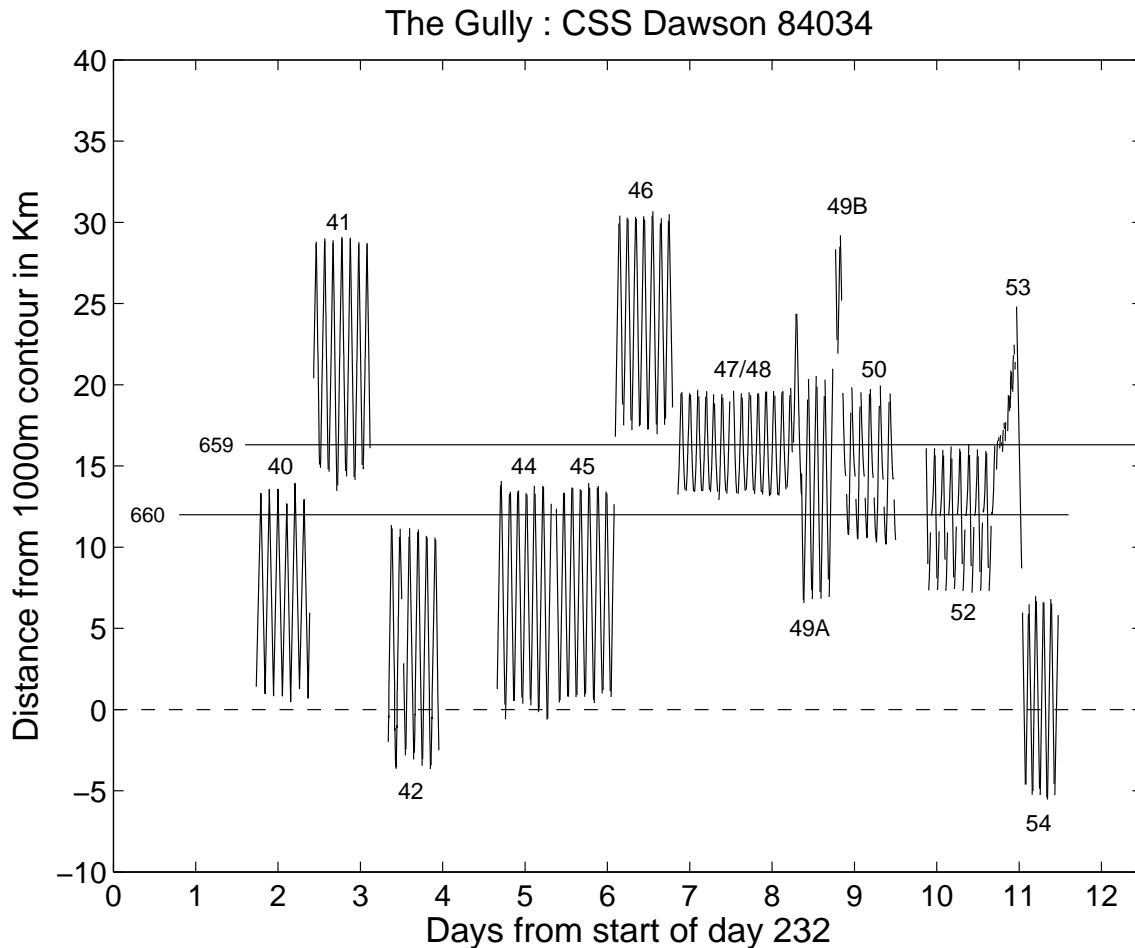


Figure 5.1.2: Time history of data collected at The Gully. Batfish data are the repeated cycling labeled as stations 40 to 54; and moorings are 659 and 660 at the distances and times shown by the solid lines. Distance is the cross-contour value to 1000 m or to maximum canyon depth.

The time sequence of events is given in Figure 5.1.2. All Batfish stations except 53 are time series; Station 53 is a tracking mode. The CTD survey was conducted immediately prior to Day 232, followed by the deployment of two moorings, 659 and 660, for the duration of the period on site as shown.

## 5.2 Processing of Batfish Data

In processing the data we followed the general procedure as at the other two sites. All stations, except 53, were time-series stations and a mean density field could be constructed for each. For station 47-48, which was sampled repeatedly over almost three semi-diurnal tidal periods, the test function in the least-squares fit (section 3.3, step 6) also included the diurnal component. Hence for that station the mean field incorporates the diurnal variation when displacements and energy at higher frequencies are considered. For tracking-mode station 53 the mean density structure is assembled from 1) extending the fields of stations 47-48, 49 and 52 and 2) using the data of station 53 at times deemed closest to neutral conditions. The mean field thus constructed is clearly more uncertain than those for the other stations. On the other hand the displacements in station 53 are large and hence the relative errors are small in both displacements and potential energy.

### 5.3 Potential Energy Contour Plots

As at the other two sites, two potential energy density contour plots are shown; one of a time-series station and the other of a tracking-mode station. Plots for all stations are shown in Appendix 5.

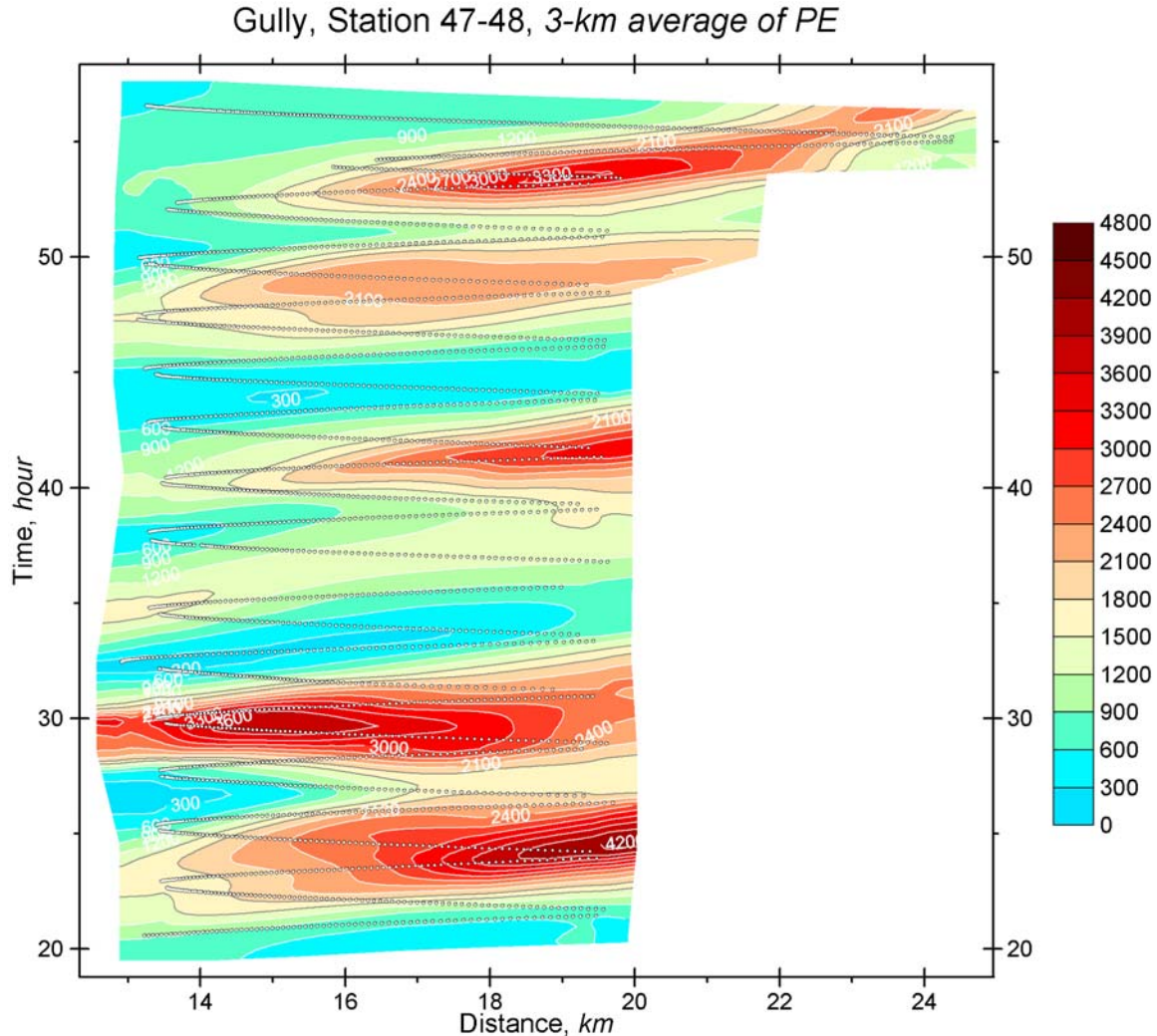


Figure 5.3.1: Potential energy during time-series station 47-48 at The Gully site. Contour lines in *Joules/m²*.

For station 47-48 the distance is measured from 43.988 N, 59.000 W (1000 m isobath near the axis of The Gully). Time refers to Julian day 238 in 1984. The geographical section of the station is set along longitude 58° 50' W, between approximate latitudes of 44.00 and 44.08 degrees N. The energy arriving in the section is generated mainly along the eastern flank of The Gully and passes through the section propagating in ENE direction. The apparent propagation speed along the section is therefore high (~ 5 km/hour). The energy densities are much higher than in the Scotian Gulf. The observed

internal tide amplitude reached values as high as 20 m. The water depth varies from 130 to 90 m.

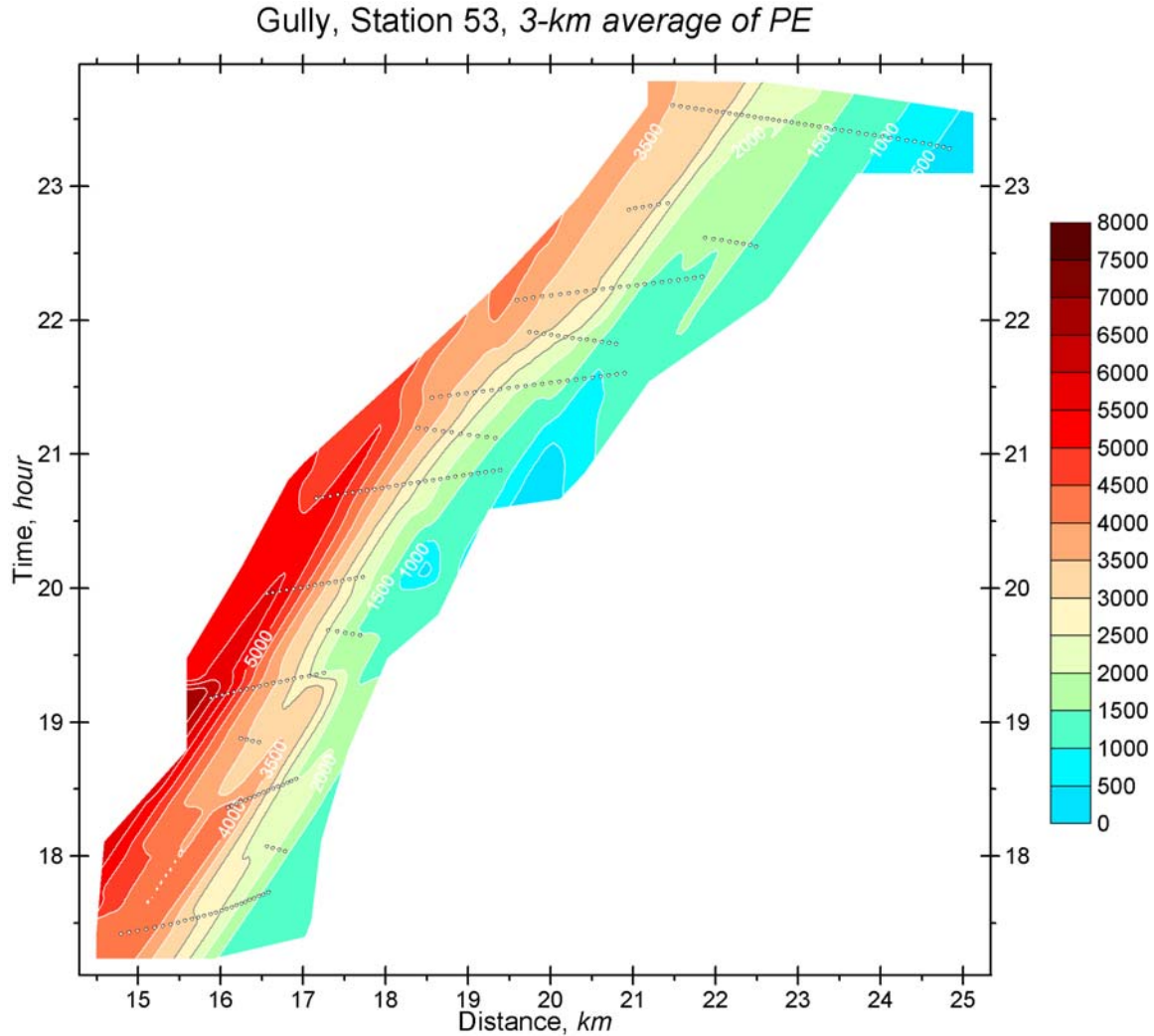


Figure 5.3.2: Potential energy in  $Joules/m^2$  at tracking-mode station 53.

The distance for tracking-mode station 53 is measured from 44.038 N, 59.030 W (from the axis of The Gully). Time refers to Julian day 242. The ship track was adjusted in each of the 15 transects so as to be transverse to the advancing wave front. At the start of the station the wave group being tracked propagated in NNE direction, with ship on course 020° (or 200°). At about 21 hours the predominant wave group propagation direction had shifted to more easterly direction and the ship's course was changed to 055° (235°). During the approximately 7 hours of tracking the wave group the ship was drifting in a NW direction at a speed of  $\sim 0.15$  m/s. The estimated propagation speed of the wave group is  $\sim 2$  km/hour.

## 5.4 Potential Energy Scatter Diagram

In the preceding section the potential energy content of internal waves for two example stations was illustrated by contouring it in time-distance domain. The same data for all stations, see Appendix 5, are presently summarized by plotting it as a function of distance only. At a given distance (measured from 1000 m isobath) variability within a tidal period as well as variability from tide to tide is included. Since the bathymetry at The Gully site is more complex than at the other two sites and the energy levels vary greatly from the Sable Island Bank to South-East side of Banquereau Bank and to eastern flank of The Gully, the summary is presented in three separate plots.

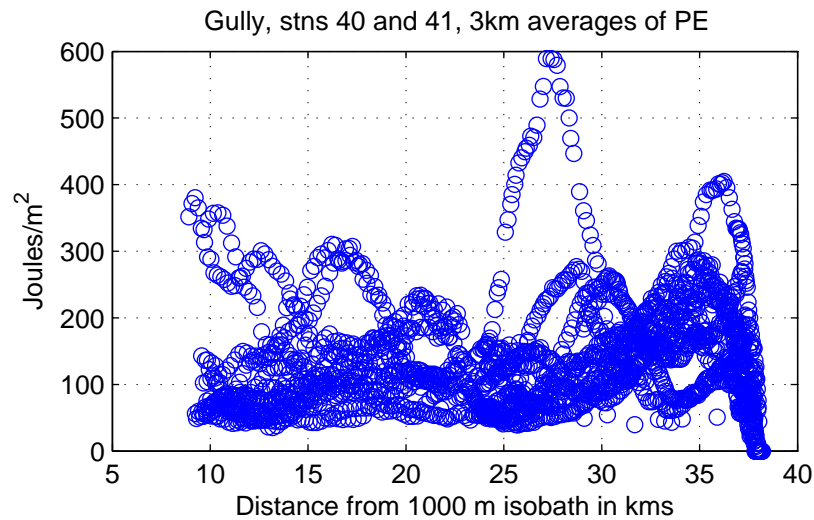


Figure 5.4.1: The Gully stations 40 and 41, Sable Island Bank, scatter plot of 3 km averages of potential energy as a function of distance from 1000 m isobath.

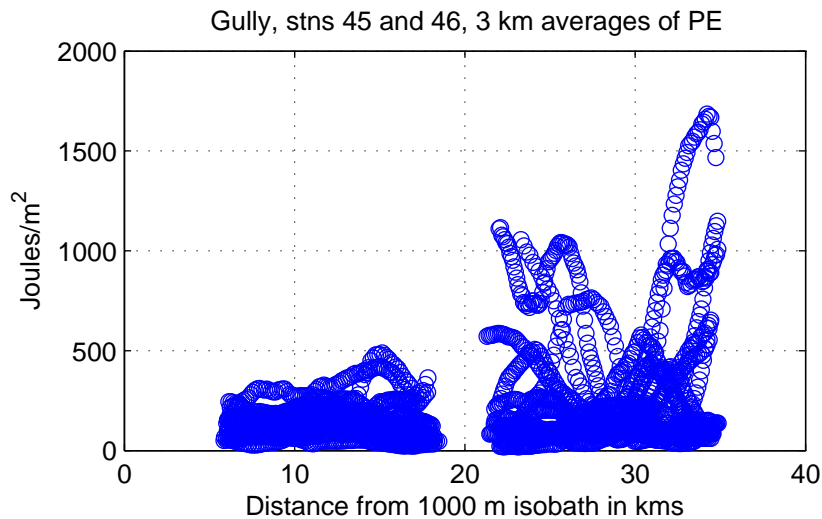


Figure 5.4.2: The Gully stations 45 and 46, S-E side Banquereau Bank, scatter plot of 3 km averages of potential energy as a function of distance from 1000 m isobath.

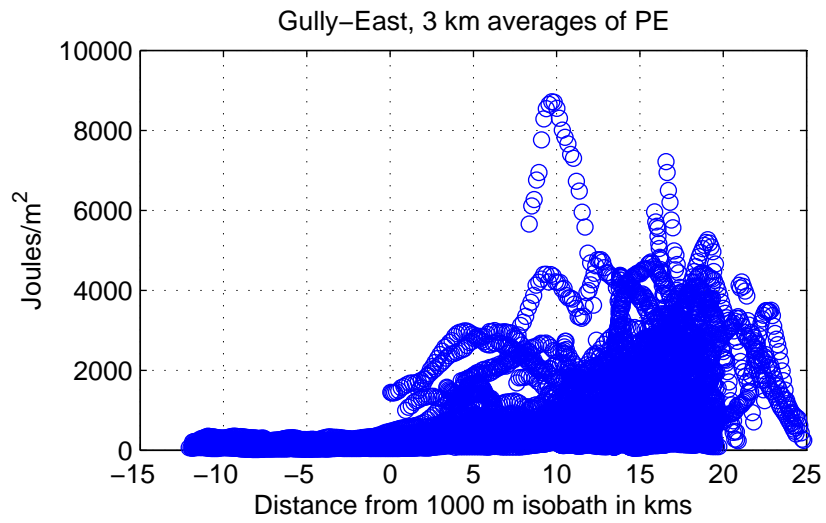


Figure 5.4.3: The Gully eastern flank stations scatter plot of 3 km averages of potential energy as a function of distance from 1000 m isobath, which is essentially the center of The Gully. Negative distances (stations 42 and 54) are on the western flank.

## 6. Modelling of Internal Tide and Comparison with Observation

### 6.1 Analytical Model

In analytical models of topographic interaction and transfer of energy from barotropic to baroclinic tide, especially for two-dimensional and linear dynamics, two parallel approaches have been used. The first of these uses normal modes or eigenfunctions, in terms of which the variables can be expanded. The second approach makes use of the ray or characteristic theory, in which the ‘critical’ and ‘near-critical’ bottom slopes as sites of optimum topographic interaction are emphasized. For periodic forcing the two approaches should, and in most cases have yielded comparable results.

Application of model results in the ocean environment is fraught with problems, not only because the interaction processes are more complicated than what the simple models represent, but also by other competing processes. The ray theory especially is sensitive to processes such as non-linearity, dispersion, dissipation, advection, etc. Our analysis of data at the three shelf edge sites shows that modal decomposition represents the results better than ray theory and that on the shelf the first mode dominates in the internal tide and especially in the large amplitude, short waves.

Keeping in mind the complexity of the interaction, but guided by the observations, we construct a very simple two-dimensional generation model for internal tides that includes the observed density structure, realistic bottom topography and barotropic tidal flux across the topography.

In considering the dynamics of the interaction, we can separate the variables into a vertically varying component and one that varies in space and time. Thus in (x,z,t)-space we express the isopycnal displacement as

$$\zeta(x, z, t) = F(x, t)Z(z) \quad (6.1,1)$$

where  $Z(z)$  is the solution of the ODE

$$Z''(z)/Z(z) = \lambda(N^2 - \omega^2)/(\omega^2 - f^2) \quad (6.1,2)$$

It is the eigenfunction equation if

$$\lambda = -k^2 \quad (6.1,3)$$

In general,  $k^2$  can have an infinite number of values, i.e. eigenvalues, corresponding to the infinite number of possible solutions, i.e. eigenfunctions or normal modes. Furthermore, if the depth of the water varies, the eigenvalues vary accordingly and the eigenfunctions are depth-specific.

For a given eigenvalue  $k_n^2$  (and eigenfunction  $Z_n(z)$ ), the function  $F_n(x, t)$  in the internal wave band,  $f^2 < \omega^2 < N^2$ , is composed of waves propagating towards  $x = \pm \infty$ . Hence the general solution for the isopycnal displacement is

$$\zeta(x, z, t) = \sum_{n=1}^{\infty} (a_n(x, t) + b_n(x, t)) Z_n(z) \quad (6.1,4)$$

where  $a_n(x, t)$  and  $b_n(x, t)$  are the components propagating towards  $\pm \infty$ , respectively. The orbital horizontal velocity of such waves is

$$u(x, z, t) = \sum_{n=1}^{\infty} c_n(x) (a_n(x, t) - b_n(x, t)) Z_n'(z) \quad (6.1,5)$$

where  $c_n(x)$  is the depth-dependent propagation speed. Using the continuity equation in the form

$$\frac{\partial \zeta}{\partial t} = \frac{\partial}{\partial x} \int_z^0 u dz \quad (6.1,6)$$

and substituting (6.1,4), (6.1,5) and introducing barotropic flow  $u_B(x, t)$ , we obtain

$$\sum_{n=1}^{\infty} \left\{ \frac{\partial}{\partial t} [a_n + b_n] + \frac{\partial}{\partial x} [(c_n(x) + u_B(x, t)) a_n - (c_n(x) - u_B(x, t)) b_n] \right\} Z_n = -z \frac{\partial}{\partial x} u_B(x, t) \quad (6.1,7)$$

After orthogonalizing (6.1,7), the evolution of each mode is expressed separately as

$$\frac{\partial a_n}{\partial t} + \frac{\partial}{\partial x} [(c_n(x) + u_B(x, t)) a_n] + \frac{\partial b_n}{\partial t} - [(c_n(x) - u_B(x, t)) b_n] = -v_n(x) \frac{\partial}{\partial x} u_B(x, t) \quad (6.1,8)$$

where

$$v_n(x) \equiv \int_{-h}^0 z N^2(z) Z_n(z) dz \bigg/ \int_{-h}^0 N^2(z) Z_n^2(z) dz \quad (6.1,9)$$

In the small-amplitude limit, the evolution of each  $a_n$  and  $b_n$  can be considered separately:



$$\begin{aligned}\frac{\partial a_n}{\partial t} + \frac{\partial}{\partial x} [(c_n(x) + u_B(x, t))a_n] &= -\frac{1}{2} \nu_n(x) Q(t) \frac{\partial}{\partial x} \frac{1}{h(x)} \\ \frac{\partial b_n}{\partial t} - \frac{\partial}{\partial x} [(c_n(x) - u_B(x, t))b_n] &= -\frac{1}{2} \nu_n(x) Q(t) \frac{\partial}{\partial x} \frac{1}{h(x)}\end{aligned}\tag{6.1,10}$$

where on the rhs we have replaced barotropic current speed with current flux  $Q$  divided by depth. The forcing function in the evolution equations (6.1,10) is thus a product of the temporally varying current flux  $Q(t)$  and a spatially varying part consisting of the gradient of inverse depth multiplied by  $\nu_n(x)$  that incorporates the properties of a particular mode and the density stratification.

Given the required input fields, i.e. stratification, current flux and topography, the equations (6.1,10) are easily solved numerically. The solutions will be degraded if, for example, the density field is imperfectly known or the current flux cannot be realistically determined. Imperfect knowledge of the density gradient will especially affect the calculation for higher modes, which moreover will be affected by the omission of interactive advection due to the lowest modes. We have therefore limited the use of (6.1,10) to the lowest (fundamental) mode.

## 6.2 Comparison with Field Measurements

For the purpose of comparison of the simple model results and field measurements the Scotian Gulf site provides the most comprehensive set of measurements of the temporal and spatial changes of the density field and the most stable semidiurnal current field (cf. Appendix 7). The construction of the mean density field was discussed in Section 3.4. It was supplemented where needed by CTD density data outside the Batfish range and used to derive the eigenfunctions  $Z_n(x, z)$ ,  $c_n(x)$  and  $v_n(x)$ . The bathymetric section at  $63.5^\circ$  W and  $\nabla(1/h)$  are shown in Figure A6.1 in Appendix 6. As  $Q(t)$  we used the semidiurnal NS current at mooring 585 (closest to the generation site), more specifically the average of currents at 45, 72 and 96 m depth, deemed representative of the depth-averaged barotropic current.

In figure 6.2.1 we show the comparison of the model predicted displacement amplitude  $a_1$  (heavy solid line),  $a_1 + b_1$  (dashed line) and displacement of isopycnals (light solid lines) at M2 frequency for  $\sigma = 26.0$  to  $26.5$  ( $\Delta\sigma = 0.1$ ) at 12, 16, 20 and 24 kms from the 1000 m isobath, which is used as the deep water starting point for integration of (6.1,10). The four frames on the left hand side (lhs) of the figure represent data from station 33 at all four chosen distances (from top to bottom), whereas the first two rhs frames represent station 37 at 12 and 16 kms and the last two station 35 at 20 and 24 kms. Thus measurements during three different days are shown in the figure. The choice of the particular set of isopycnals for comparative purposes was indicated by the functional form of  $Z_1(\sigma)$ , i.e. maximum displacement in the fundamental mode is in the range of these isopycnals.

The agreement between observation and the simple model is quite reasonable and encourages us to inquire as to the usefulness of the model in the description and analysis of observed potential energy. Although there is good agreement at the M2 frequency and at the level of maximum displacement, the displacement of other isopycnals may also contain other modes that the simple model is unable to represent. As a test at the level of potential energy, we compare integrals of energy over a M2-period. The potential energy of the observations is obtained as discussed in Section 3.3, namely by addition of the square of displacement of each discrete isopycnal, whereas the model potential energy is calculated using modal amplitude and form according to (3.2,5), but for  $n = 1$  only. Thus the model potential energy is associated with 1<sup>st</sup> mode only, whereas observed energy may contain other components in addition to the first mode.

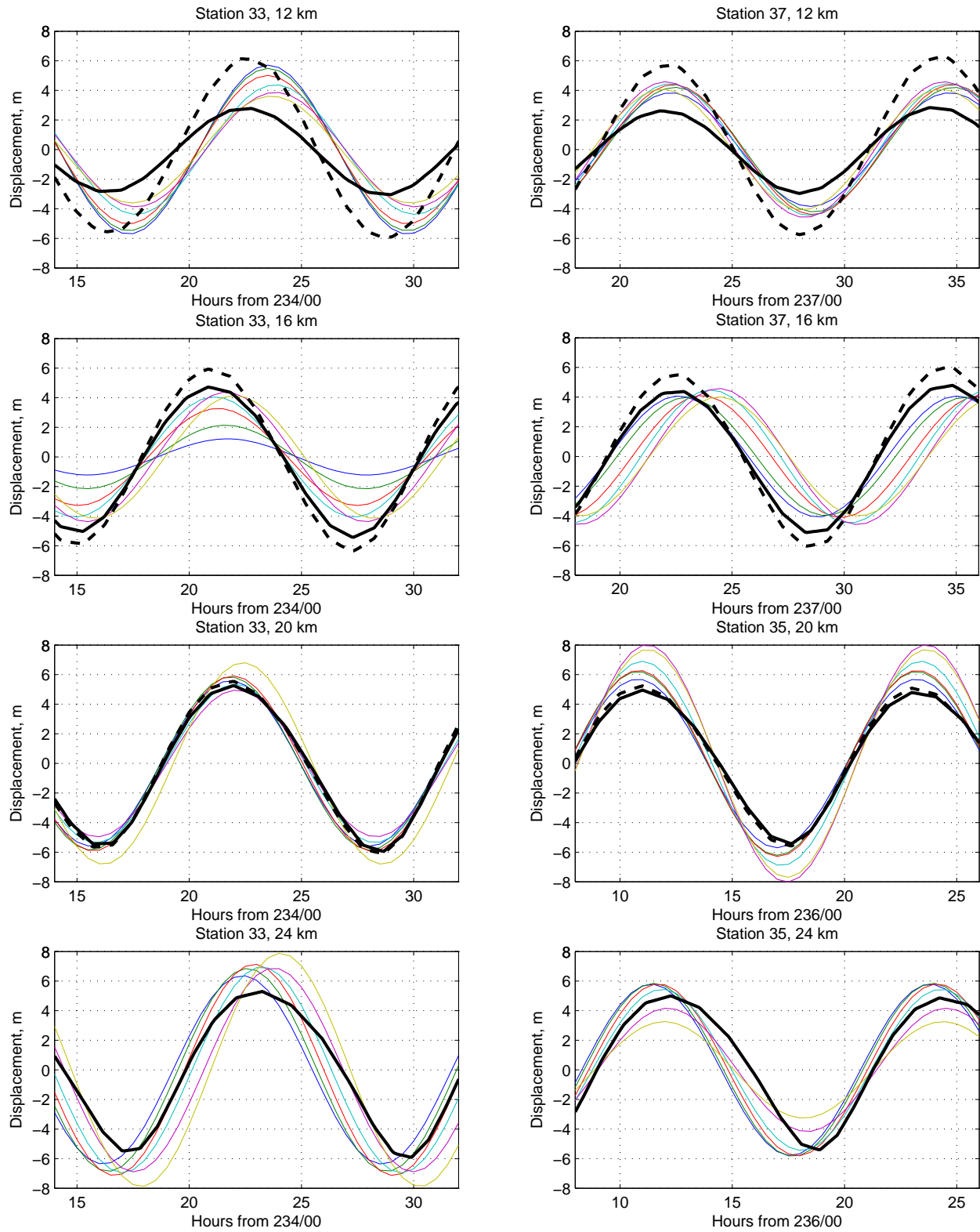


Figure 6.2.1: Comparison of predicted M2 isopycnal displacement with observations. Predicted displacement amplitude  $a_1$  (heavy solid line),  $a_1 + b_1$  (dashed line) and displacement of isopycnals (colored lines) at M2 frequency for  $\sigma = 26.0$  to  $26.5$  at 12, 16, 20 and 24 kms from 1000 m isobath.

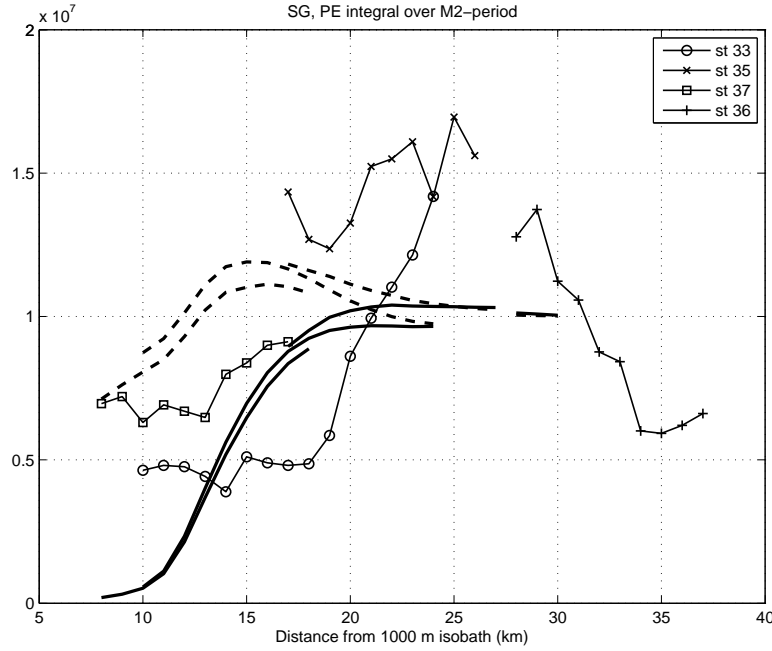


Figure 6.2.2: Comparison of M2-period integrals of potential energy.

Figure 6.2.2 shows the comparison of M2-period integrals of potential energy at various distances from the 1000 m isobath. The shoreward propagating energy in the model is shown with the heavy solid lines, the sum of both shoreward and offshore moving energy with dashed lines and the observed energy during four different tidal cycles (stations 33, 35, 36 and 37) with light solid lines and symbols. The units along the vertical axis in the figure are such that when multiplied with the propagation speed, would yield the energy per wavelength. The comparison shows that in the main generation zone ( $\sim 10 - 20$  kms) the model yields higher estimates of energy (especially when  $a_1 + b_1$  is used), but further inshore the observed energy at its maximum exceeds the model energy by  $\sim 50\%$  and yet further inshore starts declining. Hence we conclude that there are processes influencing the energy content of internal waves that the simple generation model is unable to reproduce, but that to first order the model energy estimates are in substantial agreement with observed values.

The  $a_n$  and  $b_n$  in (6.1,10) can be considered as wave particles traveling from deep to shallow water and *vice versa* respectively with speeds  $c_n(x) \pm u_B(x,t)$ . Initially they are empty, but gain (or lose) “stuff” as they traverse the region of non-zero  $\nabla(1/h(x))$ . The integral of the *rhs* of (6.1,10) is in general a convolution of spatially and temporally varying functions. In the case where the depth change is localized in a narrow region, the particle travel time through the forcing (generation) area is short. In the extreme cases of a step change in depth or a constant  $Q$ , the particle change of “stuff” reflects the instantaneous value of  $Q(t)$  or  $Q$ . In the actual cases the forcing is spread out over a finite region and  $Q(t)$  is smeared over a finite time in the convolution. At the three sites the

finite time is a fraction of the M2 forcing period. Hence the expectation is that the amplitudes of the displacements, especially on the shelf, are related to the strength of the smeared current flux  $Q$ . This implies that the potential energy in the model must be related to  $Q^2$ , perhaps not in detail, but in an averaged sense. In fact when  $Q^2(t)$  is integrated over the same M2-period as the model potential energy, we find that the ratio of the two is approximately constant for all M2-periods. With the parameters used in the model we obtain:

$$Ratio = \int_{t_0}^{t_0+T} PE_{model} dt / \int_{t_0}^{t_0+T} Q^2(t) dt = 0.52 \pm 0.02 \quad (6.2,1)$$

Integrating (6.1,10) with constant  $Q$  and other parameters unchanged, we find that change of potential energy on the shelf is related to  $Q^2$  by a factor of 0.60. The smearing of  $Q(t)$  has reduced the model potential energy to somewhat less than 90 % of the maximum. The expected response at M2 frequency surely contains higher modes in addition to the fundamental one, but their amplitudes also reflect the strength of the current flux and therefore the combined potential energy per M2 period would also be related to the integral of  $Q^2$ . This may partly contribute to the observed energies in figure 6.2.2.

The preceding comparisons and discussion has been concerned with forcing and response at M2 frequency solely. However, energy at M2 frequency is only a fraction (although a large fraction) of the total energy seen in observations and the current flux contains components at frequencies other than M2. Can we extend the relationship between the integrated energy and  $Q^2$  to other frequency bands beside M2? At least a partial answer is provided when we compare *normalized* semidiurnal and total potential energies. The normalized energies are formed as ratios similar to (6.2,1), with PE calculated from isopycnal displacement at M2 frequency and at all frequencies respectively, and for  $Q^2$  we use either the current flux squared at M2 frequency or at all frequencies  $< \sim 0.5$  cph. The comparison for the Scotian Gulf site is shown in figure 6.2.3. The normalized integrated energies during four different tidal cycles (stations 33, 35, 36 and 37) are shown at M2 frequency (solid lines) and for all potential energy (dashed lines). In the main generation zone ( $\sim 10 - 20$  kms) and some distance shoreward the normalized values for M2 and total energy are in general agreement, but diverge further inshore. We believe this to be due to energy flow from longer to shorter wavelengths, formation of solitary waves, and also due to conversion of kinetic to potential energy associated with the short waves. This and other questions will be taken up in a general discussion of results. The important conclusion we draw from figure 6.2.3 is that the integrated current flux is a useful indicator of energy being pumped into the internal wave field.

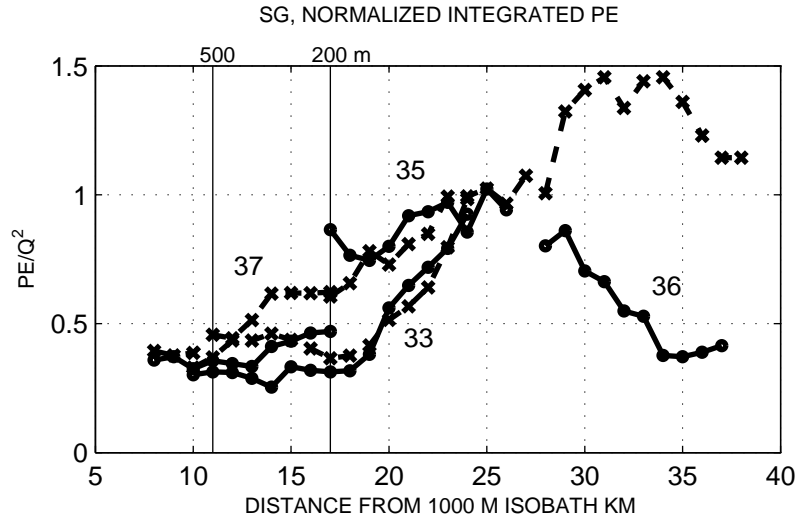


Figure 6.2.3: Normalized semidiurnal(solid lines) and total(dashed lines) potential energy for the Scotian Gulf. Two vertical lines denote water depths of 500 and 200 m.

In figures 6.2.4 to 6.2.7 are shown the normalized energies at the other two observation sites. Figure 6.2.4 summarizes the EW variation of normalized potential energy on the Grand Bank along  $47^{\circ}$  N latitude. The energy at M2 frequency during the four time-series stations (4546, 48, 49 and 50) is again plotted with solid lines and the total energy with dashed lines. The pattern of energy variation is similar to the one seen in the Scotian Gulf. However, in this case the longer length of the section allows us to see more of the dissipative part of the process.

Figure 6.2.5 depicts the energy variation on the Sable Island Bank in a section at  $59^{\circ} 30'$  W longitude (stations 40 and 41). Figure 6.2.6 shows the variation on the south-eastern side of Banquereau Bank (stations 45 and 46) and figure 6.2.7 includes three stations (44, 47 and 48) from the eastern flank of The Gully on the south-western edge of Banquereau Bank. The pattern of normalized energy variation in these three figures for The Gully differs from those in the Scotian Gulf and on the Grand Bank, but the *normalization factor* (the ratio of integrated PE and  $Q^2$ ) near the shelf break is similar at all three sites. The increased growth of energy further up on the Banquereau Bank is discussed in sections 9 and 10.

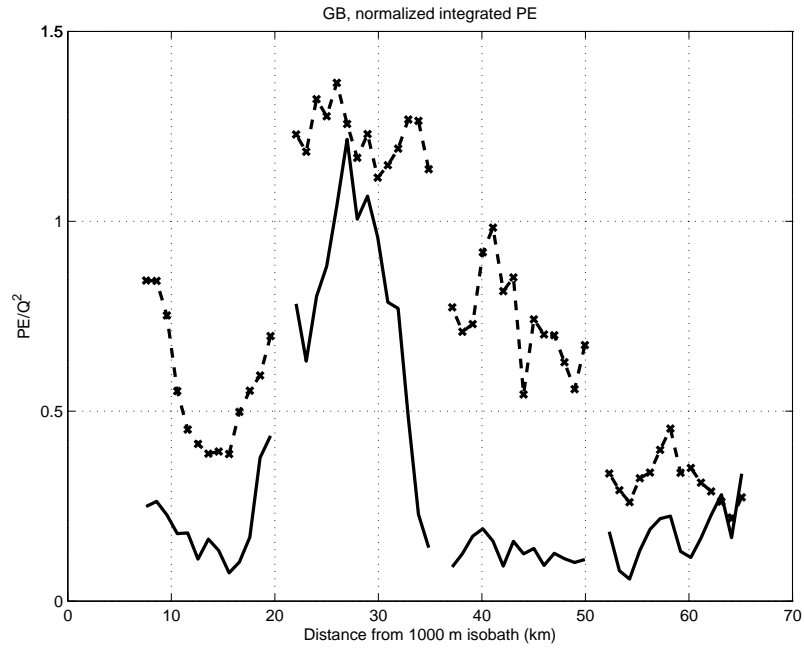


Figure 6.2.4: Normalized semidiurnal(solid lines) and total(dashed lines) potential energy for the Grand Bank.

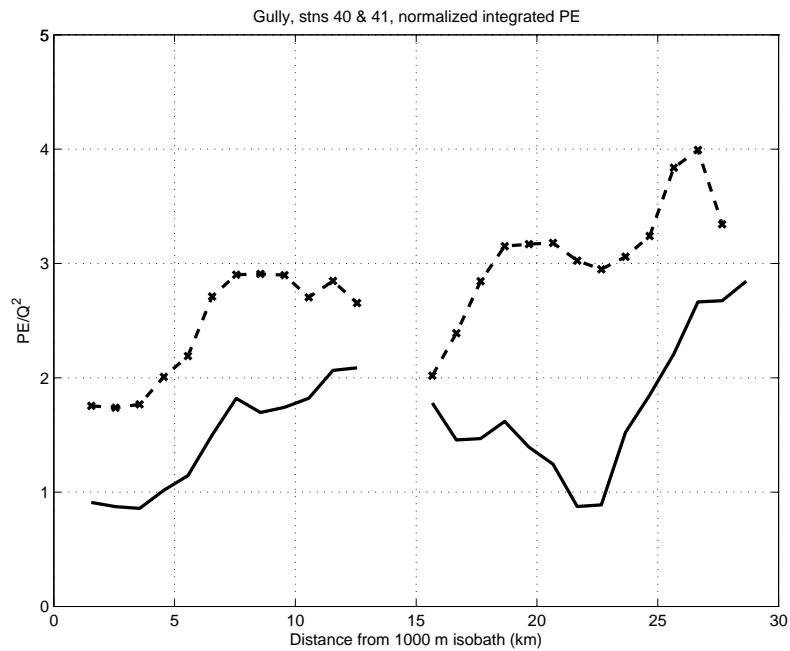


Figure 6.2.5: Normalized semidiurnal(solid lines) and total(dashed lines) potential energy for the Sable Island Bank near The Gully.

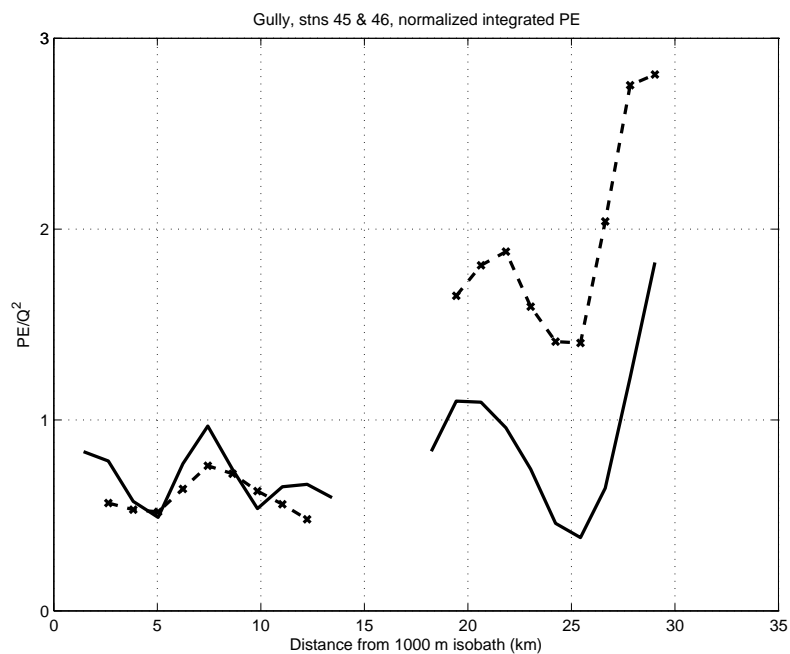


Figure 6.2.6: Normalized semidiurnal(solid lines) and total(dashed lines) potential energy for the south-eastern side of Banquereau Bank near The Gully.

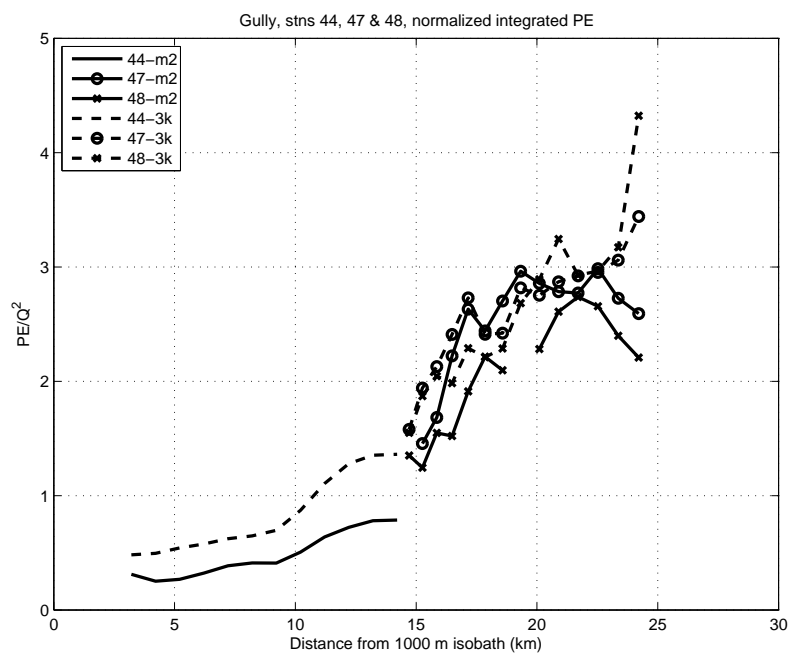


Figure 6.2.7: Normalized semidiurnal(solid lines) and total(dashed lines) potential energy for the south-western side of Banquereau Bank, east flank of The Gully.



Additional confirmation of the close connection of PE and  $Q^2$  is obtained by examining temporal change of both. On the Banquereau Bank the combined Batfish station 47-48 sampled a section at  $58^\circ 50' W$  longitude over three successive M2 tidal periods. The energy at a given location in the section is seen to vary from one tidal period to another. This can be seen in the time-distance plot of energy (Figure 5.3.1), but also when integrated energy is plotted as a function of time. Figure 6.2.8 shows the M2 tidal period integrals at four locations 3 km apart. It also shows the integral of  $Q^2$ , where the current flux  $Q$  is calculated from observed current at 67 metre depth at mooring 660, in this case in SW-NE direction. The current flux estimate is somewhat sensitive to the current component direction chosen. The choice here is a compromise between a range of directions from which the refracted energy arrives at the measuring location. It is also the direction in which the waves are propagating. In the figure the integral of  $Q^2$  has been multiplied by a factor of 4. The figure shows that the energy content in waves follows the fluctuations in the current flux, given that the other physical parameters remain the same.

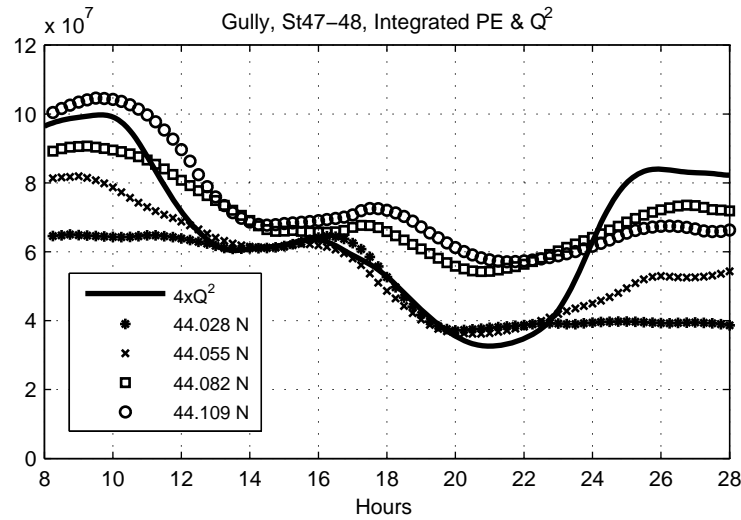


Figure 6.2.8: Temporal variability for  $Q^2$  at mooring 660 and the integrals of potential energy at four locations along Station 47-48.

## 7. Batfish Sampling Scheme

### 7.1 Problems of Resolution?

In processing the Batfish data, the sawtooth-like path of the instrument was split into successive ascending/descending portions, termed ‘casts’ a lá CTD. The position and time of each cast was specified by averaging the position and time along the slant-wise moving Batfish. The separation of the casts both in space and time would depend on the depth-range of the instrument, its vertical up and down speed and the speed of the ship. The length of the cable connecting the Batfish to the ship was long enough ( $\sim 300$  m) so that the horizontal distance between the instrument and ship could be considered as constant. For Batfish depth-range between 10 and 100 metres and typical speeds, the cast separation was 300-400 metres, reduced to about 150 metres when Batfish cycled between 10 and 50 metres depth.

Figure 7.1.1 is an illustration of the different data representations along the slanting Batfish path and the vertical ‘CTD cast’. In part (a) the elevations of isopycnals ( $0.1 \sigma$ -units apart) are plotted in the ‘cast’ form in a 3 km long section at  $63^\circ 30' \text{ W}$ . In part (b) the elevations are shown (now  $0.5 \sigma$ -units apart) on the slanting paths. The curves in (b) between the paths are drawn as a best estimate consistent with data and the expected behaviour of high-amplitude waves. Comparing (a) and (b) indicates clearly the problem of resolving properly at least some of the high-amplitude and short wavelength features, although by selective (and time consuming) reconstruction some of the un-resolved features could be reconstituted.

Since our focus has been on calculating the potential energy in 3 km sections, such as shown in figure 7.1.1, the question is how much the problem of resolving individual short high-amplitude waves affects the calculation of potential energy over longer scales? In order to estimate the amount of discrepancy between measured and actual potential energy, we have carried out a test with a group of KdV solitary waves (Figure 7.1.2), which are sampled with a ‘virtual’ Batfish. The sampling parameters are adjusted to reflect those in real observations. The ‘virtual’ Batfish is cycled both between 10 and 100 metres and 10 and 50 metres depth, and is being towed either in the direction or opposite that of the propagating waves. The ‘data’ are processed in the same way as the real data; un-corrected and corrected (for missing sigma-levels) potential energies are calculated and compared with energy in the KdV solitary waves. In carrying out the test we have the flexibility of shifting the Batfish path vis-à-vis the position of the wave group and can therefore obtain an assembly of realizations for potential energy, an advantage that is lacking in real snapshot observations. The energy comparison is summarized in Table 7.1.

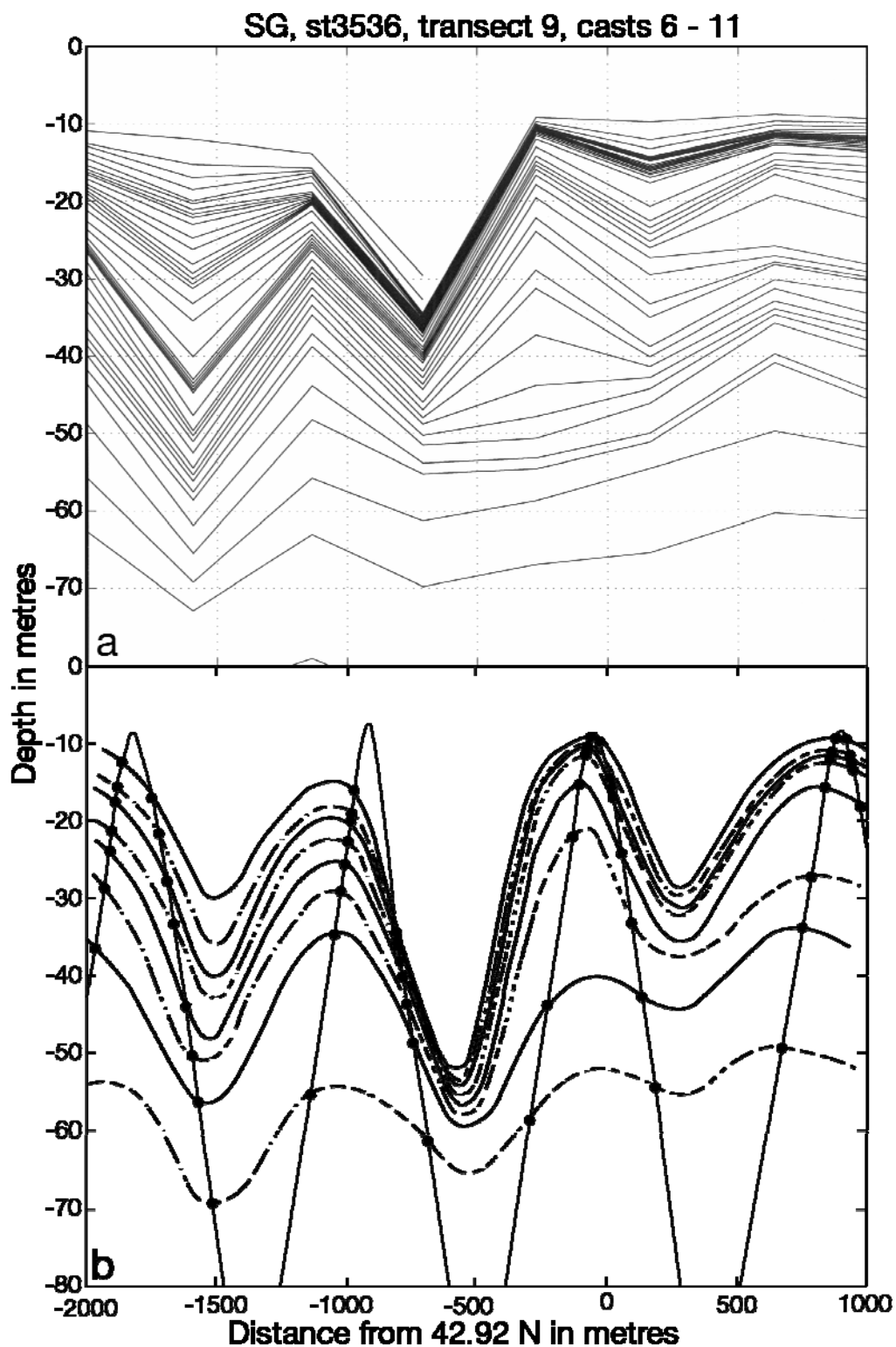


Figure 7.1.1: Example illustrating the interpretation of the Batfish data when viewed as a) a vertical cast, or b) as the more accurate slanting cast contoured as high-amplitude internal waves.

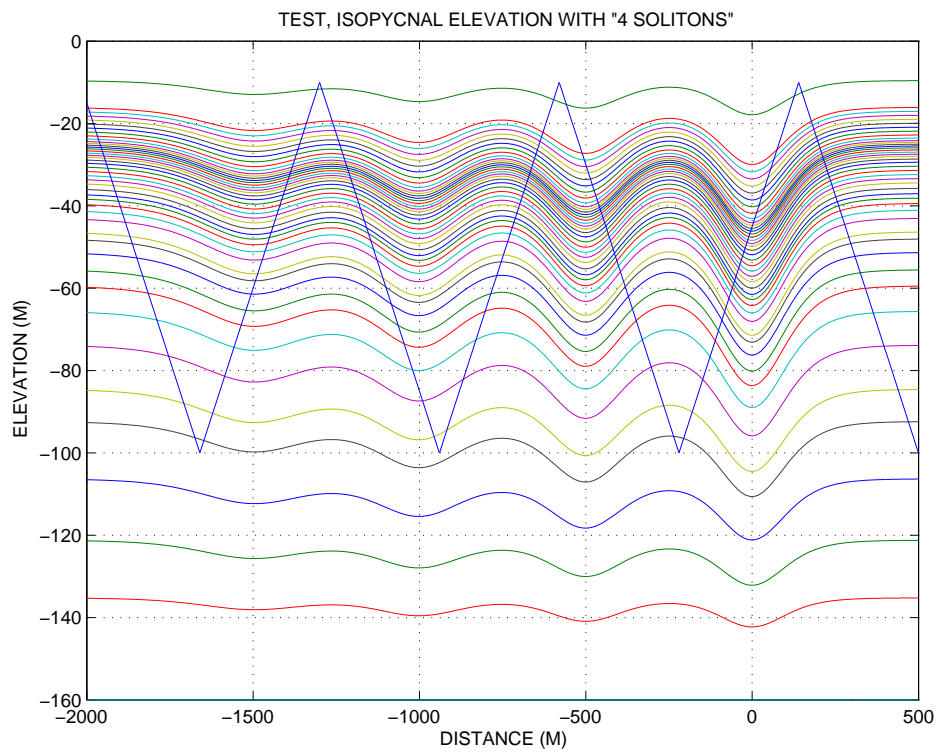
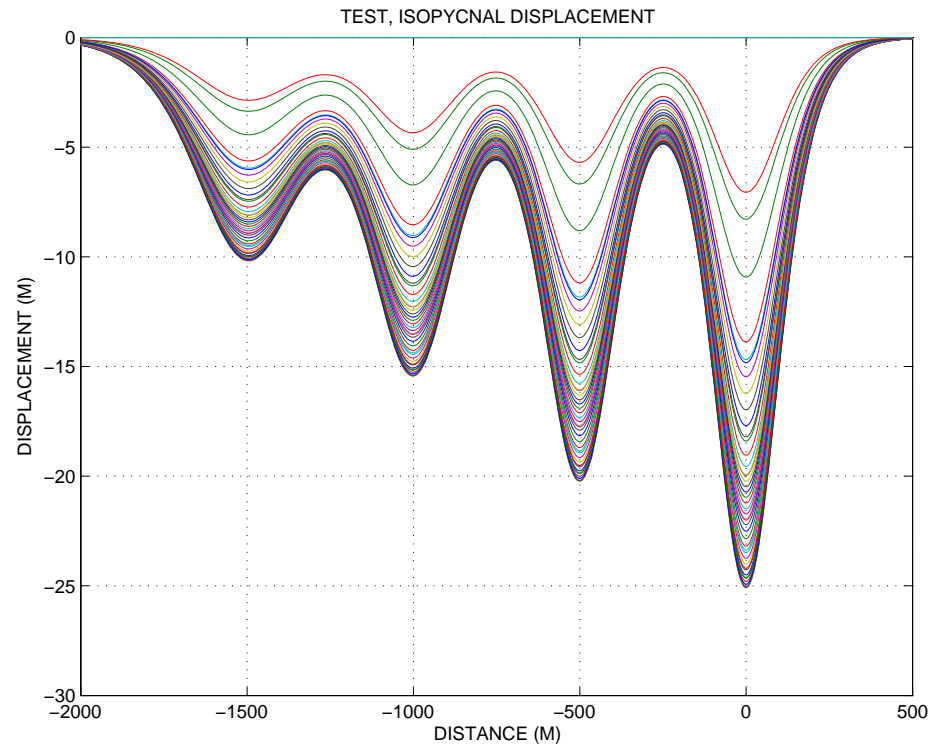


Figure 7.1.2: ‘Virtual Batfish’ sampling of a group of 4 KdV solitons. Batfish is towed in the opposite direction to wave propagation.

Table 7.1

Energy in KdV waves =  $4.36 \times 10^6$  J/m

Batfish towing direction	Depth range between			
	-10 and -50 m		-10 and -100 m	
	Mean $\times 10^{-6}$	%	Mean $\times 10^{-6}$	%
same as wave propagation	4.24	$97 \pm 3$	4.31	$99 \pm 2$
opposite to wave propagation	4.01	$92 \pm 10$	4.26	$98 \pm 10$

The tabulated values indicate that, although we may not be resolving some of the short scale features in our observations, we are estimating the potential energy over longer scales quite well. This is especially true when the Batfish travels in the same direction as the wave groups, but we are accounting for most of the energy even when the Batfish and waves travel in opposite direction. The error estimates are based on an assembly of 10 realizations for each category.

## 7.2 Density Inversions, Apparent or Real?

In most Batfish ‘casts’ both density ( $\sigma$ ) and pressure decrease/increase monotonically aside from the small-scale density fluctuations where the density gradient is small. These fluctuations are considered as noise, perhaps due to the time constant mismatch between temperature and conductivity-ratio sensors. They occur between adjacent one-second averages and their amplitude is  $< 0.1 \sigma$ -units.

However, in a number of ‘casts’ we observe larger-scale density inversions that extend over several to as much as 20 m of depth and occur in the pycnocline. The amplitude of such inversions may be as high as 1  $\sigma$ -unit. Are these inversions real or an artefact of the slant-wise path of the Batfish? To answer this question and to explore the cause of the inversions, we have looked at several cases in greater detail.

The first three cases of inversions were observed in the Scotian Gulf study area at 63° 30’ W longitude, inshore from the shelf edge, where the water depth varies little from ~ 160 m.

Case 1. In a sequence of 5 ‘casts’ density reversals are observed in 3, all occurring between ~ 15 and 35 m depth (figure 7.2.1). The same density data plotted along the Batfish path reveals, after constructing the isopycnal curves in a consistent manner (figure 7.2.2), that no density inversions are indicated. Although the Batfish intersects the same isopycnal more than once in a ‘cast’, this occurs because the rate of ascension of the Batfish in this case is small, especially in the pycnocline, and the slope of the Batfish track and the isopycnal slopes are almost equal. The estimated isopycnal slopes are consistent with the presence of a KdV solitary wave of ~ 20 m amplitude.

Case 2. A density reversal is observed in one ‘cast’ while traversing the same wave group as in Case 1 approximately 50 minutes later. The reversal is shown in the inset of figure 7.2.3. The main figure again is a construction of isopycnal elevations through data along the path of the Batfish. For  $\sigma$  approximately between 25.1 and 25.6 ( $\sigma = 25.5$  is shown) the isopycnal slopes exceed the slope of Batfish descent, which in the particular ‘cast’ is 1:5. The isopycnal slopes are also greater than the slopes expected with stably progressing solitary waves. An instability is indicated.

An additional remark regarding the figure is that the density structure in the ‘cast’ with the reversal may superficially indicate the presence of a 2<sup>nd</sup> mode in the vertical, since the near-surface isopycnals are elevated and the lower ones are depressed, but no such inference can be drawn when the horizontal dimension of the ‘cast’ is added.

Case 3. Figure 7.2.4 illustrates yet another observation of density reversal. This occurred while groups of waves were tracked as they propagated shoreward from the shelf edge. The Batfish during this observation was cycling between 5 and 45 m depth. The isopycnals for  $23 < \sigma < 23.5$ , where the reversal was seen, are shown in the shaded band in the figure. The slope of the Batfish descent is greater than 1:4, and since some isopycnal slopes are steeper than that, the wave is clearly unstable and possibly breaking.

The next three cases represent several similar events in observations on the edge of the Banquereau Bank adjacent to The Gully. In the first case shown the water depth is between 90 and 100 m, for the other two between 80 and 90 m.

Case 4. Figure 7.2.5(a) is a ‘snapshot’ of the front part of an undulating internal bore with  $\sigma$ -values as determined by ‘casts’, i.e. as function of depth only. The density inversion, shown in figure 7.2.5(b) as an inset, occurs at the very front of the bore where the isopycnals dive by more than 30 m. The observed inversion exists for  $24 < \sigma < 24.5$ , represented by the shaded region in the figure. The slope of the ascending Batfish track is  $\sim 0.4$  and some isopycnal slopes exceed this value. This is clearly an example of an unstable bore front where energy losses occur.

Case 5. The amplitude of the inversion in this case exceeded 1  $\sigma$ -unit, located in the main pycnocline (figure 7.2.6). The vertical extent of the inversion is  $\sim 10$  m. The Batfish track slope is 0.45.

Case 6. The perceived instability in this case occurs on the divergent (rear) part of the wave (figure 7.2.7), whereas in the previous examples it occurred on the convergent (front) part, seemingly the more prevalent occurrence. The vertical scale of the inversion is again  $\sim 10$  m. Batfish track slope is 0.75 and its descension rate  $\sim 2.4$  m/s.

In addition to the density inversions,  $\sigma(z)$  quite often exhibits apparent layering in the main pycnocline. The density in the layers is nearly constant. On occasion more than one layer is present separated by mini-pycnoclines. The vertical extent of these layers varies from a few to more than 10 m. They are predominantly associated with the presence of groups of large amplitude internal waves. An illustration is given in figure 7.2.8. In part (a) a section of isopycnal elevations is plotted as seen in Batfish ‘casts’. In part (b) the same section is shown, but only for  $23.5 < \sigma < 24.5$  with  $\Delta\sigma = 0.1$ .  $\sigma = 23.5, 24.0$  and  $24.5$  are shown with solid lines. The layer  $23.8 < \sigma < 24.1$  is shaded for emphasis. The energy propagation is to the right in the figure. Moving back through the waves the layer thickness increases from  $\sim 2.5$  to almost 15 m and then collapses to the background value of  $\sim 1$  m (figure 7.2.8).

We believe that both the density inversions and the layering are manifestations of active mixing processes in parts of the water column, for which the energy is drawn from the large amplitude internal waves. The dissipation of energy will be discussed more fully in Section 9.

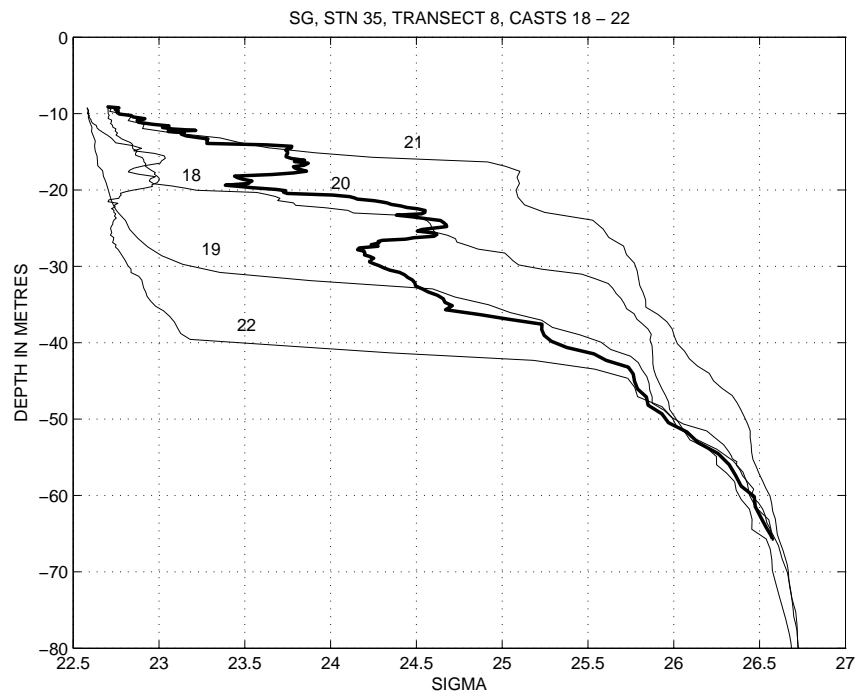


Figure 7.2.1: An example of a sequence of casts wherein density reversals are observed between the depths of 15 and 35 metres.

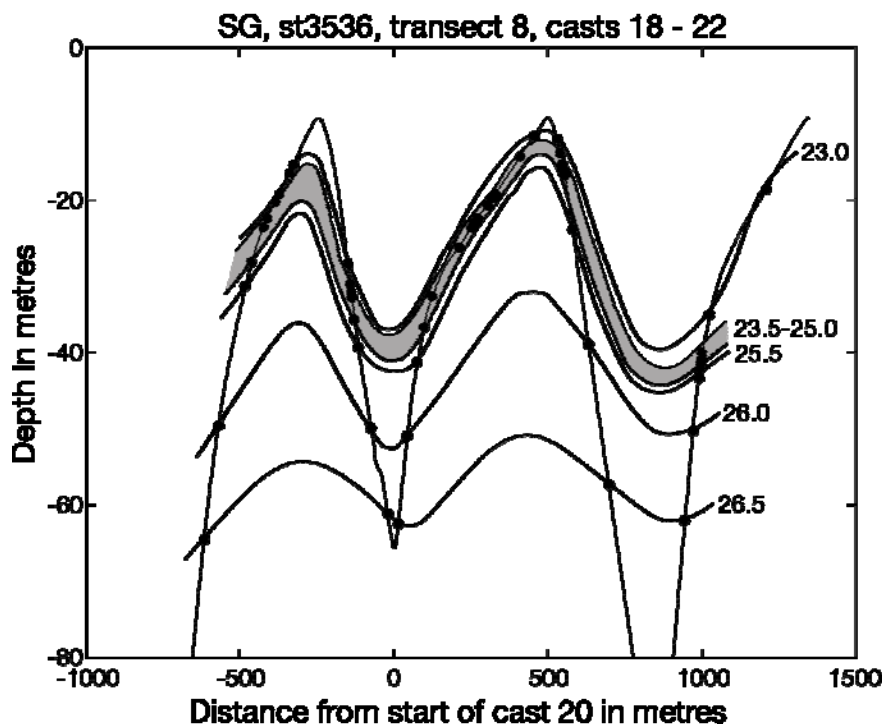


Figure 7.2.2: (see case 1 in text).



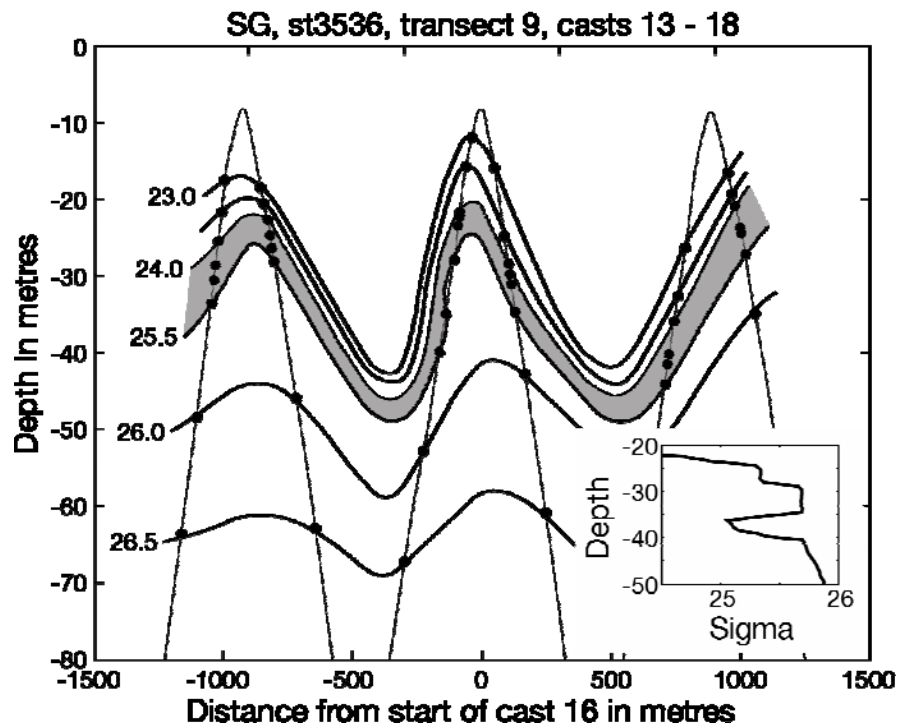


Figure 7.2.3: (see case 2 in text).

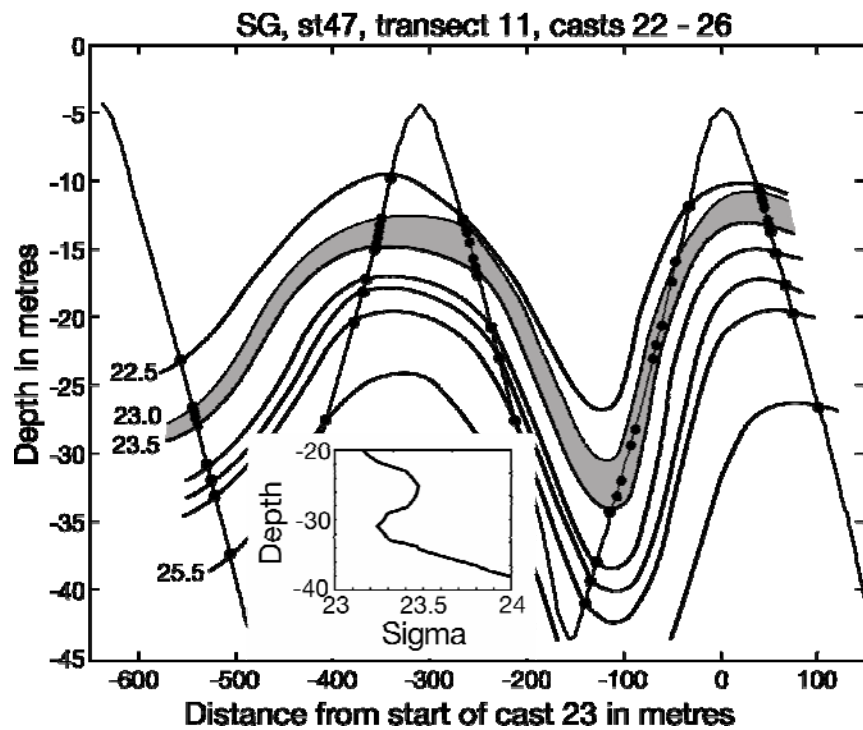


Figure 7.2.4: (see case 3 in text).

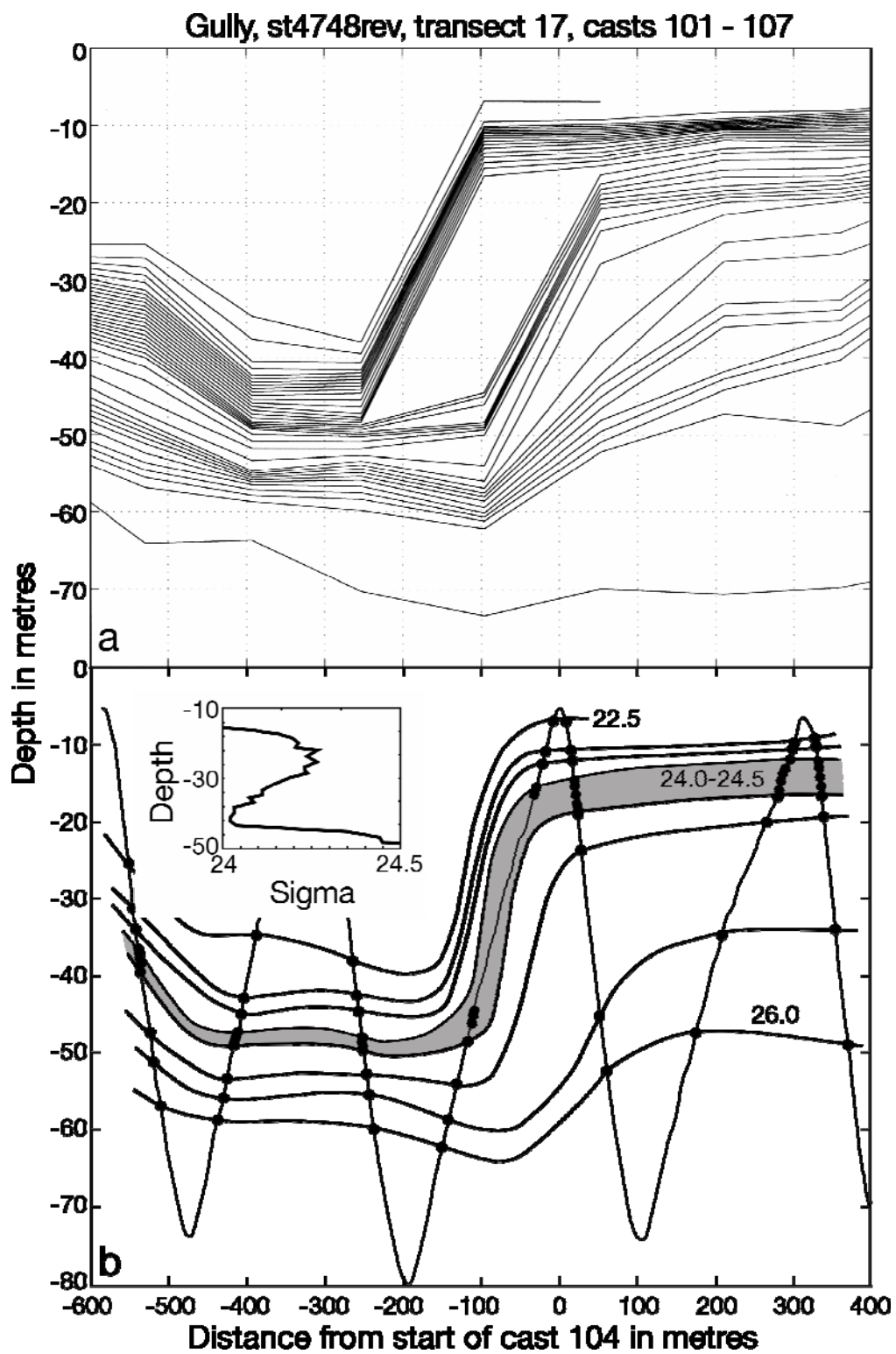


Figure 7.2.5: (see case 4 in text).

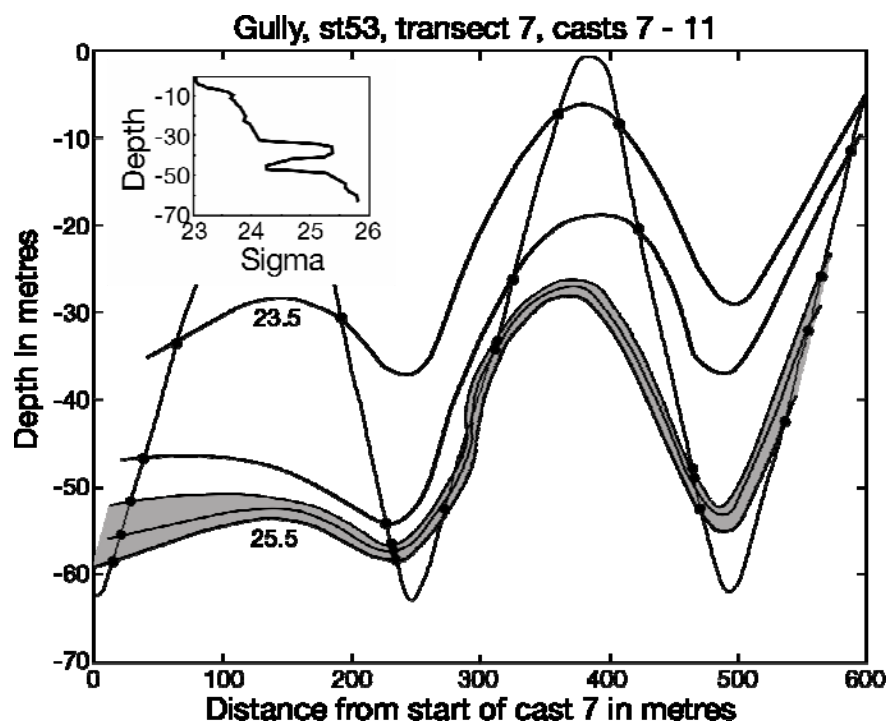


Figure 7.2.6: (see case 5 in text).

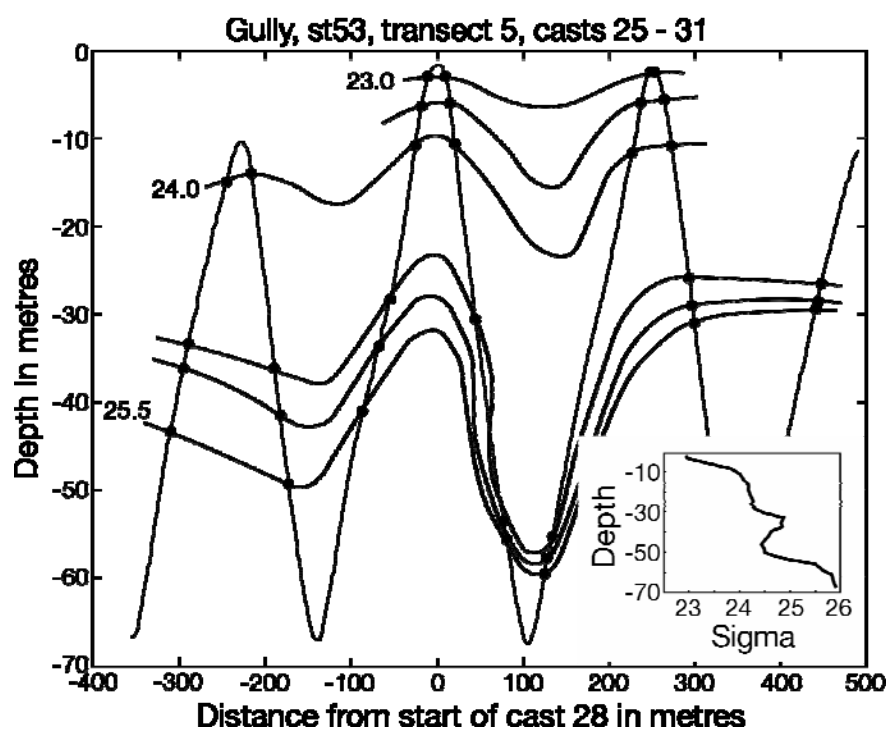


Figure 7.2.7: (see case 6 in text).

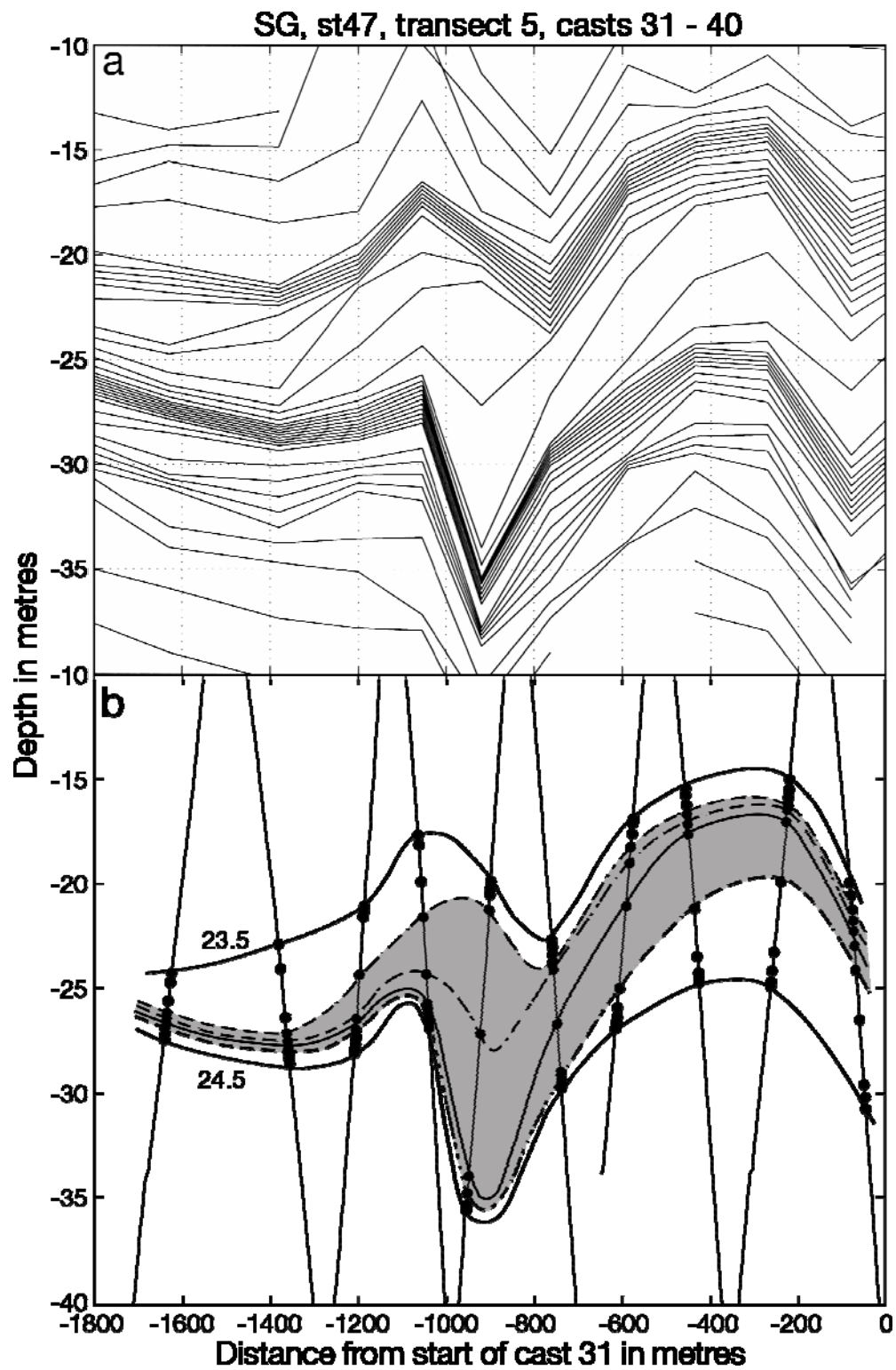


Figure 7.2.8: An example of 'layering' seen in the main pycnocline in association with the dissipation of the high-amplitude waves.

### 7.3 Comparison with Mooring Data

As described in detail in Section 3, in order to derive the mean density fields for the three sites the Batfish data from the repeated traverses of the same geographic section over at least one M2-cycle were used. In each traverse the data was sorted into overlapping geographic blocks of mostly 3 km length but on occasion also into 1 km long blocks. Block averages of time and isopycnal elevation were formed. The time-series of elevation, which was then analysed for least-squares fit, contained only as many points as the number of traverses in the section. Since each traverse lasted for approximately one hour, the time-series sampling rate at best was also once per hour. This limited sampling possibly affects the determination of the mean elevation of isopycnals, hence also the calculated displacement and the derived potential energy.

Continuous more frequent sampling of some parameters such as current speed and direction and temperature was carried out at the current meter locations. In this section we make use of recorded temperature by converting it to isopycnal displacement, which is then compared with the Batfish time-series.

The first issue to be confronted in temperature to displacement conversion is that we lack a representative temperature *vs* depth profile. Neither has the salinity been recorded at the current meters and hence we lack direct density measurements. To overcome this problem we turn to Batfish data in the vicinity of the mooring sites and look for good temperature-density correlation in the range of temperatures observed at the current meter. Suitable conditions are found close to the near-surface current meter at mooring #660 on the Banquereau Bank. From approximately 100 Batfish ‘casts’ within 2 kms from the mooring site the temperature-density relation is best represented by a cubic polynomial for  $8 < \text{temperature} < 18$  degrees. The RMS error in density for all temperatures in that range is  $< 0.06$  sigma-units.

Using the temperature-density relation, the appropriate section of the current meter temperature record is converted into a density record. Next the displacement is calculated by making use of the mean density *vs* depth data derived from Batfish time-series at the particular geographic location where the comparison is to be made.

In figure 7.3.1 are shown two comparisons of displacement as derived from current meter temperature (heavy solid line) and Batfish measurements (light solid lines). In the first comparison the Batfish time-series is formed by averaging isopycnal elevations and the sampling time in a 1 km section approximately 2 kms east of the current meter. The mean isopycnal elevations and displacements were obtained as described in Batfish Processing section. The second comparison applies to a 1.5 km section 2.5 kms south of the current meter. It is to be noted that in the Batfish data 31 individual isopycnal displacements are plotted, whereas the displacement from temperature conversion embodies all isopycnals. The comparison involves a Lagrangian and an Eulerian representation.

The overall agreement shown in figure 7.3.1, besides showing usefulness of comparing different data sources, also gives increased confidence in the results of Batfish

processing, especially the derivation of mean density fields and thus to the calculation of potential energy.

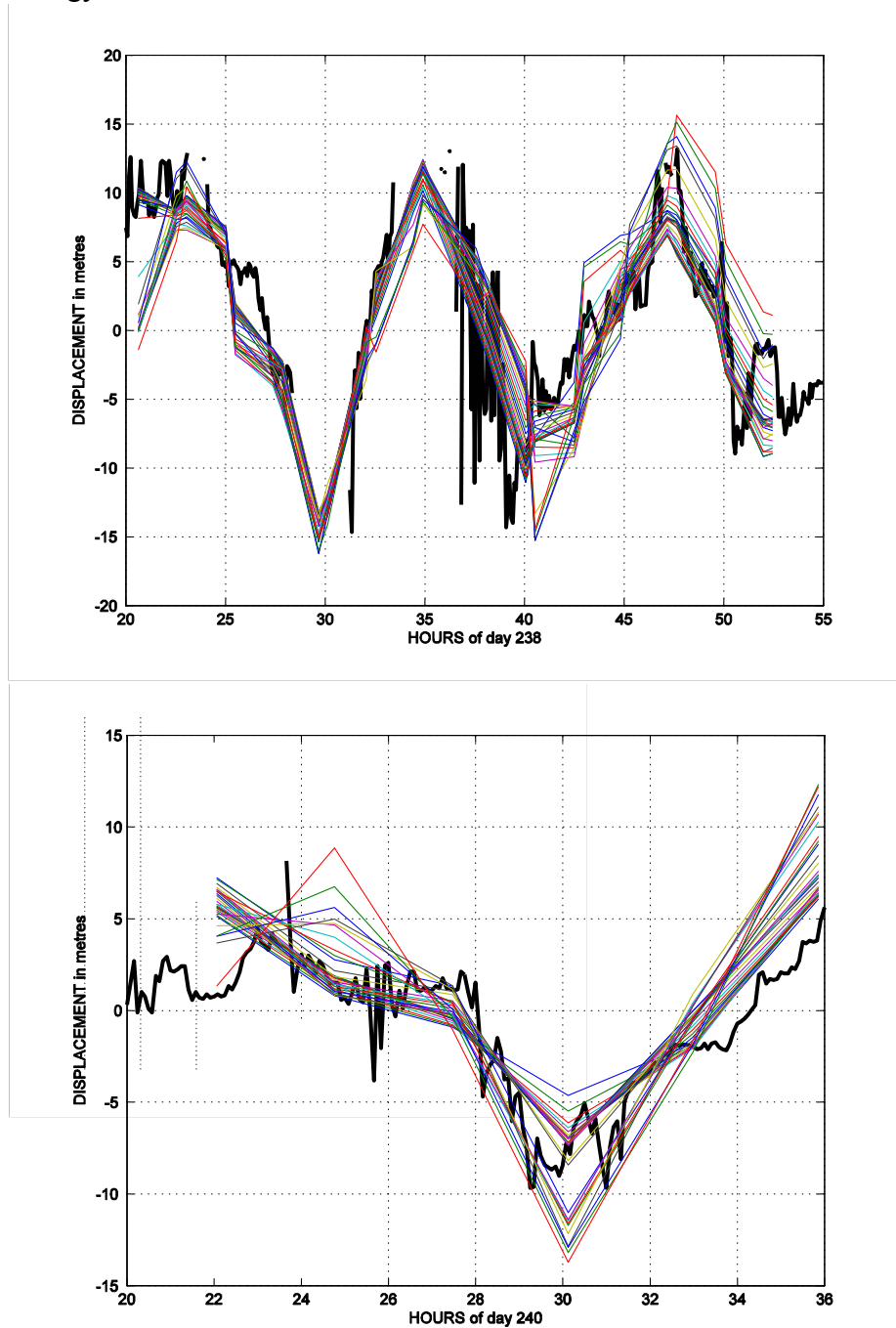


Figure 7.3.1: Two comparisons of displacement as derived from mooring time series (heavy solid line) and from Batfish (light solid lines).

## 8. Evidence for Non-linearity

### 8.1 The Non-linear Partial Differential Equation (PDE) for Isopycnal Displacement

Modal description of long internal waves, such as internal tides, has heretofore been done invariably in the framework of small-amplitude theory, in which the long wave propagation speed is independent of the wave amplitude and is determined from the standard eigenvalue equation. The first order in wave amplitude, the Korteweg-de Vries (KdV), description of solitary waves also uses the solution of the eigenvalue equation to establish the coefficients of the non-linear and dispersive terms. The vertical displacement is still described in terms of the linear modal function. However, many observations of internal solitary waves, ours included, show that moderate or large amplitudes are quite common. Referring to the present observations, the vertical displacements are especially large as observed in single Batfish ‘casts’. We have observed displacements exceeding half the water depth in undulations in advancing internal bores. They remain considerable even when data from several casts is averaged, as is done to form the 1 or 3 km averages. There is the question of how well small-amplitude theory is able to represent such observations.

A second-order theory in wave amplitude for internal solitary waves (Gear and Grimshaw 1983) used a PDE for displacement as developed by Benjamin (1966) and Miles (1979), based on previous work by Long. The formulation assumed inviscid incompressible fluid, in which the flow is steady in a frame moving with the phase speed of the wave. Although the PDE is strictly applicable only for waves of permanent form and moving with steady speed, we investigate its usefulness for describing long waves, in which both the form and speed change from one part of the wave to another. The complete two-dimensional equation is

$$\rho_0(c-u_0)^2 \left( \frac{\eta_x}{1+\eta_z} \right)_x + \left( \rho_0(c-u_0)^2 \left( \frac{\eta_z + \frac{1}{2}(\eta_z^2 - \eta_x^2)}{(1+\eta_z)^2} \right) \right)_z + \rho_0 N^2 \eta = 0 \quad (8.1,1)$$

where  $\eta(x, z)$  is the displacement from the Lagrangian coordinate  $z$ .  $\rho_0(z)$  is the basic density profile and  $u_0(z)$  the basic velocity profile,  $c$  the propagation speed and  $N^2(z)$  the square of Brunt-Väisälä frequency. The velocity components are

$$u = - \frac{(c-u_0)}{(1+\eta_z)}, \quad w = - \frac{(c-u_0)\eta_z}{(1+\eta_z)} \quad (8.1,2)$$

## 8.2 Evidence for Non-linearity in Long Waves

For long waves the variation in  $x$  is small and we disregard it in describing the vertical displacement. Moreover, if  $u_0(z) = 0$ , the equation reduces to the non-linear eigenfunction equation

$$\left( \rho_0 c^2 \left( \frac{\eta_z + \frac{1}{2} \eta_z^2}{(1 + \eta_z)^2} \right) \right)_z + \rho_0 N^2 \eta = 0 \quad (8.2,1)$$

to be solved with the boundary conditions:  $\eta = 0$  at  $z = -h$  and  $z = 0$ .

For a given density profile  $\rho_0(z)$ , the equation can be solved numerically. This was done using observed mean density fields determined from Batfish data. However, at any location the equation must be solved separately for each maximum value of displacement and yields in each case a value for  $c$ , the propagation speed. During our observations there is generally a relatively sharp pycnocline closer to the surface than bottom, whence the propagation speed increases from linear phase speed for downward displacement of isopycnals<sup>1</sup> and decreases for upward displacement. Wave crests move slower than troughs, leading to steepening of the isopycnal slopes between trough and crest and to formation of internal undulatory bores, solitary waves, etc.

Of the three case studies, the largest isopycnal displacements were encountered on the edge of the Banquereau Bank on the eastern flank of The Gully. A fixed straight section at  $58^\circ 50'$  W longitude and  $43^\circ 59' < \text{latitude} < 44^\circ 08'$  (Station 47-48 in Figure 5.1.1) was sampled repeatedly (30 transects) for nearly 36 hours. The water depths between the two ends of the section varied between 140 and 90 metres. In Figure 8.2.1 we show numerical solutions of the eigenfunction equation in water depth of 90 metres as a function of  $\sigma(z)$  and compare them with observed displacements. The comparison is made with observed displacements at two different times, at each time including 10 Batfish 'casts' ( $\approx 1.5$  km extent), in one case when the isopycnals were elevated and later as they were depressed. For both elevation and depression of isopycnals the non-linear eigenfunction is a closer representation of the data, although the difference between non-linear and linear eigenfunctions for downward displacement of isopycnals is less significant. The upward movement of isopycnals in the upper part of the water column is constrained by the near presence of the upper boundary. In Figure 8.2.2(a) we compare the non-linear solutions of elevation and depression with the displacement amplitude of the isopycnals at M2 frequency for Station 47-48 at a 1 km long section centered at  $44.1185$  N. The agreement in this case appears to be bi-modal in that for the near surface isopycnals the displacement amplitude is better represented by the non-linear solution of elevation of 20 m amplitude, whereas for the deeper isopycnals the solution of depression

---

<sup>1</sup> For any given density profile the propagation speed as a function of downward displacement reaches a maximum value, beyond which the speed decreases as the displacement amplitude increases further. In the case of solitary waves the limiting case of maximum speed (and associated maximum displacement amplitude) implies presence of broad, approximately square waves (cf. Turner and Vanden-Broeck 1988, Sandstrom and Quon 1994).



of 15 m amplitude agrees with the data better. The comparison of the M2 amplitude with eigenfunctions is different from the comparison shown in Figure 8.2.1, where elevation and depression were compared separately. The determination of M2 amplitudes implies the same up- and downward displacements, which require a whole range of eigenfunctions to represent them. When we add the M4 amplitude (a measure of non-linearity of internal tide) to M2 amplitude and compare with eigenfunctions, the best agreement is found (Figure 8.2.2(b)) with the linear eigenfunction of 16 m amplitude. This possibly answers the question posed in the introduction of this section of how well the small-amplitude theory is able to represent our observations, at least in the case of internal tides. The answer is: quite adequately. The major non-linear effect is felt by the near surface isopycnals and is significant when the upward displacements are large. The sinusoidal M2 tide does not take this non-linearity in the upper part of the water column into account, but when the non-linearity embodied in the M4 is included the displacement amplitude of the combined tide is best represented by the linear eigenfunction. For short wavelength large amplitude solitary waves, in which isopycnals are displaced downward and are not constrained by the upper boundary, the linear eigenfunction represents the data sufficiently well.

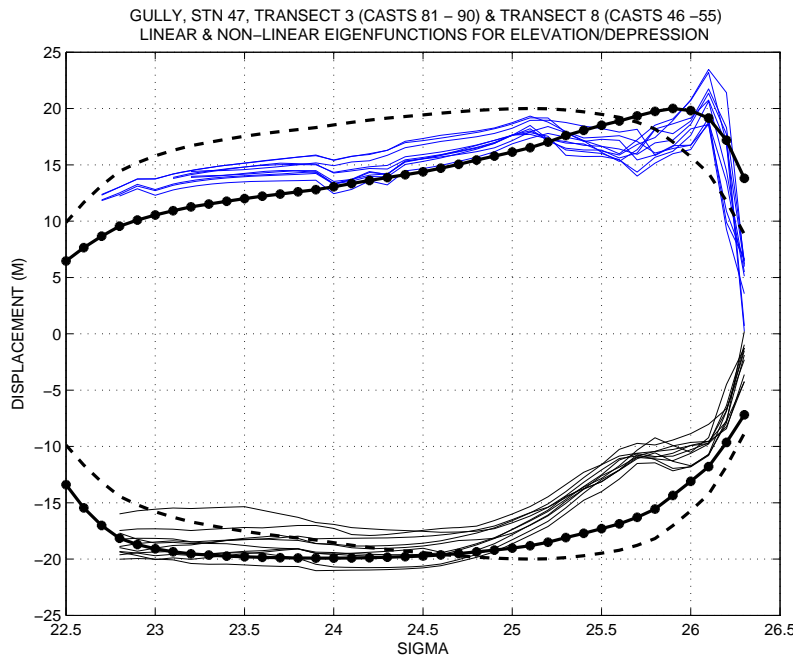


Figure 8.2.1: Comparison of observed displacement with linear (dashed line) and non-linear (solid line with markers) eigenfunctions.

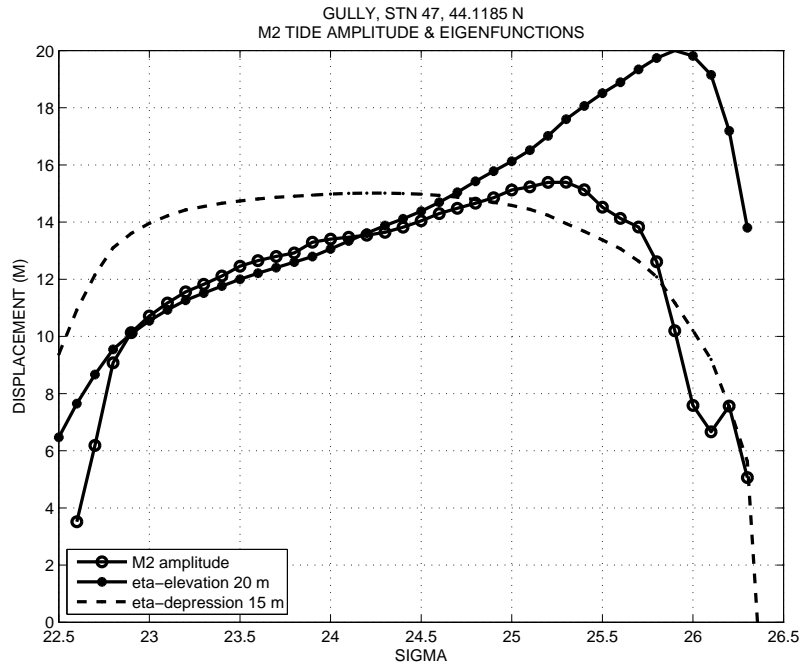


Figure 8.2.2(a): M2 tide amplitude &  $\eta$ -elevation (20 m),  $\eta$ -depression (15 m).

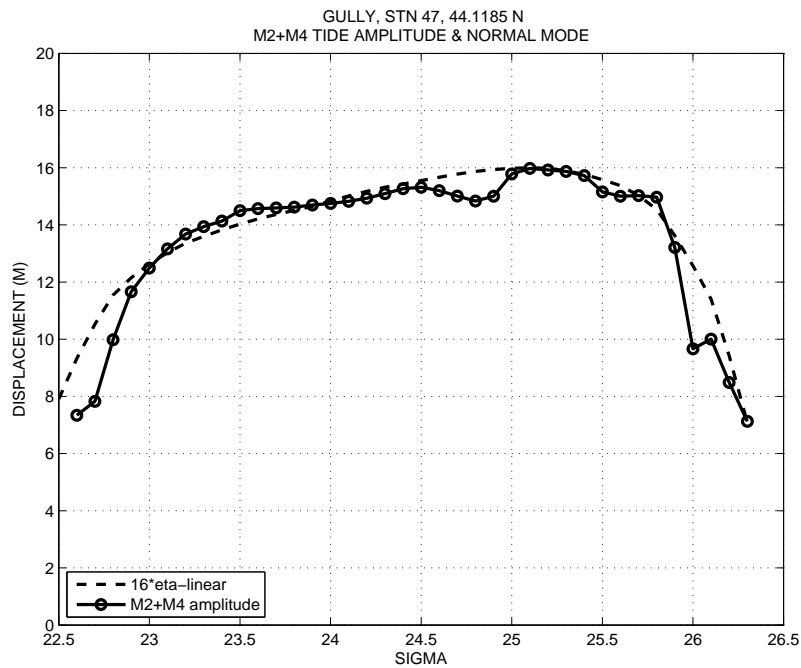


Figure 8.2.2(b): M2+M4 tide amplitude &  $\eta$ -linear of 16 m amplitude.

### 8.3 Groups of High Amplitude Internal (solitary) Waves, Internal Bores

In figure A7.1 of Appendix 7 the measured northerly current at three current meters at mooring #585 at the Scotian Gulf site is shown for a 24 hour span. In the present discussion the attention is focused on the high frequency current bursts in the two dominant groups approximately one M2 period apart. The current bursts appear as additions on top of the longer period current.

The first dominant group between approximately 63 and 65 hours occurs during a time when Batfish data were collected in the section (station 35) that included the mooring site. A comparison of nearly simultaneous current meter and Batfish data is thus possible.

The separation of the current bursts from the longer period current is done by subtracting the diurnal, inertial and semi-diurnal current components (cf. Appendix 7)<sup>2</sup> from the measured current. The result is shown in figure 8.3.1.

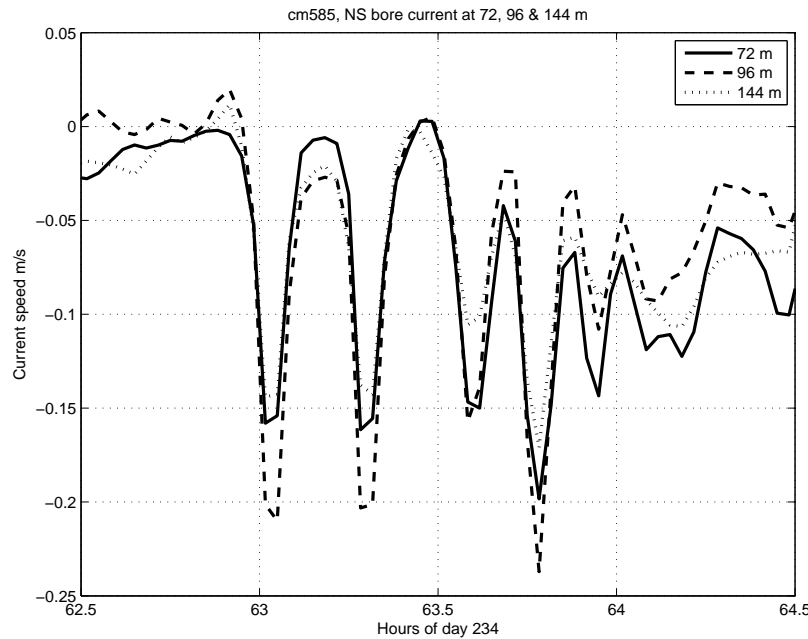


Figure 8.3.1: NS bore current at 72, 96 & 144 m at mooring #585.

The figure shows that the current bursts can be associated with a current bore, which consists of a number of overlapping individual solitary-wavelike events. We look at the first four of these waves in more detail.

The first detail to note is that at all three depths the current in the waves is coherent in the offshore direction (opposite to direction of wave propagation), but varies in strength

---

<sup>2</sup> The longer than diurnal period NS current at the mooring site is negligible. Note that at mooring #584, as shown in figure A7.2, the other low frequency components are not negligible and must be included in the separation process.

between the three current meters. The wave shapes are specified by 5 – 6 current measurements. With the sampling interval of 2 minutes, the significant duration of each wave is approximately 10 minutes. Assuming that the wave parameters can be connected by solitary-wave theory, the 5 – 6 data points in each wave are fitted to a  $\text{sech}^2$ - function. Let

$$u_i(t_i) = -a \text{sech}^2((t_i - t_0)/\tau)$$

where  $\tau$  is the time scale of the wave. The expression can also be written as

$$t_i = t_0 + \tau \ln(\sqrt{-a/u_i} + \sqrt{-a/u_i - 1})$$

and in this form is a linear relationship between  $t_0$  and  $\tau$  if the amplitude  $a$  is estimated first. A best fit straight line through the 5 – 6 points yields the values of  $t_0$  and  $\tau$ .

Figure 8.3.2 depicts the measured bore current at 96 m depth (solid line with circles) and the current of fitted four overlapping KdV solitary waves (dashed line). The standard or rms error of the fitted curve in the figure is 0.014 m/s. Integration of squared measured and fitted current over the one hour timespan in the figure yields a ratio of 0.995.

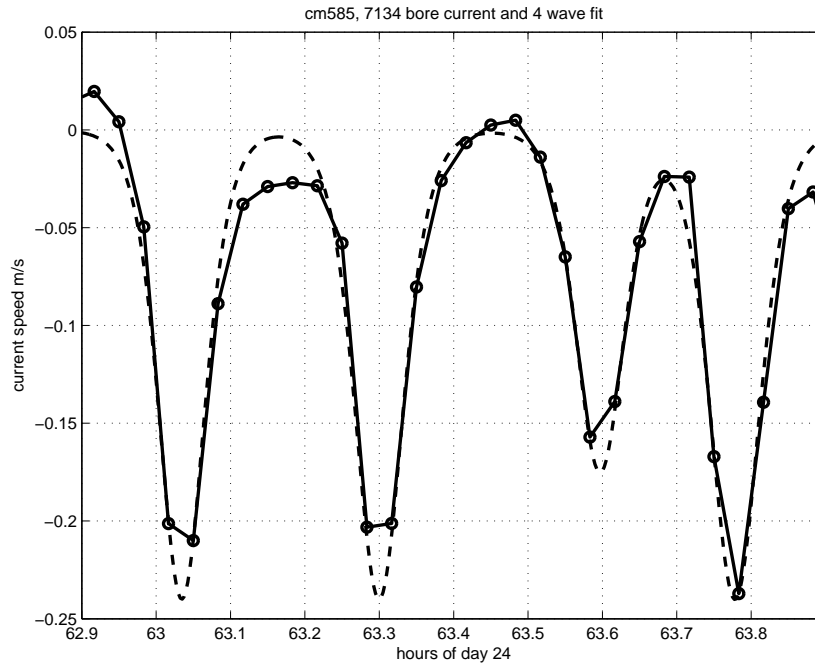


Figure 8.3.2: Four KdV-wave fit to bore current at 96 m depth.

The current speed at a given depth is related to the vertical change of displacement at that depth by (8.1,2), where the displacement is a solution of (8.1,1). The solution in this case must take the variation in  $x$  into account, since the application is to short waves.

We again assume a KdV form of solution, but solve equation (8.1,1) for the vertical part of the displacement at maximum amplitude only. Equation (8.1,1) reduces to

$$\left( \rho_0 (c - u_0)^2 \left( \frac{\eta_z + \frac{1}{2} \eta_z^2}{(1 + \eta_z)^2} \right) \right)_z + \rho_0 N^2 \eta - 2 \rho_0 (c - u_0)^2 \frac{\eta}{\lambda^2 (1 + \eta_z)} = 0 \quad (8.3,1)$$

where  $\eta(z)$  is now the vertical displacement from the Lagrangian coordinate  $z$  and  $\lambda$  is the horizontal length scale of the wave.  $\lambda$  is related to the time scale  $\tau$  by the propagation speed.  $u_0(z)$  is constructed using the current measurements from current meters at 45, 72, 96 and 144 m depths. The average of the longer period current (excluding the bore current) is calculated over the timespan of the passing of the four solitary waves and a smooth curve is fitted to the four averaged values. The current profile is nearly linear between values of -0.20 m/s at the bottom to -0.33 m/s near surface with a mean value of -0.265 m/s. The waves are propagating against the mean current and pass the mooring site with an effective speed of  $(c - \overline{u_0})$ . In the stationary (mooring site) reference frame the horizontal velocity is

$$u = \frac{(c - u_0) \eta_z}{(1 + \eta_z)} \quad (8.3,2)$$

The equation (8.3,1) has been solved numerically for a range of displacement amplitudes,  $a$ . Calculating  $\eta_z/a$  shows that thus normalized, the gradient of displacement is approximately constant for a wide range of displacement amplitudes, especially at the lower two current meters. Hence  $\eta_z = a \overline{\eta_z}$ , where  $\overline{\eta_z}$  is specific at the depth of a current meter with a possible error of less than  $\pm 5\%$ . The displacement amplitude of a KdV solitary wave can thus be determined from the wave current amplitude by

$$a = \frac{u}{\overline{\eta_z} (c - u_0 - u)} \quad (8.3,3)$$

This has been done for the four waves (cf. Figure 8.3.2) for currents at 96 and 144 m. For waves 1, 2 and 4 the amplitudes are -26 and -22 m respectively and for wave 3: -20 and -15 m. The current meter at 144 m depth is possibly too close to the bottom to account for the consistently diminished current.

For a KdV solitary wave of -26 m displacement amplitude the horizontal length scale of the wave is 100 metres. The propagation speed  $c = 0.924$  m/s and the effective speed by the mooring site is 0.66 m/s. The time scale of such a wave at the mooring is 152 seconds. For waves 1, 2 and 4 the sech<sup>2</sup>-fit provides time scales 149, 155 and 161 seconds, with the mean of 155 seconds. For a -22 m amplitude wave the calculated time scale is 163 seconds. Sech<sup>2</sup>-fit gives  $\tau = 155$  seconds. In view of such agreement the conversion of current speed to displacement is quite feasible.

The same internal bore is recorded at mooring #584, located 9.1 kms north of #585. Mooring #584 had a VACM and an Aanderaa current meter at 29 and 31 m depth, another Aanderaa meter at 132 m depth and a ThermistorChain between the two Aanderaa meters. Neither the VACM nor the top Aanderaa meter were recording the short waves due to extended averaging times, which were set deliberately for the VACM but probably accidentally for the Aanderaa meter. The passing of the wave group is seen in the ThermistorChain temperature records at several depth, but is clearly recorded at the current meter at 132 m depth. In figure 8.3.3 the measured bore current is shown together

with the four overlapping KdV solitary waves that are fitted to the data. The bore has a longer tail, which is not shown in the figure.

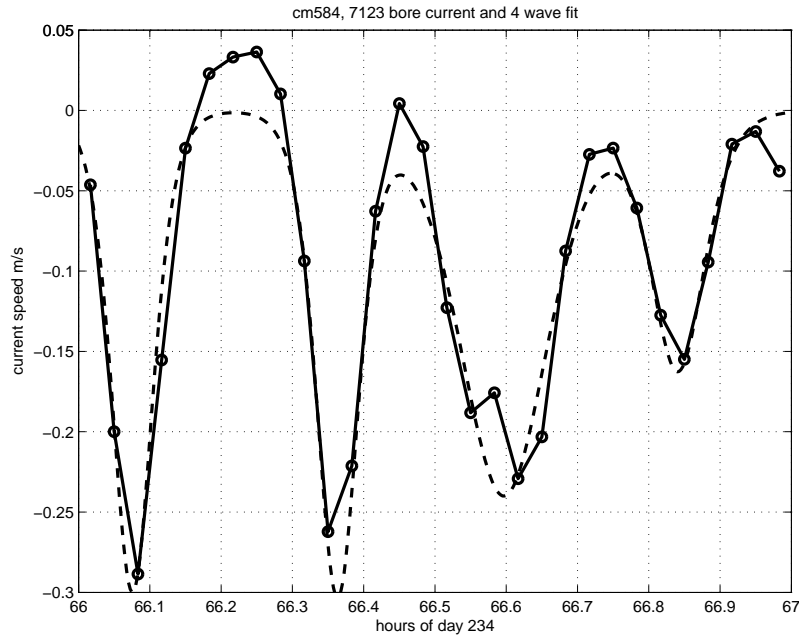


Figure 8.3.3: Bore current at 132 m at mooring #584 and four KdV-wave fit.

The four waves shown in the figure arrive at #584 3.00 to 3.06 hours after their arrival at #585. The effective propagation speed of the group is 3.0 kph or 0.83 m/s. There is an opposing current that changes during the three hours and the nature of which is uncertain, but the average magnitude of which can be estimated to be 0.15 – 0.20 m/s.

The displacement amplitude of the four waves is calculated using (8.3,3) and yields values -32, -32, -27 and -20 metres respectively. This indicates growth of energy in the four waves between the two mooring sites. The sum of potential energy of the four waves at the two mooring sites is  $\underline{6.2 \times 10^6 \text{ and } 7.5 \times 10^6 \text{ Joules / m}_x}$ .

The internal bore was observed during Batfish station 35, first in transect 8 just offshore of the mooring #585 and little less than an hour later crossing the same mooring site in transect 9. Some features of the bore are discussed in connection with sampling problems and density inversions in section 7 and parts of the bore are depicted in figures 7.1.1, 7.2.2 and 7.2.3. The four waves of the bore in Figures 8.3.2 and 8.3.3 cross the mooring sites in one hour. With a propagation ground speed of 2/3 m/s, the waves extend over 2.4 kms. Using appropriate speeds for the ship, wave propagation through the water and the opposing current, we find that when the ship travels in the wave propagation direction (transect 8), it takes  $\frac{1}{4}$  of an hour to transit the travelling bore. The bore has meanwhile advanced by another 0.6 kms. The comparable potential energy from the Batfish in this case is averaged over a 3 km distance and then multiplied by 2.4 kms. In transect 9 with the ship travelling in the opposite direction, the Batfish potential energy is averaged over

a 2 km distance and again multiplied by 2.4 kms. The largest values of averaged potential energy in transects 8 and 9 coincide with the presence of the bore. The integral values are  $6.0 \times 10^6$  and  $5.6 \times 10^6$  *Joules / m* respectively, to be compared with  $6.2 \times 10^6$  *Joules / m* from the current meter conversion above. The comparison of energies derived from the current meter and Batfish data is excellent.

The internal bores are seen in the current meter records in most semi-diurnal tidal periods, but of very variable form and strength. In some tidal periods they are stronger at the #585 mooring site, in other periods at the #584 site. At times they are seen at one site and not the other. The inference is that the formation of bores and their life-cycle may not only depend on the strength of the internal tide, but on other physical processes that influence the water column as well, processes that we have not been able to elucidate properly.

Of the other two observational sites, the current meters moored at the two locations on Grand Bank show high frequency fluctuations, some of which have bore-like characteristics. The current strengths, however, are relatively smaller than in the Scotian Gulf and the occurrences less predictable. At The Gully site, the sampling interval was too long for resolution of the short waves.

## 9. Dissipation of Internal Wave Energy

The possibility of vertical mixing of the water column by internal waves was one of the motivations to collect the data that has been analyzed in this report. The energy required to mix the water, i.e. change the potential energy of the water column, is extracted from the internal waves. We do not know explicitly how the internal wave energy is converted into turbulent mixing energy, but we have shown that the waves lose their potential energy as they propagate from where they are generated.

We have calculated the potential energy content both for tidal frequency displacements for the stations where that is possible and for all frequencies for all stations. The separation of the potential energy in this way has to be treated with caution since the two are not independent. As an example consider internal bores generated during every tidal cycle and each consisting of many KdV solitary waves. A time-series analysis will show a signal and potential energy at tidal frequency, whereas all the energy is contained in the short waves. This has a bearing on the total energy content in the waves, namely the sum of kinetic and potential energies. The partition of kinetic and potential energy is different for different scales of motion. The ratio of kinetic to potential energy in frequency space is  $(\omega^2 + f^2)/(\omega^2 - f^2)$ , where  $f$  is the local inertial frequency. For short (high frequency) waves the energies are approximately equipartitioned, whereas at our observation sites a sinusoidal M2 internal tide would contain approximately three times as much kinetic energy as potential energy.

Previously one of us (Sandstrom and Oakey 1995) has proposed a sequence of processes leading from the interaction of surface tide with topography, generation of internal tide, non-linear and dispersive evolution into shorter undulations, to dissipation of the latter. If the sequence were separated into such non-overlapping stages, the generated internal tide before evolving into shorter waves would have four times as much total energy as the measured potential energy. In the short waves the total is only twice the amount of potential energy. In the process of non-linear and dispersive evolution there must be a flow of kinetic energy of the larger scale motion into potential energy in the smaller scales. Thus the potential energy is expected to increase even as the internal tide propagates beyond the generation area. The observations (cf. section 6.2 ) indicate that this is indeed the case. It must be pointed out, however, that the processes of generation, evolution and dissipation are not sequential, but influence the observations throughout. There may be a dominant process at a given stage and the sequence of processes would be maintained in a qualitative sense, but the total energy estimation can only be done within certain limits.

Although not knowing explicitly how the internal wave energy is dissipated, we have observed several instances of unstable short waves (cf. section 7.2). The instability is most likely caused by high current shear. We have estimated the Richardson number for KdV solitary waves in the observed density fields and find that for wave amplitudes exceeding  $\sim 20$  metres,  $Ri < 1$ , and  $Ri \cong 0.25$  for amplitude  $\sim 30$  metres. Shear instability is considered as the primary cause of energy dissipation. Bottom friction, acting especially on some of the high amplitude short waves (e.g. section 8.3), must also be



considered since currents of up to 0.5 m/s at 20 metres above the bottom are recorded. We realize that these two causes of dissipation and perhaps others influence the energy content of the waves, but in this report we adopt the ‘black box’ approach to the energy budget. Internal wave energy is created, transformed and dissipated at rates that can be estimated, without knowing in detail how the processes work.

In section 6.2 in figures 6.2.3 to 6.2.7 were shown comparisons of field measurements of potential energy with the current flux squared, both integrated over a M2 tidal cycle. The energy thus normalized shows a definite pattern of variation in the cross-isobath direction, most clearly seen in the Scotian Gulf and Grand Bank data (figures 6.2.3 and 6.2.4). Both of these figures were compiled from data from time-series stations. It is possible to extend those data sets by making use of the data from tracking-mode stations. For the latter we have estimates of potential energy in 3 km sections, but no direct way of integrating the energy over a tidal cycle. The method we employ is to first compare the maximum value of energy in any 3 km section of the time-series stations to the integral of energy over M2 cycle of the same 3 km section. We calculate the ratio of the energy per M2 wavelength (having converted the temporal integral to spatial by multiplying it with the propagation speed) and energy in the 3 km section.

### 9.1 Scotian Gulf

In the Scotian Gulf the nominal value of the M2 tide wavelength is 37.5 kms. The calculated ratio varies from  $\sim 5.5$  to  $4.5$  between 8 and 38 kms from the 1000 m isobath. The ratio indicates how many 3 km sections would contain all the energy per wavelength, if all had the same maximum energy.<sup>3</sup> The decrease of the ratio as the energy propagates on the shelf is consistent with the energy being concentrated more and more in the high-amplitude, short wavelength waves that make up the bore-like features seen in the observations.

The calculated ratio is next used to convert the maximum energy in a 3 km section in all the transects of the tracking-mode stations to estimates of potential energy per internal tide wavelength. The results are plotted in figure 9.1.1. with the open circles. The crosses show the data from the time-series stations that were used to calculate the ratios. The two dotted lines are sech-shaped with maxima of  $4.25 \times 10^7$  and  $1.70 \times 10^7$  Joules/m respectively, i.e. in a 2.5 to 1 ratio. The ratio of the maxima is chosen to reflect the fact that the integrated current flux squared varies between high and low values with the same ratio, i.e. ranging between values of  $3.5 \times 10^7$  and  $1.4 \times 10^7 m^4 s^{-1}$ . Most of the data points in the figure fall between the two dotted lines, with almost all of the outliers being the estimates from the tracking-mode stations. The method of deriving them has a built-in uncertainty in the form of a rms error in the calculated ratio of energy per wavelength and in 3 km sections. The standard error in the ratio is approximately 20 %. The other obvious source of variability in the estimates is the determination of energy in the 3 km

---

<sup>3</sup> For a sinusoidal form of internal tide having the same wavelength, the ratio of energies per wavelength and in the 3 km section of maximum energy is 6.38. In a saw-tooth form of internal tide the corresponding ratio is 4.52.

sections of the tracking-mode data, especially when the ship crossed the wave groups traveling in the opposite direction, namely the problem of resolution.

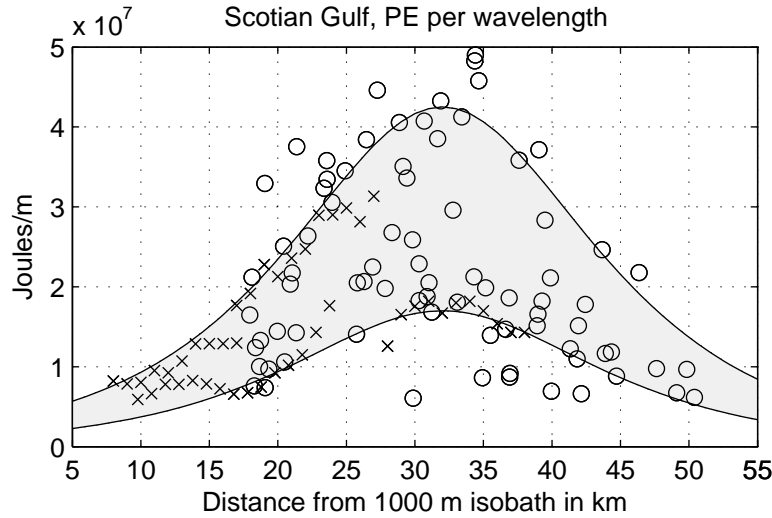


Figure 9.1.1: Potential energy per internal tide wavelength as function of distance from 1000 m isobath. Crosses show data from time-series stations, open circles from tracking-mode stations.

For dissipation estimates we consider the data in the shaded area. The maximum values of the two solid lines are related to maximum and minimum values of the integrated current flux squared by the *normalization factor*<sup>4</sup> of 1.2 (cf. figures 6.2.2 and 6.2.3). Assuming this factor to apply to intermediate values of integral of  $Q^2$ , a time-series of potential energy per wavelength at its maximum value (32 kms from the 1000 m isobath) can be formed. Furthermore, assuming that equipartition of kinetic and potential energy holds and knowing the propagation speed, the energy flux time-series can be calculated. The energy flux beyond its maximum value is assumed to diminish similar to the sech-form in the figure, i.e. fall to half of its maximum value in 13 kms. During a one week period the energy flux at 32 kms from the 1000 m isobath ( $42^\circ 58' N$ ) fluctuates between approximately 1 and 2 kW/m. Dissipation of energy between 32 and 45 kms ( $43^\circ 05' N$ ) is shown in figure 9.1.2.

It fluctuates between approximately 0.03 and 0.07 Watts/m<sup>2</sup>, with a mean value of **0.05 Watts/m<sup>2</sup>**. The authors (Sandstrom and Elliott 1984) arrived at a similar dissipation rate based on observations in the fall of 1981 in the same area. The earlier estimate relied on more incidental data than the present systematic analysis of a larger set of observations two years later.

<sup>4</sup> This normalization factor is the ratio of energy per wavelength and integral of  $Q^2$  and is equal to the normalization factor in Figure 6.2.3 multiplied by the energy propagation speed.

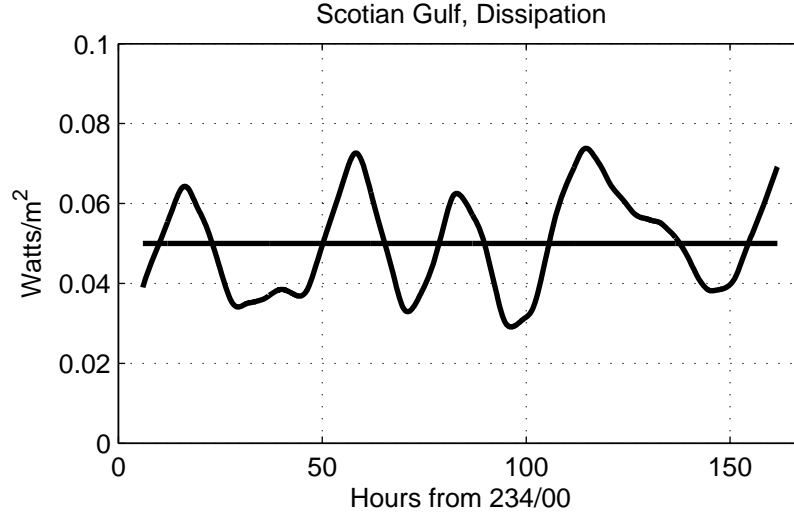


Figure 9.1.2: Inferred dissipation of energy between 32 and 45 kms from 1000 m isobath. For explanation see text above.

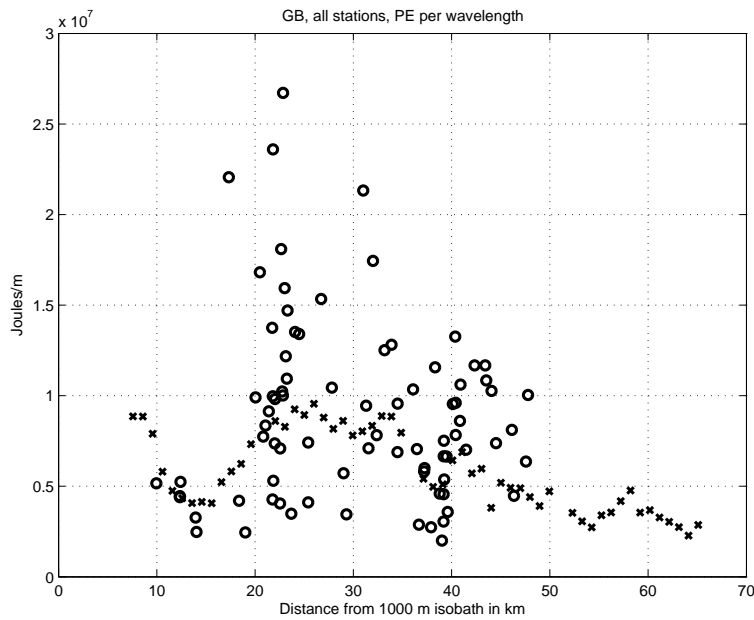


Figure 9.2.1: Grand Bank potential energy per internal tidal wavelength as a function of distance from 1000 m isobath. Crosses show time-series data, open circles tracking-mode data.

## 9.2 Grand Bank

The same method as in 9.1 is used to derive the potential energy per internal tide wavelength for all the Grand Bank stations. The result is shown in figure 9.2.1.

Comparison with the Scotian Gulf results indicates smaller energy (approximately 50 %) and much greater variability. The largest values ( $> 2 \times 10^7 \text{ Joules/m}$ ) occur for observations when the integral of  $Q^2$  was also the largest. The *normalization factor* is approximately the same as in the Scotian Gulf (see also figure 6.2.4). However, as pointed out in Appendix 6, the uncertainties of determining  $Q(t)$  for the Grand Bank data leaves the correlation of energy and the integral of  $Q^2$  also uncertain. Adding to the uncertainty, especially for the tracking mode energy estimates (open circles in the figure), is the rms error in determining the ratio of energy per wavelength and the maximum energy in 3 km sections of the time-series data. This standard error is  $\sim 25\%$ . Hence for energy dissipation estimates we rely on the time-series energy determinations (crosses in the figure).

Between 20 and 60 kms from the 1000 m isobath the potential energy per wavelength diminishes almost linearly, with energy dropping to half of its maximum value in 30 kms (approximately in one internal tide wavelength). Assuming equipartition of energy, the maximum energy flux, which occurs between 20 and 30 kms, is  $\sim 400 \text{ Watts/m}$ . Energy loss over 30 km distance is  **$0.007 \text{ Watts/m}^2$** . Compared to the Scotian Gulf estimates, both the energy flux and rate of energy dissipation are much smaller, the latter by almost a factor of ten.

### 9.3 The Gully

Compared to the other two sites, where the bottom topography could be described as approximately two-dimensional and our sectional observations as representative of conditions along some length of the shelfbreak, The Gully site presents a very different topographic picture. The Gully itself is a dominant feature with steeply sloping sides. On the western side on Sable Island Bank (Batfish stations 40 and 41, current meter mooring 659) the topography is pseudo-two-dimensional, with depth contours running mainly EW. The water depth diminishes toward top of the bank (cf. Appendix 6). The currents, as shown in Appendix 7, are very variable. The observed maximum potential energy per wavelength is smaller ( $\sim 3/4$ ) than on the Grand Bank and is almost constant as the water shallows from approximately 120 to 60 metres. The estimated energy flux is  $\sim 300 \text{ Watts/m}$ . No data for direct dissipation estimates is available. Our best guess is that it is of the same order of magnitude as on the Grand Bank.

On the eastern side of The Gully on the Banquereau Bank Batfish stations 45 and 46 form a section approximately transverse to depth contours over a depth range of nearly 1000 to less than 100 metres. The energy content of the waves remains small to moderate over deeper water. The largest values occur at the shallow water end of station 46. These will be considered together with the data from stations closer to the eastern flank of The Gully.

Station 44 forms a section across the slope of the east side of The Gully and the shelf edge to a depth of about 140 metres. It is essentially transverse to the isobaths and thus most resembles the conditions at the Scotian Gulf and the Grand Bank sites for assessing generation of baroclinic energy. Current meter mooring 660 is located about 5 kms north

of the shallow end of the section. Growth of energy (normalized) across the slope and shelf is shown in figure 6.2.7 to a distance of  $\sim 15$  kms from the 1000 m isobath. The *normalization factor* of 1.0 – 1.5 is consistent with creation of baroclinic energy at the

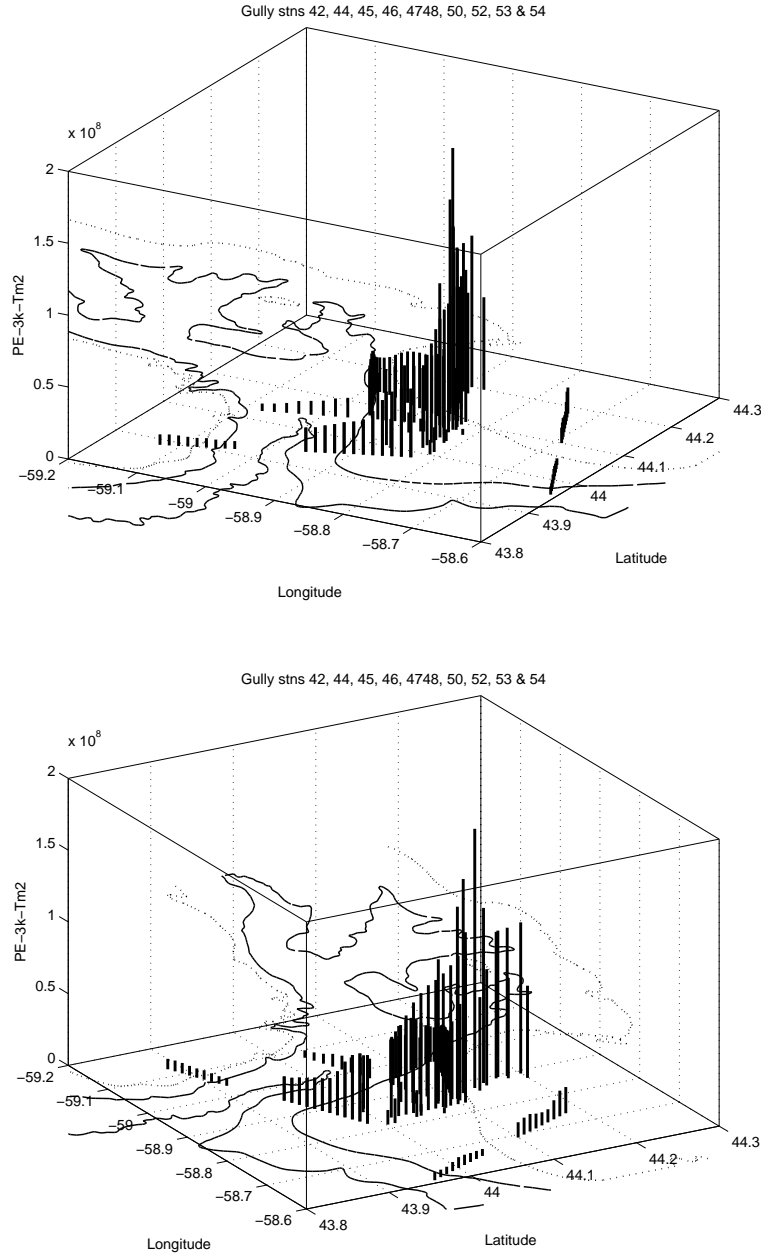


Figure 9.3.1: Gully potential energy per tidal period for 9 stations shown from two different viewpoints. 1000, 200 and 100 m isobaths are shown in the  $z=0$  plane.

other two sites. In figure 6.2.7 further growth of energy is seen during station 47 and 48. The reason for the increase is discussed in the following paragraphs.

Figure 9.3.1 shows the calculated potential energy per semidiurnal tidal period for nine Batfish stations. Stations 47 and 48 covered the same geographical section and are shown as combined data. All stations except station 53 are time-series stations. To obtain the tidal period estimates for station 53, we used the ratios of tidal period energy and maximum energy in 3 km sections from station 4748, particularly those at the northern end, which is closest geographically to station 53. Station 42 crosses the western flank of The Gully (far left in the figure) and is aligned with station 44 on the eastern flank. Station 54 is located further north across The Gully. 1000, 200 and 100 metre isobaths are shown in the figure in the  $z = 0$  plane. The data is shown from two viewpoints with azimuths 30 and 60 degrees respectively, where positive azimuth indicates counter-clockwise rotation from south. Viewpoint elevation is 30 degrees both times. The first look is up The Gully and almost lined up with the station 45 & 46 section. That section is better represented in the second look. The energy increases rapidly on the Banquereau Bank and reaches maximum values near the 100 metre isobath. Taking an average of the three largest values and adding the kinetic energy on the basis of equipartition, we obtain the maximum energy flux estimate of 4.7 kW/m. Compared to maximum value at the Scotian Gulf site, this is about three times greater. Data from station 53 indicates that in 10 kms the energy flux has decreased by  $\sim 40\%$ . The dissipation over that distance is 0.2 Watts/m<sup>2</sup>. This is about twice the energy loss calculated on the basis of observing the wave packet in station 53 (Sandstrom, Elliott and Cochrane 1989).

The concentration of energy on the eastern flank of The Gully is obvious. In contrast the energy on Banquereau Bank further to the east during station 46 is much smaller, although the water depth here is less than 100 metres. The enhanced energy can arise essentially from: (i) continued generation of baroclinic motion from interaction of barotropic flow with bottom topography, (ii) piling up of energy in shorter wavelength due to slower speed of energy flow, and (iii) channelling of energy into narrowed space by wave refraction.

In order to elucidate the issues of piling up and channelling of energy in the area of interest, we first constructed a map of energy flow isotachs. These follow quite closely the isobaths. The speeds vary approximately between 0.9 and 0.7 m/s from 200 to 80 metres of depth. To calculate the energy flow streamlines (ray paths) we make the assumption that at the 200 metre isobath the energy is flowing transverse to topography, having been generated at the top of the slope.

In figure 9.3.2 are shown rays emanating from two points on the 200 metre isobath. The figure demonstrates that the energy, spread between the two initial points, is channelled into a much narrower space in the vicinity of the 100 metre isobath. This channelling may be sensitive to the initial direction of energy propagation. Energy enhancement by a factor of 2 to 3 near the 100 metre isobath is realistic (including the adjacent shallower depths). Compared to channelling, piling up of energy due to slower propagation speed is also a factor, but smaller by an order of magnitude. The generation of local baroclinic energy is estimated to be even smaller. Topographic channelling and wave refraction are deemed to be the principal causes of observed energy enhancement.

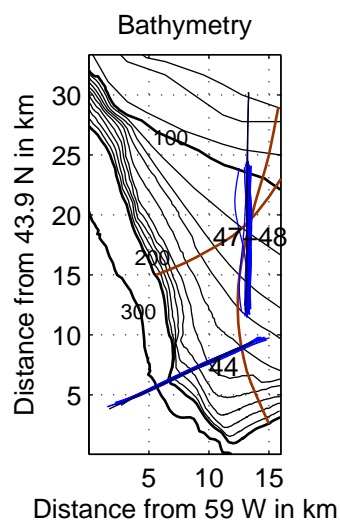


Figure 9.3.2: Bathymetry on the eastern flank of The Gully and edge of Banquereau Bank. The three heavier lines denote 300, 200 and 100 m isobaths. The brown lines are rays emanating from the 200 m isobath. Blue lines mark the Batfish track during stations 44 and 47-48.

## 10. Summary and Discussion

The analysis of observations of various parameters at three separate sites has shown both common characteristic patterns of generation, modification and dissipation of baroclinic potential energy, but also quantitative differences due to site-specific bathymetry, density stratification and barotropic current flux. It must be understood, however, that the conclusions reached apply primarily to energy distribution on the shelf (water depths  $< \sim 200$  m). In deeper water the Batfish sampling scheme provides insufficient data for determining the baroclinic energy content at depth. Thus in the Scotian Gulf we have excluded station 34 data from much of the discussion. There is an indication in the semi-diurnal tidal phases in station 34 of offshore propagation, but the displacement amplitudes of the sampled isopycnals are too small to come to any definite conclusions. The maximum displacement of the deep water first mode would be too far below the Batfish range.

The question of whether tidal mixing in the deeper waters in The Gully proper is a contributor to the cause of enhanced primary and secondary production remains unanswered based on Batfish data. However, mixing is taking place in The Gully, but in deeper layers below the Batfish range, as shown by CTD data taken along the axis of The Gully. In the vicinity of (44 N, 59 W) many density inversions are observed between 100 and 200 m depths. 20 to 25 kms toward deeper water the inversions are seen lower down in the water column, between 200 and 400 m depths. The amplitude of the inversions is as high as 0.5 sigma units and layer thicknesses of inversions are  $O(10$  m).

In Appendix 8 the CTD section is shown together with selected density and salinity profiles, followed by a brief discussion of possible causes of the inversions. Inspection of all deep water ( $> 200$  m) CTD data from continental slopes east and west of The Gully and the other two sites indicates that the inversions phenomenon is particular to The Gully proper.

In section 6 we discussed generation of baroclinic energy by interaction of barotropic current flux with variable depth in the presence of density stratification. The justification for using a very simple model for the interaction lies partly in the fact that for a two-layer system, which the actual stratification approximates, the simple-wave model is quite appropriate (cf. Sandstrom and Quon 1994). Additional justification is provided by the good agreement between model results and observations in the semidiurnal tidal band. The best agreement is found in the Scotian Gulf, where the Batfish data are most comprehensive and on-offshore current flux is determined most reliably. Based on the good agreement we normalized the generated potential energy per tidal period with the integral of square of semidiurnal current flux. We then extended the normalization to the total potential energy by comparing it with the integral of total current flux. Doing this we are able to make comparisons between the three sites<sup>5</sup>, two of which have essentially two-dimensional bathymetries and the third, The Gully, being three-dimensional. The *normalization factor* near the shelf break and just inshore of the major generation zone is

---

<sup>5</sup> The comparisons are made on the basis of total observed and normalized potential energy. In the Scotian Gulf the normalized tidal energy component is also determined quite reliably, but at the other two sites the unreliability of tidal flux determination renders the normalization very uncertain.



comparable at all three sites (of  $O(1)$ ) and the build-up of energy is similar. The reason for the consistency is to be found in the nature of the forcing function in equations (6.1,10). The spatially varying part of the forcing function is a product of  $\nabla(1/h(x))$  and  $v_1(x)$ , where  $v_1(x)$  is found to be linearly related to  $h(x)$ , varying between -0.18 and -0.25 in the Scotian Gulf as the depth decreases from 1000 to 200 metres, being constant at -0.20 on Grand Bank slope and constant at -0.25 on the east wall of The Gully. Hence the spatially varying part of the forcing function is of comparable magnitude at all the three sites. The extent of the forcing region varies to some extent between the three sites, but not enough to cause major differences in convolving spatial and temporal variation.

Inshore<sup>6</sup> from the shelf break the change of the energy content differs from site to site. The main features on the Grand Bank are similar to those in the Scotian Gulf and the longer length of the section allows us to see more of the dissipative part of the process. The differences at The Gully stations away from the shelf edge, especially on the western part of Banquereau Bank, we attribute principally to energy channelling by refraction following the generation stage at the top of the slope and shelf edge. On the western side of The Gully (stations 40 and 41) the energy levels are low and therefore the values uncertain. On the south-east edge of Banquereau Bank (stations 45 and 46), although the energy levels are higher, the uncertainty of current flux estimate from a distant current meter renders the normalization uncertain.

Based on the observed amounts of potential energy at the three sites aside from the uncertain estimates, we contend that knowing the bathymetric, stratification and current flux parameters, the estimation of baroclinic potential energy at other localities along the world's ocean margins is quite feasible.

Following the generation stage and even during it the process of transforming the larger scale motion into shorter scales occurs, with non-linearity and dispersion being the major processes in the transformation. Dissipation is expected to play a continuous role, but becomes a major factor after large amplitude short waves appear. Another process expected to occur during the transformation is the shifting balance between kinetic and potential energy. In long waves, in which the particle motions are influenced by rotation, kinetic energy dominates. In short waves the energies are approximately equipartitioned. During the transformation some of the kinetic energy is converted into potential energy. This accounts for the observed potential energy increase inshore from the wave generation area.

The potential energy increase is accompanied by its redistribution in such a way that the tidal trough becomes a repository of more of the energy in ever narrowing space. The troughs are also where energy is repacked from longer to shorter scales, an example of which is shown in figure 3.1.3.

The large amplitude short internal waves have a significant if not a dominant role in the energy transformation and dissipation processes. They may appear singly as solitary

---

<sup>6</sup> Generally toward shallower water.

waves or as groups in the form of undulatory bores, but they are ubiquitous throughout the observations. We have analysed and discussed them in various contexts. In section 7 the problem of their resolution by the Batfish sampling scheme was considered and also their role in generating shear instability. In section 8.3 their characteristics in the light of current measurements was elucidated and comparisons made with concurrent Batfish observations. Their sea surface signatures facilitated the tracking of underlying wave groups in the high energy part of the tidal trough. The observational evidence from the three sites indicates that the short internal waves can be described in terms of the model that incorporates the effects of non-linearity, dispersion and dissipation, usually called the Korteweg-deVries-Burgers (KdVB) equation. The waves are called *solitary* if the *dissipative* timescale exceeds the *dispersive* (KdV) timescale. They are called *cnoidal* if the two timescales are similar.

Ranking the observed energy at the three sites, the Grand Bank has lowest values. This can be attributed to lowest measured current flux of the three sites and the smallest  $\nabla(1/h(x))$ . The depth change is more gradual than in the other two areas. On the western side of The Gully, on Sable Island Bank, the depth change on the slope is also more gradual than around Banquereau Bank. The current flux is weaker and energy content in the waves is similar to the Grand Bank observations. In this respect the west and east sides of The Gully are considered as separate examples.

The Scotian Gulf site has received the most attention in this report, because of aforementioned comprehensiveness of observations to support analytical procedures and model testing. The energy content in waves is 3 to 4 times as large as that on the Grand Bank and dissipation estimate exceeds that of Grand Bank by almost an order of magnitude.

From the observational and analytical point of view the east side of The Gully is the most challenging. With the hindsight of present experience a better observational program could have been put in place. Yet the data at our disposal yields sufficient information to come to following conclusions. The energy content of the waves is the largest of any of the sites. The maximum values exceed those in Scotian Gulf by a factor of 4 to 5 and the dissipation estimate is larger by the same factor. The maximum energy is observed near the 100 metre isobath, and hence in shallower water than in Scotian Gulf. The reason for the enhanced energy was discussed in section 9.3 in terms of energy channelling by wave refraction.

Referring to the questions posed in the introduction, the analysis of observations from the three separate sites over a three year time span has provided answers to all of them. Not complete answers in all cases, but sufficient in order to estimate the amounts of baroclinic energy production and the rates of its dissipation. The relationship between the baroclinic and barotropic tide has been elucidated, as has been the evolution of the baroclinic tide as it propagates and its energy is re-packaged into shorter bundles called *solitary waves*. The best estimate of the *dispersive* and *dissipative* timescales is based on the observations from the Scotian Gulf and indicates that the two are similar (4 to 5 hours). The observations also indicate that non-linear and dispersive processes are present as the

internal tide is being generated, i.e. the internal tide is already being transformed as it is being formed. Based on the observations from the Banquereau Bank, we have shown how the energy content of the waves can be altered by interaction with topography, leading to wave refraction and energy channelling. A visual example of wave refraction can be seen in SLAR imagery in Figure 1, with the waves being retarded by the shallow LaHave Bank in the Scotian Gulf.

## 11. References

- Baines, P.G. 1974. The generation of internal tides over steep continental slopes. *Phil. Trans. Roy. Soc. London, Ser. A* 277: 27-58.
- Baines, P.G. 1982. On internal tide generation models. *Deep Sea Res.* 29: 307-338.
- Benjamin, T.B. 1966. Internal waves of finite amplitude and permanent form. *J. Fluid Mech.* 25: 241-270.
- Bennett, A.S. 1972. Some observations of salinity and temperature structure with a variable depth towed body. *Oceanology Int.* 72: 353-356.
- Bennett, A.S. and Huaide, T. 1986. CTD time constant correction. *Deep Sea Res.* 33(10): 1425-1438.
- Dessureault, J.-G. 1976. "Batfish" a depth controllable towed body for collecting oceanographic data. *Ocean Engineering* 3: 99-111.
- Dupont, F., Hannah, C.G., Greenberg, D.A., Cherniawsky, J.Y. and Naimie, C.E. 2002. Modelling System for Tides. *Can. Tech. Rep. Hydrogr. Ocean Sci.* 221: vii + 77pp.
- Elliott, J.A. and Sandstrom, H. 1987. Recent Applications of Towed CTD Systems to Studies of Variability and Mixing on Canadian East Coast Continental Shelves. Presented at the ICES Statutory Meeting, Santander, Spain, October 1987. *CM* 1987/C. 15.
- Gear, J.A. and Grimshaw, R. 1983. A second-order theory for solitary waves in shallow fluids. *Phys. Fluids* 26: 14-29.
- Gordon, D.C. and Fenton, D.G. (editors) 2002. Advances in Understanding The Gully Ecosystem: A Summary of Research Projects Conducted at the Bedford Institute of Oceanography (1999-2001). *Can. Tech. Rep. Fish. Aquat. Sci.* 2377: iv + 84pp.
- Halpern, D. 1976. Semidiurnal internal tides in Massachusetts Bay. *J. Geophys. Res.* 76: 6573-6584.
- Haury, L.R., Briscoe, M.G., and Orr, M.H. 1979. Tidally generated internal wave packets in Massachusetts Bay. *Nature* 278: 313-317.
- Hodgins, D.O. and Westergard, H.G. 1981. Internal waves in Davis Strait and their measurement with a real time system. *Proc. POAC* 81 V: 423-432.
- Miles, J.W. 1979. On internal solitary waves. *Tellus* 31: 456-462.

- Munro, R.G. 1982. First Davis Strait discovery overcomes offshore hazards. *World Oil* April: 85-91.
- Oakey, N.S. 1977. Octuprobe III, An instrument to measure oceanic turbulence and microstructure. Tech. Rep. BI-R-77-3, Bedford Inst. of Oceanogr., Dartmouth, Nova Scotia, Canada 52 p.
- Osborne, A.R. and Burch, T.L. 1980. Internal Solitons in the Andaman Sea. *Science* Vol. 208, 2 May, 4443: 451-460.
- Petrie, B. 1975. M2 surface and internal tides on the Scotian shelf and slope. *J. Mar. Res.* 33(3): 303-323.
- Sandstrom, H. 1976. On Topographic Generation and Coupling of Internal Waves. *Geophys. Fluid Dyn.* 7: 231-270.
- Sandstrom, H. and Elliott, J.A. 1982. Tidal Mixing at the Shelf Edge. *BIO Review* '82: 13-15.
- Sandstrom, H. and Elliott, J.A. 1984. Internal Tide and Solitons on the Scotian Shelf – a Nutrient Pump at Work. *J. Geophys. Res.* 89(C4): 6145-6425.
- Sandstrom, H. and Elliott, J.A. 1986. Atlas of Physical Oceanographic Data for Current Surge Studies on the Scotian Shelf: 1980-82. *Can. Tech. Rep. Hydrogr. Ocean Sci.* 77: iii + 261pp.
- Sandstrom, H. and Elliott, J.A. 1989a. Atlas of Physical Oceanographic Data for Current Surge Studies on the Scotian Shelf: 1983. *Can. Tech. Rep. Hydrogr. Ocean Sci.* 114: iv + 379pp. (note that the Julian days for the figures showing time vs latitude for Stations 43 and 47 are incorrect and should be smaller by one day)
- Sandstrom, H. and Elliott, J.A. 1989b. Atlas of Physical Oceanographic Data for Current Surge Studies Near the Gully, Scotian Shelf: 1984. *Can. Tech. Rep. Hydrogr. Ocean Sci.* 117: iv + 304pp.
- Sandstrom, H. and Elliott, J.A. 1989c. Atlas of Physical Oceanographic Data for Current Surge Studies on the Grand Banks of Newfoundland: 1985. *Can. Tech. Rep. Hydrogr. Ocean Sci.* 121: iv + 472pp.
- Sandstrom, H., Elliott, J.A. and Cochrane, N.A. 1989. Observing Groups of Solitary Internal Waves and Turbulence with BATFISH and Echosounder. *J. Phys. Oceanogr.* 19(7): 987-997.
- Sandstrom, H. and Quon, C. 1993. On time-dependant, two-layer flow over topography. I. Hydrostatic approximation. *Fluid Dynamics Res.* 11: 119-137.

- Sandstrom, H. and Quon, C. 1994. On time-dependent, two-layer flow over topography. II. Evolution and propagation of solitary waves. *Fluid Dynamics Res.* 13: 197-215.
- Sandstrom, H. and Oakey, N.S. 1995. Dissipation in Internal Tides and Solitary Waves. *J. Phys. Oceanogr.* 25(4): 604-614.
- Sandstrom, H. and Elliott, J.A. 2002. Tidal mixing and The Gully ecosystem. Can. Tech. Rep. Fish. Aquat. Sci. 2377. Advances in Understanding The Gully Ecosystem: A Summary of Research Projects Conducted at the Bedford Institute of Oceanography (1999-2001), D. C. Gordon Jr. and D. G. Fenton (Editors): iv + 84pp.
- Turner, R.E.L. and. Vander-Broeck, J.-M 1988. Broadening of interfacial solitary waves. *Phys. Fluids* 31: 2486-2490.

## 12. Appendices

### Appendix 1 Aircraft SLAR Data

While conducting the shipboard observation program in the Scotian Gulf in 1983 (83-024), we had noted, first visually and then with the ship's X-band radar, that a surface pattern of rough and smooth bands occurred at crossings of internal wave packets. Closer attention to these surface signatures revealed that the rough bands ("tide rips") occurred where the individual waves caused a surface convergence (above descending isopycnals), whereas the smoother bands were associated with surface divergence (above ascending isopycnals). The presence of these "tide rips" proved immensely useful in tracking groups of waves while collecting data with the Batfish. The same technique was later used at the other study sites and appeared to work under most wind/wave conditions.

We were able to put the shipboard experience to a more extensive test when, about one month after the 1983 cruise, the opportunity arose to obtain airborne radar imagery on the Scotian Shelf. A research aircraft with a SLAR (Side Looking Aperture Radar) had been working on the east coast and, when approached, agreed to a test flight on the western half of Scotian Shelf. An image of a section of initial results is shown in Figure 1.1. The SLAR is roughly equivalent to the X-band shipboard radar, but, as with the X-band, had to be adjusted to pick out the weaker signatures of the internal wave groups and ignore the saturation from stronger returns. Encouraged by the test results, the company (INTERA) was contracted to conduct three more flights over the Scotian Shelf a few days later.

In 1984 another company (MARS Ltd.) was contracted to obtain SLAR imagery over both the Grand Banks and the Scotian Shelf, with a few flights of opportunity in late winter/early spring and many more dedicated flights during the summer season. During the winter flights, apparent internal wave activity was noted only on one flight segment near the northern edge of the Grand Bank. In contrast, in the summer, surface manifestations of waves are seen near the shelf edge everywhere. A listing of flights is given in Table A1.

Figures 1.2 and 1.3(see Introduction) are composites showing the locations of the leading (or dominant) wave in a wave group. The same data are shown in Figures A1.1 and A1.2 with the addition of a grey overlay depicting the sea surface extent of SLAR imagery for all the flights. In general, the observed wave fronts were concentrated near the shelf break within a strip approximately 50 km wide, with a few exceptions where the shelf edge is deeper. The composites may show the lead wave generated from a given tidal cycle more than once as a result of multiple passes of SLAR for the same wave group, and on occasion wave groups from two tidal cycles (~ one internal tide wavelength apart) could be seen.

The SLAR imagery shows the ubiquity of presence of summertime internal wave activity all along the edges of the continental shelf off Nova Scotia and the Grand Banks of Newfoundland. It also enforces the impression, garnered from shipboard observations, that large-amplitude internal wave groups associated with internal tide decay generally within one wavelength as they propagate on-shore. However, as with the X-band radar on the ship, the SLAR is an extremely useful tool to detect the presence of waves, but cannot be used to measure their amplitude directly.

The presence of these long-crested features along the shelf edge has been part of the local knowledge in military circles and amongst other aviators for many years. Pilots from Greenwood, for example, refer to such features as the “silver-hake line”, because of their co-location with the offshore fishing fleets. The Ice Branch, AES, Ottawa, uses SLAR on aircraft to monitor ice and icebergs in northern waters. Although the ice patrol sets the SLAR sensitivity to be suitable for ice reconnaissance, we found that their images over open water did occasionally contain patterns of wave groups similar to our data. A review of Ice Branch SLAR data for the occurrence of internal waves, conducted by TARDIS Computer Consultants, is summarized in their contractor’s report (OERD library #23). Examples of wave-group or frontal features were found along most of the shelves and banks north of Newfoundland and in the channels of the Arctic islands. Two areas where wave-groups were a dominant feature are the east and the west end of Hudson Strait. Topography and tides are well suited to generate internal waves at these locations. Overall, information from the Ice Branch data is consistent with our other observations.



Table A1: SLAR Flights

	<b>1983</b>	<b>Intera Environmental Consultants Limited, Calgary</b> (VHS + paper record)
15/9	Test flight	Scotian Shelf
18,19/9	5 legs	Scotian Shelf
20/9	7 legs	Scotian Shelf
21/9	7 legs	Scotian Shelf
	<b>1984</b>	<b>MARS Ltd. Aerial Remote Sensing, Calgary</b> ( photographic negative)
22,24/3	2 legs	Grand Bank, St. John's to Halifax return
1/7	6 legs	Scotian Shelf 2E, 2W, 2 central
23/9	5 legs	Scotian Shelf 4W, 1 central
24/9	5 legs	Scotian Shelf 4E, 1 central
25/9	5 legs	Scotian Shelf, Laurentian Trough, St. Pierre Bank, Green Bank, Halifax-St. John's
26/9	4 legs	Grand Banks 4 periphery
27/9	5 legs	Grand Banks 1 St.John's S, 2SW, 1 St.Pierre, 1 Green
28/9	6 legs	Grand Banks 3 NE, 3E
29/9	4 legs	St. John's-Halifax Grand Banks S, Scotian Shelf E
30/9	6 legs	Scotian Shelf 4W, 2 central
1/10	5 legs	Scotian Shelf 2W, 2E, 1 central

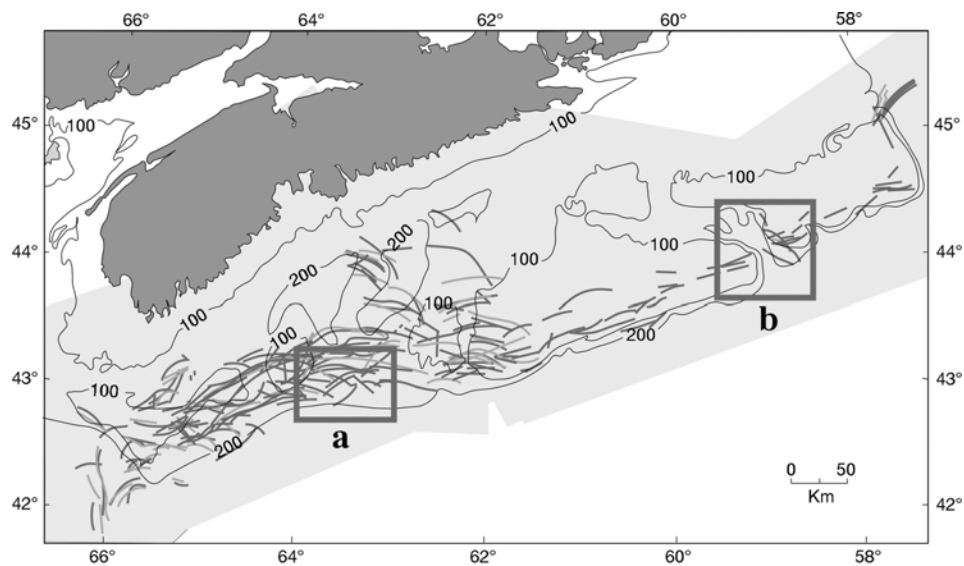


Figure A1.1: Scotian Shelf SLAR coverage is shown by the grey overlay .

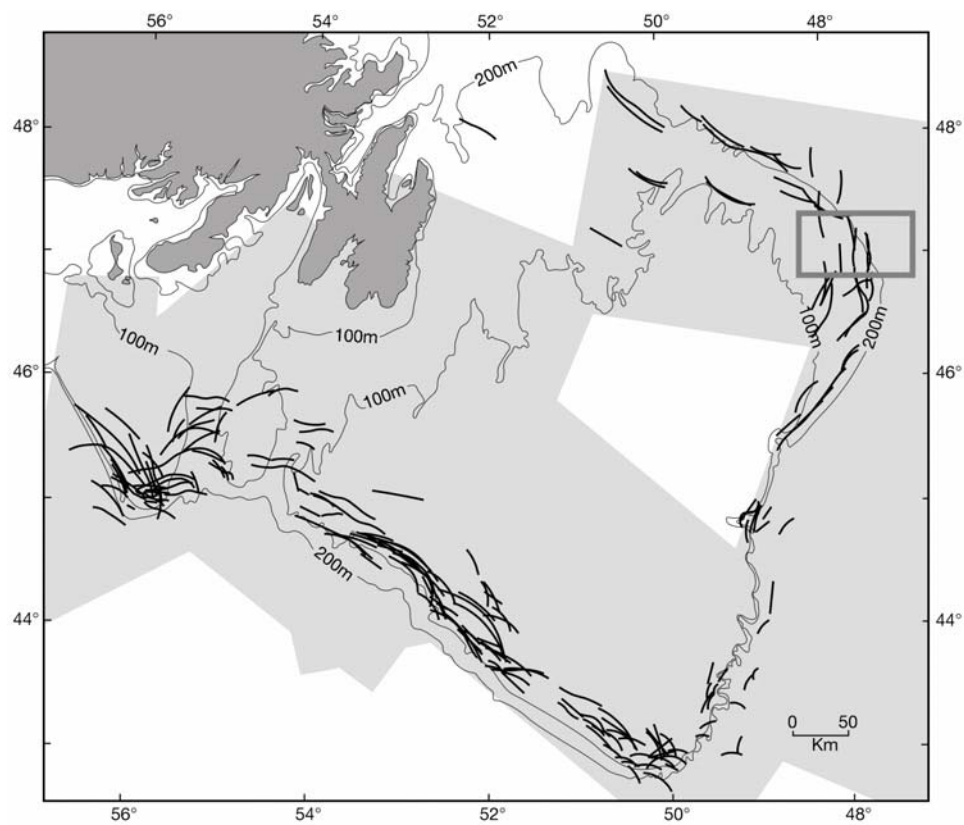


Figure A1.2: Grand Bank SLAR coverage is shown by the grey overlay.

## **Appendix 2 Bow Drill Thermistor Chain**

Based on the initial cruises(80-039 and 81-042), we were confident that a group of high-amplitude waves could be generated by the tide at sites along the Scotian Shelf, however we were uncertain as to their persistence, locations, and amplitudes. To address the question of time-variability we took opportunity to install a thermistor-chain on an off-shore drilling platform in order to monitor internal waves. The offshore industry was concerned with a number of possible environmental hazards among which the action of internal waves had been suggested by Osborne and Burch (1980). In Davis Strait, the influence of the wave-induced currents on a drill ship was noticed (Hodgins and Westergard 1981) and led to an installation of a “rip current warning system” (Munroe 1982).

The idea of placing internal wave monitoring systems on board offshore drilling platforms was discussed with oil industry representatives and received favourable response. A pilot project started in September, 1982, after a thermistor-chain was built at Bedford Institute and installed on BOWDRILL I, which was then drilling at the south-eastern edge of Banquereau Bank. The recording system consisted initially of a paper-ink analog chart recorder, which was unsatisfactory and was replaced by a digital chart recorder. In November-December of 1982, a total of 45 days of recordings were made. No scientifically useful data were gathered due to the absence of any measurable thermal structure.

In the spring of 1983, BOWDRILL I moved to another site near the edge of Banquereau Bank to drill SW Banquereau F-34 well. This site was located at 44° 03' 16"N, 58° 50' 18.5"W in 114 metres of water (Figure A2.1). The thermistor-chain with the digital chart recorder was installed and started recording on June 15, 1983. Useful data were collected until July 12, 1983. Minimal interruption in data occurred only when the chart paper had to be replaced on a weekly cycle. Six thermistors were placed in the water column at nominal depths of 20, 30, 40, 50, 60, and 70 metres.

### Data

The thermal structure during the recording period had, characteristically, a large temperature gradient in the upper 30 metres, a temperature minimum at 40-50 metres, and a slight increase in temperature below the minimum. This structure persisted with only slight changes for the whole period of observation. The four deeper thermistors at 40-70 metres depth registered closely spaced temperature traces of 2-4°C during most of the recording time. The thermistors at 20 and 30 metres, being in the seasonal thermocline, recorded higher temperatures. This characteristic or normal pattern was broken only during brief episodes, when some or all of the deeper thermistors record elevated temperatures. The typical time scale associated with higher than normal temperature is approximately 10 minutes, and on many occasions there are several of these high

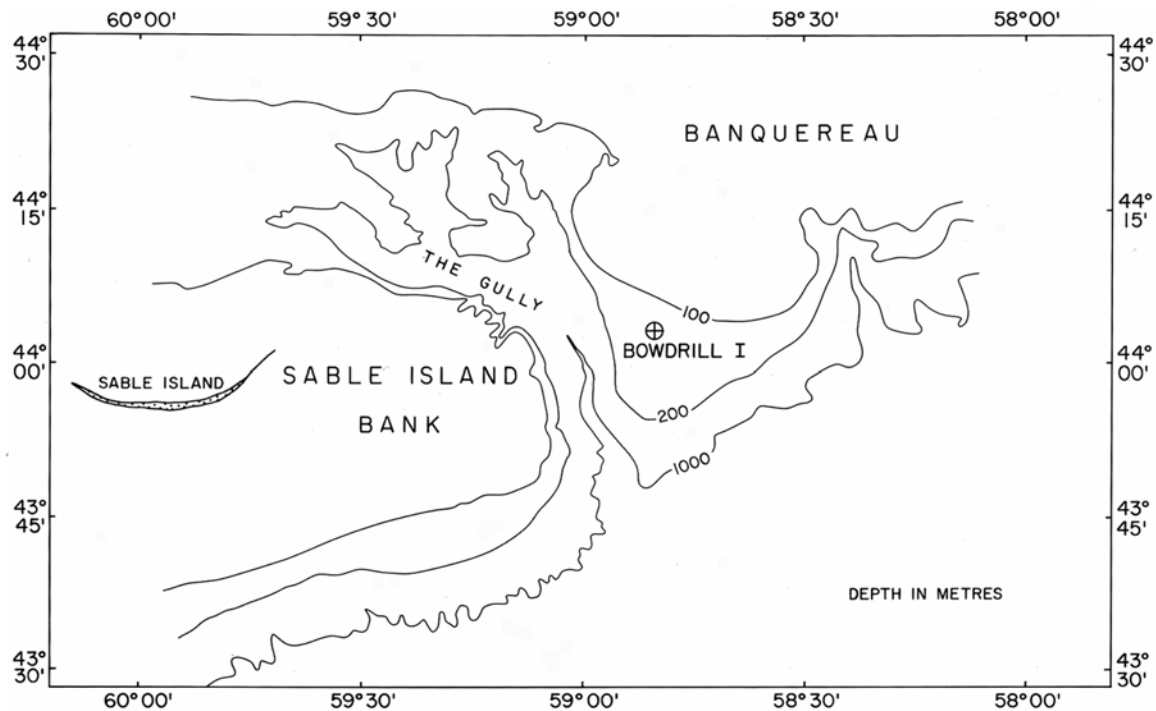


Figure A2.1: Site of BOWDRILL 1 on the Scotian shelf.

temperatures in succession. The episodes occurred in every tidal cycle, but their pattern and grouping varied from one tidal cycle to the next. Figures A2.2 to A2.13 show most of the more prominent ‘events’ for the four week recording period. In part (a) of each figure, temperature versus time is traced from the original chart record for each of the six thermistors for the periods of interest. In part (b) the time-series of selected isotherms versus depth is constructed by knowing when the particular isotherm was at the depth of the given thermistor. In part (c) the temperature versus depth profile is compared between “normal” and episodic states, based on the temperatures at the six thermistors at the designated times.

#### Discussion of data

Figures A2.2 to A2.13 show short segments of data from 12 different tidal cycles. Each segment is selected to show the dominant event during the tidal cycle. The elevation of temperature, mostly at the deeper thermistors but affecting the upper thermistors as well, can only be due to downward displacement of the whole water column. Hence the data indicate passage of groups of short waves past the thermistor-chain. Both from the time-series of isotherm position and from the temperature profiles at particular times, it is obvious that vertical displacements as large as 30 to 40 metres occur during several tidal cycles. The downward displacements are caused by large amplitude internal waves in the form of solitary internal waves or by groups of waves forming an undulatory bore. On occasion the groups consist of only a few waves, but sometimes many waves are apparent. The shape of the waves and the wave groups varies from one tidal cycle to the next. However, characteristically the time of passage of a wave group past the thermistor-chain is about 1 to 2 hours, i.e. a fraction of a tidal period.

Figure A2.14 is a summary of the observations of large amplitude internal waves for the whole observation period. The 27 days of observations have been split into 53 tidal cycles of 12.4 hours each. The start time for each cycle is indicated at the beginning of the cycle. The times of occurrence of large amplitude wave or wave groups is marked by solid blocks, which indicate the duration of each wave and the number of waves, but not their amplitude. The times of high (H) and low (L) water in Halifax are given in each tidal cycle. The figure shows that at the BOWDRILL I site the wave groups arrive predominantly at about the time of the Halifax high tide or soon after. Of the total of 53 tidal cycles there are definite wave groups in 40, or 75%, of the cycles. Of the 12 largest amplitude groups, as shown in Figures A2.2 to A2.13, four occurred during the first four days of observation, six occurred during the last week, but only two were noticeable during the two weeks from June 20 to July 3. The presence of large amplitude internal waves is thus well correlated with the strength of barotropic tidal currents, which undergo spring-neap modulation during the four weeks. The currents are strongest at the start and finish of the observation period and not as strong during the last week of June and first week of July. The observations are consistent with the idea that most of the energy in internal tides resides in the short, large-amplitude internal waves (Sandstrom and Elliott 1984), and that the strength of the internal tide reflects the strength of the barotropic tidal current (Baines 1982). The almost complete four-week record gave us the first concrete indication of the spring-neap modulation of the internal tide, which had been predicted by tidal generation models but had lacked observational evidence.

Approximately ten weeks after the thermistor-chain data were collected, an airborne radar (SLAR) survey all along the Scotian Shelf edge detected surface manifestations of internal waves at many locations, including the BOWDRILL I site. Groups of internal waves were seen propagating across the site, apparently forming inside the shelf break and moving towards shallow water.

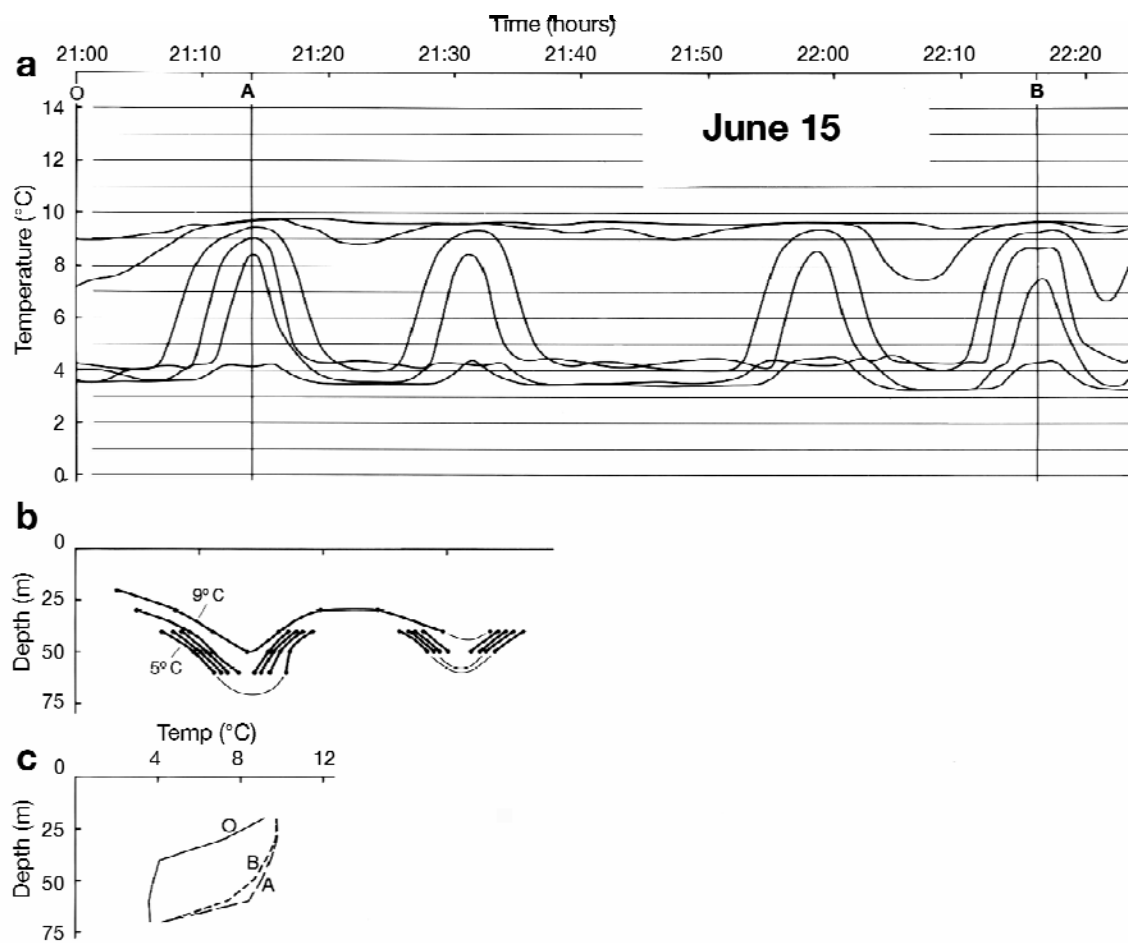


Figure A2.2

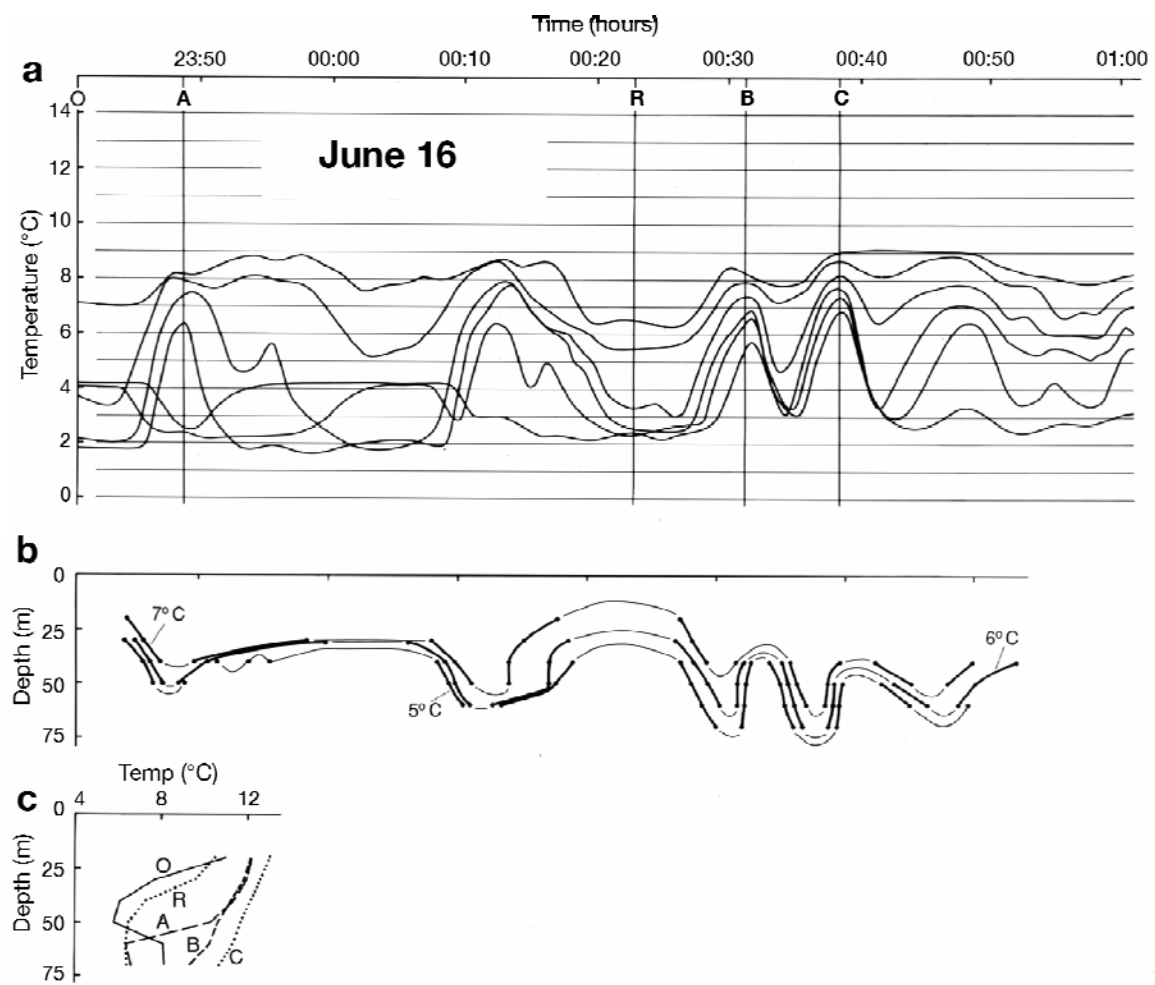


Figure A2.3

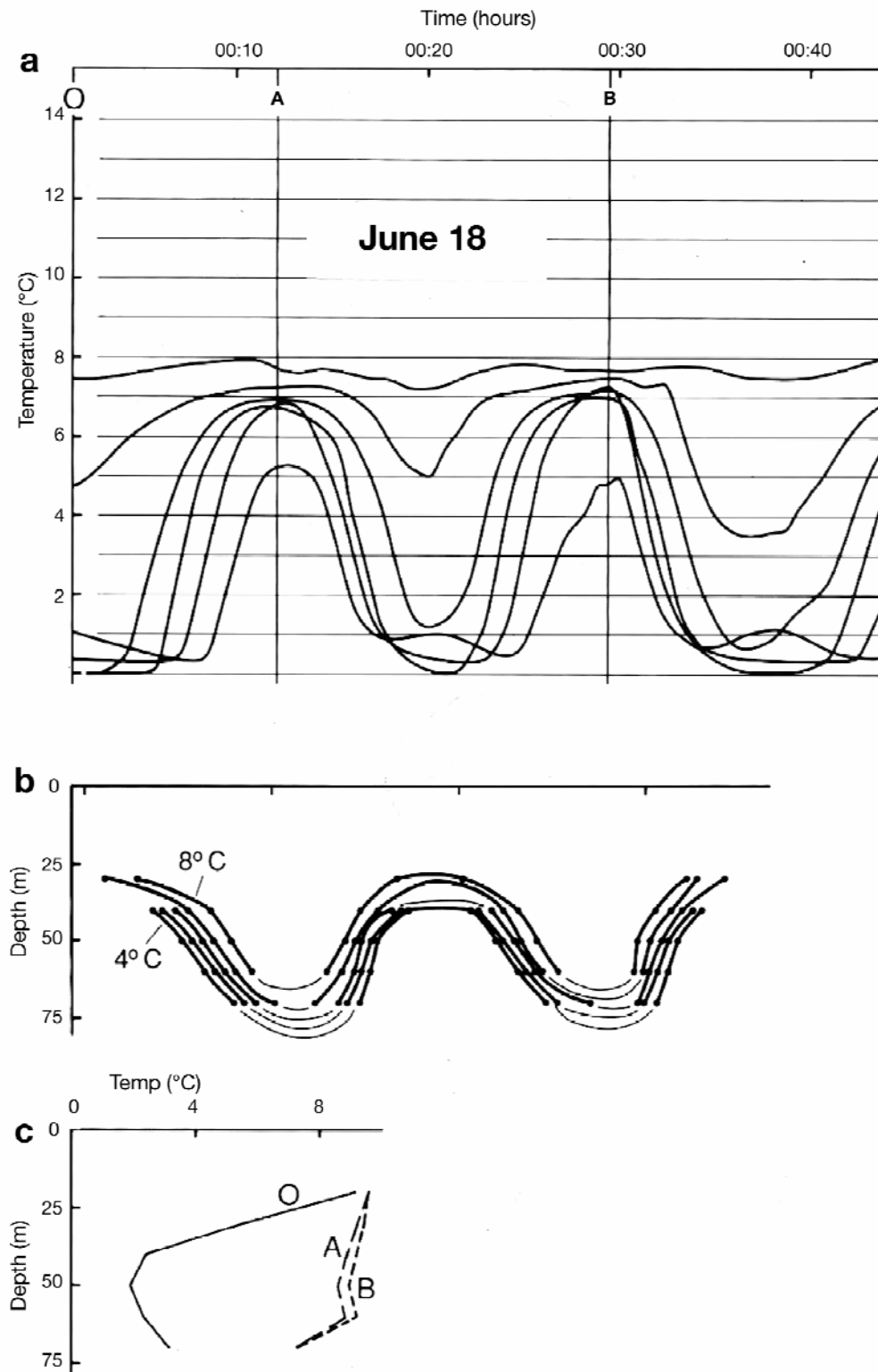


Figure A2.4



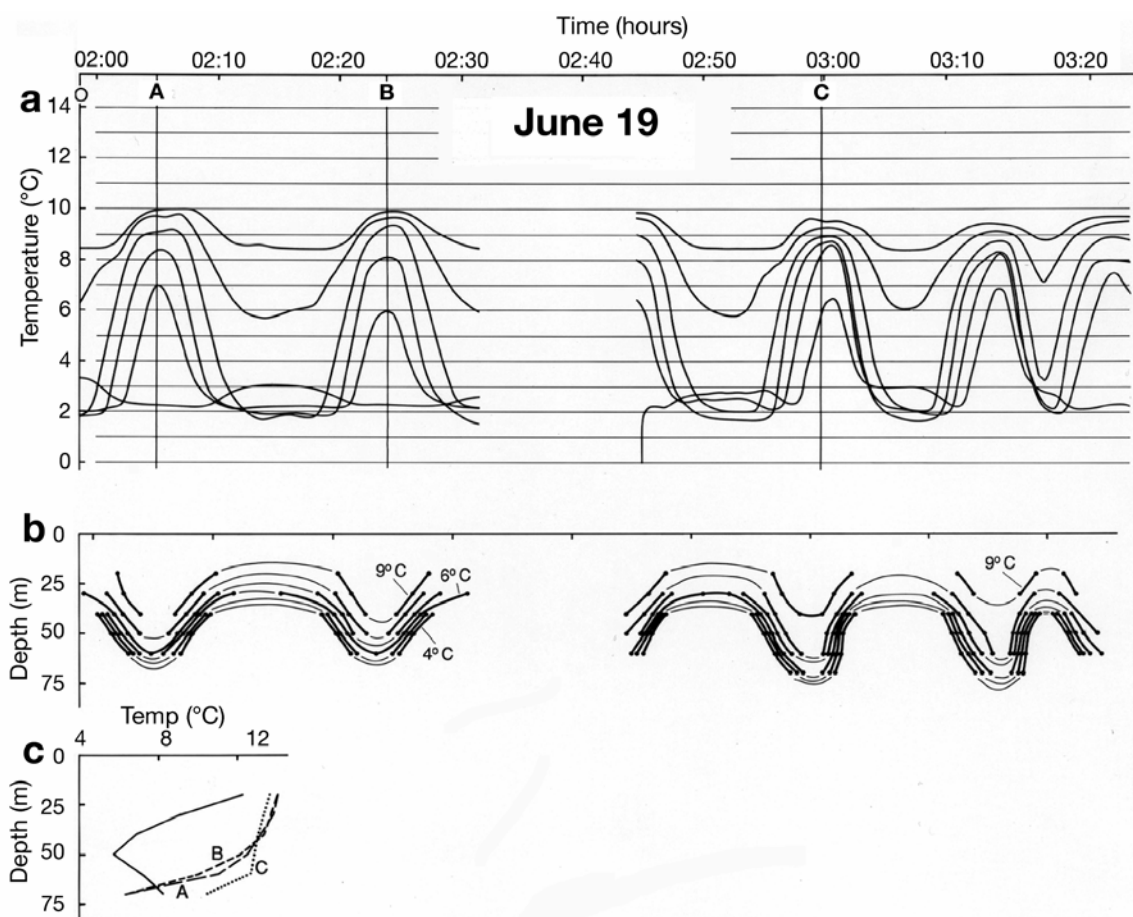


Figure A2.5

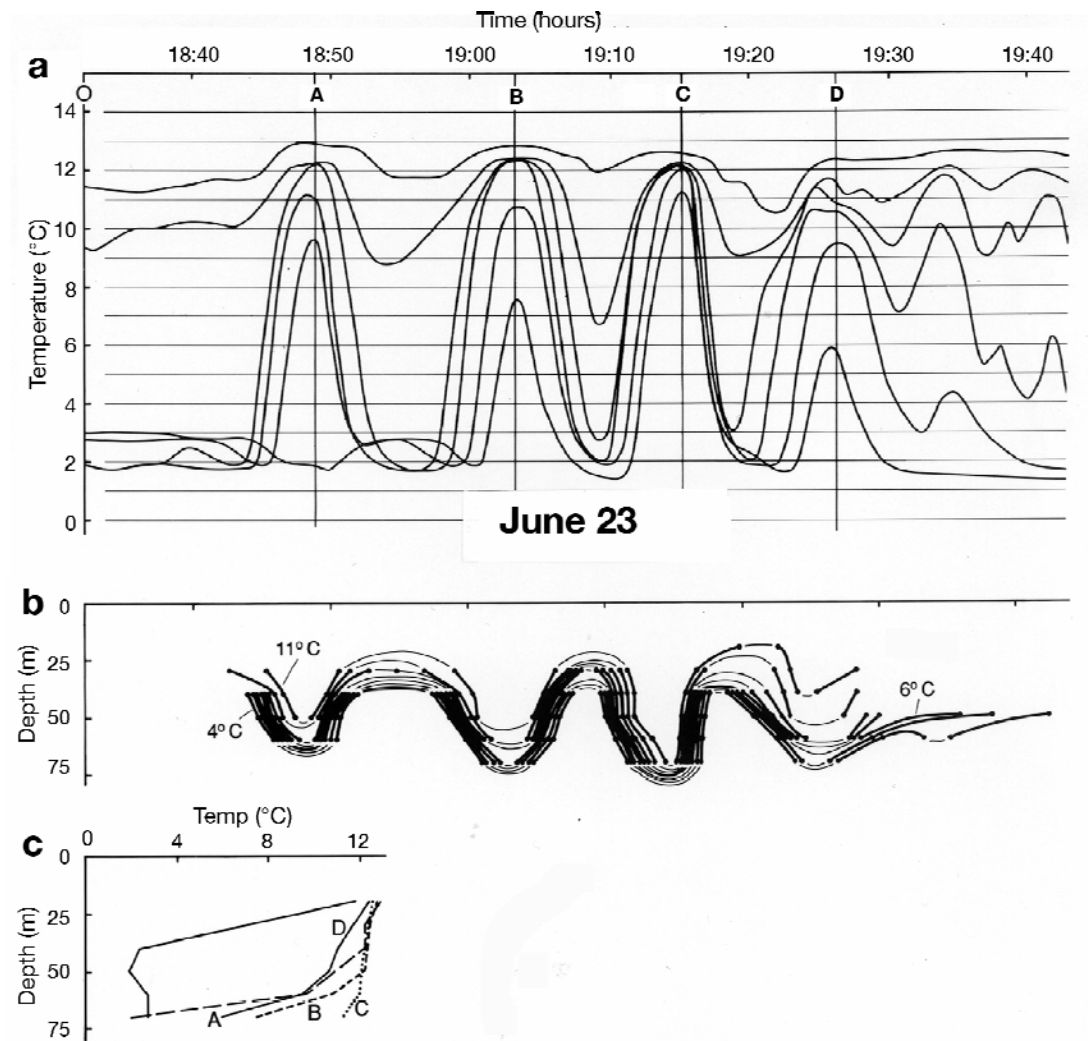


Figure A2.6

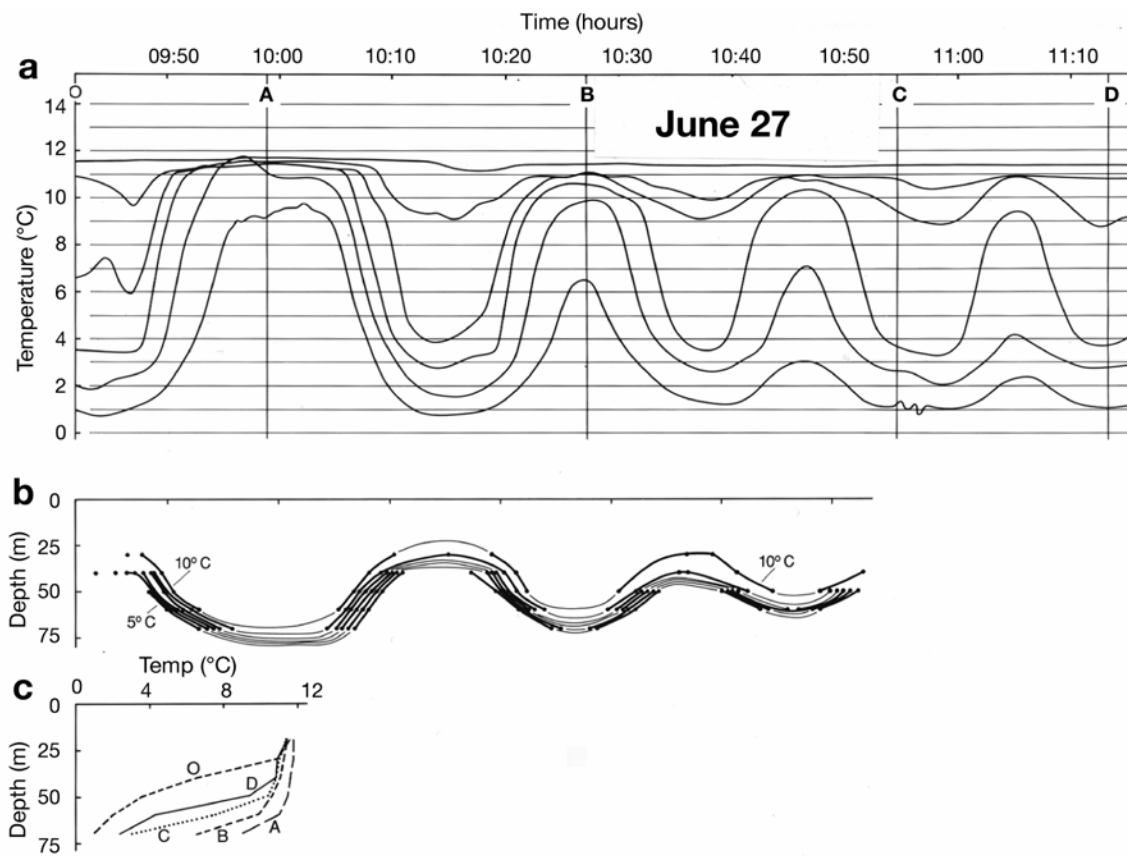


Figure A2.7

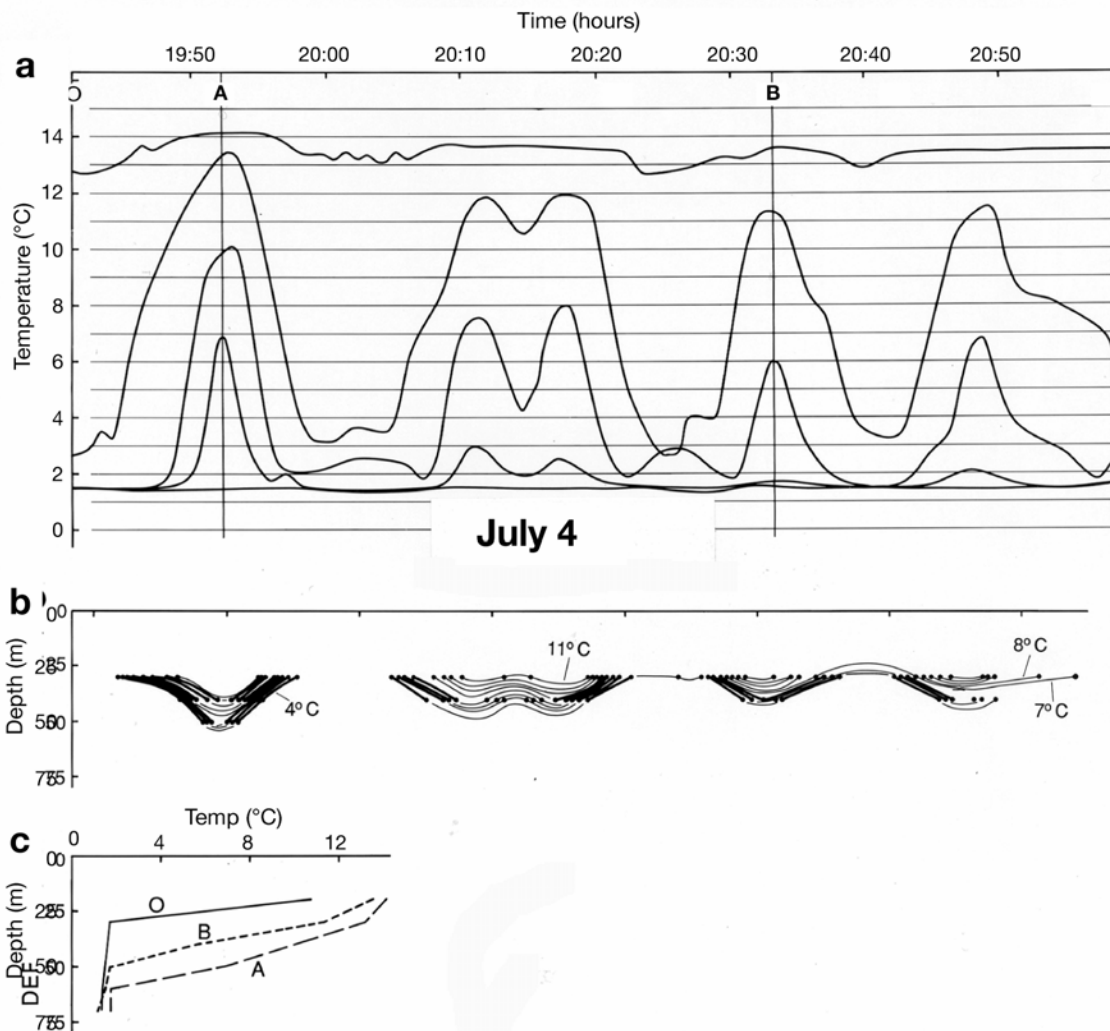


Figure A2.8

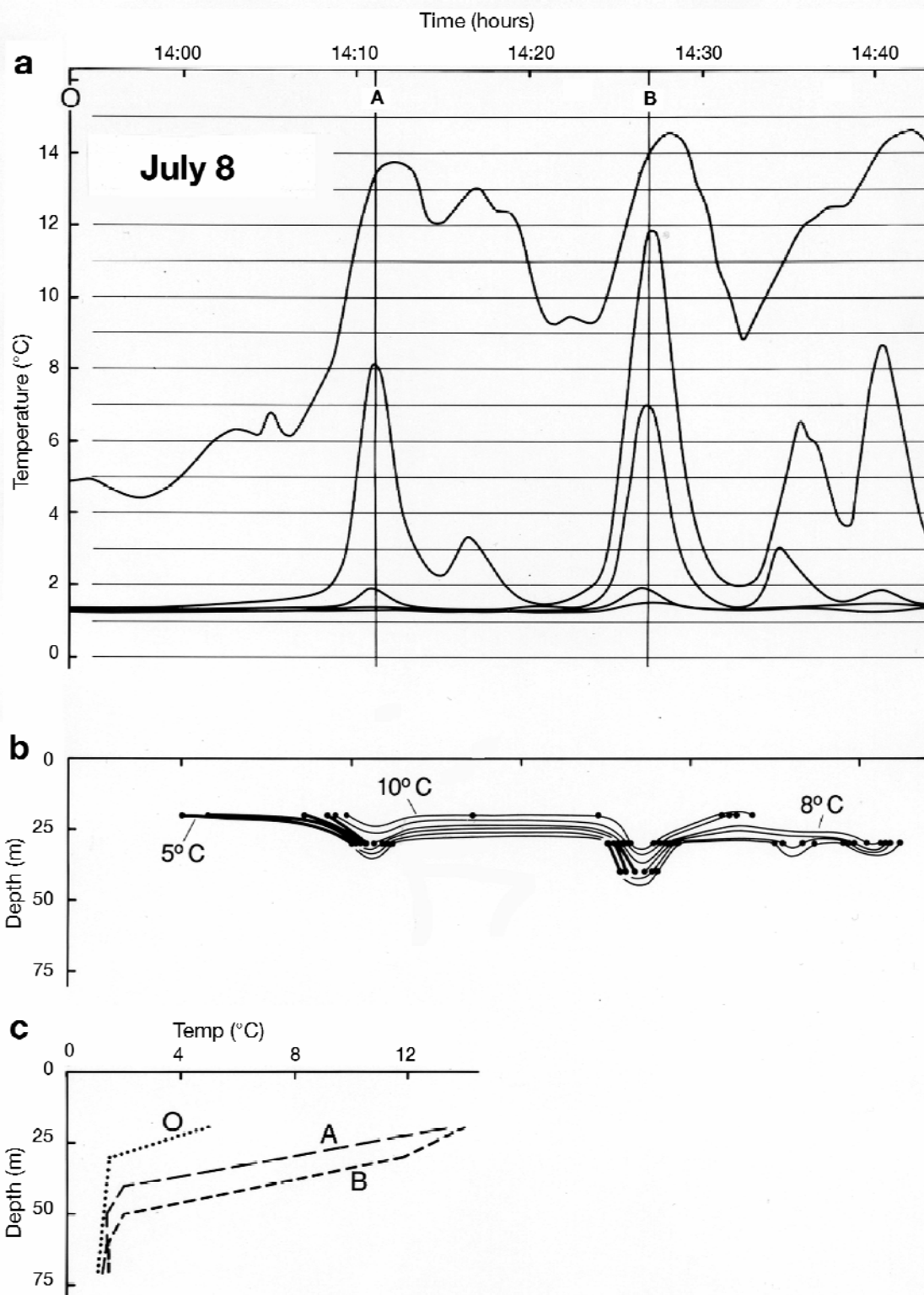


Figure A2.9

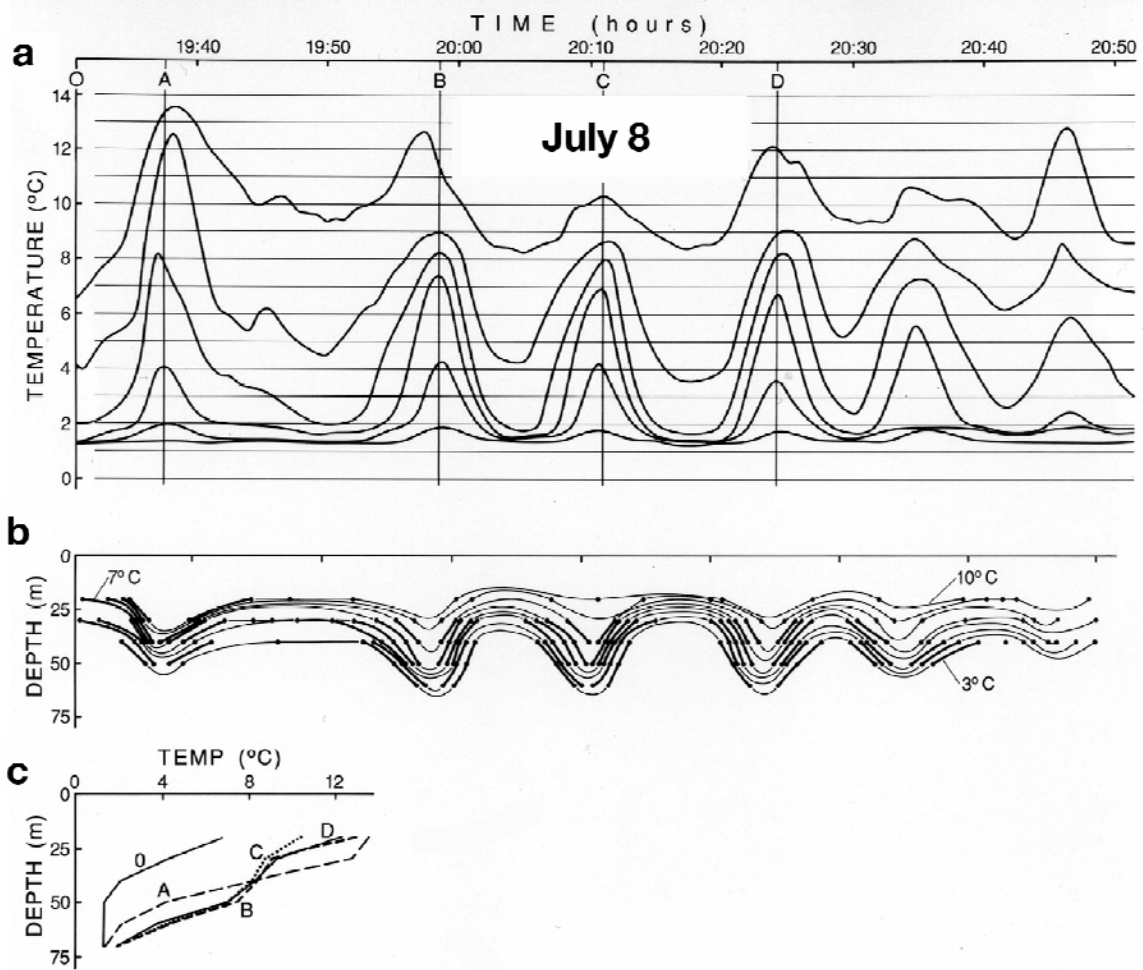


Figure A2.10

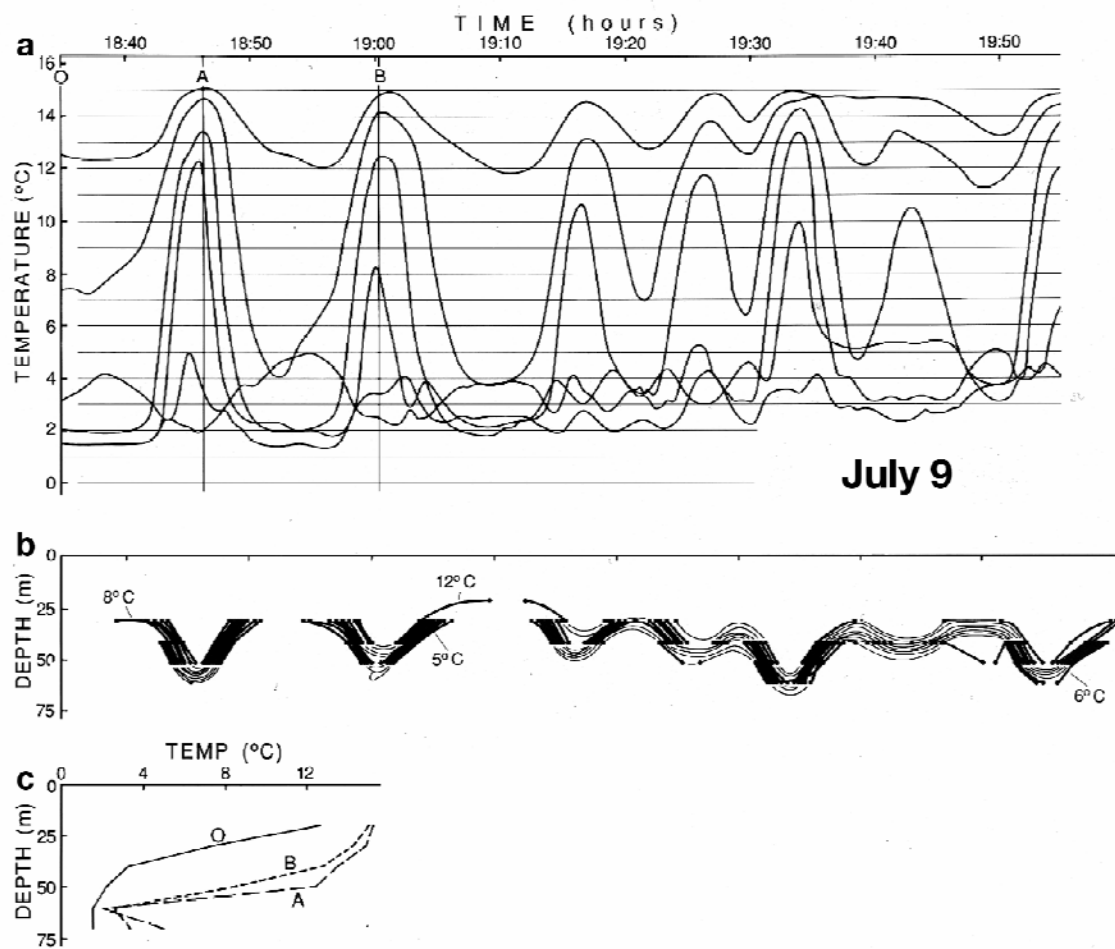


Figure A2.11

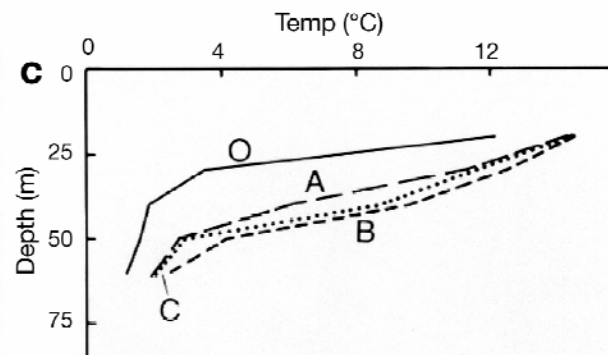
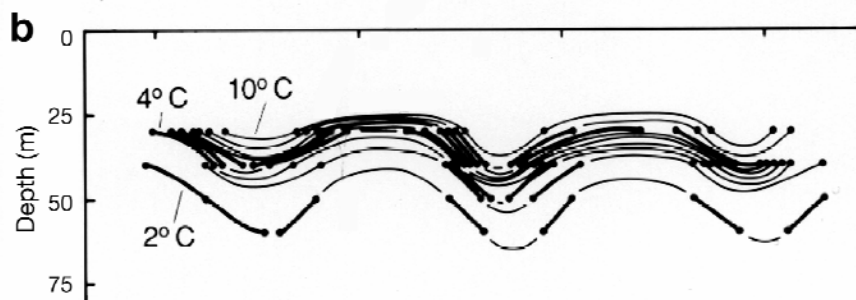
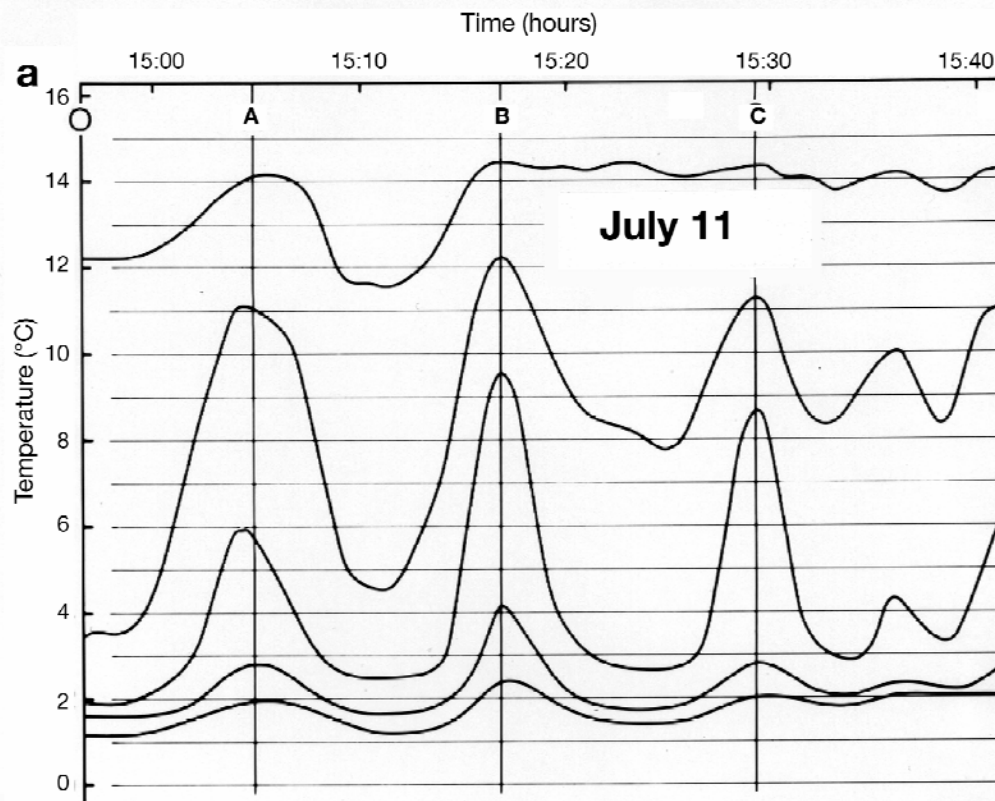


Figure A2.12



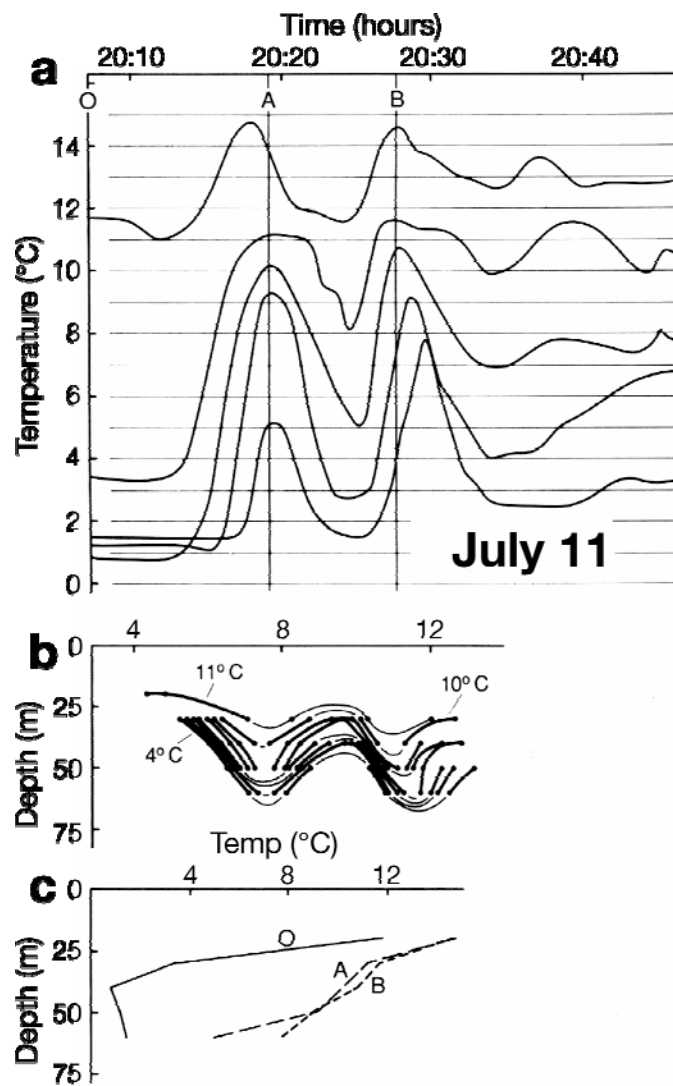


Figure A2.13

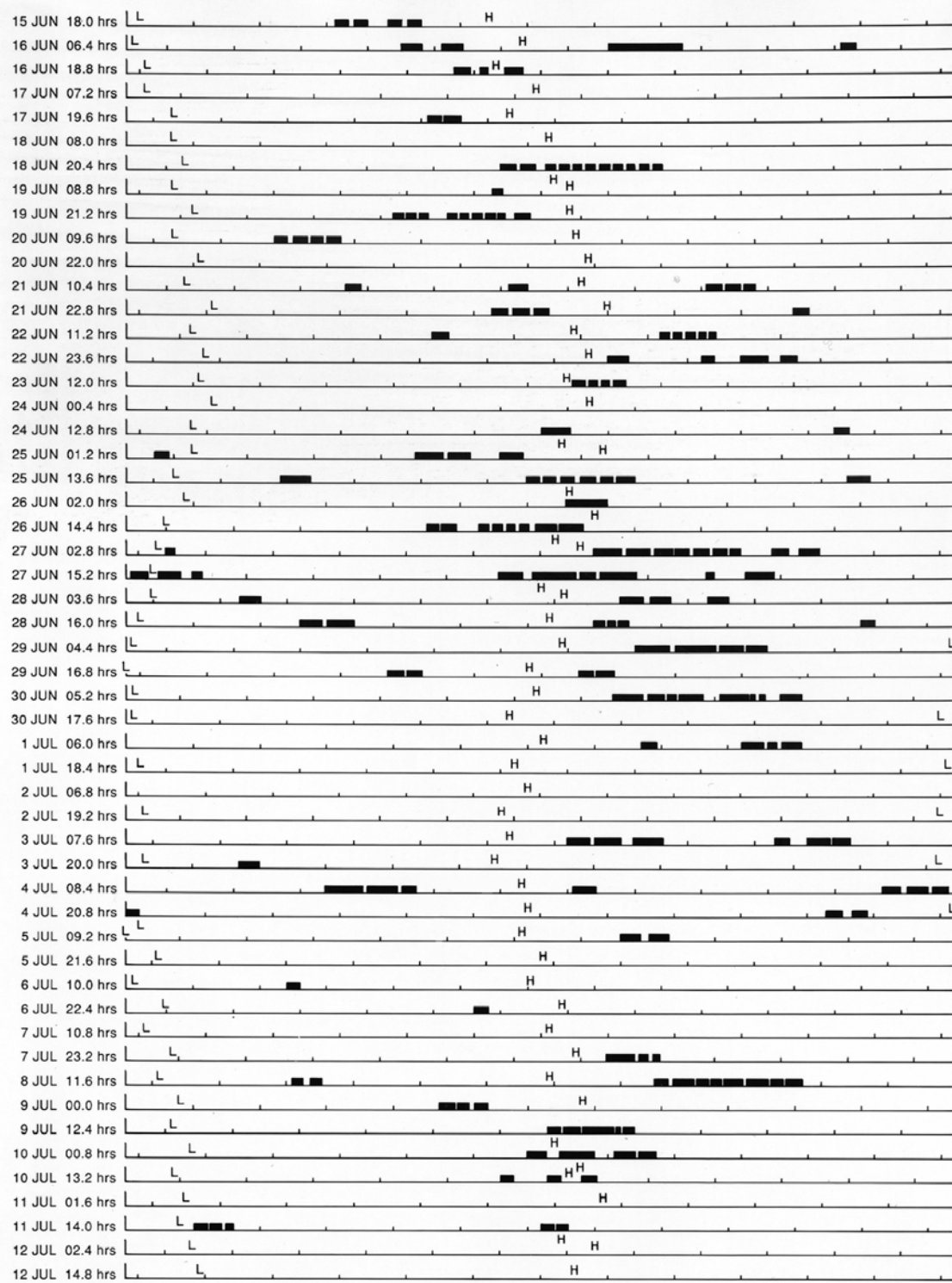


Figure A2.14: Summary of observations of large amplitude waves.

### Appendix 3 Data pitfalls, problems and solutions

In view of the large amount of Batfish data to be processed, fairly general processing procedures were devised. Each Batfish station (total of 44 stations for the three sites) consisted of only a few or as many as 16 transects. During each transect the Batfish made many tens of ascents/descents (occasionally over a hundred). A data file (archived in standard Ocean Data Format (ODF)) represented a transect (typically one hour of data). Breaking the data files into separate ascents and descents was done on the basis of pressure criterion, i.e. the breakpoints were chosen where pressure extrema occurred, either at the bottom or top of the Batfish sawtooth path. Generally this worked well. The data were split into ‘casts’ *a la* CTD. Occasionally, especially near the ends of a transect where the ship was turning to repeat the section, fluctuations in pressure occurred, giving rise to a number of very short ‘casts’. These we tried to eliminate by the simple expedient of keeping track of where the pressure extrema occurred and if they were closely bunched, the data points between them were removed. After such elimination the remaining ‘casts’ became subfiles of the transect file. In the subfiles the pressure either increased or decreased monotonically.

During subsequent data analysis it was found that in some instances (especially in a few stations) short pressure reversals had occurred in the middle of a transect and in the middle of the Batfish depth range, leading to a split in a regular cast. This generated unwanted NaN’s (Not-a-Number in MATLAB environment, wherein processing was done). The split pieces of the cast were rejoined on a case-by-case basis before the transect data was re-analyzed.

The problems associated with this Batfish sampling scheme, namely the question of resolving small scale density fluctuations due to the cast separation and the difference between the cast and slant-wise moving Batfish representation, have been discussed in section 7.1 and 7.2. The cast separation is essentially a compromise between Batfish depth range, its speed of ascent/descent and the ship’s speed, i.e. a compromise between spatial and temporal resolution. Decreasing ship’s speed would improve spatial coverage, but also lessen the number of times that a geographical location would be sampled during a tidal cycle. The speed of ascent/descent of  $\sim 1$  m/s was chosen as high as possible *vis-à-vis* the time constants of the sensors. The depth range of the Batfish during some of the tracking-mode stations was reduced to obtain better spatial resolution of the small-scale features.

When comparing some of the small-scale temperature features in Batfish and thermistor chain data and the same features in the moored current meter data (section 7.3), we encountered a problem of discrepancy in depths. The previously reported current meter depths (Canadian Technical Report of Hydrography and Ocean Sciences, Nos. 114, 117 and 121) were based on the mooring design figures. However, the mooring configuration had to be adjusted onboard ship before placing it in the water and the pressure sensors on the current meters were not reliable enough to correct the design depths. In this report the current meter depths have been adjusted, based on comparison of temperature recorded by sensors on the current meters, on the Batfish, which also has a reliable pressure sensor,

and from a temperature-chain on mooring no. 584 at the Scotian Gulf site. We estimate that the adjusted depths are correct with possibly a 2 – 3 m error. The largest adjustment had to be made for mooring no. 585 at the Scotian Gulf site, where the nominal depths were off by more than 20 m.

## Appendix 4 Stability of the Extended Mean Density Field

For the computation of displacements of the sigma surfaces for the tracking mode data, an 'extended mean density field' was constructed from data collected by Batfish and CTD casts. The final form is shown by Figure 3.4.1, and discussion on accuracy and stability is covered in Section 3.4. A significant feature in the mean field is the frontal gradient associated with a long-shore current found at about 43° N. Based on well defined temperature features that could be monitored in the Batfish and CTD sections some shifting of the front could be followed as depicted by the dashed curves shown in Figure 3.1.2. A more detailed analysis of the temperature record from a sensor located within the frontal region provided additional conformation of a relatively stable positioning of the front during the tracking mode phase. An asterisk( \*) plotted in Figure 3.4.1 at 78m depth and 42.98° N is the location of a current meter with added temperature sensor. To use this temperature signal to monitor density, a 'correlation sigma' was constructed from the Batfish data collected during the tracking mode time period. Shown in Figure A4.1 is the linear fit to Batfish sigma vs temperature for all occasions when the Batfish was passing the mooring. Based on this correlation, Figure A4.2 is the variability in 'correlation sigma' throughout the tracking mode phase. The time period for the tracking mode and the value of the extended mean density field is given by the solid bar in Figure A4.2. The high frequency 'spikes' in the correlation sigma we interpret to be dominated by the vertical displacements, including the wave groups, and the lower frequency variability due mainly to horizontal motion by the tide. This interpretation

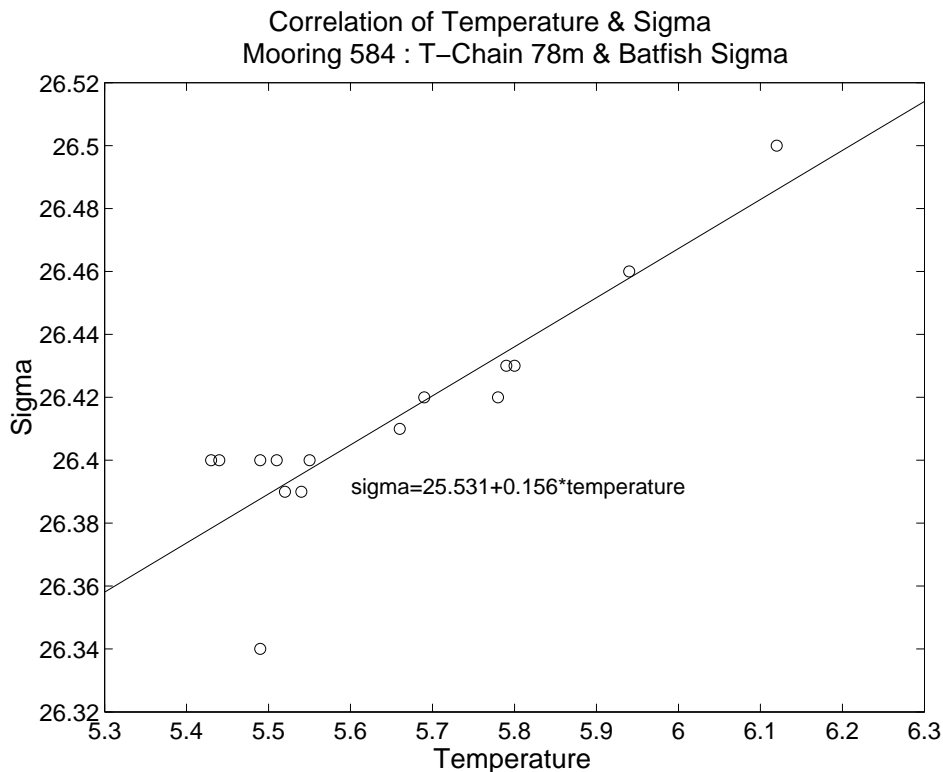


Figure A4.1: Correlation of BATFISH sigma with mooring 584 temperature at 78m.

would confirm that the sigma at this one location and depth remained within about 0.1 over the tracking mode data collection phase.

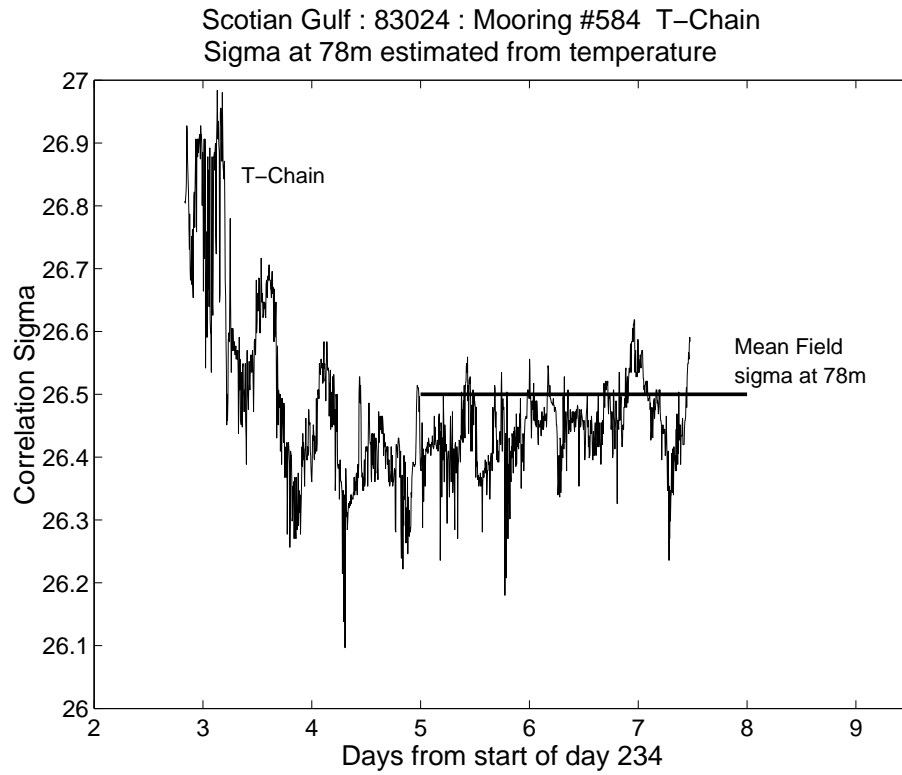


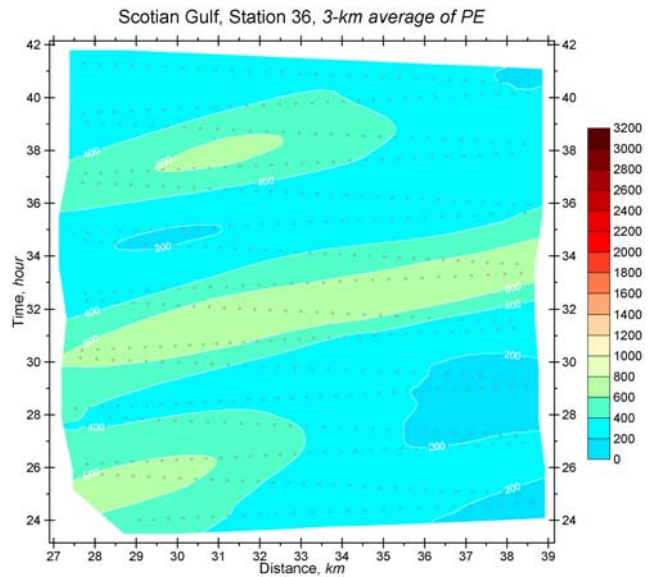
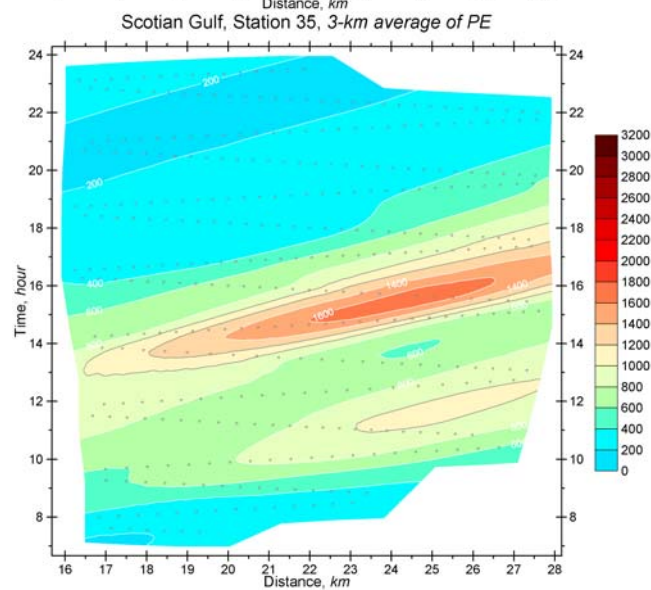
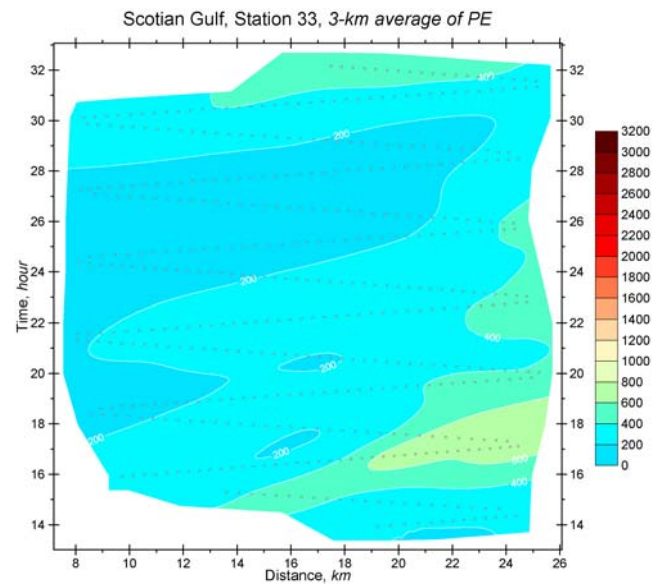
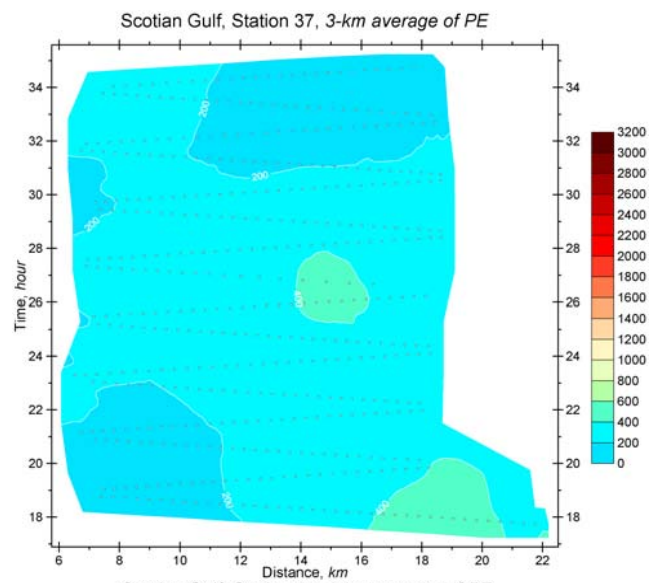
Figure A4.2: Correlation sigma at the location marked by an asterisk in Figure 3.4.1. The solid horizontal line spans the days of the tracking mode data.

## Appendix 5 Potential Energy Contour Plots

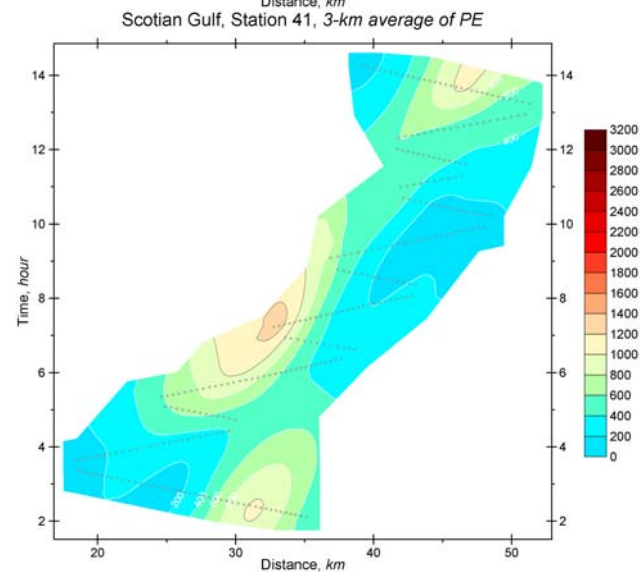
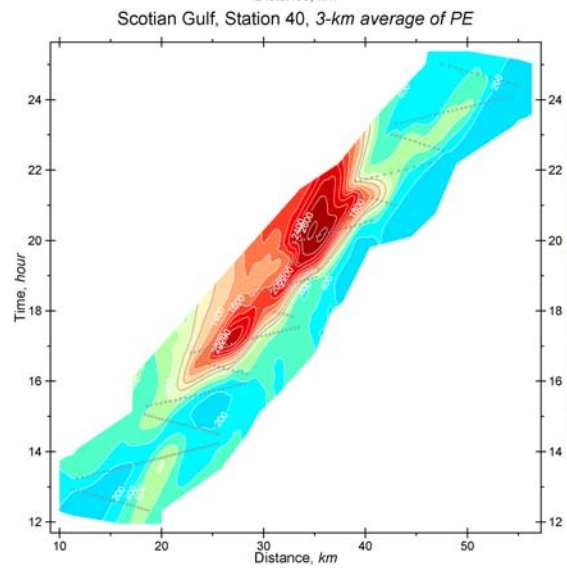
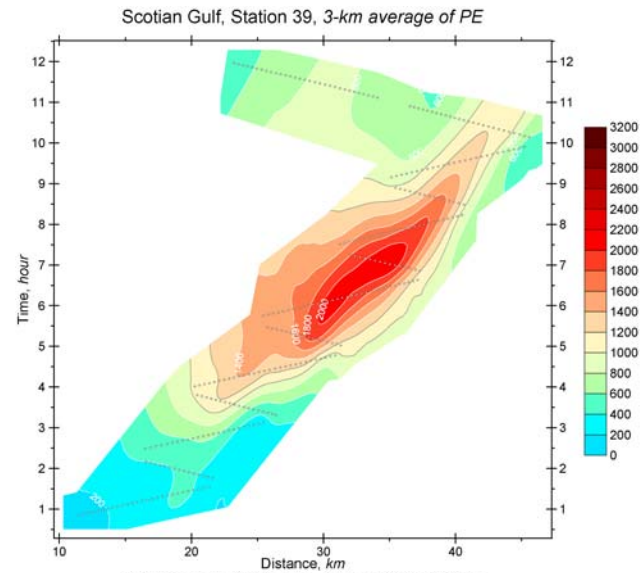
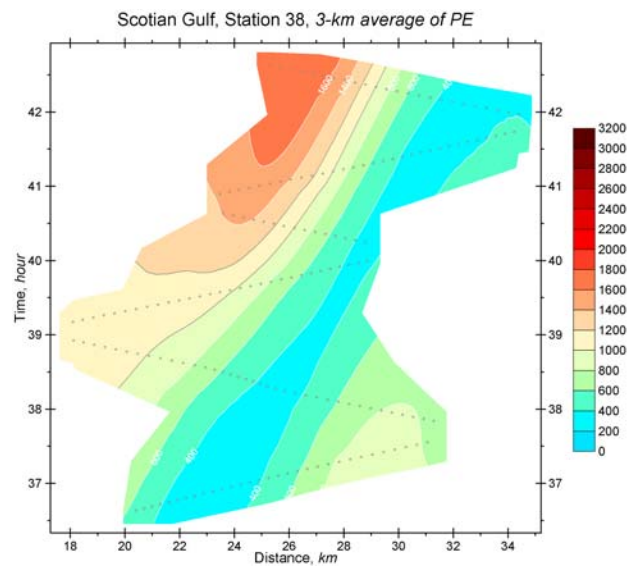
In sections 3.5, 4.3 and 5.3 examples of 3 km averages of energy density in distance-time plots were shown. The two examples in each section represented one time-series station and one tracking-mode station. Here we present the energy density plots for all the stations from the three sites. The units of energy density in each case are in *Joules/m<sup>2</sup>*, but depending on the site and the station location, the contour intervals and limit may vary. The smallest chosen contour interval is 100 *Joules/m<sup>2</sup>*. On the Banquereau Bank, where the highest energy was observed, a contour interval as high as 1000 *Joules/m<sup>2</sup>* is used. The energy density averaged over 3 km is plotted for all the stations. The 1 km average and the non-averaged data is plotted for some tracking-mode stations, both at the Scotian Gulf and The Gully site, especially when the Batfish depth-range was reduced and consequently spatial sampling rate was increased.

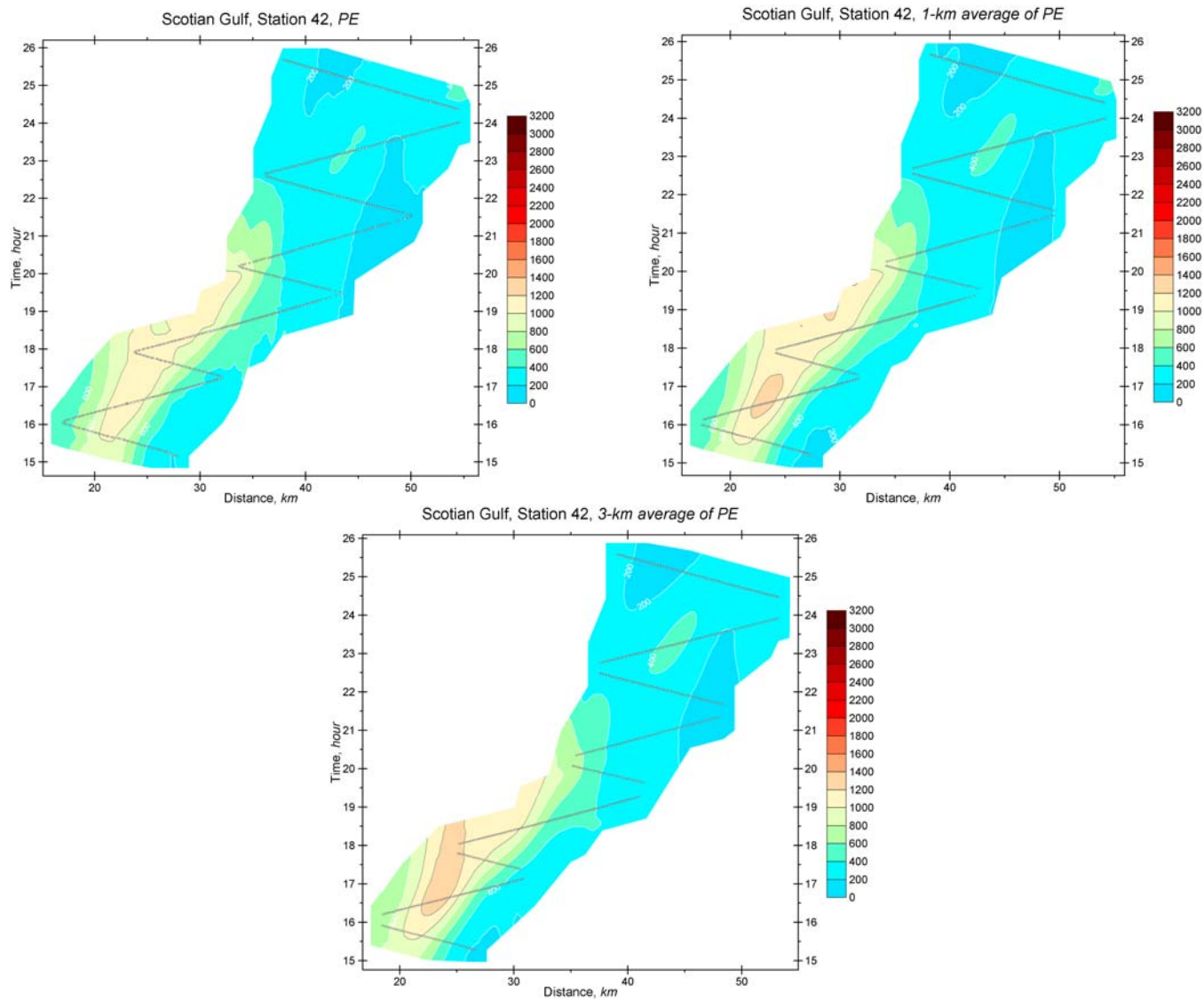
The plots are arranged in the following sequence:

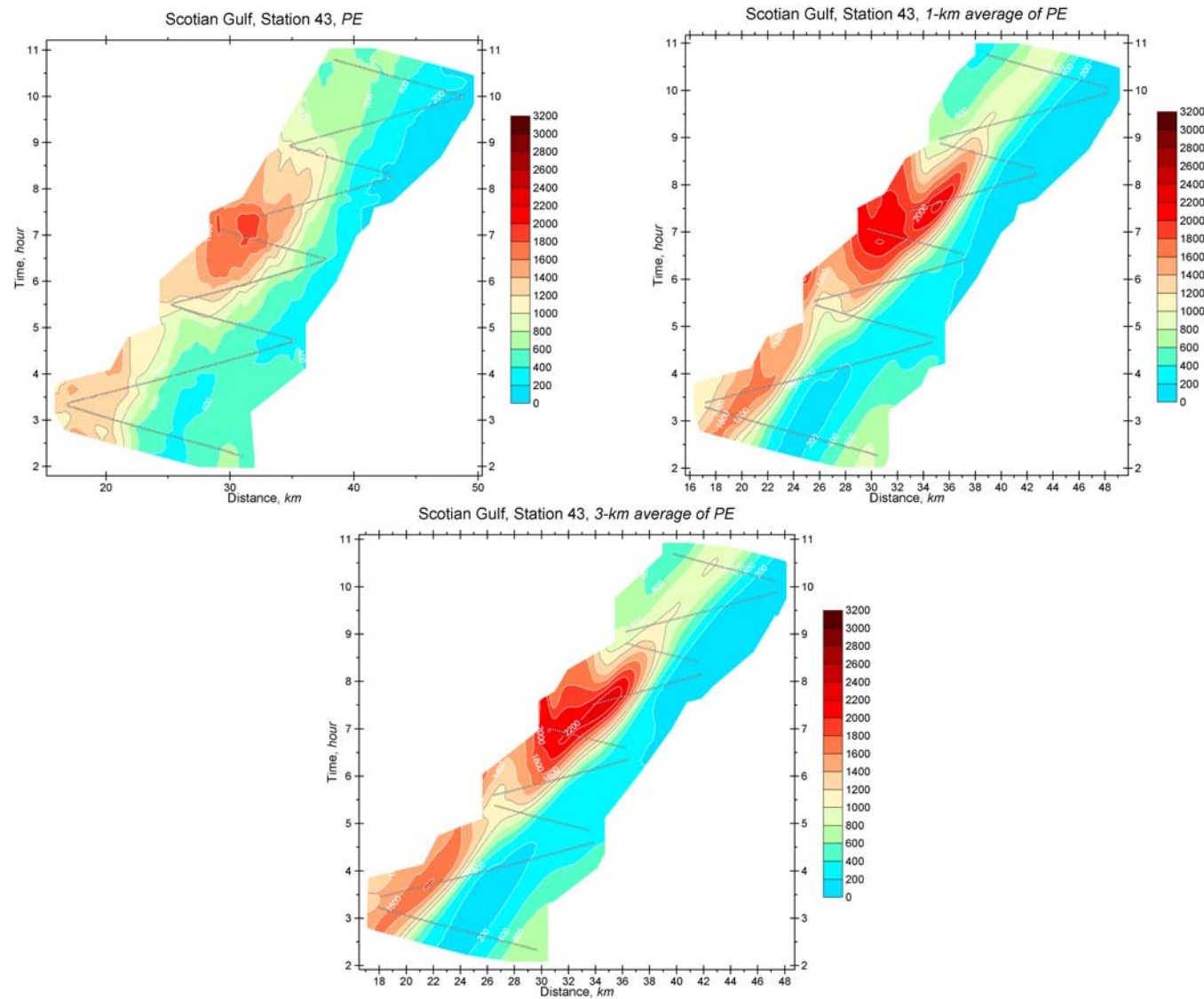
1. Scotian Gulf time-series stations 37, 33, 35 and 36. The order is chosen to reflect increasing distance from the 1000 m isobath.
2. Scotian Gulf tracking-mode stations 38, 39, 40, 41, 42, 43 and 47. Stations 42, 43 and 47 have plots of non-averaged and averaged over 1 km data in addition to averaged over 3 km data.
3. Gully time-series stations 40, 41, 42, 44, 45, 46, 47-48, 49a, 49b, 50, 52 and 54.
4. Gully tracking-mode station 53, including non-averaged, averaged over 1 km and 3 km data.
5. Grand Bank time-series stations 50, 49, 48 and 45-46, representing increasing distance from the 1000 m isobath.
6. Grand Bank tracking-mode stations 52, 53, 54, 55, 57, 58, 60 and 61.

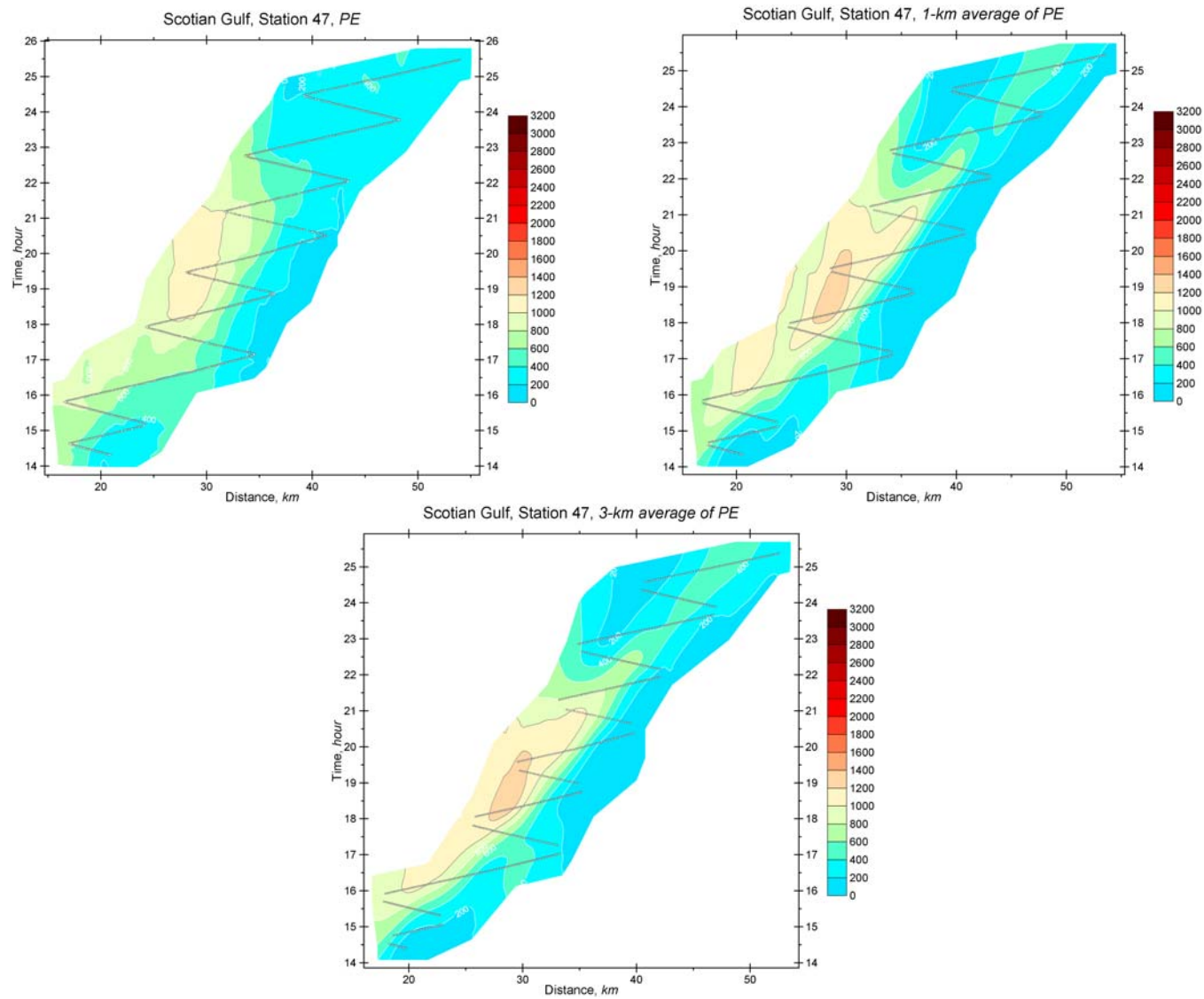




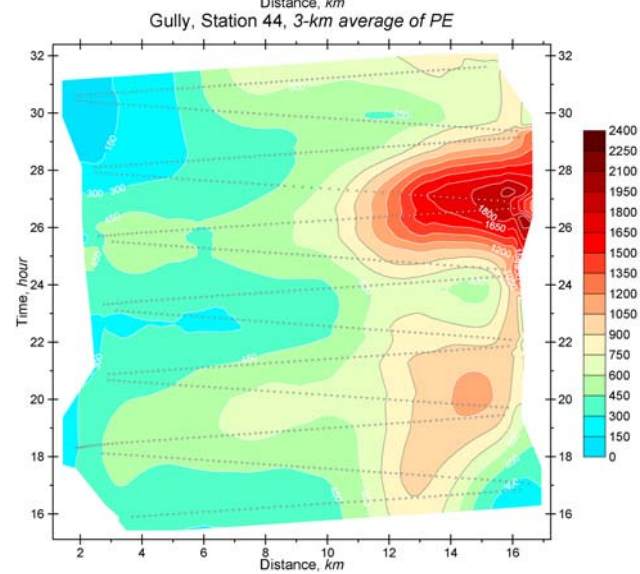
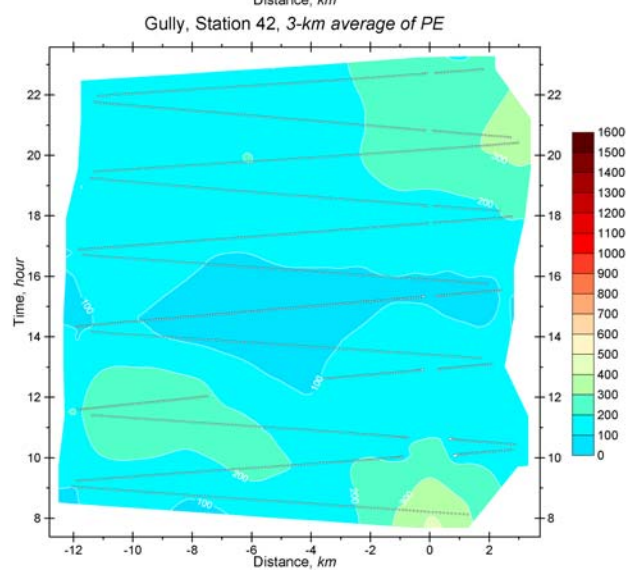
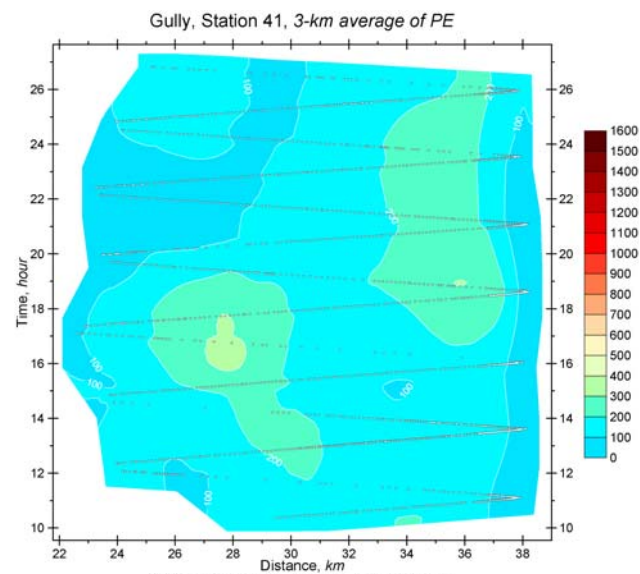
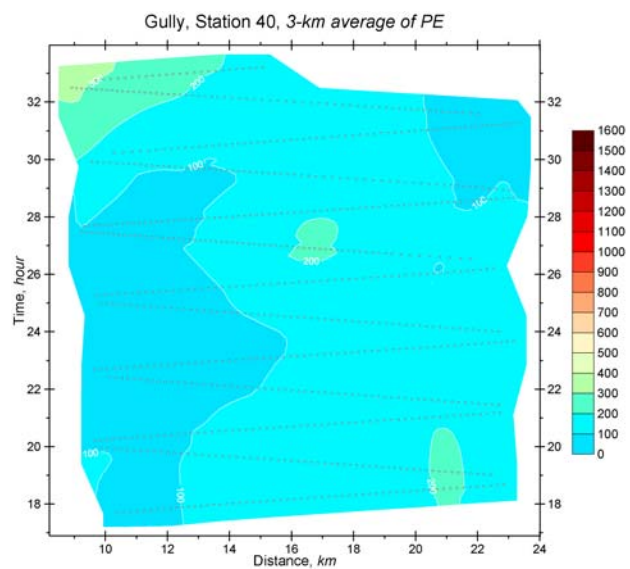


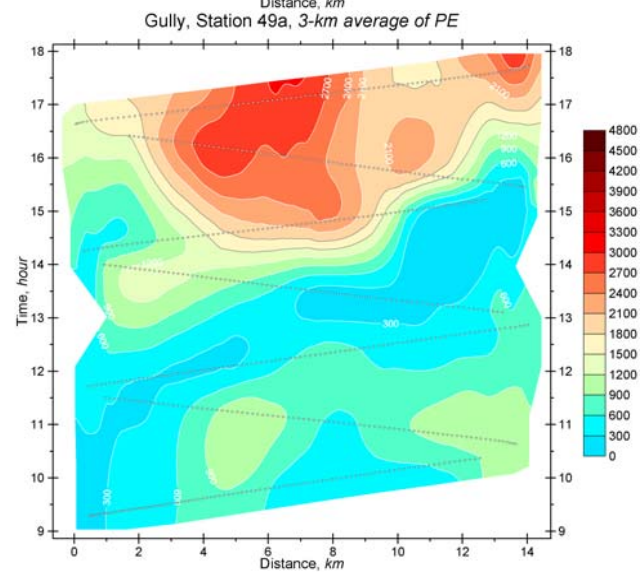
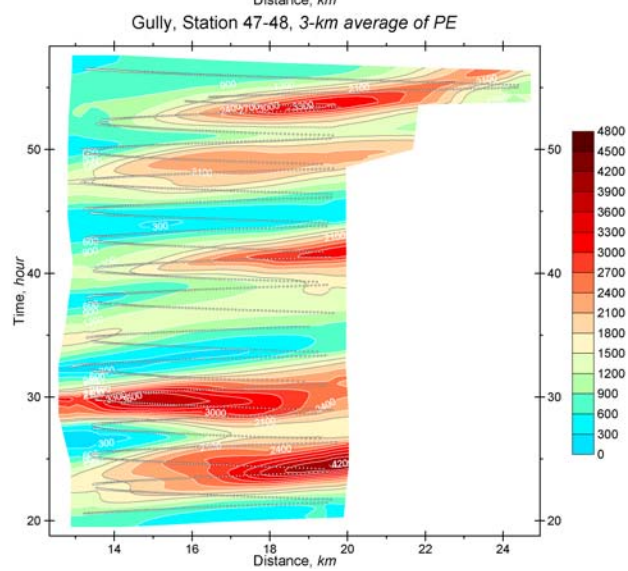
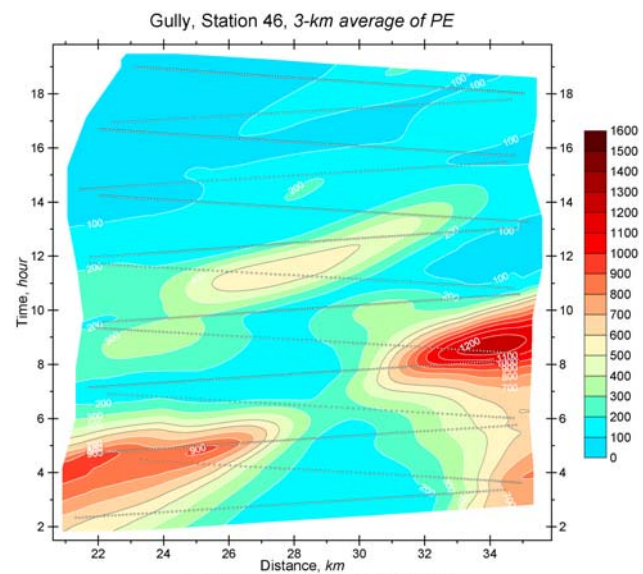
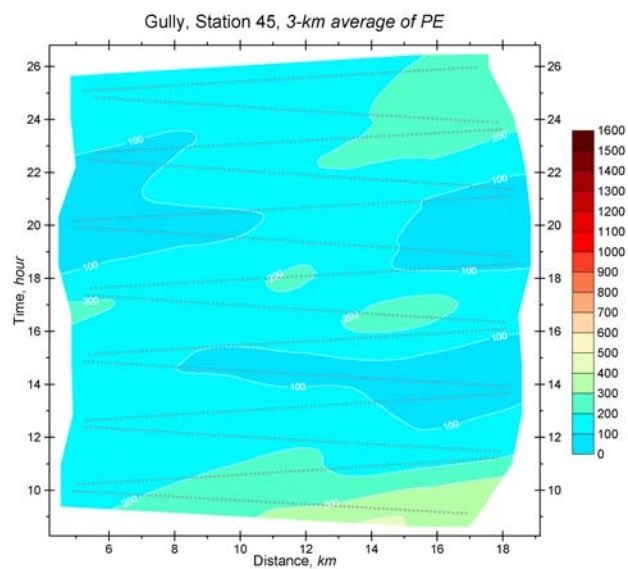


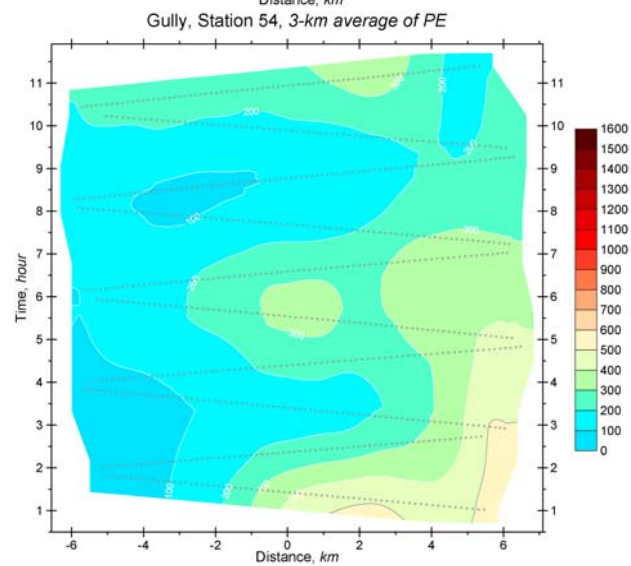
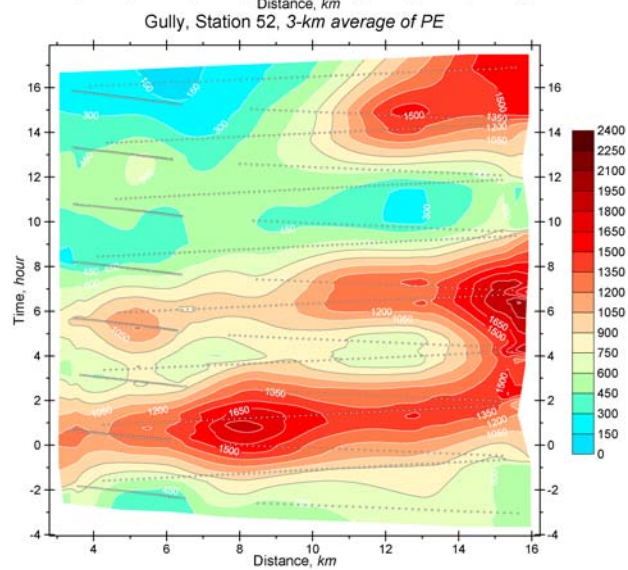
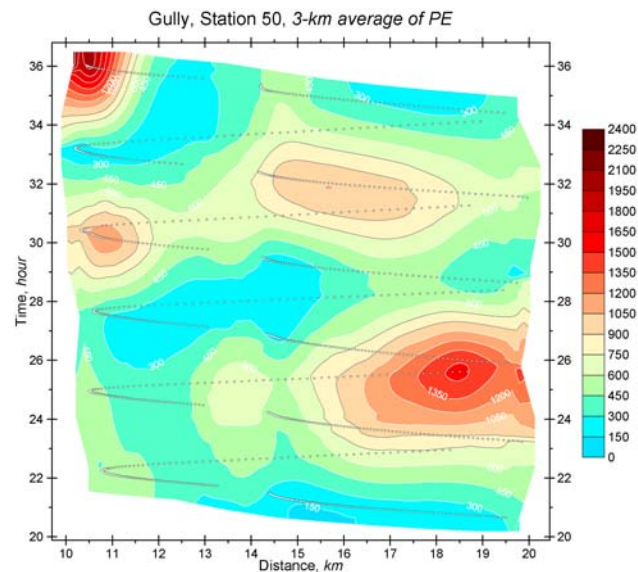
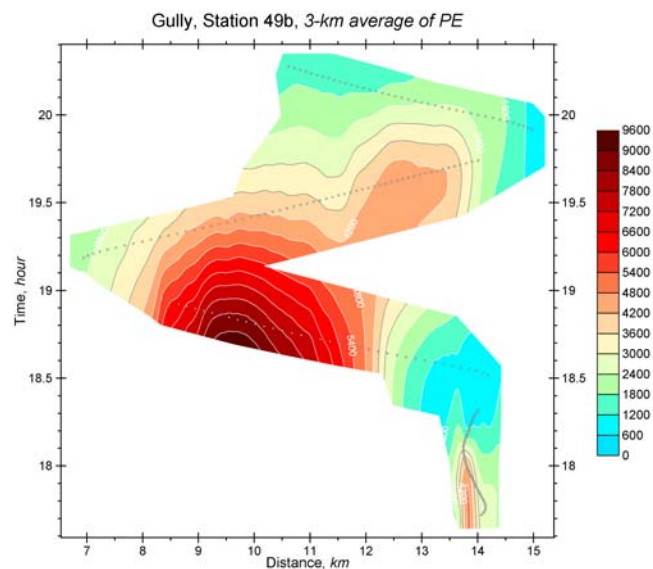




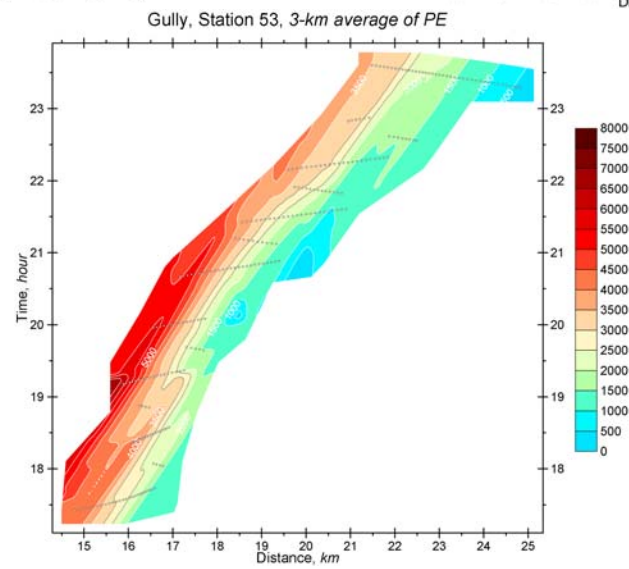
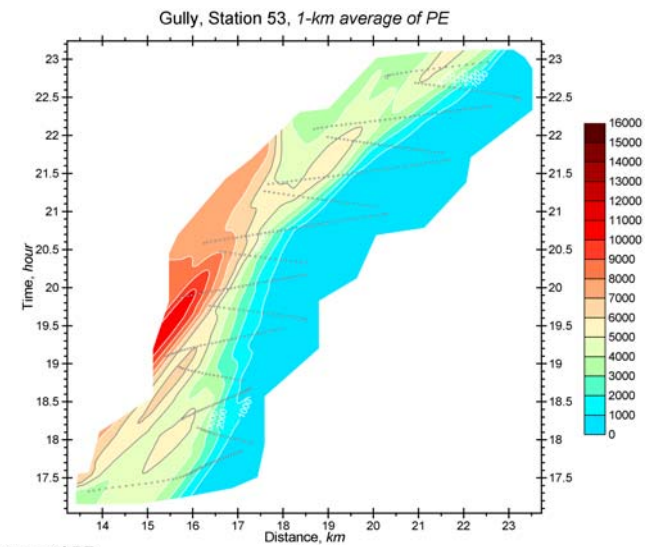
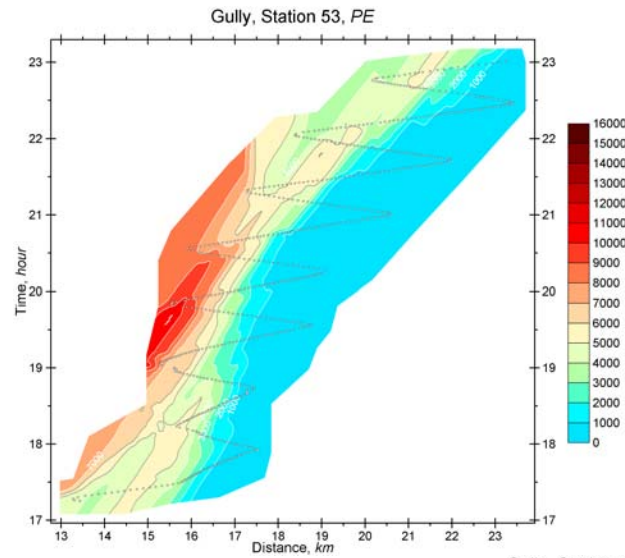




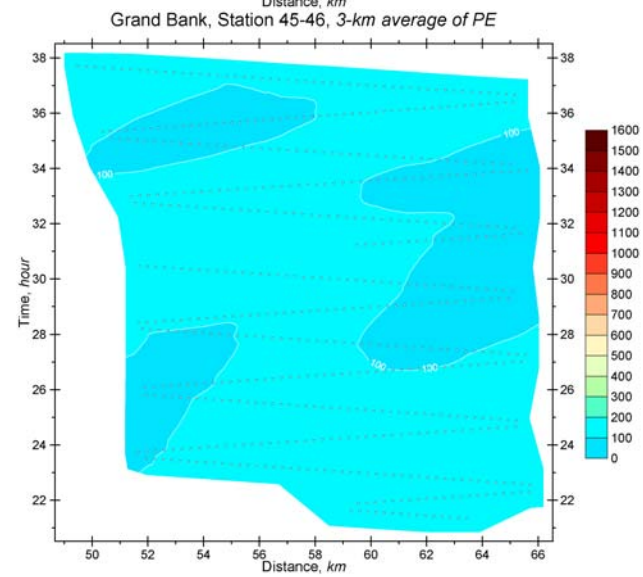
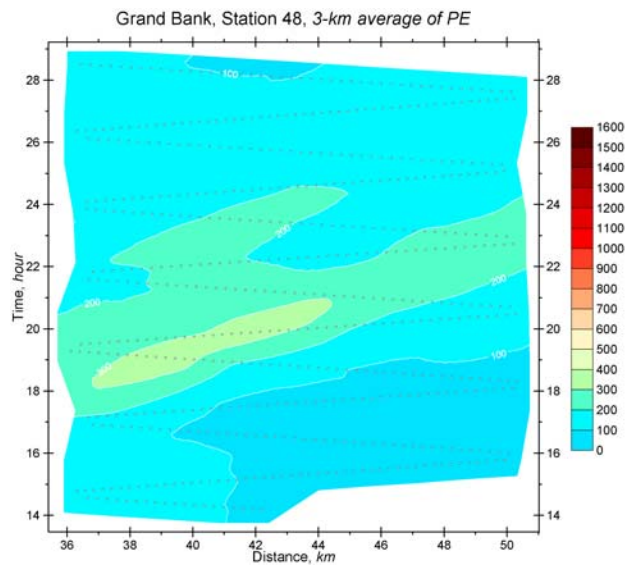
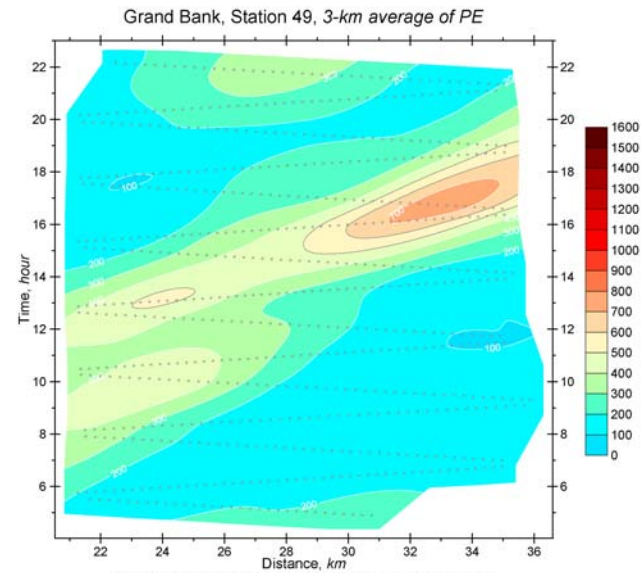
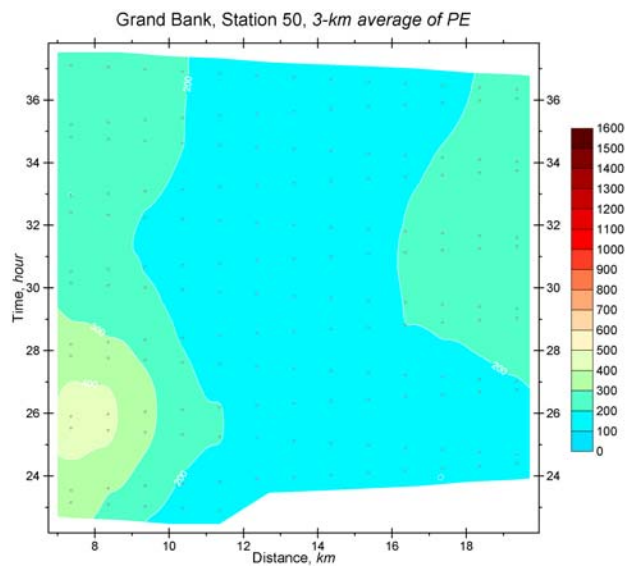


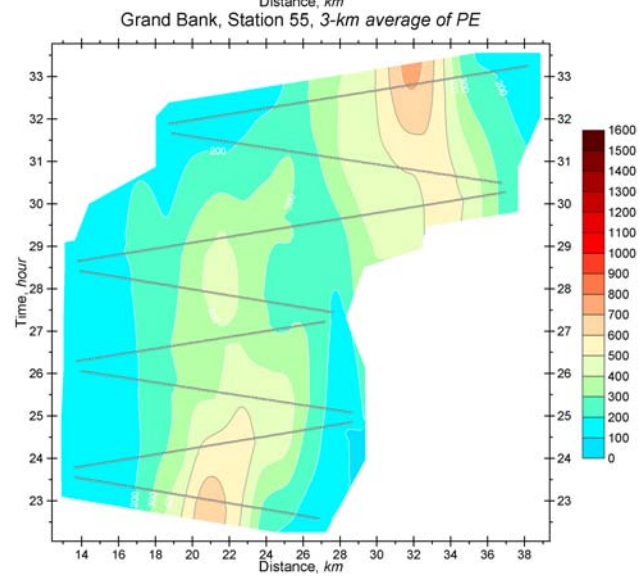
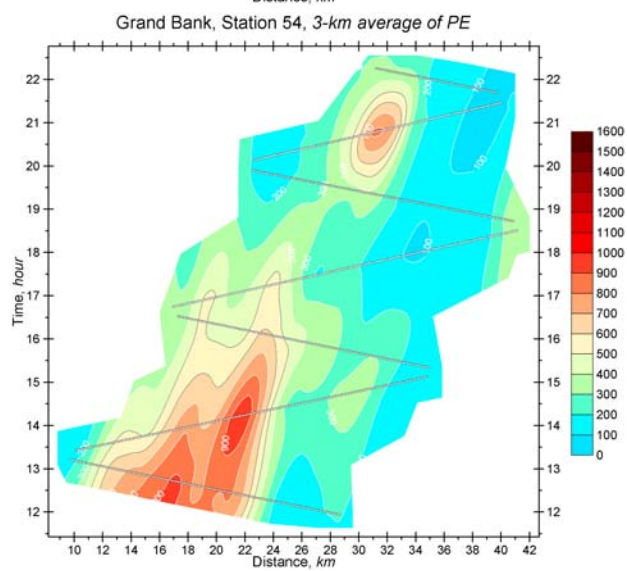
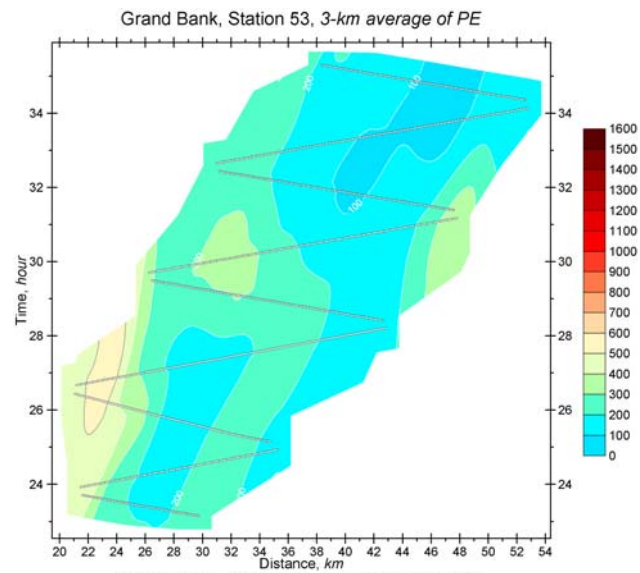
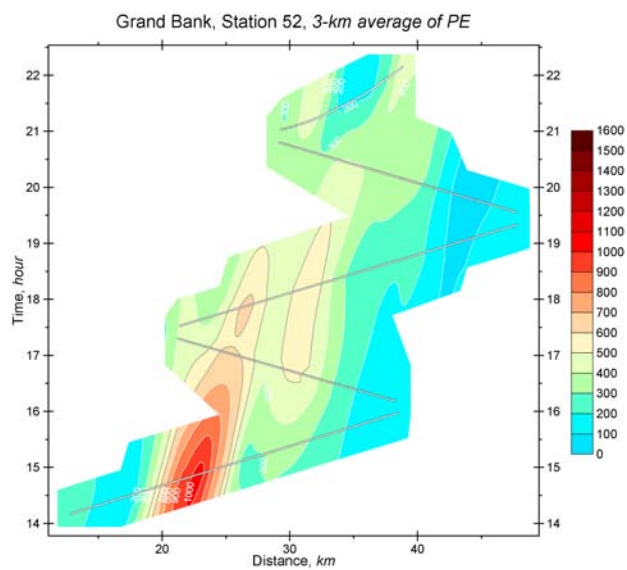


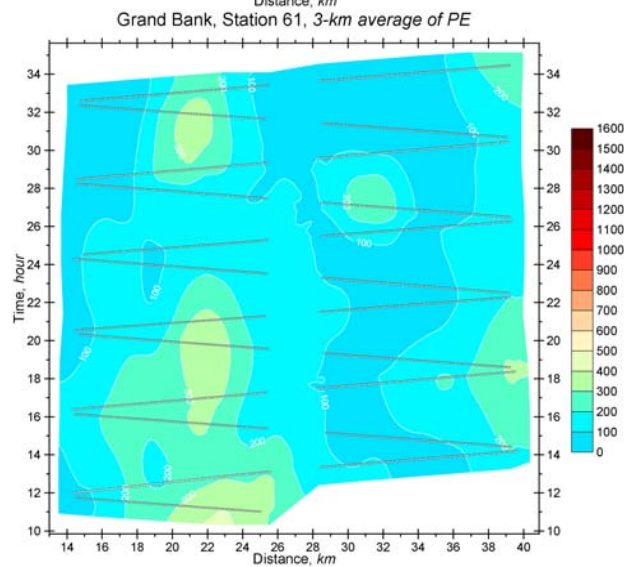
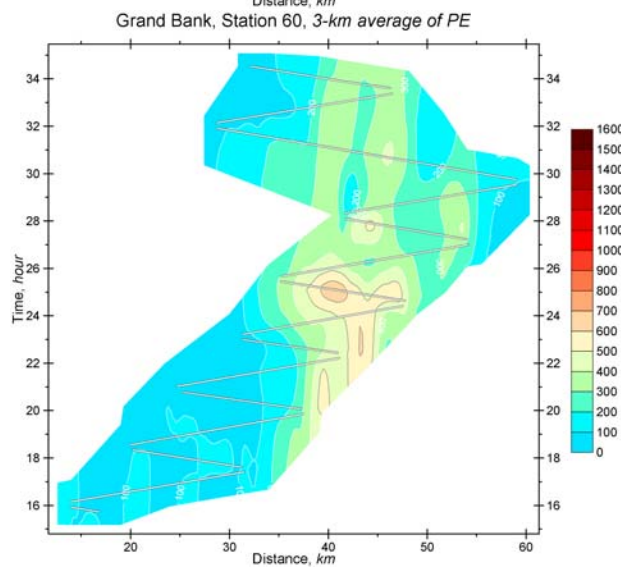
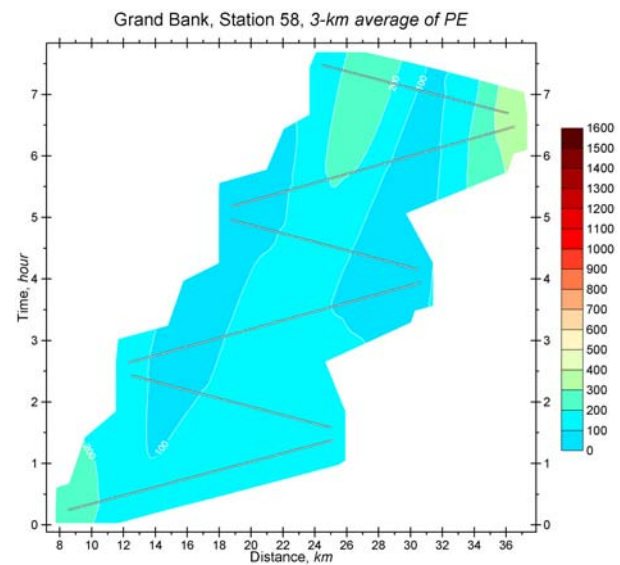
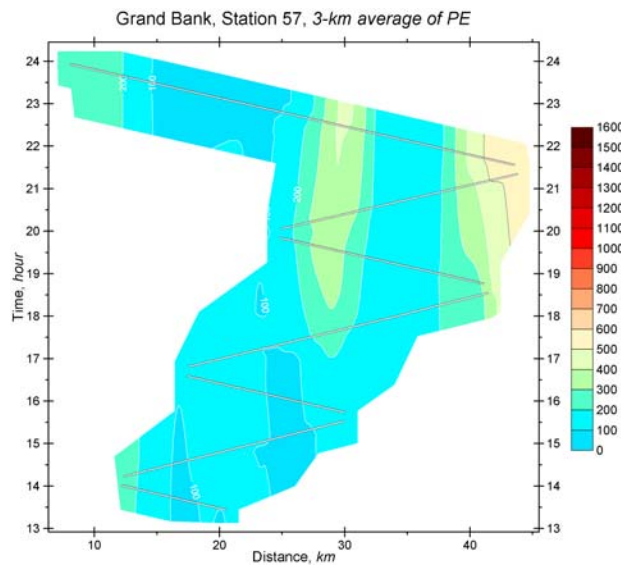












## Appendix 6 Forcing Functions

For modelling of the interaction of barotropic current flux with topography and generation of a baroclinic response (Section 6, equation (6.1,10)), we required the following input fields: current flux  $Q(t)$ , bathymetry  $h(x)$  and the mean density field expressed as  $\sigma(x,z)$ . These fields would also suffice for more complex two-dimensional interaction models than the one used in this report. Of the three sites, The Gully area is clearly three-dimensional from a modelling point of view and therefore outside the scope of the simple model. The development of the forcing functions will therefore only be carried out for the Scotian Gulf and the Grand Bank sections.

Of the input fields, the depth  $h(x)$  and its derivative  $\nabla(1/h(x))$  are invariant for a bathymetric cross-section. These are shown in Figure A6.1 for Scotian Gulf at  $63^\circ 30' W$  longitude as part (a), for Grand Bank at  $47^\circ N$  latitude as part (b) and for comparative purposes on the two sides of The Gully, namely for the Sable Island Bank at  $59^\circ 30' W$  longitude as part (c) and for three sections across the south-west and south-east slopes of Banquereau Bank (see Figure 5.1.1 in section 5) as part (d).

The mean density field  $\sigma(x,z)$  was constructed primarily by analysis of Batfish time series data as discussed in section 3.4 and augmented by CTD data outside the depth-range of the Batfish (generally  $-100 < z < -10$  m). Undoubtedly the CTD density data includes instantaneous variations from the mean field, but the effects of these variations, being at depths where the density gradient is small, are also small in the derivation of eigenfunctions, propagation speeds and the function  $v(x)$ <sup>7</sup> (6.1,9). In Figure A6.2(a) the density field  $\sigma(x,z)$  for the Scotian Gulf is shown together with the bottom depth. The range of isopycnals is between 22.4 and 27.8 and they are shown 0.1  $\sigma$ -units apart. The eigenfunctions and eigenvalues were obtained by solving the linear ODE (6.1,2) for a number of positions on the slope and the shelf. Eigenvalues at these positions yield the appropriate propagation speeds. The product of  $v(x)$  and  $\nabla(1/h(x))$  forms  $ff(x)$ , the  $x$ -dependent part of the rhs of (6.1,10). The function  $ff(x)$  is depicted in Figure A6.2(b) for the Scotian Gulf and Grand Bank. In Figure A6.2(c) the integrals of  $ff(x)$  are shown.

For current flux  $Q(t)$  the decision was made to use measured current at both sites (cf. comparison of measured and modeled currents in Appendix A7). At both sites the current meter moorings were some distance inshore from the principal generation area. The current meter locations are shown with stars in figures A6.1 (a) and (b). In the Scotian Gulf the mooring 585 is closest to shelf edge. The semi-diurnal current, especially the NS component is consistent at all four functioning current meters (at 45, 72, 96 and 144 m depths). The current at 72 metres depth represents the average current of all four meters very closely, and hence the current at 72 m depth was multiplied by the water depth at that location to yield  $Q(t)$ .

On the Grand Bank the mooring 698 is closest to the shelf edge. Here we consider the EW current component as input for  $Q(t)$ . However, the uncertainties of determining  $Q(t)$

---

<sup>7</sup> In the case of two different density layers,  $v$  is the depth of the interface. For more general stratifications,  $v$  for the fundamental mode is approximately the depth of maximum modal displacement.

are greater than in the Scotian Gulf. The mooring 698 was farther away from the principal generation area than for mooring 585 and the currents are weaker and less consistent. The currents at mooring 699, which is separated from 698 by about the same distance as the generation region, are also different than those at mooring 698, adding to the uncertainty. Still, the best available option was to use the EW current component at 32 m depth multiplied by the water depth as  $Q(t)$ .

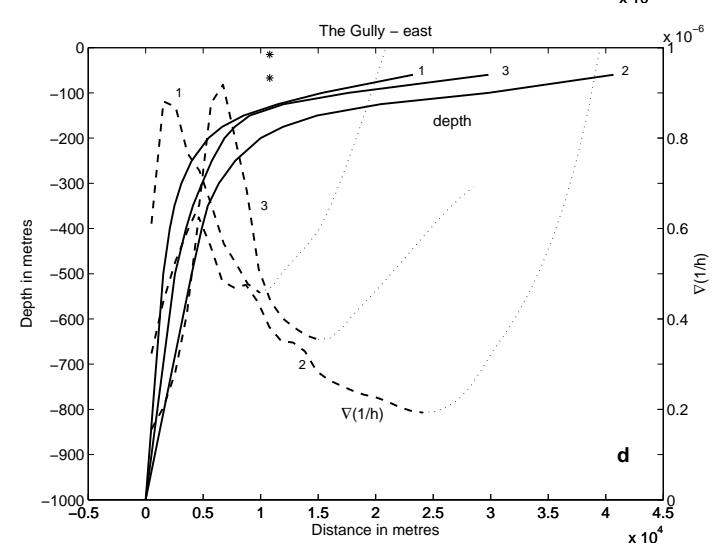
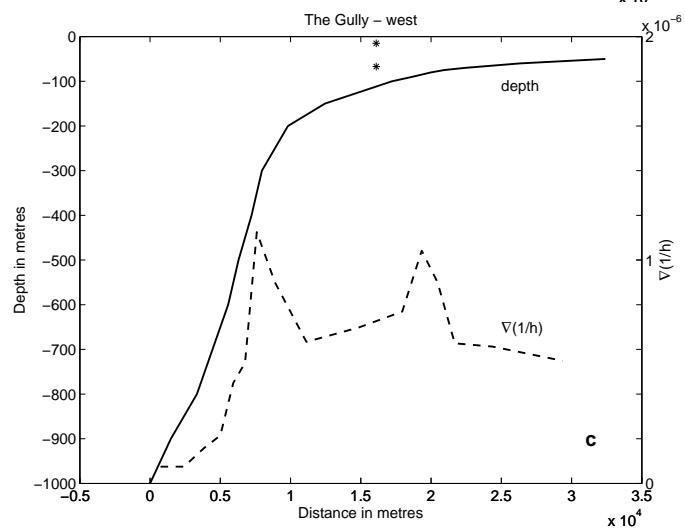
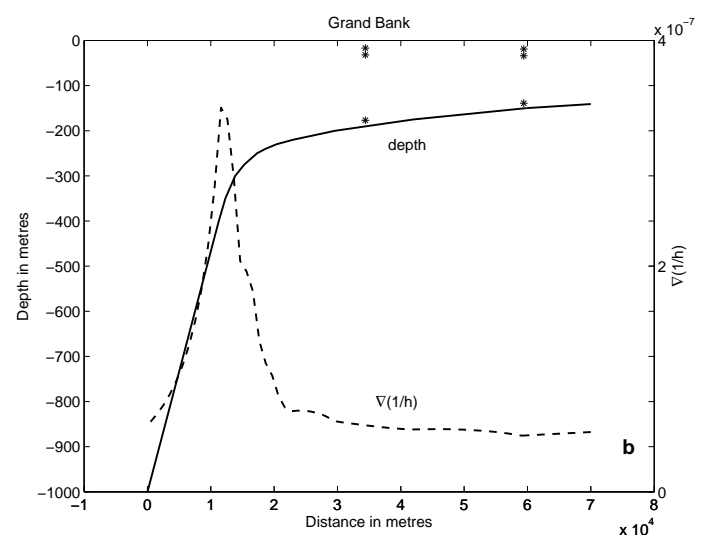
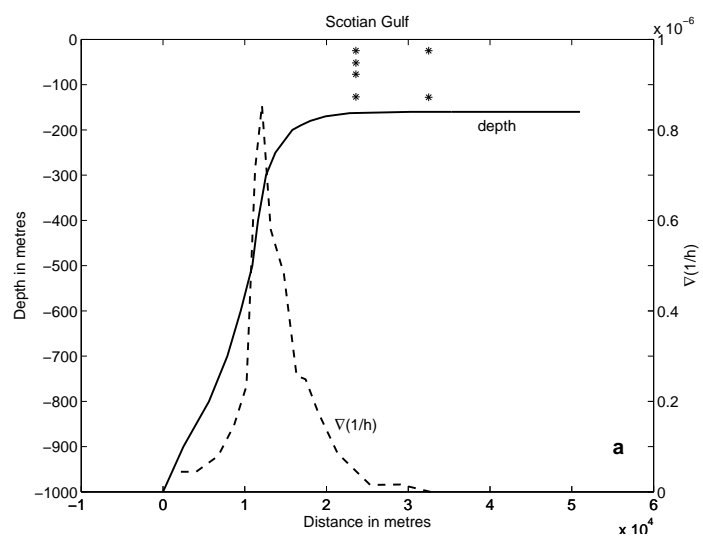


Figure A6.1: Depth  $h(x)$  and  $\nabla(1/h(x))$

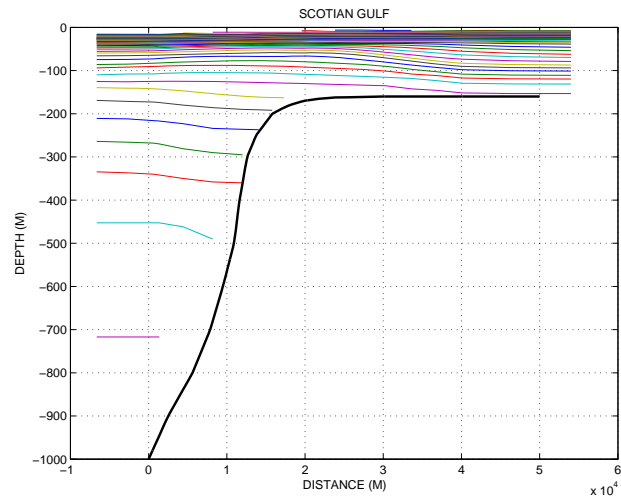


Figure A6.2(a)

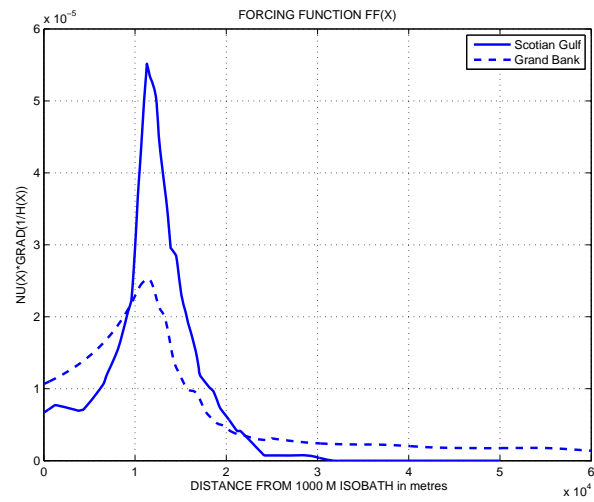


Figure A6.2(b)

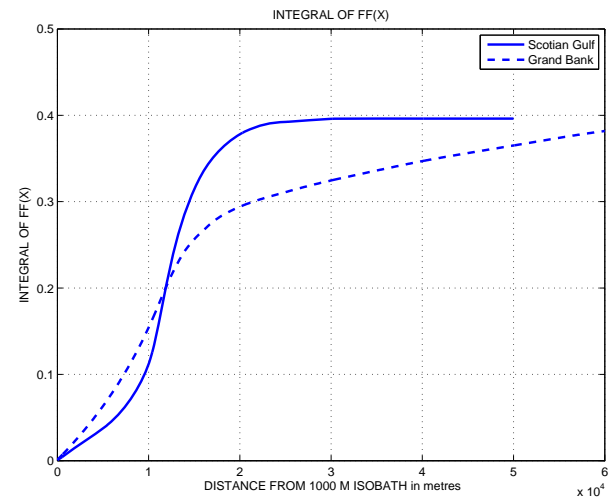


Figure A6.2(c)

## Appendix 7 Current Meters and Analysis of Currents

At all three sites we deployed current meter moorings for the duration of each study. The technical details and an overview of current data is found in the four data atlases (Canadian Technical Report of Hydrography and Ocean Sciences, No.'s 77, 114, 117 and 121)<sup>8</sup>. In the present discussion the data from apparently properly functioning current meters only are considered. At each site two moorings were deployed, with meters generally both in the surface mixed layer and at depth. The sampling rates of the meters were set depending partly on the conditions at a given site and partly on the type of current meter used. Thus at the Scotian Gulf site we used Vector Averaging Current Meters (VACM's) at 29 m and 45 m depth on moorings 584 and 585 respectively, with an averaged sample every 15 minutes. The other meters were the Aanderaa type, set to sample every 2 minutes. At the Grand Bank site all meters were of the Aanderaa type, again sampling every 2 minutes. At The Gully site the two moorings, one on each side of The Gully, had current meters of the Aanderaa type at depths of 15 and 67 m sampling every 5 minutes. The 2 minute sampling rate was adopted in order to resolve the high amplitude but short (both in space and time) internal waves, although at The Gully site, as a compromise between resolution and current meter battery life, a 5 minute sampling rate was used.

In processing the current meter data, generally the EW and NS components are treated separately and recombined when that is needed.

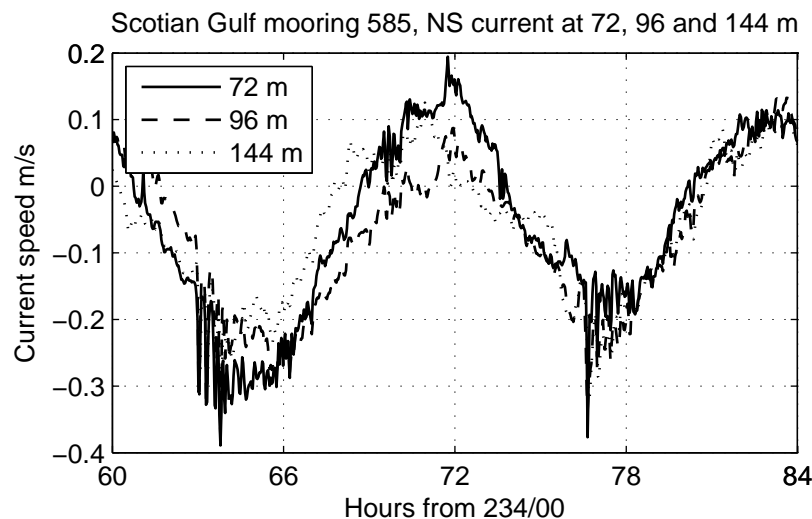


Figure A7.1: Current meter data from the Scotian Gulf site.

Figure A7.1, a sample of the data, depicts the measured northerly current at three current meters (depths of 72, 96 and 144 m) over a 24 hour period at mooring # 585 at the Scotian Gulf site. The figure illustrates the presence of the high frequency current bursts

<sup>8</sup> In report # 114 the current meter depths at mooring 585 are incorrect. The depths given as 25, 27, 52, 77, 102 and 127 metres should be replaced by 45, 48, 72, 96, 120 and 144 metres. Similarly the depths at mooring 584 should be 29, 31 and 132 m.



of approximately 2 hour duration associated with the longer period (in this case predominantly semidiurnal) tidal scale motion.

To separate the high and low frequency components, a Butterworth high-pass filter was applied to a current record, with the cutoff frequency of  $\sim 0.5$  cph. The high frequency part of the record was not processed any further, but was used in conjunction with Batfish observations to understand the characteristics of the high amplitude (solitary) wave groups, especially at times when Batfish sampled in the vicinity of a particular current meter mooring.

The procedure adopted for determining the tidal frequency components in the record, was the following:

1. A discrete Fourier transform of the record, computed with a fast Fourier transform (FFT) in the MATLAB environment, is obtained. The periodograms are displayed in Figures A7.2-4.
2. A dominant component is determined (in all records it is either the diurnal, inertial or semidiurnal component).
3. A complex demodulation is performed to extract the dominant component. This involves shifting the appropriate frequency to zero by multiplying the record with cosine and sine at that frequency and lowpass filtering of the results. A Butterworth lowpass filter is used. Care was needed in choosing a cutoff frequency, since the separation of the inertial component from the two major tidal components is  $\sim 0.5$  cpd. A cutoff frequency of about half that value is used. Another problem with the Butterworth filter with such a low cutoff frequency is the tapering off of the result particularly at the far end of the data record. This problem is to a great extent overcome by reversing the data record and performing the complex demodulation on the reversed record and then recombining the results of the original and reversed records by joining parts of both.
4. A new data record is formed by subtracting the result of step 3 from the earlier data record and steps 1 – 3 are repeated.

For all current meter records at all three sites the diurnal, semidiurnal and inertial components were extracted. The remainders had in general some energy at very low frequency ( $< 0.5$  cpd) and varying amounts of energy at higher frequencies, i.e. M3 (and or MO3, MK3, etc), M4, but also at beat frequencies between the major tidal and inertial components. Generally the higher frequency components had low energies, a notable exception being the current record from 15 m depth on mooring # 660 (Figure A7.3) on the eastern side of The Gully, in which the current amplitude at M4 frequency exceeds 0.1 m/s and at times is larger than the current at M2 frequency.

The relative strengths of the three major components at the three (or four, if west and east of The Gully are considered separately) sites vary considerably. This would be expected in the case of the inertial current *vis-à-vis* the tidal components, but the variation in the latter is also very evident. The relative strengths also vary depending on the depth of the current meter and on whether the EW or NS current is considered. Figures A7.2, 3 and 4 summarize the frequency content of both EW and NS current records at the three sites.

The power at various frequencies is plotted *versus* frequency, but since it is calculated for discrete frequencies, which in general do not coincide exactly with frequencies where power resides, the calculated power peak is an underestimate of the actual power. However, since the Discrete Fourier Transform is used only as an indicator of relative strengths of power in the spectrum, the discrepancy in the present context is of little importance.<sup>9</sup>

At the Scotian Gulf site (Figure A7.2) clearly the semidiurnal (M2, N2, S2, ...) tidal component dominates the spectrum, stronger in on/offshore (NS) than in the alongshore (EW) direction and stronger at the outer mooring (#585) than at the inshore mooring (#584). The presence of the diurnal component is more evident in the alongshore direction and the inertial current appears at the inshore mooring equally strong in both directions. The tidal current variations with depth will be discussed in conjunction with comparisons of the demodulated signal with currents predicted by a model (WebTide).

The current at The Gully site (Figure A7.3), both west (mooring #659) and east (mooring #660) of The Gully, contains strong diurnal and inertial components in addition to a semidiurnal component, any one of the three being the strongest at a given depth or current direction.

On the Grand Bank (Figure A7.4), the inertial component dominates at the outer (#698) mooring and is strongly present at the inshore (#699) mooring. The semidiurnal component is stronger again in the on/offshore (EW) direction and the diurnal component is relatively strong at the inshore mooring.

Figures A7.5 to 10 show the diurnal and semidiurnal current components at all six current meter moorings (two at each site), with EW current on the left and NS current on the right in each figure. For each mooring two or more current meter records from different depths have been included. Also included in each figure is a tidal model (WebTide) derived current (see Dupont et al. 2002) at each mooring site. One reason for including the comparison was to investigate the feasibility of using the tidal model derived current as an input in our internal tide generation modelling, arguing that if the comparisons were favourable at our current meter moorings, the model results could be used as a proxy for tidal flux,  $Q$ , calculation in the internal tide generation region. This turns out not to be the case. Even in the case of most favourable comparison, namely at the Scotian Gulf site, there is a discrepancy between the measured and modelled currents, although quite good agreement is found in the phases of both the diurnal and semidiurnal tide. The largest discrepancies in current (also in phase) are found at the Grand Bank moorings and are large on both sides of The Gully. The discrepancy on the Grand Bank was noted by Dupont *et al* (2002). Our decision therefore was to use the measured semidiurnal current in estimating the tidal flux  $Q$ .

---

<sup>9</sup> The power at any discrete frequency is equivalent to  $\frac{1}{2}$  of the amplitude of the component at that frequency squared and summed over the number of data points. If the amplitude of the component varies with time the power represents some average amplitude.

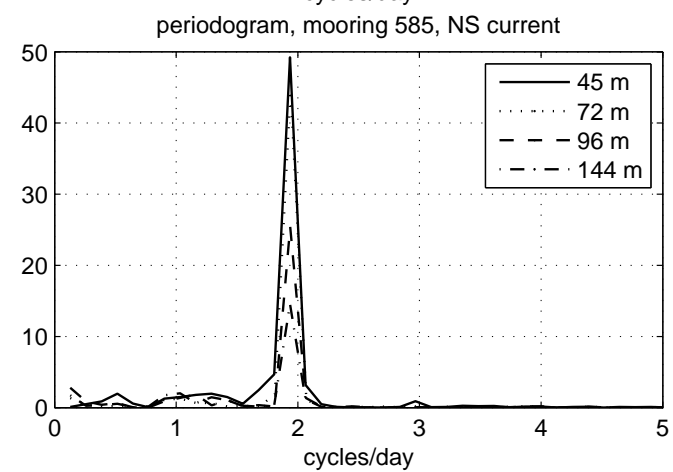
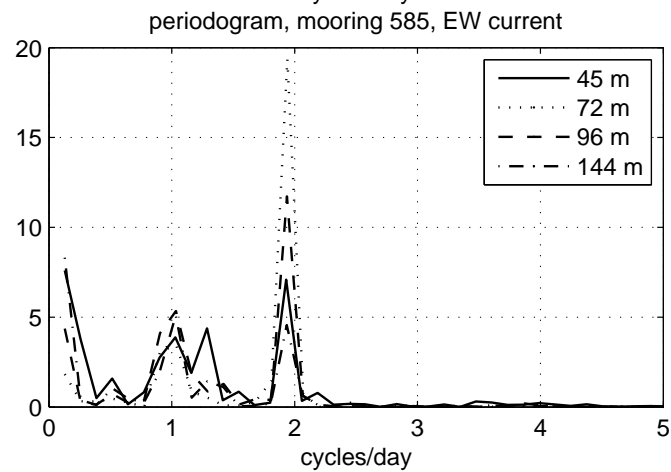
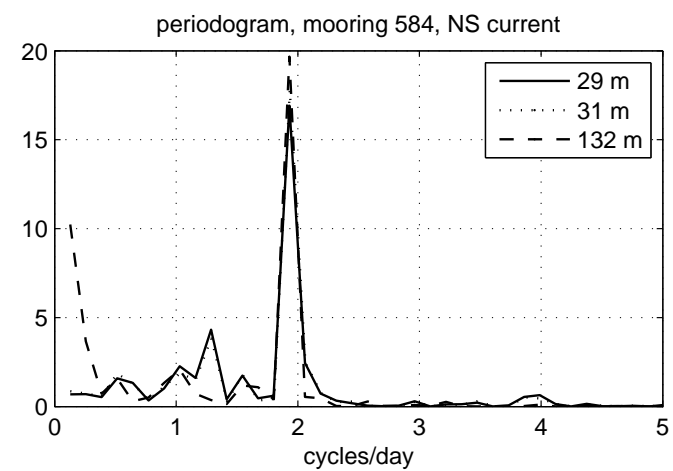
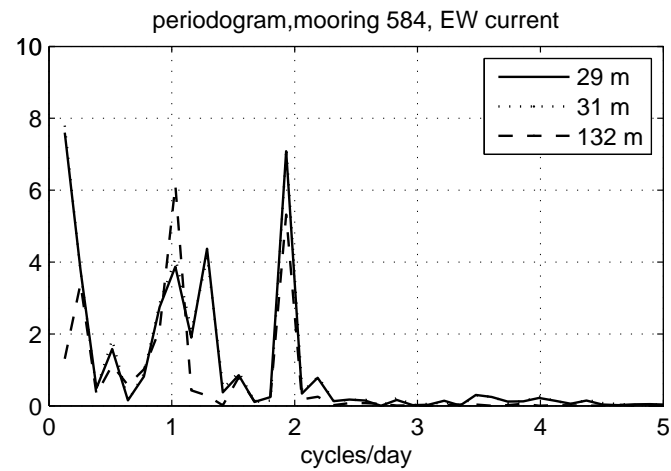


Figure A7.2: Periodograms of EW and NS components of currents from Scotian Gulf moorings 584 and 585.

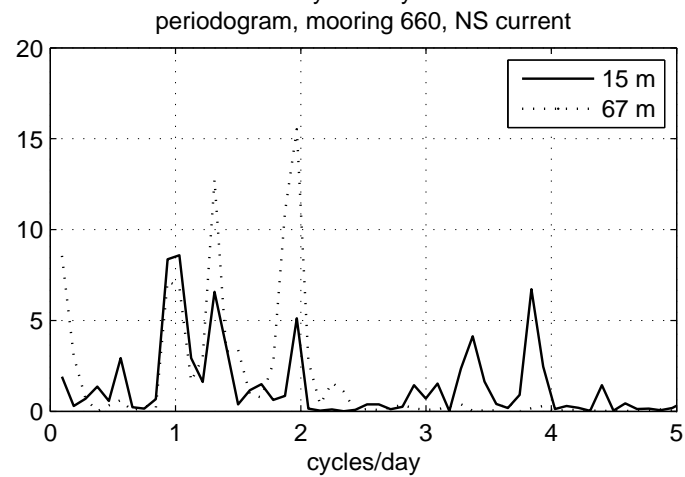
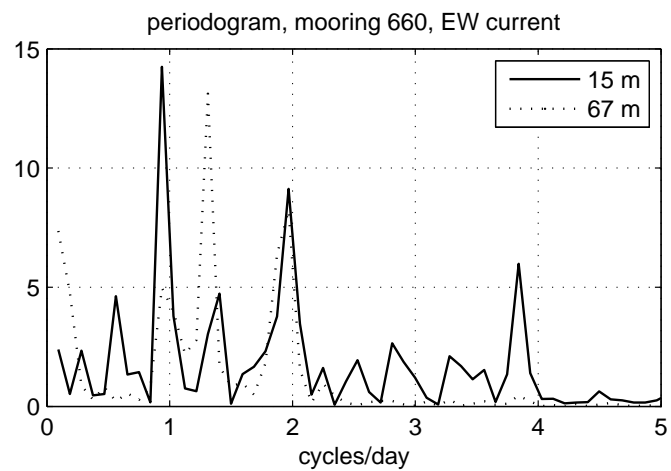
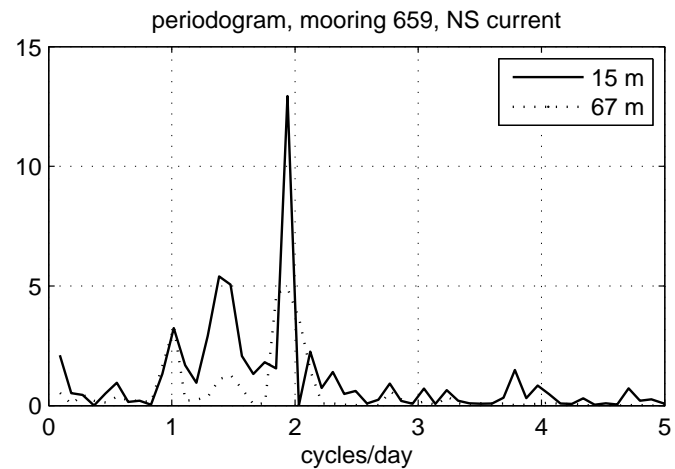
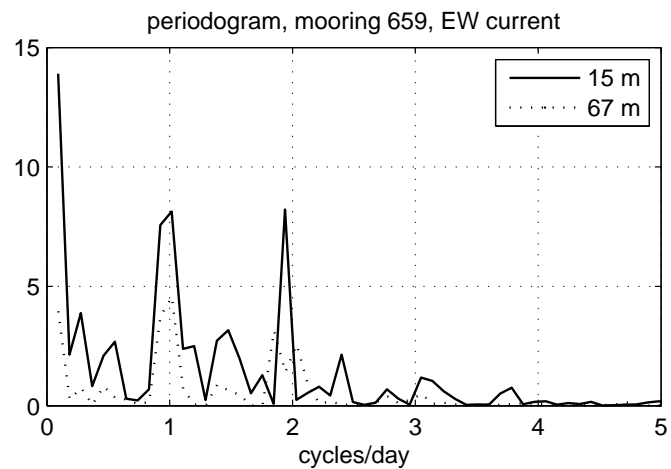


Figure A7.3: Periodograms of EW and NS components of currents. The Gully moorings 659 and 660.

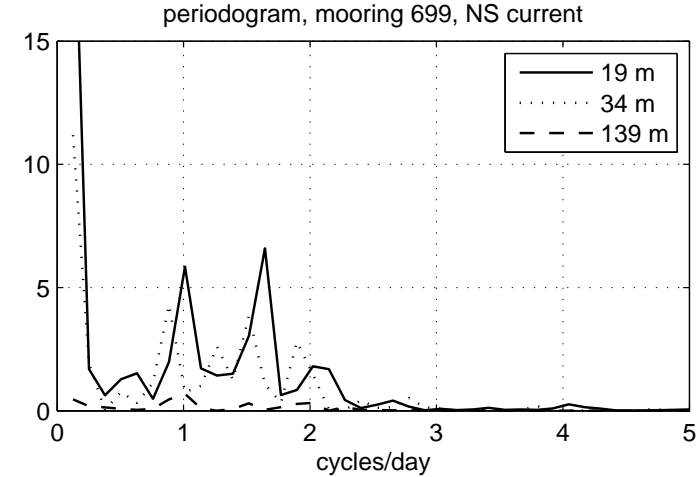
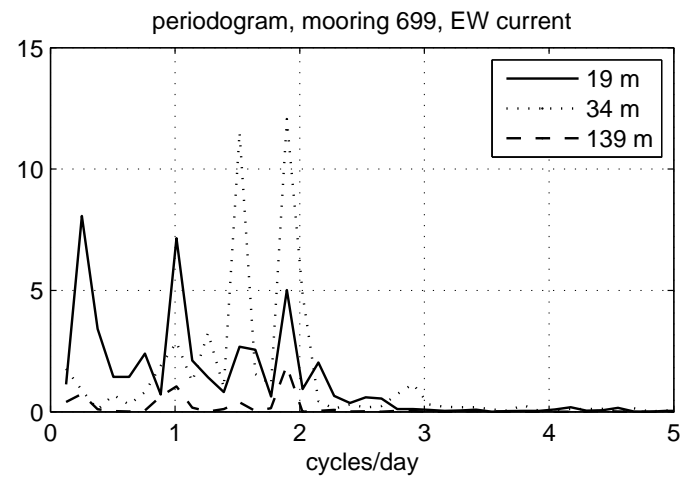
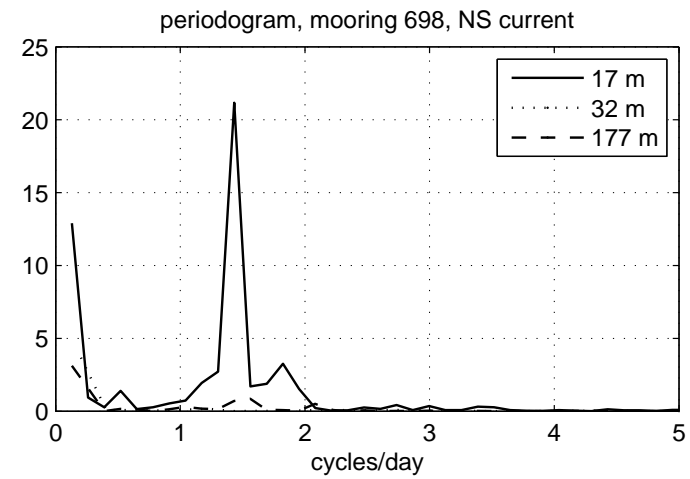
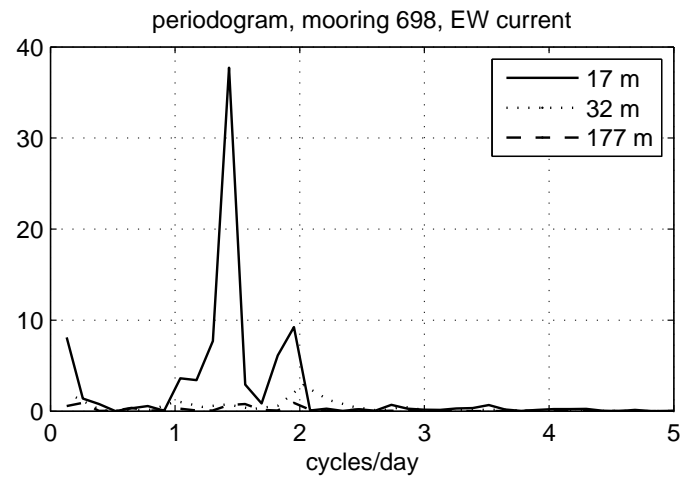


Figure A7.4: Periodograms of EW and NS components of currents from Grand Bank moorings 698 and 699.

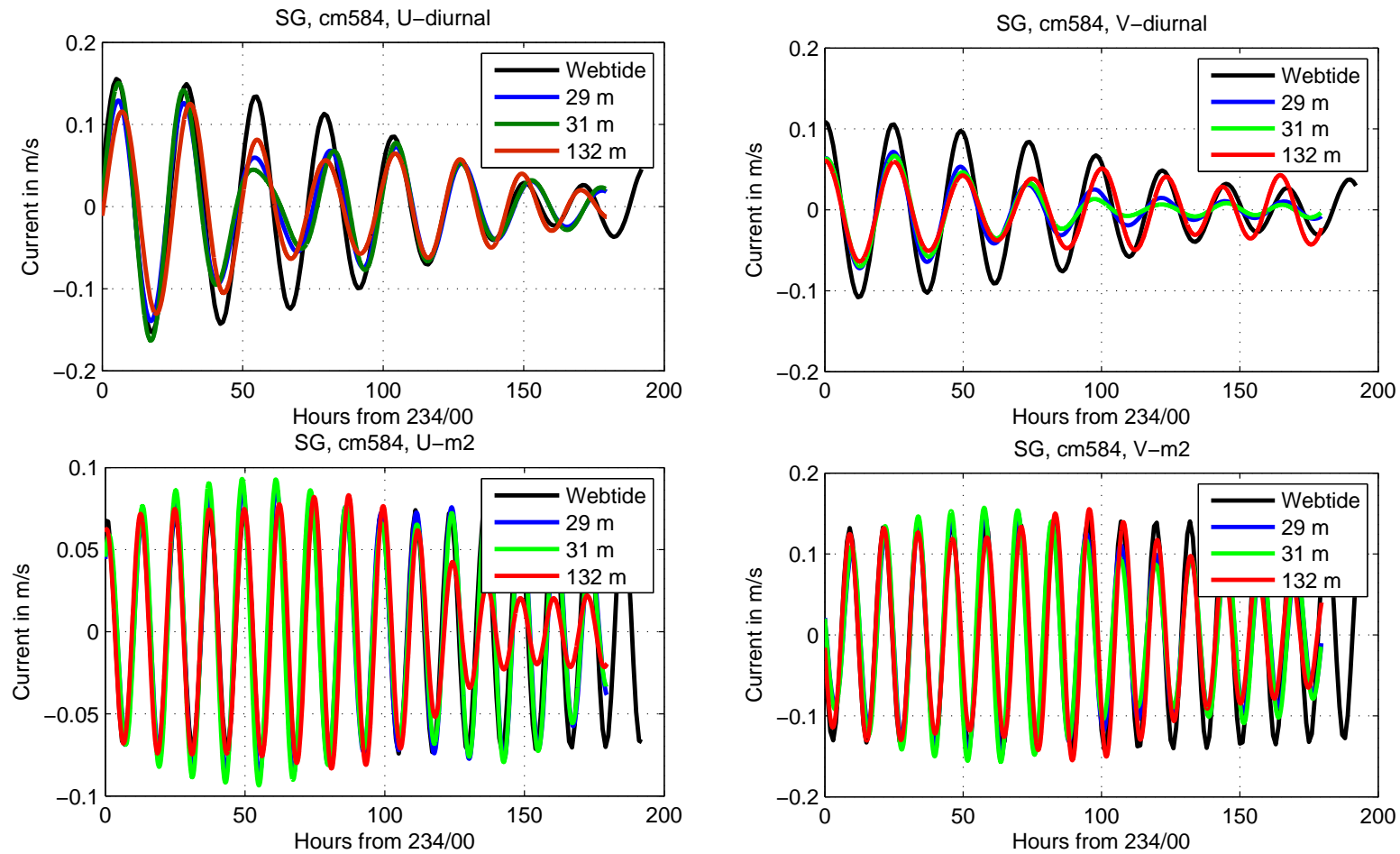


Figure A7.5: Diurnal and semi-diurnal current components at mooring 584 and barotropic current from WebTide.

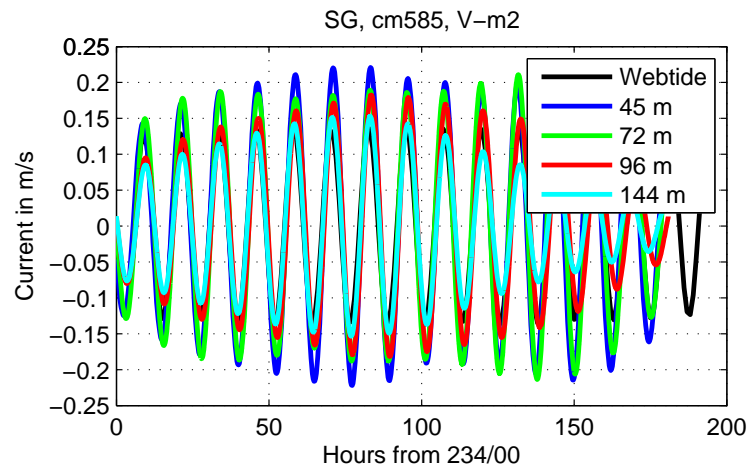
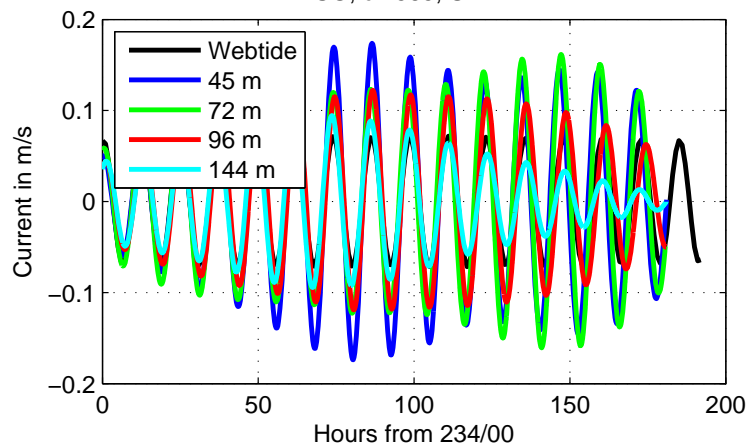
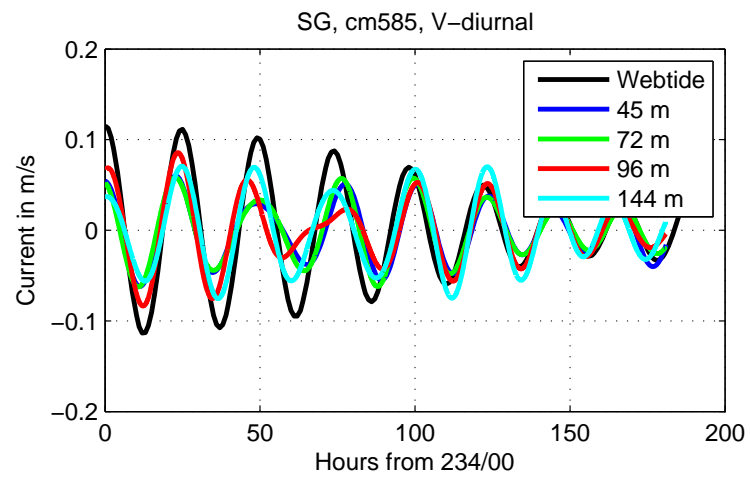
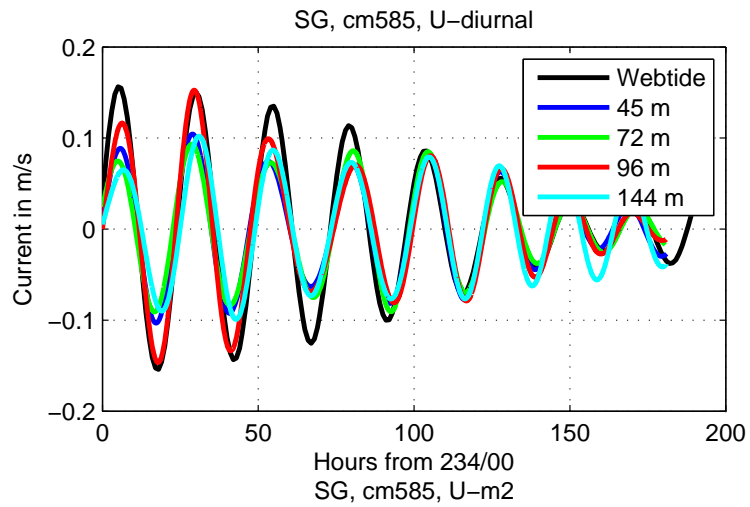


Figure A7.6: Diurnal and semi-diurnal current components at mooring 585 and barotropic current from WebTide.

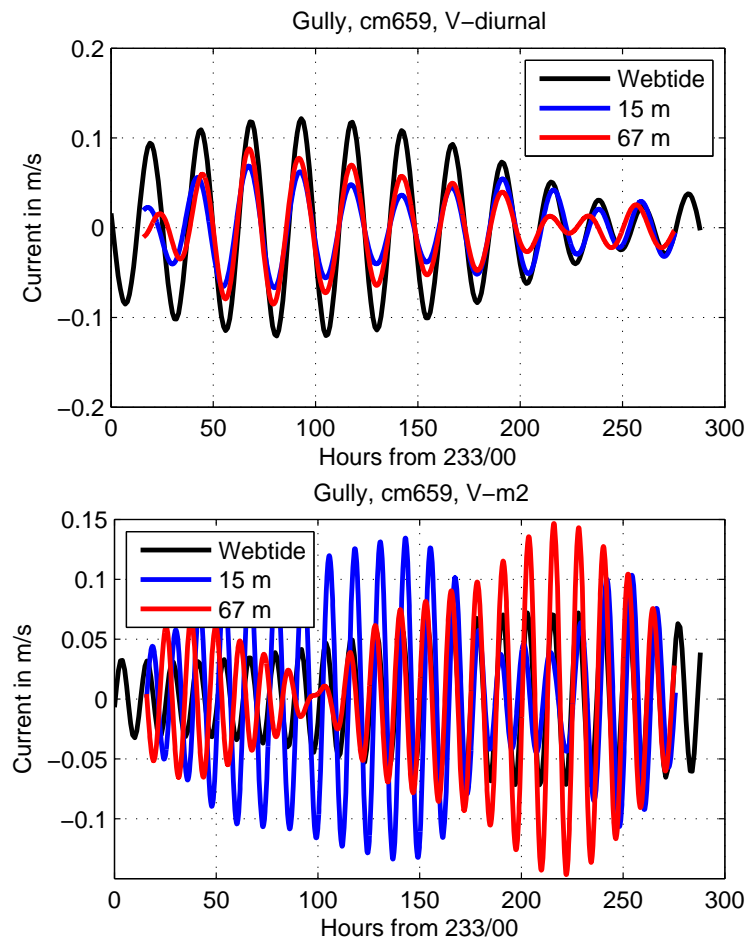
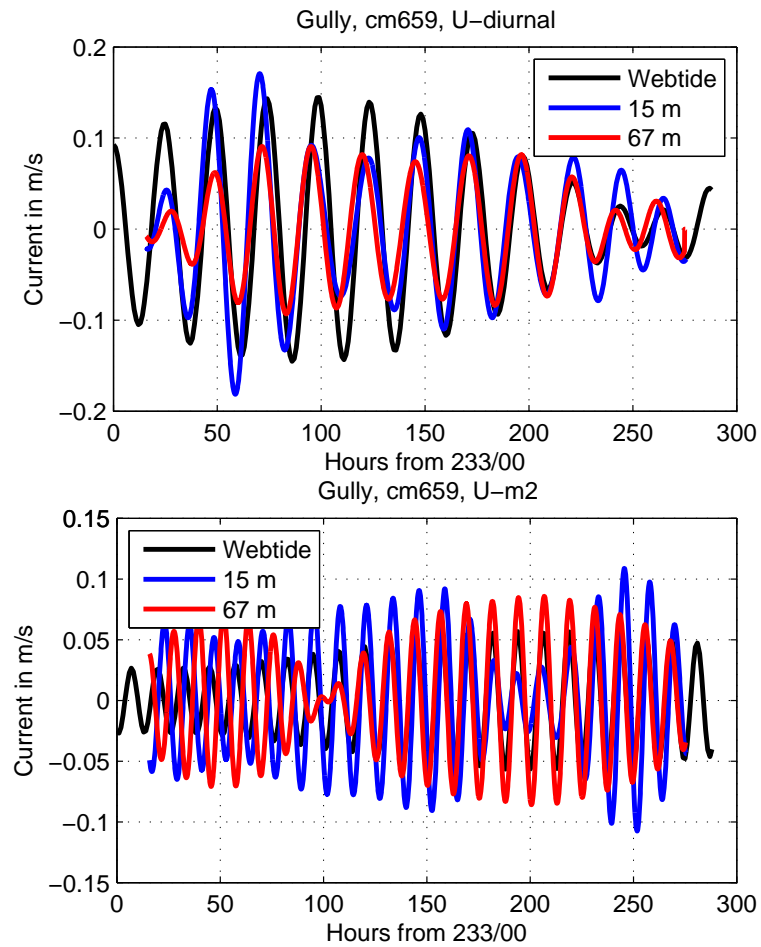


Figure A7.7: Diurnal and semi-diurnal current components at mooring 659 and barotropic current from WebTide.



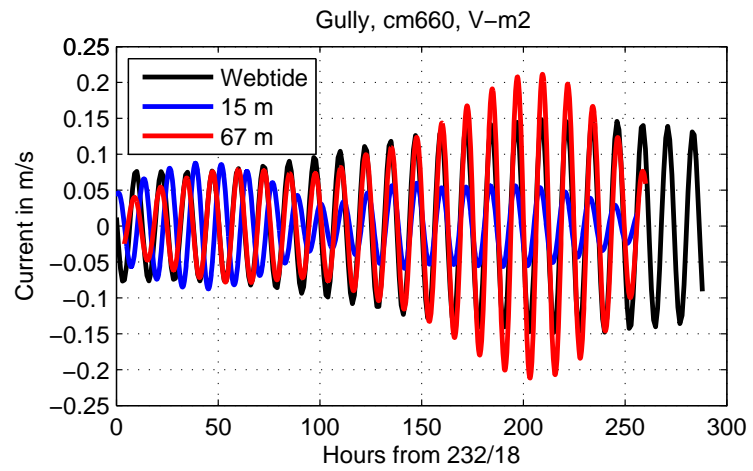
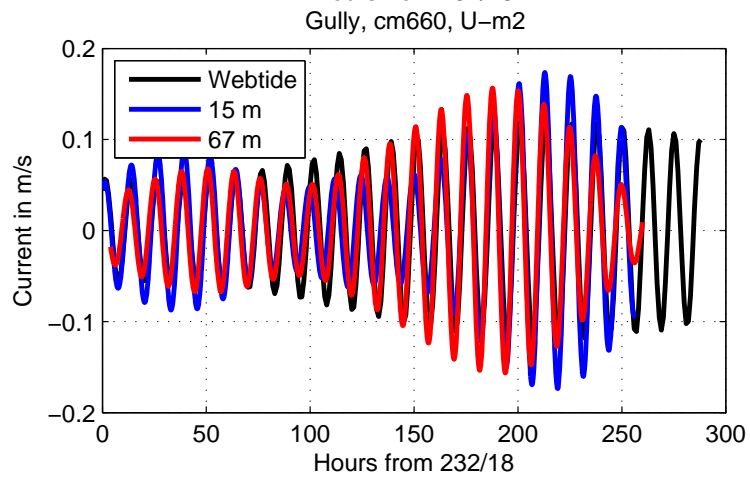
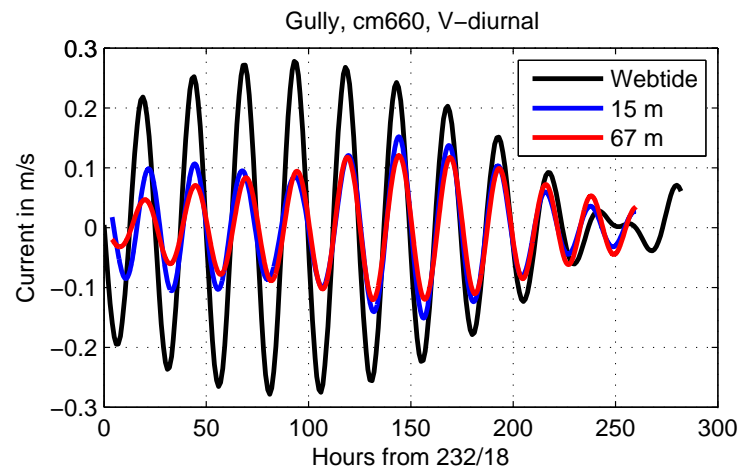
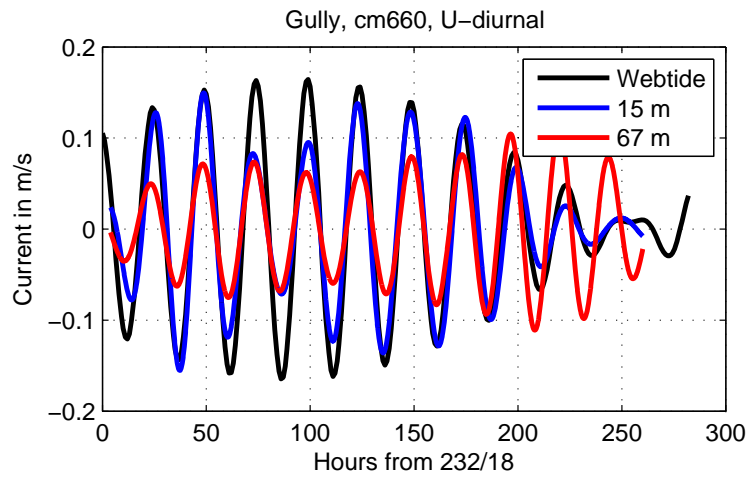


Figure A7.8: Diurnal and semi-diurnal current components at mooring 660 and barotropic current from WebTide.

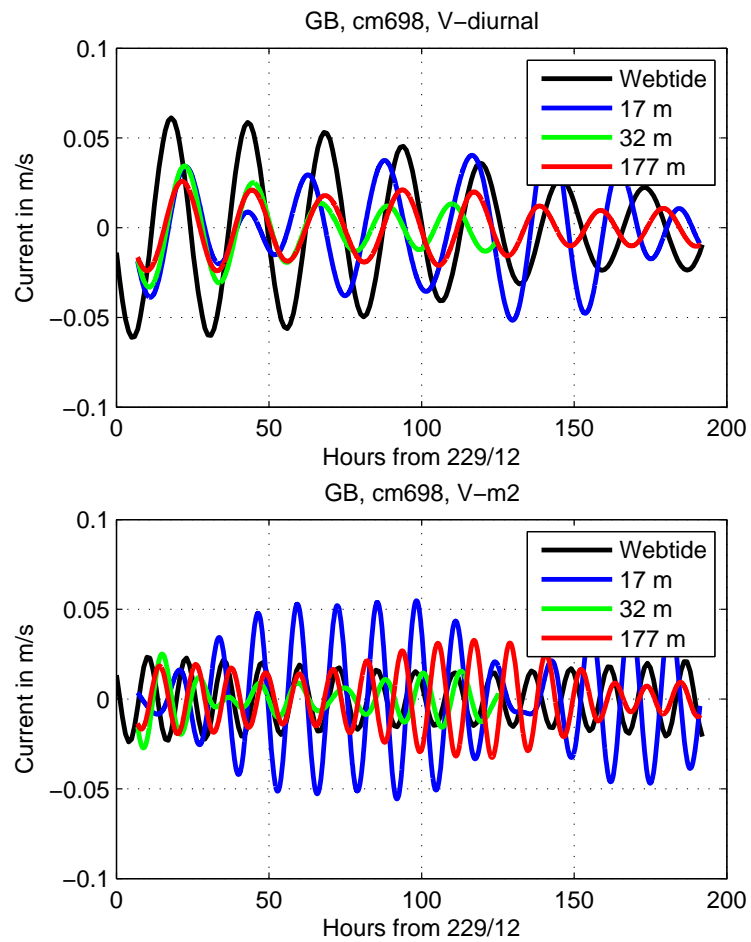
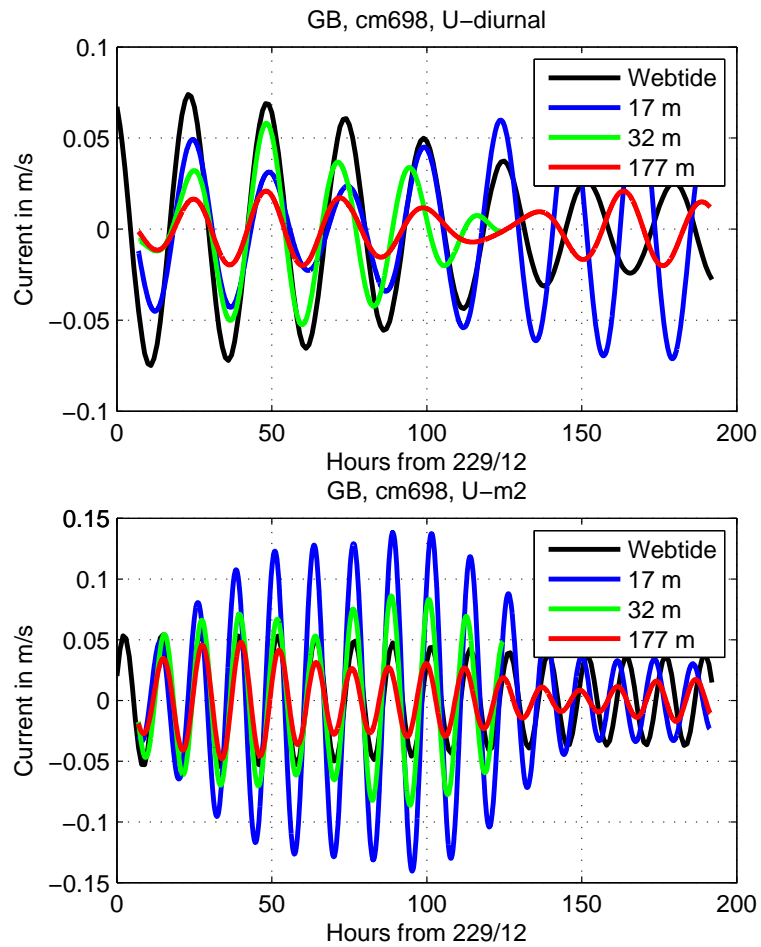


Figure A7.9: Diurnal and semi-diurnal current components at mooring 698 and barotropic current from WebTide.

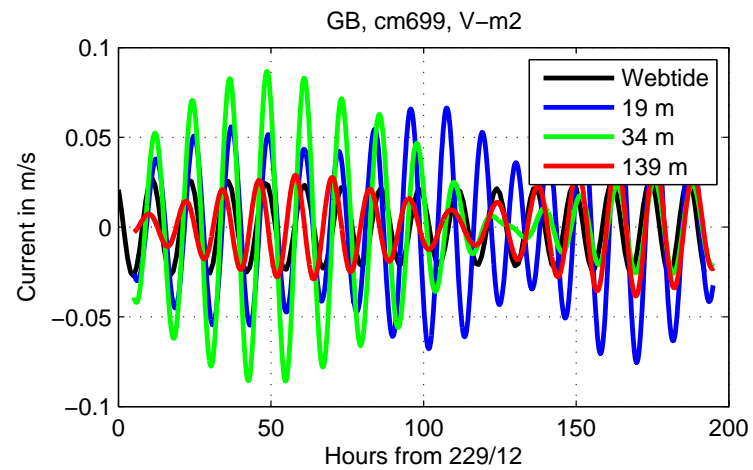
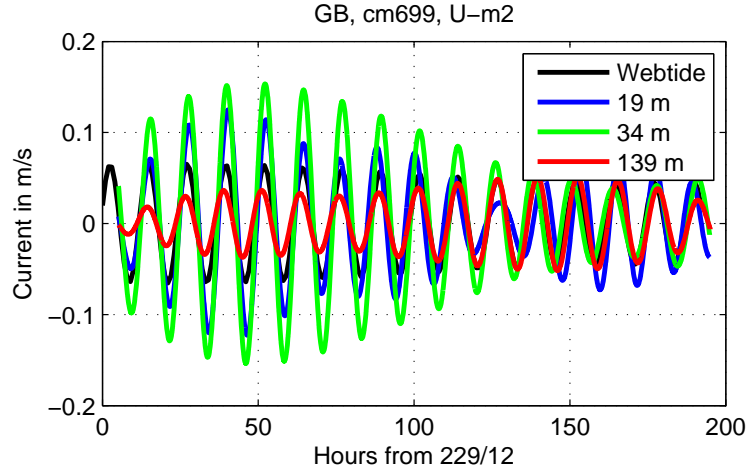
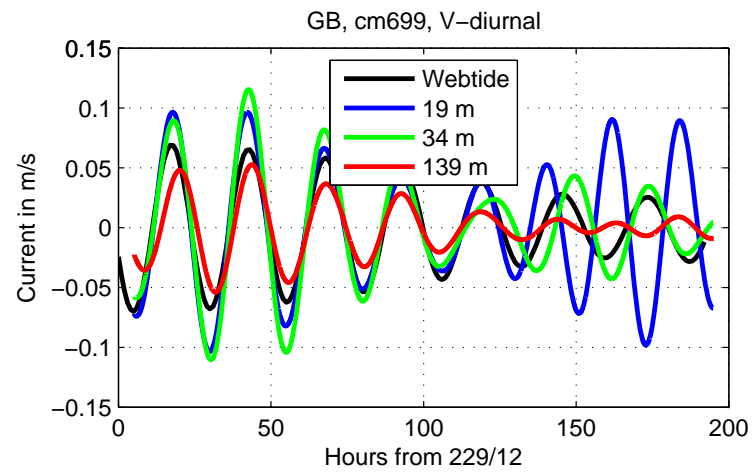
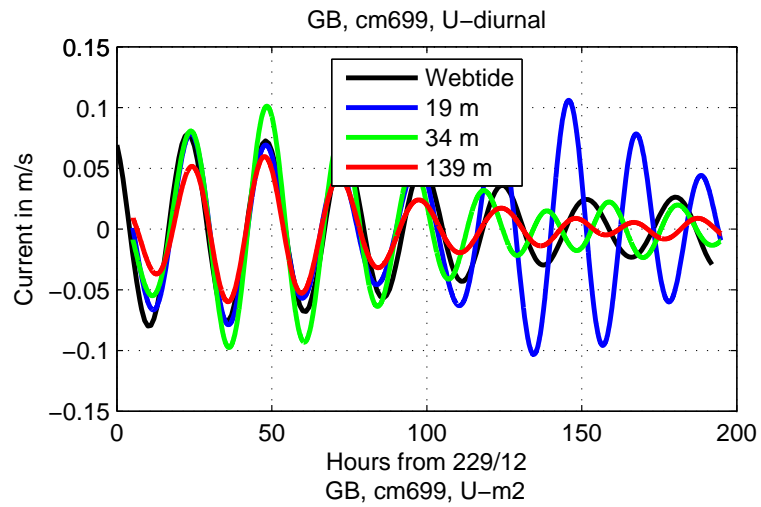


Figure A7.10: Diurnal and semi-diurnal current components at mooring 699 and barotropic current from WebTide.

## Appendix 8 CTD section in The Gully

As shown in Figure 5.1.1, three CTD sections were obtained at The Gully site before the Batfish program commenced. The center section in essence followed the axis of The Gully, starting in little more than 200 metres of water depth and ending in water exceeding 2000 metres in depth. The CTD sampling was limited to the top 400 metres. The density increased from surface to 400 metres by approximately 6 sigma units (21.5 to 27.5). In Figure A.8.1 the density field has been contoured with 60 equally spaced sigma levels (MATLAB 7.3.0 contouring package). The blank area between 50 and 150 metres for stations 15 to 17 is due to missing data.

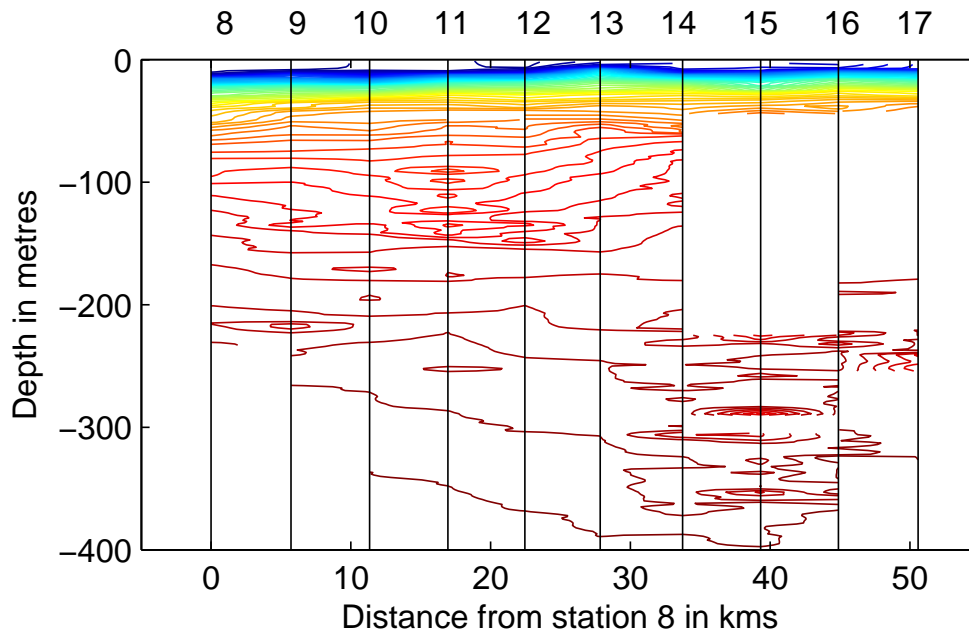


Figure A8.1: Gully density section. CTD casts 8 to 17, between hours 5 to 15 of day 232/1984.

Our attention is drawn to density reversals (closed contours, intrusions) in CTD stations 9 to 12 and again in stations 14 to 16, primarily in the upper 200 metres in the first set and between 200 and 400 metres in the second. Figure A8.2 shows gradients of density, temperature and salinity for stations 11 and 12 between 50 and 150 metres depth and Figure A8.3 shows the same parameters for stations 14 and 16 between 200 and 400 metres.

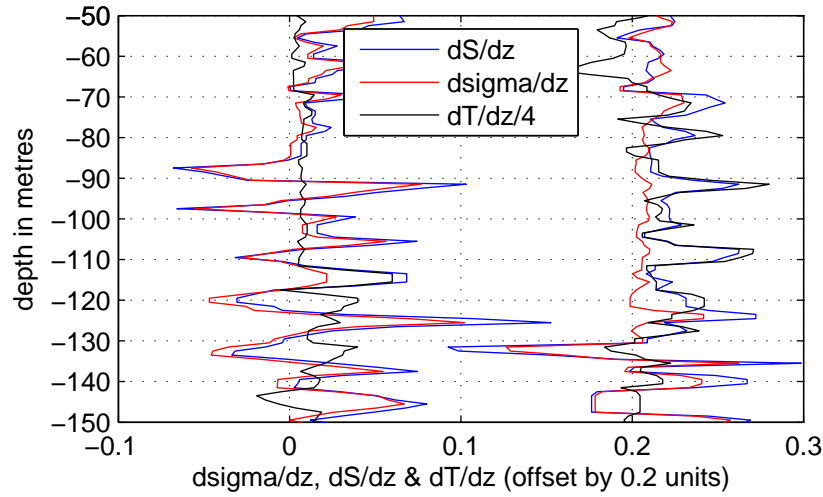


Figure A8.2: Gradients of density, salinity and temperature for stations 11 and 12. The temperature gradient is divided by 4.

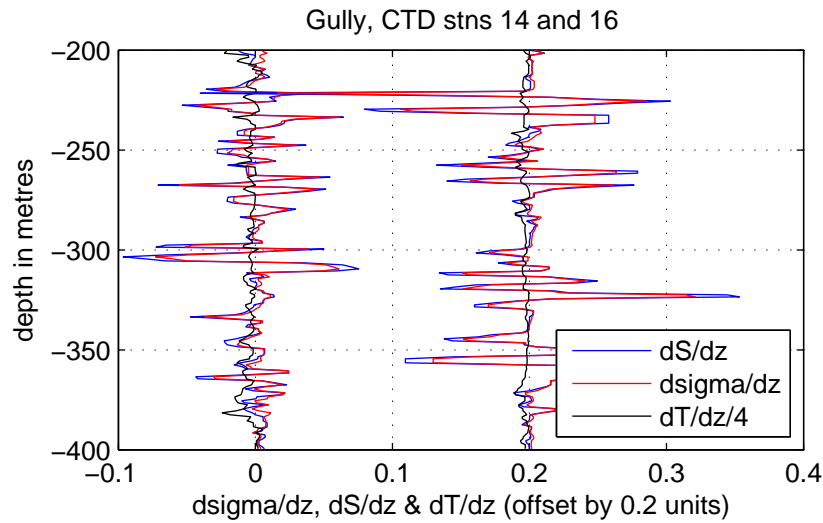


Figure A8.3: Gradients of density, salinity and temperature for stations 14 and 16. The temperature gradient is divided by 4.

Unstable layering (negative density gradients) is seen in both figures. In Figure A8.2 the unstable layer separation is approximately 10 – 12 metres and somewhat less in Figure A8.3. The density reversals are correlated with corresponding salinity reversals, whereas temperature changes play a minor role. The density reversals are signatures of active turbulence and mixing over significant ranges of depth.

In Figure A8.2 we also note layering between approximately 70 and 120 metres depth in station 12. In this case the salinity and temperature gradients are correlated, whereas density gradient remains stable. The layer separation is again  $O(10\text{ m})$ . Perhaps ‘fossil turbulence’?

Layered structure can also be seen in the main pycnocline. It can be discerned in all parameter gradient plots. These are best displayed after the gradient data has been averaged over a depth range such as 10 metres and the averaged values been deducted to show the departure from the average. This has been done in Figure A8.4, where data for stations 8, 10, 12, 14 and 16 are shown for the first 50 metres of depth.

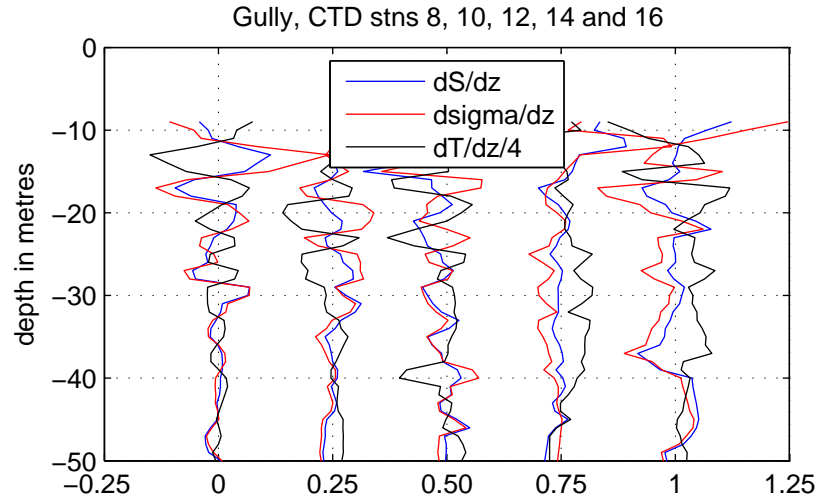


Figure A8.4: The differences of gradients of density, salinity and temperature from their average over 10 metres. The temperature gradient is divided by 4. Offset between stations is 0.25 units.

The prime cause for the unstable density layering, turbulence and mixing is undoubtedly shear instability. We have observed this process in shallower water on Banquereau Bank and in Scotian Gulf. The layering in the pycnocline as seen in Figure A8.4 may be remnant of previous turbulence, possibly on Banquereau Bank and being advected over The Gully. The instabilities in deeper water are generated *in situ*. The sources for shear, that generate them, are probably varied. Persistent and strong currents occur in the deeper parts of The Gully (Greenan, personal communication) and vary with depth. The amount of shear that they produce cannot be estimated at present. In keeping with the subject matter of this report, we estimate the possible contribution of internal tide to shear instability.

Assuming that the internal tide in The Gully proper is mainly semi-diurnal and of first mode in the vertical, we construct the eigenfunctions for various depths, which allows us to estimate the tidally produced current shear, given the displacement amplitude of the mode. The Richardson Number ( $Ri$ ) can then be estimated. CTD station 13 density profile, in which no significant reversals occur, is used for eigenfunction calculation. The depth at which the mode has its maximum displacement and where maximum current shear occurs varies with total water depth. Thus going from 200 to 1000 meters water depth, the maximum depth of current shear goes from 50 to 440 metres. The average  $N^2$  (Väisälä frequency squared) between 100 and 150 metres is  $4.2 \times 10^{-5}$  and  $1.4 \times 10^{-5}$  between 250 and 400 metres. With maximum current shear located at 125 metres, a tidal

displacement amplitude of 10 metres would be sufficient to lower  $Ri$  to 1 and 20 metres would lower it to  $\frac{1}{4}$ . With maximum shear at 250 metres displacement amplitudes of 12 and 24 metres would lead to the same  $Ri$ . Such displacement amplitudes are quite feasible. The western end of Batfish station 44 was adjacent to CTD station 13. The analysis of the M2 internal tide showed increasing displacement amplitudes from surface to almost 100 metres with the largest values approaching 10 metres in amplitude. We suggest that internal tide (perhaps in conjunction with other sources of shear) can generate sufficient shear to lead to instability.